

DESIGN AND PROPERTIES OF NOVEL URANIUM-CONTAINING
LAYERED AND FRAMEWORK MATERIALS

Except where reference is made to the work of others, the work described in this dissertation is my own or was done in collaboration with my advisory committee.
This dissertation does not include proprietary or classified information.

Tatiana Yurievna Shvareva

Certificate of Approval:

Peter Livant
Associate Professor
Chemistry

Thomas E. Albrecht-Schmitt, Chair
Associate Professor
Chemistry

Holly R. Ellis
Assistant Professor
Chemistry

Andreas J. Illies
Professor
Chemistry

Joe F. Pittman
Interim Dean
Graduate School

DESIGN AND PROPERTIES OF NOVEL URANIUM-CONTAINING
LAYERED AND FRAMEWORK MATERIALS

Tatiana Yurievna Shvareva

A Dissertation

Submitted to

the Graduate Faculty of

Auburn University

in Partial Fulfillment of the

Requirements for the

Degree of

Doctor of Philosophy

Auburn, Alabama
December 15, 2006

DESIGN AND PROPERTIES OF NOVEL URANIUM-CONTAINING
LAYERED AND FRAMEWORK MATERIALS

Tatiana Yurievna Shvareva

Permission is granted to Auburn University to make copies of this dissertation at its discretion, upon request of individuals or institutions and at their expense. The author reserves all publication rights.

Signature of Author

Date of Graduation

VITA

Tatiana Yurievna (Solonskaya) Shvareva, daughter of Yuri A. Solonsky and Galina A. (Shabalina) Solonskaya, was born on April 8, 1973, in St. Petersburg, Russia. She graduated from High School N. 419, Petergoff District, St. Petersburg in 1990, and then from St. Petersburg State University in 1995. She obtained a Bachelor of Science degree in Chemistry under the direction of Dr. Nadezhda S. Grigorova and Dr. Florentina A. Belinskaja. She entered Graduate School at Auburn University in the fall of 2003 to pursue a Doctoral degree in Chemistry under the guidance of Dr. Thomas E. Albrecht-Schmitt. She married Alexey Y. Shvarev, son of Yevgeniy A. Shvarev and Inna N. (Gulika) Shvareva on July 6th, 1996.

DISSERTATION ABSTRACT

DESIGN AND PROPERTIES OF NOVEL URANIUM-CONTAINING
LAYERED AND FRAMEWORK MATERIALS

Tatiana Y. Shvareva

Doctor of Philosophy, December 15, 2006
(B. S., St. Petersburg State University, 1995)

217 Typed Pages

Directed by Thomas E. Albrecht-Schmitt

Ten uranyl-containing frameworks and one layered material have been synthesized under hydrothermal conditions. These compounds belong to eight structure types, not previously described. They are constructed from uranyl units in different coordination environments, phosphate or iodate anions, and incorporate main group or transition metal polyhedra. Six materials were found to have selective ion exchange properties. Their stabilities at elevated temperatures were examined. Thermally stable ion exchangers could be recommended for the further investigations under the simulated conditions of nuclear waste. Introduction of transition metals also leads to the appearance of non-linear optical and magnetic properties. A new synthetic method for the production of uranyl-containing framework materials is also proposed.

ACKNOWLEDGMENT

I wish to express my sincerest gratitude to all people, inside and outside of the Chemistry Department, who helped me during this work. But the very first, I would like to thank my research advisor, Professor Thomas E. Albrecht-Schmitt. He opened the world of material chemistry to me, introduced and made me feel welcome in the actinide research community. Now I leave his group with certain wish to spend my entire career in actinide material science and to make him proud.

I would like to thank all former and present group members, whom I worked with: Richard, Phil, Tyler, Shehee, Jin (especially Jin), Ling, Travis, Noel and Yu for friendly and very helpful atmosphere in the group. In addition I need to thank little Angie Mustain for being very good student and very good friend.

I am also very grateful to my committee members, Dr. Illies, Dr. Livant and Dr. Ellis for their advice and help along the way.

I would like to express my especially warm ‘thank you’ to Dr. Lorraine Wolf and Dr. David Stanbury for the greatest help that I could ever imagine during my last year here at Auburn. They made my trip to Texas possible and I will never forget it.

I would like to thank my parents for supporting me in any decision that I have ever made. I owe them a lot for never-ending patience and ‘therapy’ when I was discouraged.

And finally I need to say that this work would never have been done without understanding, patience and day-by-day support of my love, Barbara, and Alexey, the greatest luck in my life.

Thank you all very much.

Style manual or journal used:

American Chemical Society style

Computer software used:

Microsoft Word 2000, Microsoft Excel, Atom v. 6.0, Adobe Illustrator 10

TABLE OF CONTENTS

LIST OF FIGURES	xv
LIST OF TABLES	xxiii
CHAPTER 1. INTRODUCTION	1
CRYSTAL CHEMISTRY OF URANIUM (VI) UNDER HYDROTHERMAL CONDITIONS.....	2
HIGH-LEVEL NUCLEAR WASTE (HLNW)	10
ION-EXCHANGE	14
ION-EXCHANGE LAYERED AND THREE-DIMENSIONAL INORGANIC MATERIALS FOR SELECTIVE Cs ⁺ AND Sr ²⁺ UPTAKE.....	16
MAIN GROUP AND TRANSITION METAL PHOSPHATES	24
REFERENCES	27
 CHAPTER 2. CRYSTAL CHEMISTRY AND ION-EXCHANGE PROPERTIES OF THE LAYERED POTASSIUM URANYL IODATE, K[UO ₂ (IO ₃) ₃].....	32
ABSTRACT.....	32
INTRODUCTION	33

EXPERIMENTAL.....	34
SYNTHESIS $K[UO_2(IO_3)_3]$	35
CRYSTALLOGRAPHIC STUDIES	35
ION EXCHANGE	36
RESULTS AND DISCUSSION	39
SYNTHESIS	39
STRUCTURE. $K[UO_2(IO_3)_3]$	39
ION EXCHANGE STUDIES	42
CONCLUSIONS.....	45
REFERENCES	47

CHAPTER 3. SYNTHESSES, STRUCTURES, AND ION-EXCHANGE PROPERTIES OF THE THREE-DIMENSIONAL FRAMEWORK URANYL GALLIUM

PHOSPHATES, $Cs_4[(UO_2)_2(GaOH)_2(PO_4)_4] \cdot H_2O$ AND $Cs [UO_2Ga(PO_4)_2]$	50
ABSTRACT.....	50
INTRODUCTION	51
EXPERIMENTAL.....	53
SYNTHESIS. $Cs_4[(UO_2)_2(GaOH)_2(PO_4)_4](H_2O)$ (UGaP1).....	54
SYNTHESIS. $Cs[UO_2Ga(PO_4)_2]$ (UGaP2)	54
CRYSTALLOGRAPHIC STUDIES	54
ION EXCHANGE STUDY	60
THERMAL ANALYSIS	60
RESULTS AND DISCUSSION	60

SYNTHESES	60
STRUCTURE $\text{Cs}_4[(\text{UO}_2)_2(\text{GaOH})_2(\text{PO}_4)_4](\text{H}_2\text{O})$ (UGaP1)	61
STRUCTURE $\text{Cs}[\text{UO}_2\text{Ga}(\text{PO}_4)_2]$ (UGaP2)	67
THERMAL ANALYSIS	70
ION EXCHANGE	75
CONCLUSIONS	78
REFERENCES	79

CHAPTER 4. SYNTHESIS, STRUCTURES AND PROPERTIES OF THE MULTIFUNCTIONAL URANYL VANADIUM PHOSPHATE

FRAMEWORKS	83
ABSTRACT	83
INTRODUCTION	84
EXPERIMENTAL	85
SYNTHESIS. $\text{Cs}_2[\text{UO}_2(\text{VO}_2)_2(\text{PO}_4)_2] \cdot n\text{H}_2\text{O}$ ($\text{UV}^{\text{V}}\text{P}$)	85
SYNTHESIS. $\text{K}_4(\text{UO}_2)(\text{VO})_4(\text{OH})_2(\text{PO}_4)_4$ ($\text{KUV}^{\text{IV}}\text{P}$)	86
SYNTHESIS. $\text{Rb}_4(\text{UO}_2)(\text{VO})_4(\text{OH})_2(\text{PO}_4)_4$ ($\text{RbUV}^{\text{IV}}\text{P}$)	86
CRYSTALLOGRAPHIC STUDIES	86
THERMAL ANALYSIS	87
NON-LINEAR OPTICAL PROPERTIES	87
MAGNETIC PROPERTIES	92
ION EXCHANGE STUDIES	93
RESULTS AND DISCUSSION	94

SYNTHESES	94
STRUCTURE. $\text{Cs}_2[\text{UO}_2(\text{VO}_2)_2(\text{PO}_4)_2] \cdot n\text{H}_2\text{O}$ ($\text{UV}^{\text{V}}\text{P}$).....	95
STRUCTURE. $\text{K}_4(\text{UO}_2)(\text{VO})_4(\text{OH})_2(\text{PO}_4)_4$ ($\text{KUV}^{\text{IV}}\text{P}$) AND $\text{Rb}_4(\text{UO}_2)(\text{VO})_4(\text{OH})_2(\text{PO}_4)_4$ ($\text{RbUV}^{\text{IV}}\text{P}$).....	98
THERMAL ANALYSIS	104
NON-LINEAR OPTICAL PROPERTIES	108
MAGNETIC PROPERTIES	108
ION EXCHANGE STUDY	115
CONCLUSIONS.....	116
REFERENCES	117

CHAPTER 5. HYDROTHERMAL SYNTHESIS AND STRUCTURAL

CHARACTERIZATION OF $\text{Cs}_{1.52}[(\text{UO}_2)(\text{TiOH}_{0.48})(\text{PO}_4)_2] \cdot n\text{H}_2\text{O}$ AND

$\text{Cs}_{1.35}[(\text{UO}_2)(\text{GeOH}_{0.65})(\text{PO}_4)_2] \cdot n\text{H}_2\text{O}$	120
ABSTRACT.....	120
INTRODUCTION	121
EXPERIMENTAL.....	123
SYNTHESIS. $\text{Cs}_{1.52}[(\text{UO}_2)(\text{TiOH}_{0.48})(\text{PO}_4)_2] \cdot n\text{H}_2\text{O}$ (UTiP)	124
SYNTHESIS. $\text{Cs}_{1.35}[(\text{UO}_2)(\text{GeOH}_{0.65})(\text{PO}_4)_2] \cdot n\text{H}_2\text{O}$ (UGeP).....	124
CRYSTALLOGRAPHIC STUDIES	125
RESULTS AND DISCUSSION	129
SYNTHESES	129
STRUCTURE	129

CONCLUSIONS.....	137
REFERENCES	140
CHAPTER 6. GENERAL ROUTE TO THREE-DIMENSIONAL FRAMEWORK	
URANYL TRANSITION METAL PHOSPHATES WITH ATYPICAL	
STRUCTURAL MOTIFS: THE CASE EXAMPLES OF	
$\text{Cs}_2\{(\text{UO}_2)_4[\text{Co}(\text{H}_2\text{O})_2]_2(\text{HPO}_4)(\text{PO}_4)_4\}$, $\text{Cs}_2\{(\text{UO}_2)_4[\text{Ni}(\text{H}_2\text{O})_2]_2(\text{HPO}_4)(\text{PO}_4)_4\}$,	
AND $\text{Cs}_{3+x}[(\text{UO}_2)_3\text{CuH}_{4-x}(\text{PO}_4)_5]\cdot\text{H}_2\text{O}$	144
ABSTRACT.....	144
INTRODUCTION	145
EXPERIMENTAL.....	146
SYNTHESIS. $\text{Cs}_2\{(\text{UO}_2)_4[\text{Co}(\text{H}_2\text{O})_2]_2(\text{HPO}_4)(\text{PO}_4)_4\}(\text{UCoP})$	146
SYNTHESIS. $\text{Cs}_2\{(\text{UO}_2)_4[\text{Ni}(\text{H}_2\text{O})_2]_2(\text{HPO}_4)(\text{PO}_4)_4\}(\text{UNiP})$	147
SYNTHESIS. $\text{Cs}_{3+x}[(\text{UO}_2)_3\text{CuH}_{4-x}(\text{PO}_4)_5]\cdot\text{H}_2\text{O}(\text{UCuP})$	147
X-RAY STRUCTURAL ANALYSIS	147
THERMAL ANALYSIS	148
UV-VIS-NIR DIFFUSE REFLECTANCE SPECTRA.....	156
MAGNETIC PROPERTIES.....	156
ION EXCHANGE STUDIES	157
RESULTS AND DISCUSSION	158
SYNTHESES	158
STRUCTURE. $\text{Cs}_2\{(\text{UO}_2)_4[\text{Co}(\text{H}_2\text{O})_2]_2(\text{HPO}_4)(\text{PO}_4)_4\}(\text{UCoP})$	
AND $\text{Cs}_2\{(\text{UO}_2)_4[\text{Ni}(\text{H}_2\text{O})_2]_2(\text{HPO}_4)(\text{PO}_4)_4\}(\text{UNiP})$	159

STRUCTURE . $\text{Cs}_{3+x}[(\text{UO}_2)_3\text{CuH}_{4-x}(\text{PO}_4)_5]\cdot\text{H}_2\text{O}$ (UCuP)	162
UV-VIS-NIR DIFFUSE REFLECTANCE STUDY	171
MAGNETIZATION MEASUREMENTS.....	174
THERMAL ANALYSIS	178
ION EXCHANGE PROPERTIES	183
CONCLUSIONS	184
REFERENCES	186
CHAPTER 7. SUMMARY.....	189

LIST OF FIGURES

Figure 1. 1. The UO_2^{2+} cation in tetragonal bipyramidal, pentagonal bipyramidal, and hexagonal bipyramidal environments as common building units for uranyl structure formation. They can be interconnected by corner- or edge-sharing with each other or other building units in order to construct different structure types	5
Figure 1. 2. The structure of $(\text{C}_4\text{N}_2\text{H}_{12})\text{U}_2\text{O}_4\text{F}_6$ composed of only uranyl pentagonal bipyramids (green). Piperazinium cations are located in the channels of the framework	6
Figure 1. 3. The structure of $\text{K}_2[(\text{UO}_2)_2(\text{VO})_2(\text{IO}_6)_2\text{O}]\cdot\text{H}_2\text{O}$ is built from distorted octahedral building units only. UO_6 polyhedra are shown in green, VO_6 –in light blue, and IO_6 – in red color. K^+ cations along with water molecules occupy the tunnels. The UO_2^{2+} uranyl unit exists as a nearly linear trans dioxo unit	7
Figure 1. 4. The structure of $\text{Li}_2(\text{UO}_2)_4(\text{WO}_4)\text{O}$ is an example of a three-dimensional structure with no channels. Li^+ cations located in the voids of uranyl tungstate layers are not seen from this projection. UO_6 polyhedra are green, WO_6 – shown in violet color	9

Figure 1. 5. Chiral channels extended along c axis make the uranyl molybdate $(\text{NH}_4)_4[(\text{UO}_2)_5(\text{MoO}_4)_7](\text{H}_2\text{O})_5$ potentially applicable for enantio-selective separation. NH_4^+ cations are not shown, UO_7 polyhedra are green, MoO_4 tetrahedra are blue	11
Figure 1. 6. A view of the crystal structure of $\text{Na}_2\text{Ti}_2\text{O}_3(\text{SiO}_4)\cdot\text{H}_2\text{O}$ along the $[001]$ direction. Yellow squares depict TiO_6 octahedra, orange - SiO_4 tetrahedra, green balls – Na^+ cations. Four out of the total eight Na^+ cations are located in the channels, the other four (on the silicate groups) – in small cavities. Copied from reference 50 with author's permission	18
Figure 1. 7. This fragment depicts interconnection of octahedral units in the structure of $\text{Na}_2\text{Nb}_{2-x}\text{Ti}_x\text{O}_{6-x}(\text{OH})_x\cdot\text{H}_2\text{O}$. Blue polyhedra represent disordered NbO_6 and TiO_6 octahedra. Yellow polyhedra are Na coordination spheres, participating in the framework. Copied from reference 52 with author's permission	23
Figure 2. 1. A view of the pentagonal bipyramidal coordination environment around uranium center in KUI that is formed from UO_2^{2+} linear cation connected with five iodate groups through the equatorial plane	41
Figure 2. 2. An illustration of the $\frac{2}{\infty}[\text{UO}_2(\text{IO}_3)_3]^{1-}$ sheets in KUI that extend in the $[ab]$ plane	43
Figure 2. 3. A view along the b axis of KUI showing that the monodentate iodate anion protrudes in between the layers, providing its terminal oxo	

atoms for forming interactions with the K^+ cations that reside between the layers	44
Figure 3. 1. A view of the one-dimensional ${}^1_{\infty}[\text{Ga}(\text{OH})(\text{PO}_4)_2]^{4-}$ chains composed of corner-sharing GaO_6 octahedra and bridging PO_4 tetrahedra that extend along the c axis in $\text{Cs}_4[(\text{UO}_2)_2(\text{GaOH})_2(\text{PO}_4)_4] \cdot \text{H}_2\text{O}$ (UGaP1). 50% probability ellipsoids are depicted	63
Figure 3. 2. A depiction of the one-dimensional ${}^1_{\infty}[\text{UO}_2(\text{PO}_4)_2]^{4-}$ chains in $\text{Cs}_4[(\text{UO}_2)_2(\text{GaOH})_2(\text{PO}_4)_4] \cdot \text{H}_2\text{O}$ (UGaP1). 50% probability ellipsoids are depicted	67
Figure 3. 3. An illustration of the three-dimensional ${}^3_{\infty}[(\text{UO}_2)_2(\text{GaOH})_2(\text{PO}_4)_4]^{4-}$ anionic lattice of $\text{Cs}_4[(\text{UO}_2)_2(\text{GaOH})_2(\text{PO}_4)_4] \cdot \text{H}_2\text{O}$ (UGaP1) that has intersecting channels running down the b and c axes. These channels house Cs^+ cations and water molecules. Cs is shown in magenta, UO_7 pentagonal bipyramids are shown in green, GaO_6 octahedra in blue, and PO_4 tetrahedra in yellow	69
Figure 3. 4. A view of the one-dimensional ${}^1_{\infty}[\text{Ga}(\text{PO}_4)_2]^{3-}$ gallium phosphate chains in $\text{Cs}[\text{UO}_2\text{Ga}(\text{PO}_4)_2]$ (UGaP2) formed from fused eight-membered rings of alternating corner-shared GaO_4 and PO_4 tetrahedra. 50% probability ellipsoids are depicted	70
Figure 3. 5. An illustration of the one-dimensional ${}^1_{\infty}[\text{UO}_2(\text{PO}_4)_2]^{4-}$ chains in $\text{Cs}[\text{UO}_2\text{Ga}(\text{PO}_4)_2]$ (UGaP2). 50% probability ellipsoids are depicted	72

Figure 3. 6. A depiction of the three-dimensional ${}^3_{\infty}[\text{UO}_2\text{Ga}(\text{PO}_4)_2]^{1-}$ framework in $\text{Cs}[\text{UO}_2\text{Ga}(\text{PO}_4)_2]$ (UGaP2) with intersecting channels running down the a and b axes. Cs is shown in magenta, UO_7 pentagonal bipyramids are shown in green, GaO_4 tetrahedra in blue, and PO_4 tetrahedra in yellow.....	73
Figure 3. 7. DSC data of UGaP1 demonstrate relative stability of the structure at temperatures below 400 °C. Two peaks at 150 °C and 172 °C correspond to lost of surface and interstitial water respectively.....	74
Figure 3. 8. DSC data of UGaP2.....	77
Figure 4. 1. Depiction of the channels of $\text{UV}^{\text{V}}\text{P}$, extended along b and c axes, occupied by Cs^+ cations. Green – uranium, blue – vanadium, yellow – phosphorus, purple – cesium centers	97
Figure 4. 2. The fundamental building unit of $\text{UV}^{\text{V}}\text{P}$ shown in 50% probability thermal ellipsoids	100
Figure 4. 3. Thermal ellipsoid plot of the fundamental unit of $\text{K}_4(\text{UO}_2)(\text{VO})_4(\text{OH})_2(\text{PO}_4)_4$ ($\text{KUV}^{\text{IV}}\text{P}$) and $\text{Rb}_4(\text{UO}_2)(\text{VO})_4(\text{OH})_2(\text{PO}_4)_4$ ($\text{RbUV}^{\text{IV}}\text{P}$) at 50% probability.....	101
Figure 4. 4. Depiction of essential building blocks of the structures of $\text{KUV}^{\text{IV}}\text{P}$ and $\text{RbUV}^{\text{IV}}\text{P}$. V_2O_9 dimer, constructed from two vanadium octahedra, sharing two equatorial and one axial oxygen atoms (top) and vanadyl phosphate layers (bottom). Cations (purple) occupy the channels $2.8 \text{ \AA} \times 4.4 \text{ \AA}$ along c axis. Blue - vanadium polyhedra, yellow – phosphate groups	104

Figure 4. 5. Depiction of the channels in the framework of $\text{KUV}^{\text{IV}}\text{P}$ and $\text{RbUV}^{\text{IV}}\text{P}$, filled with K^+ or Rb^+ cations, extended along a axis. Blue - vanadium, yellow – phosphorus, green – uranium centers, purple – K^+ or Rb^+ cations	106
Figure 4. 6. A view of the framework of $\text{KUV}^{\text{IV}}\text{P}$ and $\text{RbUV}^{\text{IV}}\text{P}$ along the b axis	107
Figure 4. 7. DSC data for the structure of $\text{UV}^{\text{V}}\text{P}$ demonstrate thermal stability up to 510 °C	108
Figure 4. 8. DSC data for the structure of $\text{KUV}^{\text{IV}}\text{P}$. Several endothermic events between 160 °C and 550 °C reveal gradual structural transformations with increase of temperature	110
Figure 4. 9. Magnetization of $\text{UV}^{\text{V}}\text{P}$ as a function of applied magnetic field at 5 K. Line is the linear fit to the data	111
Figure 4. 10. Magnetic susceptibility of $\text{UV}^{\text{V}}\text{P}$ as a function of temperature with a 10000 G magnetic field	112
Figure 4. 11. Magnetization of $\text{RbUV}^{\text{IV}}\text{P}$ as a function of applied magnetic field at 5 K. Line is the linear fit to the data	114
Figure 4. 12. Magnetic susceptibility of $\text{RbUV}^{\text{IV}}\text{P}$ as a function of temperature. Line is the fit to Curie-Weiss behavior. Inset show the temperature dependence of the inverse magnetic susceptibility	115
Figure 5. 1. Thermal ellipsoid plot of $\text{Cs}_{1.52}[(\text{UO}_2)(\text{TiOH}_{0.48})(\text{PO}_4)_2] \cdot n\text{H}_2\text{O}$ (UTiP) shown at 50% probability	132
Figure 5. 2. Depiction of one-dimensional titanium phosphate or germanium phosphate and uranyl phosphate chains in UTiP or UGeP.	

Violet - titanium or germanium polyhedra, yellow-phosphate tetrahedra, green-uranyl building units	133
Figure 5. 3. The framework of UTiP and UGeP. The channels along the <i>c</i> axis are filled with Cs ⁺ cations (purple) and water molecules (red). Violet octahedra represent Ti or Ge, yellow – phosphate, and green – uranium centers	137
Figure 6. 1. The fundamental building unit of UCoP includes three crystallographically unique U centers, two in pentagonal bipyramidal, and one in hexagonal bipyramidal environment, three tetrahedral P centers, and Co octahedra. 50% probability thermal ellipsoids are represented. UNiP is isostructural with UCoP.....	162
Figure 6. 2. View down the <i>c</i> axis of the uranyl phosphate layers in UCoP and UNiP. One of the phosphate anions is disordered and is shown in ball-and-stick format. Uranium polyhedra are in green and phosphate are in yellow	163
Figure 6. 3. An illustration of the three-dimensional structure of UCoP and UNiP as viewed down the <i>b</i> axis. Uranium polyhedra are in green, phosphate in yellow, cobalt or nickel in orange. Purple centers represent the Cs ⁺ cations	165
Figure 6. 4. A view of the uranyl tetragonal and pentagonal bipyramids, square planar Cu and phosphate tetrahedra in UCuP with 50% probability ellipsoids	169
Figure 6. 5. Depiction of uranyl phosphate layers in UCuP. Uranyl polyhedra are	

in green and phosphates are in yellow	171
Figure 6. 6. View of the three-dimensional structure of UCuP wherein the Cu ^{II} centers link uranyl phosphate layers together. Uranium polyhedra are in green, phosphate in yellow, and copper in blue. Some of the Cs ⁺ sites have been omitted for clarity	172
Figure 6. 7. UV-vis-NIR diffuse reflectance spectrum of UCoP. F(R) corresponds to Kubelka-Monk function and relates reflectance data to the absorption spectra. ³⁷	174
Figure 6. 8. UV-vis-NIR diffuse reflectance spectrum of UNiP. F(R) corresponds to Kubelka-Monk function and relates reflectance data to the absorption spectra. ³⁷	175
Figure 6. 9. UV-vis-NIR diffuse reflectance spectrum for UCuP. F(R) corresponds to Kubelka-Monk function and relates reflectance data to the absorption spectra. ³⁷	177
Figure 6. 10. Magnetization of UCoP as a function of applied magnetic field at 5 K. Line is the linear fit to the data.....	178
Figure 6. 11. Magnetic susceptibility of UCoP as a function of temperature. Line is the fit to Curie-Weiss behavior. Inset show the temperature dependence of the inverse magnetic susceptibility with a linear fit.	179
Figure 6. 12. Magnetization of UCuP as a function of applied magnetic field at 5 K. Line is the linear fit to the data.	180
Figure 6. 13. Magnetic susceptibility of UCuP as a function of temperature. Line is the fit to Curie-Weiss behavior. Inset show the temperature	

dependence of the inverse magnetic susceptibility	181
Figure 6. 14. DSC data for UCoP	183
Figure 6. 15. DSC data for UCuP	184

LIST OF TABLES

Table 1. 1. The Most Significant Contributors to the Radiation Dose from HLNW	13
Table 1. 2. Crystallographic Data for $\text{Na}_2\text{Ti}_2\text{O}_3(\text{SiO}_4)\cdot\text{H}_2\text{O}$ (TiSi-1), $\text{HM}_3\text{Ti}_4\text{O}_4(\text{SiO}_4)\cdot\text{H}_2\text{O}$ (TiSi-2) and $\text{Na}_2\text{Nb}_{2-x}\text{M}_x\text{O}_{6-x}(\text{OH})_x\cdot\text{H}_2\text{O}$ (SOMS)	19
Table 1. 3. The Comparative Table of Distribution Coefficients for Sr^{2+} , K_{DSr} , of $\text{Na}_4\text{Ti}_9\text{O}_{20}\cdot n\text{H}_2\text{O}$, $\text{Na}_2\text{Ti}_2\text{O}_3(\text{SiO}_4)\cdot\text{H}_2\text{O}$, and $\text{HK}_3\text{Ti}_4\text{O}_4(\text{SiO}_4)\cdot\text{H}_2\text{O}^{64}$ in Different HLNW Simulants	21
Table 2. 1. Crystallographic Data for $\text{K}[\text{UO}_2(\text{IO}_3)_3]$ (KUI)	37
Table 2. 2. Atomic Coordinates and Equivalent Isotropic Displacement Parameters for $\text{K}[\text{UO}_2(\text{IO}_3)_3]$ (KUI)	38
Table 2. 3. Selected Bond Distances (Å) and Angles (°) for $\text{K}[\text{UO}_2(\text{IO}_3)_3]$ (KUI)	40
Table 3. 1. Crystallographic Data for $\text{Cs}_4[(\text{UO}_2)_2(\text{GaOH})_2(\text{PO}_4)_4]\cdot\text{H}_2\text{O}$ (UGaP1) and $\text{Cs}[\text{UO}_2\text{Ga}(\text{PO}_4)_2]$ (UGaP2)	57
Table 3. 2. Atomic Coordinates and Equivalent Isotropic Displacement Parameters for $\text{Cs}_4[(\text{UO}_2)_2(\text{GaOH})_2(\text{PO}_4)_4]\cdot\text{H}_2\text{O}$ (UGaP1)	58
Table 3. 3. Atomic Coordinates and Equivalent Isotropic Displacement Parameters for $\text{Cs}[\text{UO}_2\text{Ga}(\text{PO}_4)_2]$ (UGaP2)	60
Table 3. 4. Selected Bond Distances (Å) and Angles (°) for $\text{Cs}_4[(\text{UO}_2)_2(\text{GaOH})_2(\text{PO}_4)_4]$ (UGaP1)	64

Table 3. 5. Selected Bond Distances (\AA) and Angles ($^{\circ}$) for $\text{Cs}[\text{UO}_2\text{Ga}(\text{PO}_4)_2]$ (UGaP2)	72
Table 4. 1. Crystallographic Data for $\text{Cs}_2[\text{UO}_2(\text{VO}_2)_2(\text{PO}_4)_2] \cdot n\text{H}_2\text{O}$ ($\text{UV}^{\text{V}}\text{P}$), $\text{K}_4(\text{UO}_2)(\text{VO})_4(\text{OH})_2(\text{PO}_4)_4$ ($\text{KUV}^{\text{IV}}\text{P}$) and $\text{Rb}_4(\text{UO}_2)(\text{VO})_4(\text{OH})_2(\text{PO}_4)_4$ ($\text{RbUV}^{\text{IV}}\text{P}$).....	89
Table 4. 2. Atomic Coordinates and Equivalent Isotropic Displacement Parameters for $\text{Cs}_2[\text{UO}_2(\text{VO}_2)_2(\text{PO}_4)_2] \cdot n\text{H}_2\text{O}$ ($\text{UV}^{\text{V}}\text{P}$)	90
Table 4. 3. Atomic Coordinates and Equivalent Isotropic Displacement Parameters for $\text{K}_4(\text{UO}_2)(\text{VO})_4(\text{OH})_2(\text{PO}_4)_4$ ($\text{KUV}^{\text{IV}}\text{P}$).....	91
Table 4. 4. Atomic Coordinates and Equivalent Isotropic Displacement Parameters for $\text{Rb}_4(\text{UO}_2)(\text{VO})_4(\text{OH})_2(\text{PO}_4)_4$ ($\text{RbUV}^{\text{IV}}\text{P}$)	92
Table 4. 5. Selected Bond Distances (\AA) and Angles ($^{\circ}$) for $\text{Cs}_2[\text{UO}_2(\text{VO}_2)_2(\text{PO}_4)_2] \cdot n\text{H}_2\text{O}$ ($\text{UV}^{\text{V}}\text{P}$)	98
Table 4. 6. Selected Bond Distances (\AA) and Angles ($^{\circ}$) for $\text{K}_4(\text{UO}_2)(\text{VO})_4(\text{OH})_2(\text{PO}_4)_4$ ($\text{KUV}^{\text{IV}}\text{P}$). Data for $\text{Rb}_4(\text{UO}_2)(\text{VO})_4(\text{OH})_2(\text{PO}_4)_4$ ($\text{RbUV}^{\text{IV}}\text{P}$) are given in parathensis.....	102
Table 5. 1. Crystallographic Data for $\text{Cs}_{1.52}[(\text{UO}_2)(\text{TiOH}_{0.48})(\text{PO}_4)_2] \cdot n\text{H}_2\text{O}$ (UTiP) and $\text{Cs}_{1.35}[(\text{UO}_2)(\text{GeOH}_{0.65})(\text{PO}_4)_2] \cdot n\text{H}_2\text{O}$ (UGeP)	127
Table 5. 2. Atomic Coordinates and Equivalent Isotropic Displacement Parameters for $\text{Cs}_{1.52}[(\text{UO}_2)(\text{TiOH}_{0.48})(\text{PO}_4)_2] \cdot n\text{H}_2\text{O}$ (UTiP)	128
Table 5. 3. Atomic Coordinates and Equivalent Isotropic Displacement Parameters for $\text{Cs}_{1.35}[(\text{UO}_2)(\text{GeOH}_{0.65})(\text{PO}_4)_2] \cdot n\text{H}_2\text{O}$ (UGeP).....	129
Table 5. 4. Selected Bond Distances (\AA) and Angles ($^{\circ}$) for	

$\text{Cs}_{1.52}[(\text{UO}_2)(\text{TiOH}_{0.48})(\text{PO}_4)_2] \cdot n\text{H}_2\text{O}$ (UTiP).....	135
Table 5. 5. Selected Bond Distances (\AA) and Angles ($^\circ$) for	
$\text{Cs}_{1.35}[(\text{UO}_2)(\text{GeOH}_{0.65})(\text{PO}_4)_2] \cdot n\text{H}_2\text{O}$ (UGeP)	136
Table 6. 1. Crystallographic Data for $\text{Cs}_2\{(\text{UO}_2)_4[\text{Co}(\text{H}_2\text{O})_2]_2(\text{HPO}_4)(\text{PO}_4)_4\}$	
(UCoP), $\text{Cs}_2\{(\text{UO}_2)_4[\text{Ni}(\text{H}_2\text{O})_2]_2(\text{HPO}_4)(\text{PO}_4)_4\}$ (UNiP) and	
$\text{Cs}_{3+x}[(\text{UO}_2)_3\text{CuH}_{4-x}(\text{PO}_4)_5] \cdot \text{H}_2\text{O}$ (UCuP)	151
Table 6. 2. Atomic Coordinates and Equivalent Isotropic Displacement Parameters	
for $\text{Cs}_2\{(\text{UO}_2)_4[\text{Co}(\text{H}_2\text{O})_2]_2(\text{HPO}_4)(\text{PO}_4)_4\}$ (UCoP).....	152
Table 6. 3. Atomic Coordinates and Equivalent Isotropic Displacement Parameters	
for $\text{Cs}_2\{(\text{UO}_2)_4[\text{Ni}(\text{H}_2\text{O})_2]_2(\text{HPO}_4)(\text{PO}_4)_4\}$ (UNiP)	154
Table 6. 4. Atomic Coordinates and Equivalent Isotropic Displacement Parameters	
for $\text{Cs}_{3+x}[(\text{UO}_2)_3\text{CuH}_{4-x}(\text{PO}_4)_5] \cdot \text{H}_2\text{O}$ (UCuP).....	156
Table 6. 5. Selected Bond Distances (\AA) and Angles ($^\circ$) for	
$\text{Cs}_2\{(\text{UO}_2)_4[\text{Co}(\text{H}_2\text{O})_2]_2(\text{HPO}_4)(\text{PO}_4)_4\}$ (UCoP)	166
Table 6. 6. Selected Bond Distances (\AA) and Angles ($^\circ$) for	
$\text{Cs}_2\{(\text{UO}_2)_4[\text{Ni}(\text{H}_2\text{O})_2]_2(\text{HPO}_4)(\text{PO}_4)_4\}$ (UNiP).....	167
Table 6. 7. Selected Bond Distances (\AA) and Angles ($^\circ$) for	
$\text{Cs}_{3+x}[(\text{UO}_2)_3\text{CuH}_{4-x}(\text{PO}_4)_5] \cdot \text{H}_2\text{O}$ (UCuP)	170

CHAPTER 1

INTRODUCTION

The successful test of the first nuclear reactor at the University of Chicago in 1942¹ changed the course of history. This experiment initiated not only the “Manhattan Project”, and later the production of nuclear power,² but it also produced the first portion of highly radioactive nuclear waste. Since that time the search for appropriate long-term storage conditions for high-level nuclear waste (HLNW) and spent nuclear fuel (SNF), as well as investigations into possibilities for the reduction of the total nuclear waste amounts became an issue of world-wide importance.³⁻⁶ The detailed knowledge about the fundamental chemistry of actinides is an essential basis for predicting the behavior of waste under different environmental conditions. Interactions of SNF with underground water and formation of the alteration phases under storage conditions⁶⁻⁹, or the mobility of actinides in soils⁶ are just a couple of selected issues that will be addressed herein.

The separation of the major fission products ¹³⁷Cs and ⁹⁰Sr from SNF is critical to the proper storage of radioactive waste.^{3,4} These two radionuclides with half-lives of 30.2 and 28.5 years, respectively, are the source of 99% of the present radioactivity in the HLNW storage tanks. They are distributed between salt cake – the solid portion of the waste on the top, and liquid portions - hydroxide sludge and alkaline supernatant.³ The removal of Cs⁺ and Sr²⁺ will significantly reduce the total amount of nuclear waste. One of the proposed techniques for such removal, ion-exchange, also will allow the transfer of

Cs^+ and Sr^{2+} from liquid to the solid phase, and will make the final disposal possible. This method requires the use of layered or framework materials, that should have a high capacity and selectivity for Cs^+ and Sr^{2+} , be resistant to elevated temperature and radiation damage, and should be easily synthesized.¹⁰

The general purpose of this research project is to expand the existing knowledge of the crystal chemistry of uranium compounds with novel structural topologies, to develop new synthetic methods, and address potential applications of these materials. The other major goal is to synthesize uranium-containing layered or three-dimensional compounds with ion-exchange properties selective for Cs^+ or Sr^{2+} . These materials in exchanged form will be able to tightly hold ^{137}Cs or ^{90}Sr , and provide safe and dense storage environments for U and ^{137}Cs or ^{90}Sr simultaneously.

CRYSTAL CHEMISTRY OF URANIUM (VI) UNDER HYDROTHERMAL CONDITIONS

Uranium is found as a component of approximately 200 mineral crystal structures.^{11,12} The majority of these minerals are present in the oxidizing zones of U deposits and should be accurately studied in both prospects as deeply stored nuclear waste and as potential products of oxidation of SNF and its interaction with water (alteration phases) in the geological repository locations. Precise investigation of the structures, as well as the stability and properties of uranium compounds synthesized under hydrothermal conditions, will help researchers to understand and predict the behavior of uranium phases in expected geological sites.

The term “hydrothermal synthesis” usually refers to all reactions having water as a solvent carried out at temperatures between the boiling and supercritical points of water and at pressures above 1 bar.¹³ These temperature and pressure conditions were chosen for our experiments due to similar conditions for the geological formation of minerals. In addition, hydrothermal synthesis potentially allows for the synthesis of compounds with lower densities through the incorporation of water in the structures versus more dense products that are typically isolated from high temperature reactions.

In the majority of both uranium-containing solids and solutions that are of an oxidizing nature, U is present in the +6 oxidation state. In order to maintain such a high positive charge, two short U=O bonds in trans arrangement with an average U=O distance of 1.79(3) Å are formed,¹² yielding approximately linear $[\text{UO}_2]^{2+}$ cation. Because these two oxygen atoms donate their electron density to the uranium center and hence stabilize the high oxidation state of U, they seldom participate in bond formation with other units. According to bond valence sum calculations based on the uranyl-oxygen distances, these two axial oxygen atoms contribute more than half to the valence of the uranium center.¹⁴ The concept of bond valence sum can be used in solid state chemistry in order to estimate bond lengths of a metal in a given oxidation state or to calculate the valence of the atom from the known distances.¹⁵

Interactions between uranyl and other donor atoms occur in the equatorial plane where the metal center can be coordinated with four, five, or six ligands, with distances ranging from 2.2 Å to 2.6 Å. Thus, traditionally the basic building unit for uranyl-containing compounds can be drawn as tetragonal, pentagonal, or hexagonal bipyramids terminated at each apex by two uranyl oxygen atoms. These three basic uranyl polyhedra

can be combined through various modes of corner or edge sharing with each other (Figure 1.1), or by bridging with other building units, to yield a myriad of crystal structure topologies.^{11,12}

Due to the presence of two terminal oxygen atoms, one direction for the connectivity in uranyl bipyramids is eliminated, yielding structures that are generally layered. In fact, more than 65% of all known structures of uranyl containing compounds are sheets.^{11,12} For the formation of the compounds with three-dimensional structure, where building blocks are interconnected in all three directions, usually, but not always, non-uranyl polyhedra are incorporated into the structure that give additional directions for bond formation.

There are several strategies for the building of three-dimensional structures that contain uranium. Very few three-dimensional structures are built from uranyl building units only.¹⁶⁻¹⁸ For instance, $(C_4N_2H_{12})U_2O_4F_6$ consists of only one type of building units - UO_2F_5 pentagonal bipyramids, which are connected by U-F-U bonds.¹⁸ This structure also can be described as an open-framework because of the presence of several large channels, extended along different directions that are filled with charge-balancing piperazinium cations (Figure 1.2).

The other synthetic approach includes incorporation of octahedra of other metals such as V or W in the structure.^{19,20} $K_2[(UO_2)_2(VO)_2(IO_6)_2O] \cdot H_2O$ (Figure 1.3) is constructed entirely from distorted octahedral building units.¹⁹ The UO_6 distortion in this structure is associated with the formation of short uranyl bonds and nonequality of equatorial U-O bond lengths, VO_6 – with the presence of short vanadyl V=O bond

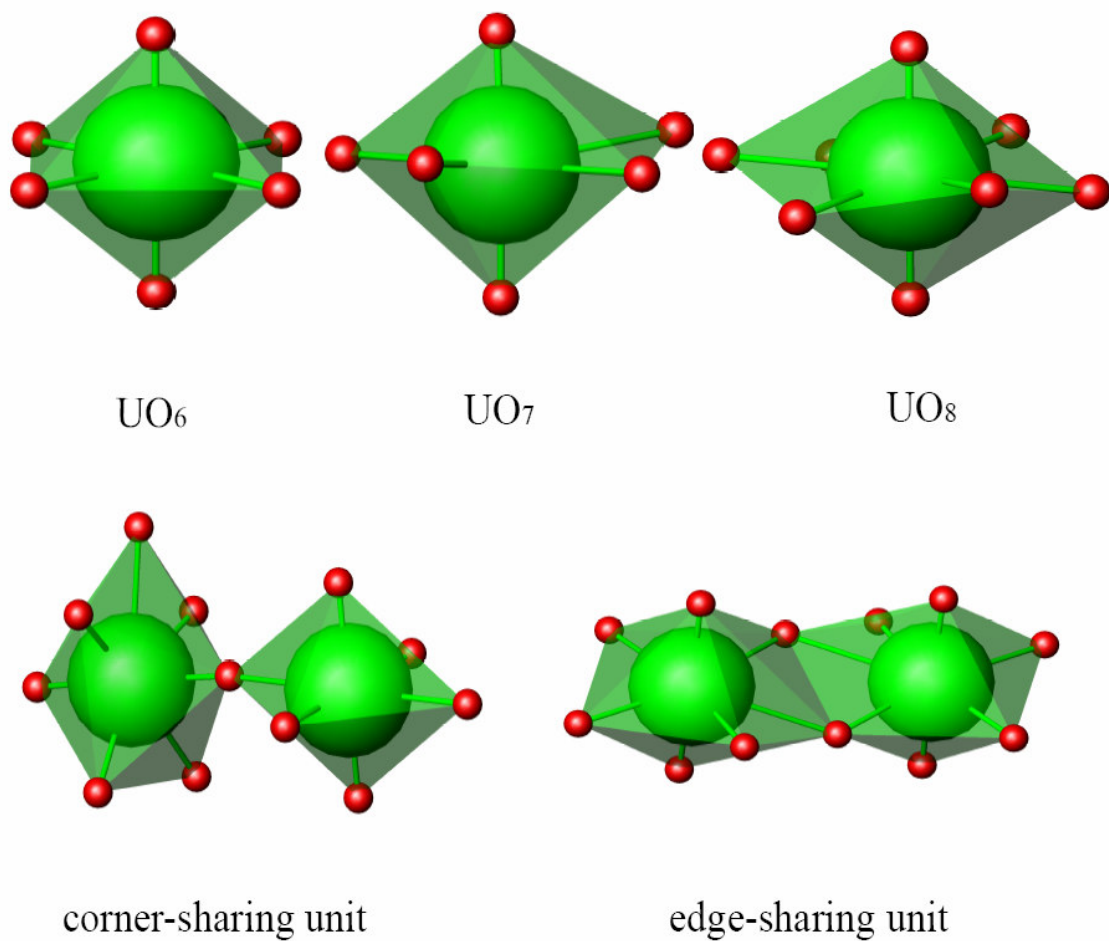


Figure 1. 1. The UO_2^{2+} cation in tetragonal bipyramidal, pentagonal bipyramidal, and hexagonal bipyramidal environments as common building units for uranyl structure formation. They can be interconnected by corner- or edge-sharing with each other or other building units in order to construct different structure types.

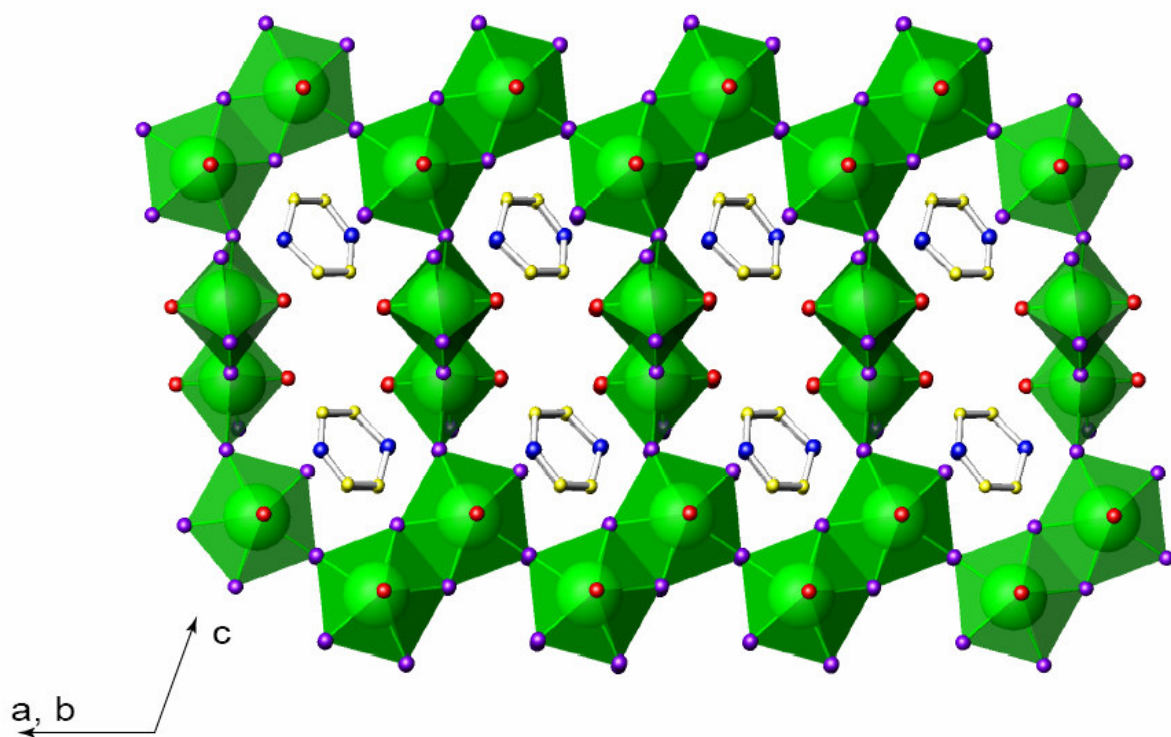


Figure 1. 2. The structure of $(C_4N_2H_{12})U_2O_4F_6$ composed of only uranyl pentagonal bipyramids (green). Piperazinium cations are located in the channels of the framework.

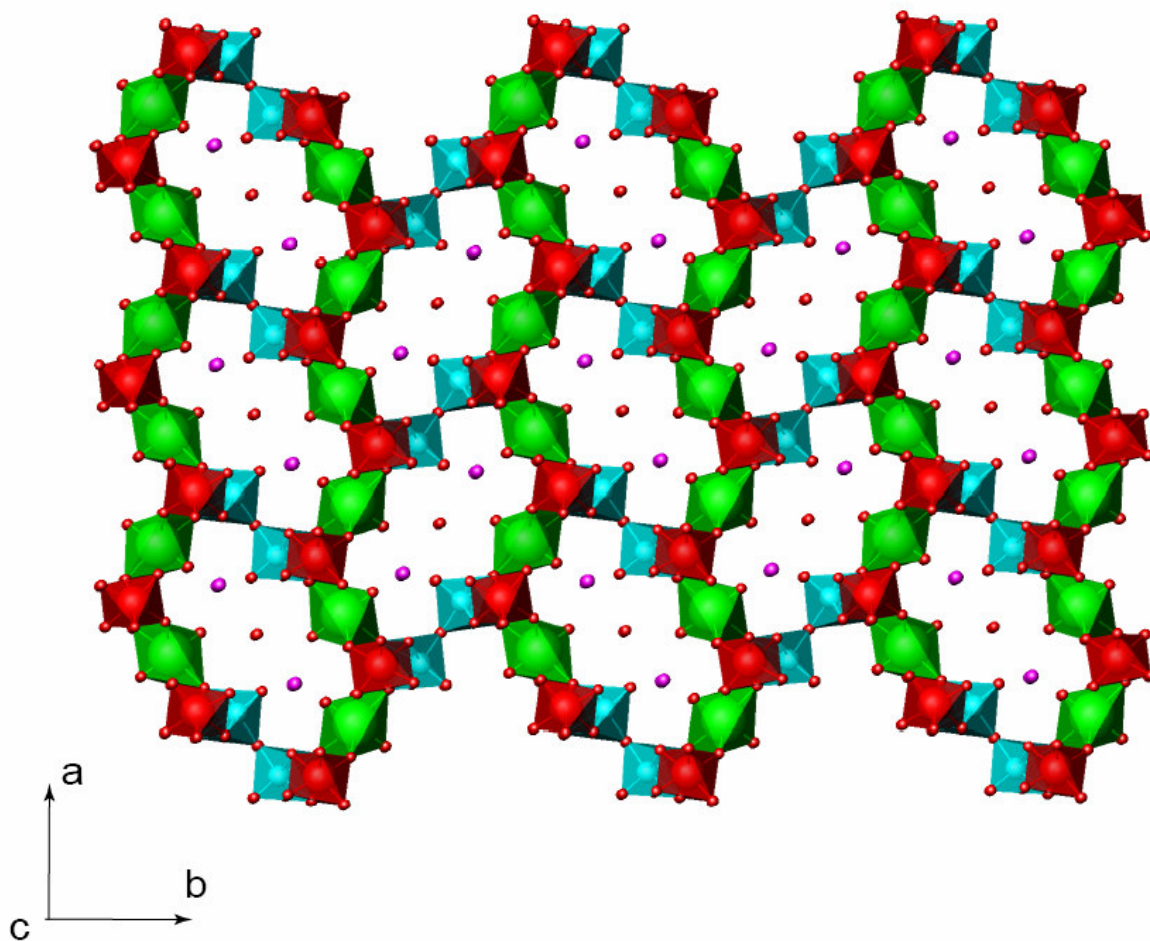


Figure 1. 3. The structure of $\text{K}_2[(\text{UO}_2)_2(\text{VO})_2(\text{IO}_6)_2\text{O}] \cdot \text{H}_2\text{O}$ is built from distorted octahedral building units only. UO_6 polyhedra are shown in green, VO_6 – in light blue, IO_6 – in red, and K^+ cation – in magenta. K^+ cations along with water molecules occupy the tunnels.

(1.58(1) Å) and a long bond in the trans-position relative to V=O (2.38(1) Å). IO₆ octahedra also show variations in I-O bond length from 1.84(1) Å to 1.93(1) Å. The octahedra create an open-framework structure with channels in two perpendicular directions, both occupied by K⁺ cations.

Li₂(UO₂)₄(WO₄)O (Figure 1.4) is an example of a three-dimensional, but non-open-framework structure.²⁰ Very small channels are present only in the [$\bar{1}$ 10] direction, and they are not filled with cations. Instead, Li⁺ cations are located within the voids in the plane of layers. Despite the absence of channels, this material was reported to have high cationic conductivity, comparable with Li β-alumina and LiSiCON materials.²⁰

Most of the uranyl-containing three-dimensional materials are built from uranyl units and tetrahedral anions, such as phosphate or arsenate,²¹⁻²⁶ sulfate,²⁷ silicate,²⁸⁻³³ vanadate^{34,35} or others. These structures can be constructed in many different manners, such as the interconnection of one-dimensional chains or layers by single building blocks, intersection of several one-dimensional chains extended along different axes, or by other methods.

We hypothesized that the introduction of octahedral building units containing main group (Ga, In, Ge) or transitional metal (Ti, V, Co Ni, Cu) to uranyl and tetrahedral building blocks might lead to the formation of new types of three-dimensional structures with new topologies.

There are 54 framework types known for uranyl-containing compounds today.¹² Due to the vast amount of stored depleted uranium with low radioactivity that has to be utilized in the near-term perspective, an extensive search for new practical applications

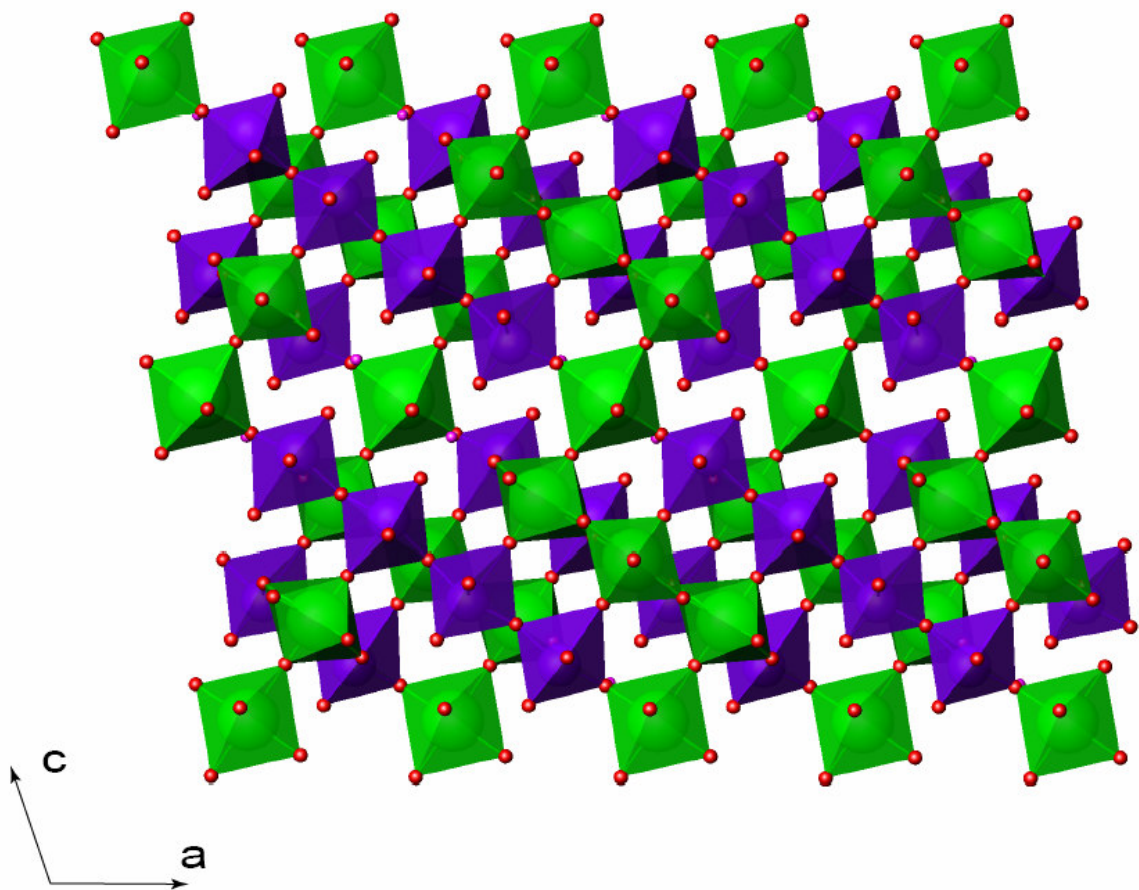


Figure 1. 4. The structure of $\text{Li}_2(\text{UO}_2)_4(\text{WO}_4)\text{O}$ is an example of a three-dimensional structure with no channels. Li^+ cations located in the voids of uranyl tungstate layers are not seen from this projection. UO_6 polyhedra are green, WO_6 – shown in violet color.

for these structures is being conducted. For example, $\text{Na}(\text{UO}_2)_4(\text{VO}_4)_3$ and $\text{Li}(\text{UO}_2)_4(\text{VO}_4)_3$ can serve as ionic conductors due to the migration of Na^+ and Li^+ cations in two intersecting channels within the structure.³⁴

Chiral uranyl molybdates $[(\text{C}_2\text{H}_5)_2\text{NH}_2]_2(\text{UO}_2)_4(\text{MoO}_4)_5(\text{H}_2\text{O})](\text{H}_2\text{O})$ ³⁶ and $(\text{NH}_4)_4[(\text{UO}_2)_5(\text{MoO}_4)_7](\text{H}_2\text{O})_5$ ³⁷ (Figure 1.5) both have large channels extended along the [001] direction with a chiral topology as required by space group ($P6_522$ and $P6_1$ respectively). In terms of tubular building units, the internal structure of these channels can be described as a double-helix, where both chains form spirals with axes parallel to [001]. Structures with these types of channels can potentially find applications in enantioselective separation and catalysis.³⁷

We proposed that our new uranyl main group or transition metal phosphate materials synthesized within this project can potentially serve as ion-exchange and storage materials for immobilization of radioactive ^{137}Cs and ^{90}Sr from nuclear waste solutions.

HIGH-LEVEL NUCLEAR WASTE (HLNW)

At the present time, HLNW produced in the processing of uranium and plutonium, is stored in 273 underground carbon-steel tanks.³ This storage strategy needs to be changed due to leakage of radioactive waste into the soil, and the potential long-term impact of this to the environment. The deep geological repository in the Yucca Mountain area, Nevada, was proposed as the safest way for ultimate disposal.

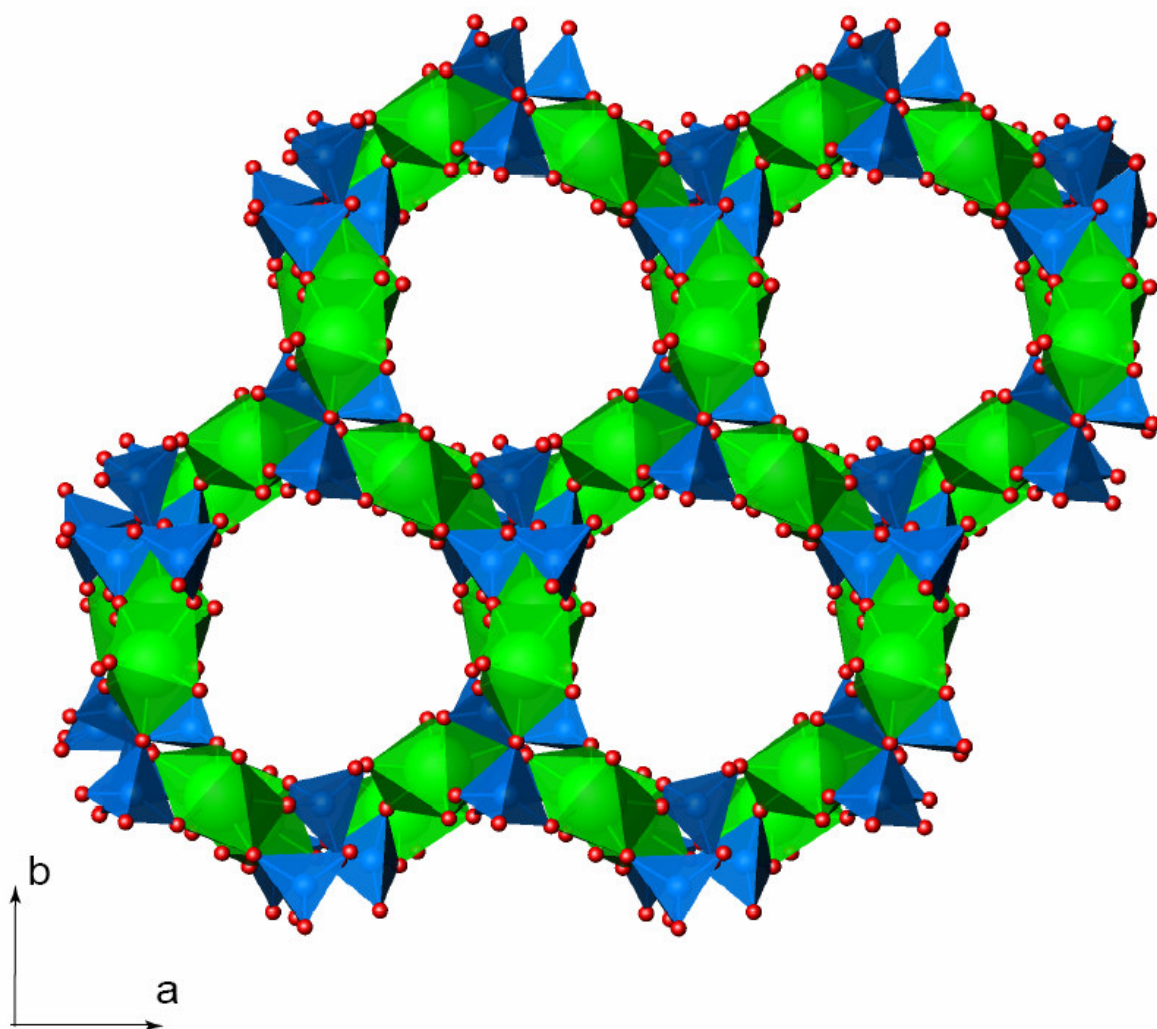


Figure 1. 5. Chiral channels extended along the c axis make the uranyl molybdate $(\text{NH}_4)_4[(\text{UO}_2)_5(\text{MoO}_4)_7](\text{H}_2\text{O})_5$ potentially applicable for enantio-selective separation. NH_4^+ cations are not shown, UO_7 polyhedra are green, MoO_4 tetrahedra are blue.

It is apparent that the application of geological disposal methods requires pretreatment of highly inhomogeneous waste in order to convert it to a solid form and to separate long-living isotopes pertinent for geological deposition from short-living isotopes and low-activity portions.

The main input to the present radioactivity in the tanks is from ^{137}Cs and ^{90}Sr . These isotopes are major dose contributors only during the first 100 years of deposition. (Table 1.1) Their removal from the tanks will significantly reduce the total amount of waste prepared for the geological repository and will make this process more reasonable.

Solvent extraction is the method currently used for ^{137}Cs and ^{90}Sr separation.³ ^{90}Sr is extracted by 4,4'(5')-di-(tert-butylcyclohexano)-18-crown-6 in an organic solution of 1.5 M TBP and hydrocarbon diluent called Isopar L[®] (SREX process).^{3,4} Tests in actual waste containers demonstrated that SREX reduces the activity of waste in the tanks after ^{90}Sr extraction to 0.04 Ci/L, which can be considered as low-level waste activity.³ ^{137}Cs can be separated by various crown ethers or cobalt dicarbollide dissolved in a very polar solvent such as nitrobenzene.^{3,4} This process removes over 99.998% of the ^{137}Cs . In order to co-extract both radionuclides simultaneously, polyethylene glycol can be added to the polar solvent-cobalt dicarbollide system.³

Other techniques such as in-tank precipitation of ^{137}Cs with sodium tetraphenylborate or membrane separation were proposed for removal of ^{137}Cs and ^{90}Sr , but several issues, such as pretreatment of the solutions, capacity of the separation, stability of precipitating agents and membranes in actual waste, and volume dependence still need to be optimized.³

Table 1. 1. The most significant contributors to the radiation dose from HLNW.⁶

Radionuclide	Half-life	Activity (Ci/canister), Time out of Reactor			
		10 years	100 years	1000 years	10000 years
⁹⁰ Sr	29 years	1.4×10^5	1.5×10^4	3.5×10^{-6}	0
⁹⁰ Y	64 years	1.4×10^5	1.5×10^4	3.5×10^{-6}	0
⁹⁹ Tc	2.13×10^5 years	3.2×10^1	3.2×10^1	3.2×10^1	3.2×10^1
¹⁰⁶ Ru	369 days	1.3×10^3	0	0	0
¹⁰⁶ Rh	2.18 hours	1.3×10^3	0	0	0
¹²⁵ Sb	2.73 years	1.6×10^3	0	0	0
¹²⁹ I	1.59×10^5 years	1.8×10^{-4}	1.8×10^{-4}	1.8×10^{-4}	1.8×10^{-4}
¹³⁴ Cs	2.06 years	1.9×10^4	0	0	0
¹³⁷ Cs	30.1 years	2.0×10^5	2.4×10^4	2.3×10^{-5}	0
¹⁴⁴ Ce	284.4 days	3.5×10^2	0	0	0
¹⁴⁷ Pm	2.64 years	1.8×10^4	8.1×10^{-7}	0	0
¹⁵⁴ Eu	8.6 years	1.0×10^4	2.1×10^2	0	0
²²⁶ Ra	1600 years	2.5×10^{-7}	2.6×10^{-6}	1.6×10^{-4}	6.5×10^{-3}
²²⁹ Th	7340 years	9.6×10^{-8}	1.7×10^{-6}	1.6×10^{-4}	1.3×10^{-2}
²³⁰ Th	7.7×10^4 years	4.9×10^{-5}	7.4×10^{-5}	8.8×10^{-4}	8.1×10^{-3}
²¹³ Pa	3.25×10^4 years	5.7×10^{-5}	5.7×10^{-5}	6.0×10^{-5}	8.8×10^{-5}
²³³ U	1.58×10^5 years	3.4×10^{-5}	3.4×10^{-5}	3.5×10^{-3}	3.6×10^{-2}
²³⁷ Np	2.14×10^6 years	8.1×10^{-1}	8.1×10^{-1}	8.8×10^{-1}	8.8×10^{-1}
²³⁸ Pu	87.8 years	2.4×10^2	1.2×10^2	2.8×10^{-1}	0
²³⁹ Pu	2.439×10^4 years	3.8	3.8	4.7	9.6
²⁴⁰ Pu	6540 years	1.0×10^1	2.0×10^1	1.8×10^1	7.3
²⁴¹ Pu	15 years	7.4×10^1	1.1×10^1	7.2×10^{-1}	3.4×10^{-1}
²⁴¹ Am	433 years	4.1×10^2	3.8×10^2	8.1×10^1	3.4×10^{-1}
²⁴³ Am	7370 years	4.0×10^1	4.0×10^1	3.7×10^1	1.7×10^1
²⁴² Cm	163 days	1.6×10^1	1.1×10^1	1.8×10^{-1}	0
²⁴⁴ Cm	17.9 years	4.0×10^3	1.3×10^2	0	0

Ion-exchange is also considered as a prospective method for the separation of short-lived ^{137}Cs and ^{90}Sr radionuclides.

ION-EXCHANGE

Ion-exchange is a stoichiometric equilibrium process between the ions of the exchanger and ions of the media in which the exchanger is immersed. In the case of an insoluble anionic matrix, containing exchangeable cations, and a solution that contains cations, available for exchange, the reaction can be written as:



where M^- is the negatively charged insoluble matrix, A^+ and B^+ are exchangeable cations, and barred symbols represent the solid phase.³⁸

The properties of any ion-exchange material can be described in capacity and selectivity terms.³⁹⁻⁴⁰

The measurements of uptake values c or distribution coefficients K_D can characterize the capacity of ion-exchange material that illustrates the amount of ions that can be replaced in the unit mass of solid.

Uptake c may be expressed as:

$$c = \frac{(C_{in} - C_{fin})V}{zm} \quad (2)$$

where C_{in} and C_{fin} are concentrations of B^+ solution before and after ion-exchange, m is mass of the dry sample, z – charge of the cation and V is aliquot volume of the solution.

K_D might be calculated as:

$$K_D = \frac{\overline{C_B}}{C_B} \quad (3)$$

where C_B is the concentration of B^+ in solid phase (barred) and solution, or

$$K_D = \frac{(C_{in} - C_{fin}) V}{C_{fin} m} \quad (4)$$

The selectivity constant describes the affinity of material for exchange of the cation A^+ over the B^+ :

$$K_{A/B} = \frac{\overline{C_A}}{C_A} \frac{C_B}{\overline{C_B}} \quad (5)$$

where C_A and C_B are concentrations of the cations A^+ and B^+ , respectively (barred symbols represent the solids).

For organic resins, capacity and selectivity are controlled by synthetic and pretreatment conditions. In general, the resin is based on the hydrocarbon matrix with introduced functional groups, whose nature and strength define the functionality of the material. The water content or swelling of the resin is inversely related to the degree of crosslinking in the hydrocarbon matrix and determines the capacity values.³⁸ Due to the highly reproducible ion-exchange capacities (~2 meq/g of dry sample), and predictable properties, organic resins are one of the best-known methods today for conventional water purification as well as the special ultrapure water pretreatment in pharmaceuticals, electronics, and other highly technological industries. It is also widely used in extraction metallurgy, medicine, and agriculture.³⁸

There is no straightforward theory that clarifies the origin of selectivity of inorganic framework ion-exchange materials. Size, charge, and magnitude of hydration

energy of exchanged cations, charge distribution of the matrix, structural features, degree of solution loading are just several major issues that should be considered and combined in order to explain ion-exchange properties for every particular material. Arrangements of all factors are able to favor the formation of the inorganic exchange materials with up to 9 meq/g uptake values (Na^+ exchange in titanium silicates¹⁰) and high selectivity to chosen cations. High resistance to temperature and radiation damage, and low cost of synthesis make inorganic ion-exchange materials highly competitive for the removal of ^{137}Cs and ^{90}Sr isotopes.

ION-EXCHANGE LAYERED AND THREE-DIMENSIONAL INORGANIC MATERIALS FOR SELECTIVE Cs^+ AND Sr^{2+} UPTAKE

Many layered and framework compounds with remarkable selectivity for Cs^+ or Sr^{2+} were tested under conditions relevant to nuclear waste. Ammonium molybdophosphate (AMP) possesses a high capacity for Cs^+ , but its application in the highly basic media is limited.⁴¹

Potassium cobalt hexacyanoferrate, a three-dimensional compound with a cubic face-centered structure, belonging to the Prussian Blue family, was extensively studied due to the high uptake of Cs^+ in the presence of interfering cations over the pH range of 1 to 13.^{42,43} The framework is built out of iron atoms, that reside in corners and face centers of the unit cell, cobalt atoms, located at the edges, and exchangeable potassium cations occupying the body center. Low thermal stability resulting in decomposition of the sorbent at temperatures above 240 °C⁴⁴ has restricted the application of the material, and has driven the search for alternatives.

The structure of sodium nonatitanate $\text{Na}_4\text{Ti}_9\text{O}_{20}\cdot n\text{H}_2\text{O}$ is still not well-resolved.⁴⁵ This semicrystalline compound with promising ion-exchange properties has a layered structure with an interlayer distance that depends on the water content, and can be as large as 10.0 Å.⁴⁶ Batch and column experiments in two waste simulants, that differ in the content of citric acid, Na_4EDTA , iminodiacetic acid, sodium gluconate, and other complex-forming agents, demonstrated that sodium nonatitanate is applicable for ion-exchange with an extremely high K_d for Sr^{2+} of 2.35×10^5 mL/g at the volume to mass ratio of 200 and 3.96×10^4 mL/g at volume to mass ratio of 1000 at waste solutions with no formation of complex occurring.^{47,48}

The family of titanium silicates has been considered as the most promising sorbents for Cs^+ and Sr^{2+} removal from nuclear waste for many years. The structure of sodium titanium silicate $\text{Na}_2\text{Ti}_2\text{O}_3(\text{SiO}_4)\cdot\text{H}_2\text{O}$ (commercial product name IONSIV® IE-911) belongs to the hexagonal space group $P4_2/mcm$.^{3,49,50} (Figure 1.6) The crystallographic data are given in the Table 1.2. It is a framework material constructed from Ti four-member group clusters bridged by silicate groups in the a and b directions, with channels formed along the c axis. In every cluster titanium octahedra are pairwise edge-shared, with pairs rotated by 90°. In addition to tunnels, where four Na^+ cations are located, there are small framework cavities located perpendicular to the channels, also occupied by Na^+ cations.

This material is selective to Cs^+ with K_d values ranging from 581 mL/g to 870 mL/g in different simulants.^{63,64} At a $\text{pH}>12$, measured uptake value for the protonated form is ~1.9 meq/g, which corresponds only to 25% of the total calculated exchange

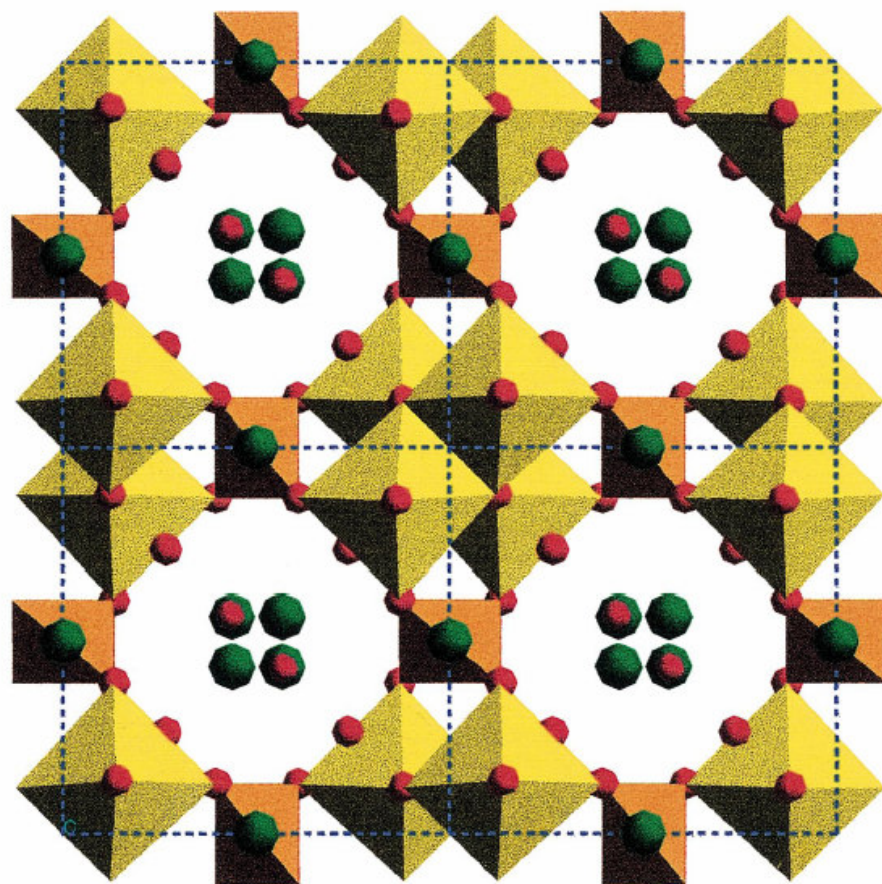


Figure 1.6. A view of the crystal structure of $\text{Na}_2\text{Ti}_2\text{O}_3(\text{SiO}_4) \cdot \text{H}_2\text{O}$ along the $[001]$ direction. Yellow squares depict TiO_6 octahedra, orange - SiO_4 tetrahedra, green balls – Na^+ cations. Four out of the total eight Na^+ cations are located in the channels, the other four (on the silicate groups) – in small cavities. Copied from reference 50 with author's permission.

Table 1.2. Crystallographic data for $\text{Na}_2\text{Ti}_2\text{O}_3(\text{SiO}_4)\cdot\text{H}_2\text{O}$ (**TiSi-1**), $\text{HM}_3\text{Ti}_4\text{O}_4(\text{SiO}_4)\cdot\text{H}_2\text{O}$ (**TiSi-2**) and $\text{Na}_2\text{Nb}_{2-x}\text{M}_x\text{O}_{6-x}(\text{OH})_x\cdot\text{H}_2\text{O}$ (**SOMS**)

Compound	TiSi-1	TiSi-2	SOMS
Crystal System	tetragonal	cubic	monoclinic
Space group	$P4_2/mcm$ (No. 132)	$P\bar{4}3m$ (No. 215)	$C2/c$ (No.15)
a (Å)	7.8082(2)	7.7644(3)	16.940(3)
b (Å)	7.8082(2)	7.7644(3)	5.033(5)
c (Å)	11.9735(4)	7.7644(3)	16.466(3)
α (°)	90	90	90
β (°)	90	90	114.00
γ (°)	90	90	90
Z	4	1	8
$R(F)$	0.055	0.055	0.0629
R_w	0.142	0.114	0.1606

capacity of the $\text{H}_2\text{Ti}_2\text{O}_3(\text{SiO}_4)\cdot\text{H}_2\text{O}$. This phenomenon, as well as preferred selectivity to Cs^+ relative to other alkaline cations, can be easily explained using coordination distances and ionic radius data for Cs^+ : only two out of four exchanged cations can occupy the tunnel simultaneously, but bond distances of coordinated Cs^+ are very close to the sum of Cs^+ and O^{2-} ionic radii. At the same time Na^+ can compete for ion-exchange selectivity in the mixed solutions, occupying framework cavity sites.⁴⁸

For Sr^{2+} cation exchange, sodium titanium silicate possesses the highest observed in this family of the compounds K_D values of $\sim 3.0 \times 10^5$ mL/g. This high selectivity might be ascribed to the presence of Sr^{2+} as $\text{Sr}(\text{OH})^+$ in the strongly basic conditions of nuclear waste and possibility of $\text{Sr}(\text{OH})^+$ occupying both tunnel and cavity exchange sites.

The other member of the titanium silicate family, a compound with the structure of mineral pharmacosiderite type $\text{HM}_3\text{Ti}_4\text{O}_4(\text{SiO}_4)\cdot\text{H}_2\text{O}$ ($\text{M}=\text{K}, \text{Na}$), has a framework built similarly to that described above.^{10,50} All differences between these two related structures, and their ion-exchange properties can be ascribed to the cubic nature of pharmacosiderite and its space group. (Table 1.2) Titanium clusters are connected now in all three directions equivalently, which produces a system of perpendicular channels, parallel to all three axes. Three potential ion-exchange sites are placed in the cube face centers and one in the cubic body center of the unit cell. After Cs^+ exchange, three face sites can be selectively filled with Cs^+ cations and the body site remains in the protonated form (or occupied by smaller cations) due to the restricted space requirements. K_{DCs} in alkaline solutions is 15360 mL/g, which can be compared with K_{DRb} - 6190 mL/g, K_{DK} - 2580 mL/g, and K_{DLi} - 630 mL/g. The distribution coefficients are summarized in the

Table 1.3. Distribution coefficients for Sr^{2+} , K_{DSr} , of $\text{Na}_4\text{Ti}_9\text{O}_{20}\cdot n\text{H}_2\text{O}$, $\text{Na}_2\text{Ti}_2\text{O}_3(\text{SiO}_4)\cdot\text{H}_2\text{O}$, and $\text{HK}_3\text{Ti}_4\text{O}_4(\text{SiO}_4)\cdot\text{H}_2\text{O}^{64}$ in different HLNW simulants.

Compound	K_{DSr} , mL/g		
	NCAW simulant *		101SY-Cs5 simulant **
	V:m = 200	V:m = 1000	V:m = 200
$\text{Na}_4\text{Ti}_9\text{O}_{20}\cdot n\text{H}_2\text{O}$	2.35×10^5	3.96×10^4	295
$\text{Na}_2\text{Ti}_2\text{O}_3(\text{SiO}_4)\cdot\text{H}_2\text{O}$	2.70×10^5	2.26×10^5	231
$\text{HK}_3\text{Ti}_4\text{O}_4(\text{SiO}_4)\cdot\text{H}_2\text{O}$	2.02×10^5	5.00×10^3	31

* The composition of NCAW is restricted only to presence of 0.43 M Al^{3+} , 5×10^{-4} M Cs^+ , 0.12 M K^+ , 4.99 M Na^+ , 5×10^{-5} M Rb^+ , 2.7×10^{-7} M Sr^{2+} , 0.23 M carbonate, 0.09 M fluoride, 3.4 M hydroxide, 1.67 M nitrate, 0.43 M nitrite, 0.15 M sulfate, and 0.025 M phosphate.

** In addition in 101SY-Cs5 present 4.2×10^{-3} M Ca^{2+} , 1.96×10^{-4} M Fe^{3+} , 4.2×10^{-4} M Mo^{4+} , 2.5×10^{-4} M Ni^{2+} , 5.0×10^{-4} M Zn^{2+} , 5.0×10^{-3} M citric acid, 5.0×10^{-3} M Na_4EDTA , 0.031 M iminodiacetic acid, 2.5×10^{-4} M Na_3 nitrilotriacetate, 0.013 M sodium gluconate.

partially explain the preference of the structure for Cs^+ in terms of its hydration energy, which is not high enough to deny the introduction of cations into the relatively small channels.^{10,50} Reported Sr^{2+} selectivity for pharmacosiderite structure in HLNW simulants with different pH values and Cs^+ content is lower than for other titanium silicates and titanates.^{47,48} The ion-exchange data were also measured in reference to the degree of the crystallinity of the material. Results revealed participation of both absorption and ion-exchange mechanisms in the separation of Sr^{2+} .

Recently Sandia National Laboratory invented a new series of compounds named Sandia Octahedral Molecular Sieves (SOMS).⁵¹⁻⁵⁴ They are sodium niobate-based framework materials with the general formula $\text{Na}_2\text{Nb}_{2-x}\text{M}_x\text{O}_{6-x}(\text{OH})_x \cdot \text{H}_2\text{O}$, where M could be Ti or Zr with $x < 0.4$. (Table 1.2) Substitution of pentavalent Nb coordination octahedra with tetravalent Ti or Zr coordination octahedra plays the same role as a substitution of Si with Al in zeolite structures. It creates an anionic charge within the matrix that must be balanced. The overall structure consists of double chains of edge-shared octahedra of NbO_6 and TiO_6 (ZrO_6) extending along the b axis. These chains are intersected with layers of edge-shared NaO_6 octahedra and this structural interaction forms a negatively charged framework. The fragment of the structure is depicted in the Figure 1.7. There are two different sorts of Na^+ cations in this compound: framework Na octahedra that participate in the matrix formation and Na^+ counter cations located in the channels that balance negative charge of the matrix. These latter cations are exchangeable.

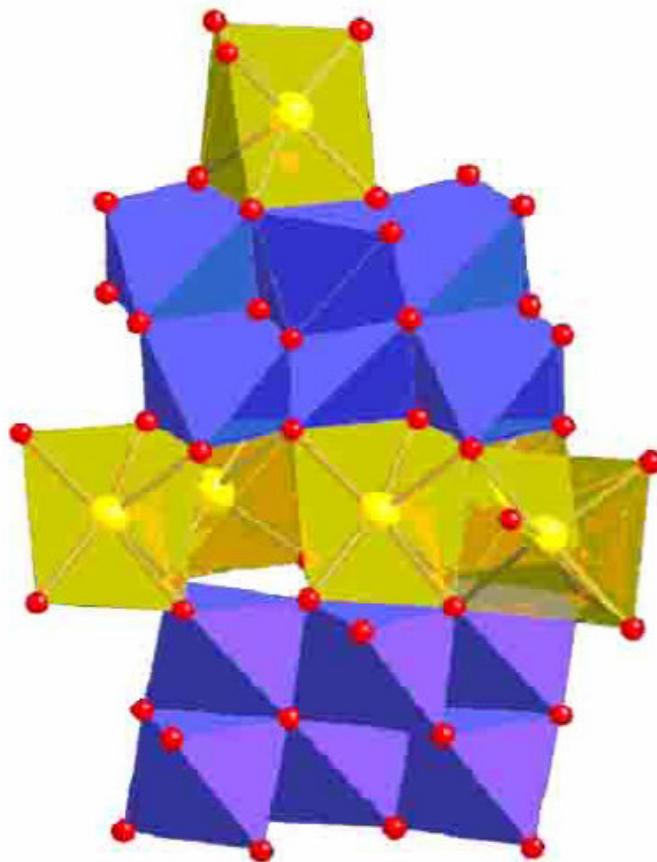


Figure 1.7. This fragment depicts interconnection of octahedral units in the structure of $\text{Na}_2\text{Nb}_{2-x}\text{Ti}_x\text{O}_{6-x}(\text{OH})_x \cdot \text{H}_2\text{O}$. Blue polyhedra represent disordered NbO_6 and TiO_6 octahedra. Yellow polyhedra are Na coordination spheres, participating in the framework. Copied from reference 52 with author's permission.

SOMS materials demonstrate exceptional selectivity toward all alkaline-earth cations relative to alkali metal cations. For instance, the K_D value of SOMS-1 (Nb:Ti ratio is 4:1) in Na form for Ba^{2+} , Sr^{2+} , and Mg^{2+} are all above 99800 mL/g, but the K_D values for Li^+ , K^+ , and Cs^+ do not exceed 150 mL/g. Upon heating they have one-step phase transformation to perovskite type sodium niobate NaNbO_3 without any intermediate stages like amorphization or decomposition. Measured enthalpies of formation of hydrated, dehydrated, and dense forms of materials proved that dense perovskite structure is more thermodynamically favorable and may serve as a permanent ceramic host phase for the storage of ^{90}Sr .⁵¹⁻⁵⁴

MAIN GROUP AND TRANSITION METAL PHOSPHATES

There have been countless remarkable catalysts,⁵⁵⁻⁵⁸ ion-exchangers,^{59,60} conductors⁶⁰ and many other materials with other applications in the area of various main group and transition metal phosphates.⁶¹ Along with useful properties, they display extraordinary structural diversity. For instance, among aluminum phosphates alone there are more than 40 different framework types. One eminent example is aluminophosphate VPI-5, which contains 18-membered ring channels with a diameter of 13 Å.⁶²

Vanadium phosphates, including $(\text{VO})_2\text{P}_2\text{O}_7$, NaVOPO_4 , $\text{CaV}_2(\text{P}_2\text{O}_7)$,⁶³ $\text{VOPO}_4 \cdot 2\text{H}_2\text{O}$, $\text{VOHPO}_4 \cdot 0.5\text{H}_2\text{O}$, $\text{VO}(\text{H}_2\text{PO}_4)_2$ ⁵⁶ and others, represent, probably, the largest group of catalysts within one class of compounds. Vanadyl pyrophosphate $(\text{VO})_2\text{P}_2\text{O}_7$, for example, is currently used in industry for the oxidation of butane to maleic anhydride. Its structure consist of the double chains of edge-sharing VO_6 octahedra, interconnected by pyrophosphate groups into the framework.⁶⁴ These pairs of VO_6 octahedra are associated

with active sites, where dehydrogenation of butane occurs.⁶⁵ Other authors⁶⁶ address the high oxidation activity of $(\text{VO})_2\text{P}_2\text{O}_7$ and other vanadium phosphate catalysts to the presence of $\text{V}=\text{O}$ double bonds at the active VO_6 sites and the ability of oxygen from $\text{V}=\text{O}$ to attack the reactants leading to the oxidative hydrogenation reaction.

In contrast, the group of nickel phosphates illustrates the extraordinary flexibility of their properties in this small group of compounds. Two 24-membered ring framework compounds $\text{Ni}_{18}(\text{HPO}_4)_{14}(\text{OH})_3\text{F}_9(\text{H}_3\text{O}^+, \text{NH}_4^+)_4 \cdot 12\text{H}_2\text{O}$ (VSB-1)⁵⁷ and $\text{Ni}_{20}[(\text{OH})_{12}(\text{H}_2\text{O})_6][(\text{HPO}_4)_8(\text{PO}_4)_4] \cdot 12\text{H}_2\text{O}$ (VSB-5)⁵⁸ demonstrate a variety of properties. VSB-1 exhibits ion-exchange properties, antiferromagnetic ordering at 10 K and thermal stability up to temperatures above 550 °C, as well as shape-selective catalytic activity in the hydroxylation of phenol.⁶⁷ VSB-5 also possesses good temperature resistance and antiferromagnetic ordering.⁵⁸ It also might serve as a hydrogenation catalyst upon calcination due to the availability of Ni sites, and as hydrogen storage material.⁶⁸

The ion-exchange properties of layered transition metal phosphates $\text{Ti}(\text{HPO}_4)_2 \cdot \text{H}_2\text{O}$, $\text{Zr}(\text{HPO}_4)_2 \cdot \text{H}_2\text{O}$, $\text{Hf}(\text{HPO}_4)_2 \cdot \text{H}_2\text{O}$, $\text{Ge}(\text{HPO}_4)_2 \cdot \text{H}_2\text{O}$, $\text{Sn}(\text{HPO}_4)_2 \cdot \text{H}_2\text{O}$, and $\text{Pb}(\text{HPO}_4)_2 \cdot \text{H}_2\text{O}$ are well characterized.⁵⁹ The interlayer spacing, ranging between 7.56 Å and 7.8 Å, is confined by the oxygen atoms of the phosphate groups, which could be protonated. As a consequence, the ion-exchange properties of these compounds depend strongly on the pH, and reveal the maximal ion-exchange capacities between 4.17 meq/g for $\text{Hf}(\text{HPO}_4)_2 \cdot \text{H}_2\text{O}$ and 7.76 meq/g for $\text{Ti}(\text{HPO}_4)_2 \cdot \text{H}_2\text{O}$ in strongly basic conditions.

The other titanium phosphate, potassium titanyl phosphate KTiOPO_4 (KTP) is one of the best known nonlinear optical materials.⁶⁹ The cause of frequency doubling

properties lies in the overall polarity of the structure, consisting of chains of highly distorted corner-sharing TiO_6 octahedra, connected by phosphate tetrahedra.

As a summary of this short review and many other main group or transition metal phosphates not mentioned above, one can conclude that the presence of metal centers in these compounds are the source of their diverse properties. We anticipate that the addition of the main group or transition metal centers in uranyl phosphate structures could also enrich their properties and could make uranyl-containing materials potentially applicable.

REFERENCES

1. Fermi, E. *Proceedings of the American Philosophy Society*, **1946**, 90, 20.
2. Rhodes, R. *The Making the Atomic Bomb*; Simon and Schuster, 1986.
3. Schulz, W. W.; Lombardo, N. J. *Science and Technology for Disposal of Radioactive Tank Wastes*, Proceedings of the ACS Symposium on Science and Technology for Disposal of Radioactive Tank Wastes, September, 7-11, Las Vegas, Nevada, 1997.
4. *Disposal of Radioactive Waste*, Proceedings of the Information Meeting NEA, April, 12-14, Paris, 1972.
5. *Alternative High-Level Waste Treatments at the Idaho National Engineering and Environmental Laboratory*, National Academy Press, 1999.
6. Brookins, D. G. *Geochemical Aspects of Radioactive Waste Disposal*, Springer-Verlag: New-York, 1984.
7. Finch, R. J.; Buck, E. C.; Finn P. A.; Bates, J. K. in *Scientific Basis for Nuclear Waste Management XXII*, Materials Research Society Symposium Proceedings, **1999**, 556, 431.
8. Finn, P. A.; Hoh, J. C.; Wolf, S. F.; Slater, S. A.; Bates, J. K. *Radiochim. Acta*, **1996**, 74, 65.
9. Wronkiewicz, D. J.; Bates, J. K.; Gerding, T. J.; Veleckis, E.; Tani, B. S. *J. Nucl. Mater.* **1992**, 190, 107.
10. Clearfield, A. "Inorganic Ion Exchangers, Past, Present and Future" in *Solvent Extraction and Ion Exchange*, **2000**, 18, 655.
11. Burns, P. C.; Miller, M. L.; Ewing, R. C. *Can. Mineral.* **1996**, 34, 845.

12. Burns, P. C. *Can. Mineral.* **2005**, 43, 1839.
13. Rabenau, A. *Angew. Chem.* **1985**, 97, 1017.
14. Burns, P. C.; Ewing, R. C.; Hawthorne, F. C. *Can. Mineral.* **1997**, 35, 1551.
15. Brese, N. E.; O'Keeffe, M. *Acta Cryst.* **1991**, B47, 192.
16. Li, Y.; Cahill, C. L.; Burns, P. *Chem. Mater.* **2001**, 13, 4026.
17. Li, Y.; Burns, P. *Can. Mineral.* **2000**, 38, 1433.
18. Halasyamani, P. S.; Walker, S. M.; O'Hare, D. *J. Am. Chem. Soc.* **1999**, 121, 7415.
19. Sykora, R. E.; Albrecht-Schmitt, T. E. *Inorg. Chem.* **2003**, 42, 2179.
20. Obbade, S.; Yagoubi, S.; Dion, C.; Saadi, M.; Abraham, F. *J. Solid State Chem.* **2004**, 177, 1681.
21. Locock, A. J.; Burns, P. C. *J. Solid State Chem.* **2002**, 163, 275.
22. Locock, A. J.; Burns, P. C. *J. Solid State Chem.* **2002**, 167, 226.
23. Locock, A. J.; Burns, P. C. *J. Solid State Chem.* **2003**, 175, 372.
24. Locock, A. J.; Burns, P. C. *J. Solid State Chem.* **2003**, 176, 18.
25. Burns, P. C.; Alexopoulos, C. M.; Hotchkiss, P. J.; Locock, A. J. *Inorg. Chem.* **2004**, 43, 1816.
26. Locock, A. J.; Burns, P. C. *J. Solid State Chem.* **2004**, 177, 2675.
27. Doran, M.; Norquist, A. J.; O'Hare, D. *Chem. Commun. (Cambridge)* **2002**, 24, 2946.
28. Li, Y.; Burns, P. C. *J. Nucl. Mater.* **2001**, 299, 219.
29. Wang, X.; Huang, J.; Liu, L.; Jacobson, A. J. *J. Mater. Chem.* **2002**, 12, 406.
30. Wang, X.; Huang, J.; Jacobson, A. J. *J. Amer. Chem. Soc.* **2002**, 124, 15190.
31. Huang, J.; Wang, X.; Jacobson, A. J. *J. Mater. Chem.* **2003**, 13, 191.

32. Chen, C.-S.; Kao, H.-M.; Lii, K.-H. *Inorg. Chem.* **2005**, *44*, 935.
33. Chen, C.-S.; Chiang, R.-K.; Kao, H.-M.; Lii, K.-H. *Inorg. Chem.* **2005**, *44*, 3914.
34. Obbade, S.; Dion, C.; Rivenet, M.; Saadi, M.; Abraham, F. *J. Solid State Chem.* **2004**, *177*, 2058.
35. Obbade, S.; Dion, C.; Saadi, M.; Yagoubi, S.; Abraham, F. *J. Solid State Chem.* **2004**, *177*, 3909.
36. Krivovichev, S. V.; Cahill, C. L.; Nazarchuk, E. V.; Burns, P. C.; Armbruster, Th.; Depmeier, W. *Micropor. Mesopor. Mater.* **2005**, *78*, 209.
37. Krivovichev, S. V.; Cahill, C. L.; Burns, P. C. *Inorg. Chem.* **2003**, *42*, 2459.
38. Harland, C. E. *Ion Exchange: Theory and Practice*, 2nd ed.; Royal Society of Chemistry, 1994.
39. Helfferich, F. C. *Ion-Exchange*, Dover Science, 1995.
40. Clearfield, A. *Inorganic Ion Exchange Materials*, CRC Press, 1982.
41. Todd, T. A.; Mann, N. R.; Tranter, T. J.; Sebesta, F.; John, J.; Motl, A. *J. Radioanal. Nucl. Chem.* **2002**, *254*, 47.
42. Harjula, R.; Lehto, J.; Wallace, J. *Waste Management*, Tucson, Arizona, **1987**, 93.
43. Lehto, J.; Paaanen, A.; Harjula, R. *J. Radioanal. Nucl. Chem.* **1992**, *164*, 39.
44. Lehto, J.; Pettersson, M.; Hinkula, J.; Raesaenen, M.; Elomaa, M. *Thermochim. Acta* **1995**, *265*, 25.
45. Lehto, J.; Clearfield, A. *J. Radioanal. Nucl. Chem. Lett.* **1987**, *118*, 1.
46. Clearfield A.; Lehto, J. *J. Solid State Chem.* **1988**, *73*, 98.
47. Behrens, E. A.; Sylvester, P.; Clearfield, A. *Env. Sci. Technol.* **1998**, *32*, 101.

48. Sylvester, P.; Behrens, E. A.; Graziano, G. M.; Clearfield, A. *Sep. Sci. Technol.* **1999**, *34*, 1981.
49. Poojary, D. M.; Cahill, R. A.; Clearfield, A. *Chem. Mater.* **1994**, *6*, 2364.
50. Clearfield, A. *Solid State Sci.* **2001**, *3*, 103.
51. Nyman, M.; Tripathi, A.; Parise, J. B.; Maxwell, R. S.; Harrison, W. T. A.; Nenoff, T. M. *J. Am. Chem. Soc.* **2001**, *123*, 1529.
52. Nyman, M.; Tripathi, A.; Parise, J. B.; Maxwell, R. S.; Nenoff, T. M. *J. Am. Chem. Soc.* **2002**, *124*, 1704.
53. Xu, H.; Nyman, M.; Nenoff, T. M.; Navrotsky, A. *Chem. Mater.* **2004**, *16*, 2034.
54. Nenoff, T. M.; Pless, J. D.; Michaels, E.; Phillips, M. L. F. *Chem. Mater.* **2005**, *17*, 950.
55. Bordes, E.; Courtine, P. *J. Catal.* **1979**, *57*, 236.
56. Hutchings, G. J. *J. Mater. Chem.* **2004**, *14*, 3385.
57. Guillou, N.; Gao, Q.; Nogués, M.; Morris, R. E.; Hervieu, M.; Férey, G.; Cheetham, A. K. *C. R. Acad. Sci. Paris*, **1999**, *t.2, Serie II*, 387.
58. Guillou, N.; Gao, Q.; Forster, P. M.; Chang, J.- S.; Nogués, M.; Park, S.- E.; Férey, G.; Cheetham, A. K. *Angew. Chem., Int. Ed. Engl.* **2001**, *40*, 15.
59. Clearfield, A. *Ann. Rev. Mater. Sci.* **1984**, *14*, 205
60. Clearfield, A. *Chem. Rev.* **1988**, *88*, 125.
61. Cheetham, A. K.; Férey, G.; Loiseau, T. *Angew. Chem., Int. Ed. Engl.* **1999**, *38*, 3268.
62. Davis, M. E.; Saldarriaga, C.; Montes, C.; Garces, J. M.; Crowder, C. *Nature* **1988**, *331*, 698.

63. Boudin, S.; Guesdon, A.; Leclaire, A.; Borel, M.-M. *Int. J. Inorg. Mater.* **2000**, 2, 561.
64. Torardi C. C.; Calabrese, J. C. *Inorg. Chem.* **1984**, 23, 1308.
65. Bordes, E.; Courtine, P. *J. Chem. Soc., Chem. Commun.* **1985**, 5, 294.
66. Ai, M. *Catalysis Today* **2003**, 85, 193.
67. Chang, J.- S.; Hwang, J.- S.; Jhung, S. H.; Park, S. - E.; Fèrey, G.; Cheetham, A. K. *Angew. Chem., Int. Ed. Engl.* **2004**, 43, 2819.
68. Forster, P. M.; Juergen, E.; Chang, J.- S.; Park, S. - E.; Fèrey, G.; Cheetham, A. K. *J. Am. Chem. Soc.* **2003**, 125, 1309.
69. Wang, J.; Wei, J.; Liu, Y.; Yin, X.; Hu, X.; Shao, Z.; Jiang, M. *Progr. Cryst. Grow. Character. Mater.* **2000**, 40, 3.

CHAPTER 2

CRYSTAL CHEMISTRY AND ION-EXCHANGE PROPERTIES OF THE LAYERED POTASSIUM URANYL IODATE, $\text{K}[\text{UO}_2(\text{IO}_3)_3]$

ABSTRACT

Single crystals of potassium uranyl iodate, $\text{K}[\text{UO}_2(\text{IO}_3)_3]$ (**KUI**), were grown under mild hydrothermal conditions. The structure of **KUI** contains two-dimensional ${}^2_{\infty}[\text{UO}_2(\text{IO}_3)_3]^{1-}$ sheets extending in the $[ab]$ plane that consist of approximately linear UO_2^{2+} cations bound by iodate anions to yield UO_7 pentagonal bipyramids. There are three crystallographically unique iodate anions, two of which bridge between uranyl cations to create sheets, and one that is monodentate and protrudes in between the layers in cavities. K^+ cations have long ionic contacts with oxygen atoms from the layers forming an eight-coordinate distorted dodecahedral geometry. These cations join the ${}^2_{\infty}[\text{UO}_2(\text{IO}_3)_3]^{1-}$ sheets together. Ion-exchange reactions were carried out that indicate the selective uptake of Cs^+ over Na^+ or K^+ by **KUI**. Crystallographic data (193 K, $\text{MoK}\alpha$, $\lambda = 0.71073$ Å): **KUI**, orthorhombic, $Pbca$, $a = 11.495(1)$ Å, $b = 7.2293(7)$ Å, $c = 25.394(2)$ Å, $Z = 8$, $R(F) = 1.95\%$ for 146 parameters with 2619 reflections with $I > 2\sigma(I)$.

INTRODUCTION

Uranyl iodates have been known since at least the early 1900s with the correct composition of $\text{UO}_2(\text{IO}_3)_2(\text{H}_2\text{O})$ being reported in 1913.¹ The precipitation of uranyl iodate as its hydrate has been used as a method of quantifying uranium for almost fifty years.^{2,3} The speciation of uranyl iodates in solution and subsequent precipitation has also been implicated in the fate of ^{129}I ($t_{1/2} = 1.7 \times 10^7$ y), a key fission product in spent nuclear fuel.⁴ $\text{UO}_2(\text{IO}_3)_2(\text{H}_2\text{O})$ was also used as an early probe of the effects of radiation damage on uranium-bearing materials.⁵ Despite the importance of iodate in uranyl chemistry, the solid-state structure of a uranyl iodate was not known until Weigel and Engelhardt reported that $\text{UO}_2(\text{IO}_3)_2(\text{H}_2\text{O})$ was isostructural with $\text{UO}_2(\text{BrO}_3)_2(\text{H}_2\text{O})$, the latter structure being identified by X-ray powder diffraction methods.⁶

In recent years uranyl iodates have been a rapidly expanding group of compounds prepared via hydrothermal conditions, whose structures are dominated by the formation of one-dimensional topologies. These one-dimensional structures are known for relatively simple compounds such as $\text{UO}_2(\text{IO}_3)_2$,⁷ as well as for materials that incorporate a diverse set of ligands e.g. $\text{Cs}_2[(\text{UO}_2)_3\text{Cl}_2(\text{IO}_3)(\text{OH})\text{O}_2] \cdot 2\text{H}_2\text{O}$,⁸ $\text{Rb}[(\text{UO}_2)(\text{CrO}_4)(\text{IO}_3)(\text{H}_2\text{O})]$,⁹ and $\text{A}_2[(\text{UO}_2)(\text{MO}_4)(\text{IO}_3)_2]$ ($\text{A} = \text{K}, \text{Rb}, \text{Cs}; \text{M} = \text{Cr}, \text{Mo}$).^{9,10} Unidimensional features occur in additional uranyl iodates that incorporate μ_3 -oxo atoms such as $\text{A}_2[(\text{UO}_2)_3(\text{IO}_3)_4\text{O}_2]$ ($\text{A} = \text{K}, \text{Rb}, \text{Tl}$) and $\text{AE}[(\text{UO}_2)_2(\text{IO}_3)_2\text{O}_2]$ ($\text{AE} = \text{Sr}, \text{Ba}, \text{Pb}$),^{11,12} and in complex low-symmetry compounds like $\text{K}_3[(\text{UO}_2)_2(\text{IO}_3)_6](\text{IO}_3) \cdot \text{H}_2\text{O}$.¹³ Two-dimensional structures are less common, but are known for $\text{UO}_2(\text{IO}_3)_2(\text{H}_2\text{O})$ ^{6,7} and $\text{Ag}_4(\text{UO}_2)_4(\text{IO}_3)_2(\text{IO}_4)_2\text{O}_2$.¹⁴ One of the key features of the uranyl iodate system is the presence of a stereochemically active lone-pair of

electrons on the I(V) center. The nonbonding nature of these electron pairs can cause the loss of a second dimension of connectivity, thereby leading to the formation of one-dimensional topologies that are in some cases seemingly excised from previously known two-dimensional compounds.^{11,12} These lone-pairs also have the ability to align in the solid-state to create polar structures, albeit this is rare in uranyl compounds because the approximately linear uranyl cations often reside on, or are related by, centers of inversion or higher symmetry. In fact, all uranyl iodates known to date are centrosymmetric. If the discussion is expanded to include compounds containing NpO_2^+ , NpO_2^{2+} , and PuO_2^{2+} , then three actinyl iodates are known to form polar structures, $\text{NpO}_2(\text{IO}_3)$,¹⁸ $\text{NpO}_2(\text{IO}_3)_2 \cdot \text{H}_2\text{O}$,¹⁹ and $\text{PuO}_2(\text{IO}_3)_2 \cdot \text{H}_2\text{O}$,²⁰ all of which crystallize in the polar space group $Pna2_1$. If the composition is allowed to diverge further by considering all uranyl compounds with anions containing nonbonding electrons, then a few other acentric structures can be identified for $\text{PbUO}_2(\text{SeO}_3)_2$ ²¹ and $\text{Na}_8(\text{UO}_2)_6(\text{TeO}_3)_{10}$.²² Members of the uranyl family of compounds with oxoanions of Sb(III) and Bi(III) are thus far found to be centrosymmetric.^{23,24} Channels can also be created to house the lone-pair of electrons in these types of compounds, which occurs in $\beta\text{-AgNpO}_2(\text{SeO}_3)$.¹⁸ Herein we report the preparation, crystal structure, and ion-exchange properties of a new layered uranyl iodate, $\text{K}[\text{UO}_2(\text{IO}_3)_3]$ (**KUI**).

EXPERIMENTAL

Syntheses. UO_3 (99.8%, Alfa-Aesar), H_5IO_6 (99%, Alfa-Aesar), NaOH (97%, Aldrich), NaCl (99.99%, Aldrich), KOH (85.8%, Fisher), KCl (99%, Aldrich), K_2CO_3 (99%, Aldrich), CsCl (99.9%, Aldrich), CsOH (99.9%, Aldrich) and V_2O_5 (99.95%, Alfa-

Aesar) were used as received. Distilled and Millipore filtered water with a resistance of 18.2 M Ω ·cm was used in all reactions. Reactions were run in Parr 4749 23-mL autoclaves with PTFE liners. Accumet Basic AB 15 pH-meter was used for potentiometric measurements. SEM/electron dispersive analysis by X-ray (EDX) analyses were performed using a JEOL 840/Link Isis instrument. K, U, and I percentages were calibrated against standards. Typical results were surprisingly good and are within 1% of ratios determined from single crystal X-ray diffraction. *Warning: While the UO₃ contains depleted U, standard precautions for handling radioactive materials should be followed.*

K[$\text{UO}_2(\text{IO}_3)_3$]. UO₃ (0.269 g, 0.940 mmol), K₂CO₃ (0.130 g, 0.940 mmol), V₂O₅ (0.171 g, 0.940 mmol), H₅IO₆ (0.429 g, 1.88 mmol), and 1.5 mL of deionized water were loaded into the 23 mL autoclave. The pH of the initial mixture was 1.1. The autoclave was heated to 180 °C in a box furnace for 72 h, and cooled at a rate of 9 °C/h to room temperature. The product mixture consisted of a colorless solution with a pH of 2.9 over a bright yellow precipitate containing tablets of **KUI**. The product was washed with methanol and allowed to dry. Crystals were separated from the mixture for further study. Yield 0.26 g (33% yield based on the U). EDX analysis provided K:U:I ratio of 1:1:3 (21%:19%:60%). IR (KBr, cm⁻¹): 902 (ν_3 , UO₂²⁺), 857 (ν_1 , UO₂²⁺), 832 (ν , IO₃⁻), 817 (ν , IO₃⁻), 808 (ν , IO₃⁻), 786 (ν , IO₃⁻), 763 (ν , IO₃⁻), 733 (ν , IO₃⁻), 525 (δ , IO₃⁻).

Crystallographic Studies. A tablet of **KUI** with dimensions of 0.133 x 0.046 x 0.013 mm was mounted on a thin glass fiber with epoxy, secured on a goniometer head, cooled to -80 °C with an Oxford Cryostat, and optically aligned on a Bruker SMART APEX CCD X-ray diffractometer using a digital camera. Intensity measurements were

performed using graphite monochromated Mo-K α radiation from a sealed tube with a monocapillary collimator. SMART was used for preliminary determination of the cell parameters and data collection control. The intensities of reflections of a sphere were collected by a combination of 3 sets of exposures (frames). Each set had a different ϕ angle for the crystal and each exposure covered a range of 0.3° in ω . A total of 1800 frames were collected with an exposure time per frame of 30 s.

Determination of integrated intensities and global cell refinement were performed with the Bruker SAINT (v 6.02) software package using a narrow-frame integration algorithm. An analytical absorption correction²⁵ was applied followed by a semi-empirical absorption correction using SADABS.²⁶ The program suite SHELXTL (v 6.12) was used for space group determination (XPREP), structure solution (XS), and refinement (XL).²⁵ The final refinement included anisotropic displacement parameters for all atoms and a secondary extinction parameter. Additional crystallographic details are listed in Table 2.1. Atomic coordinates and equivalent isotropic displacement parameters are given in Table 2.2.

Ion-exchange studies. 0.01 M NaCl, 0.01 M KCl, and 0.01 M CsCl solutions were used for the study of the ion-exchange properties of **KUI** for Na⁺, K⁺, and Cs⁺ ions, respectively. All samples were equilibrated in the solutions for three days. The concentrations of the solutions before and after uptake were measured with ion-selective electrodes.²⁷ The mass to volume ratio was 1:1000 (0.01 g for 10 ml of solution).

Table 2.1. Crystallographic data for K[$\text{UO}_2(\text{IO}_3)_3$] (**KUI**).

Compound	KUI
Formula mass	833.83
Color and habit	yellow tablet
Crystal system	orthorhombic
Space group	<i>Pbca</i> (No. 61)
a (Å)	11.495(1)
b (Å)	7.2293(7)
c (Å)	25.394(2)
α (°)	90
β (°)	90
γ (°)	90
V (Å ³)	2110.3(3)
Z	8
T (°C)	193 K
λ (Å)	0.71073
$2\theta_{\text{max}}$	56.64
ρ_{calcd} (g cm ⁻³)	5.249
$\mu(\text{Mo } K\alpha)$ (cm ⁻¹)	246.03
$R(F)$ for $F_o^2 > 2\sigma(F_o^2)$ ^a	0.0195
$R_w(F_o^2)$ ^b	0.0458

$$^a R(F) = \sum \|F_o\| - |F_c| / \sum |F_o|. \quad ^b R_w(F_o^2) = \left[\sum \left[w(F_o^2 - F_c^2)^2 \right] / \sum wF_o^4 \right]^{1/2}.$$

Table 2.2. Atomic Coordinates and Equivalent Isotropic Displacement Parameters for $\text{K}[\text{UO}_2(\text{IO}_3)_3]$ (**KUI**).

Atom	Symmetry ^a	<i>x</i>	<i>y</i>	<i>z</i>	$U_{\text{eq}} (\text{\AA}^2)$ ^a	Occup.
U(1)	8 <i>c</i> 1	0.0255(1)	0.0351(1)	0.6519(1)	0.009(1)	1
I(1)	8 <i>c</i> 1	0.0654(1)	0.4563(1)	0.5630(1)	0.013(1)	1
I(2)	8 <i>c</i> 1	-0.2992(1)	0.1366(1)	0.6557(1)	0.011(1)	1
I(3)	8 <i>c</i> 1	0.3409(1)	0.0593(1)	0.7031(1)	0.010(1)	1
K(1)	8 <i>c</i> 1	0.1642(1)	-0.9480(2)	0.4781(1)	0.026(1)	1
O(1)	8 <i>c</i> 1	0.0605(3)	0.3375(4)	0.6280(1)	0.012(1)	1
O(2)	8 <i>c</i> 1	-0.0357(3)	0.3232(5)	0.5246(1)	0.018(1)	1
O(3)	8 <i>c</i> 1	0.1980(3)	0.3599(5)	0.5391(1)	0.021(1)	1
O(4)	8 <i>c</i> 1	-0.1523(3)	0.2142(5)	0.6423(1)	0.016(1)	1
O(5)	8 <i>c</i> 1	-0.3464(3)	0.1100(5)	0.5888(1)	0.019(1)	1
O(6)	8 <i>c</i> 1	-0.3497(3)	0.3740(4)	0.6669(2)	0.017(1)	1
O(7)	8 <i>c</i> 1	0.2277(3)	0.0367(5)	0.6539(1)	0.014(1)	1
O(8)	8 <i>c</i> 1	0.2723(3)	0.2224(5)	0.7463(1)	0.016(1)	1
O(9)	8 <i>c</i> 1	0.4362(3)	0.2138(4)	0.6671(1)	0.014(1)	1
O(10)	8 <i>c</i> 1	0.0261(3)	0.0927(5)	0.7202(1)	0.015(1)	1
O(11)	8 <i>c</i> 1	0.0272(3)	-0.0278(4)	0.5842(1)	0.014(1)	1

^a Symmetry describes multiplicity, Wyckoff parameter and symmetry of the atomic site.

^b U_{eq} is defined as one-third of the trace of the orthogonalized \mathbf{U}_{ij} tensor.

RESULTS AND DISCUSSION

Syntheses. The reaction of UO_3 with KIO_4 and V_2O_5 under mild basic hydrothermal conditions has been previously shown to result in the formation of $\text{K}_2[(\text{UO}_2)_2(\text{VO})_2(\text{IO}_6)_2\text{O}]\cdot\text{H}_2\text{O}$ in high yield.²⁸ In an effort to explore both the compositional space of this reaction and the effects of pH on product formation we have continued to investigate this reaction. In acidic conditions $\text{K}[\text{UO}_2(\text{IO}_3)_3]$ (**KUI**) is formed in moderate yield from similar reactants (K_2CO_3 and H_5IO_6 instead of KIO_4) that yielded $\text{K}_2[(\text{UO}_2)_2(\text{VO})_2(\text{IO}_6)_2\text{O}]\cdot\text{H}_2\text{O}$.

Structure. $\text{K}[\text{UO}_2(\text{IO}_3)_3]$. The structure of **KUI** consists of an approximately linear UO_2^{2+} cation with $\text{U}=\text{O}$ distances of 1.777(3) and 1.785(3) Å and an $\text{O}=\text{U}=\text{O}$ angle of 178.39(15)°. (Table 2.3) This moiety is bound by five iodate anions to form a pentagonal bipyramidal coordination environment around the uranium center as is depicted in Figure 2.1. A similar building unit also occurs in one-dimensional $\text{K}_3[(\text{UO}_2)_2(\text{IO}_3)_6](\text{IO}_3)\cdot\text{H}_2\text{O}$,¹³ although the overall connectivity and dimensionality is different from **KUI**. The $\text{U}-\text{O}$ bond distances in the equatorial plane range from 2.304(3) to 2.432(3) Å. These oxygen atoms are approximately planar and deviate from planarity by only approximately 0.08 Å. There are three crystallographically unique iodate anions in **KUI**. Two of these anions bridge between two uranyl cations and have one terminal oxygen atom. The bridging versus terminal $\text{I}-\text{O}$ bond distances can be differentiated with bridging distances occurring from 1.811(3) to 1.834(3) Å, whereas the terminal $\text{I}-\text{O}$ distances are both shorter at 1.793(3) Å. The third iodate anion is monodentate and has a bridging $\text{I}-\text{O}$ distance of 1.862(3) Å, and two terminal distances of 1.782(3) and 1.796(3) Å.

Table 2.3. Selected Bond Distances (Å) and Angles (°) for K[UO₂(IO₃)₃] (**KUI**).

Bond Lengths (Å)			
U(1)–O(1)	2.304(3)	I(1)–O(2)	1.796(3)
U(1)–O(4)	2.432(3)	I(1)–O(3)	1.782(3)
U(1)–O(6)	2.363(3)	I(2)–O(4)	1.812(3)
U(1)–O(7)	2.325(3)	I(2)–O(5)	1.793(3)
U(1)–O(9)	2.396(3)	I(2)–O(6)	1.834(3)
U(1)–O(10)	1.785(3)	I(3)–O(7)	1.811(3)
U(1)–O(11)	1.777(3)	I(3)–O(8)	1.793(3)
I(1)–O(1)	1.862(3)	I(3)–O(9)	1.812(3)
Angles (°)			
O(10)–U(1)–O(11)	178.39(15)	O(5)–I(2)–O(6)	98.72(16)
O(3)–I(1)–O(11)	99.18(17)	O(4)–I(2)–O(6)	91.97(15)
O(3)–U(1)–O(1)	98.46(15)	O(8)–I(3)–O(7)	99.50(15)
O(2)–I(1)–O(1)	102.40(15)	O(8)–I(3)–O(9)	99.77(15)
O(5)–I(2)–O(4)	97.84(16)	O(7)–I(3)–O(9)	98.19(15)

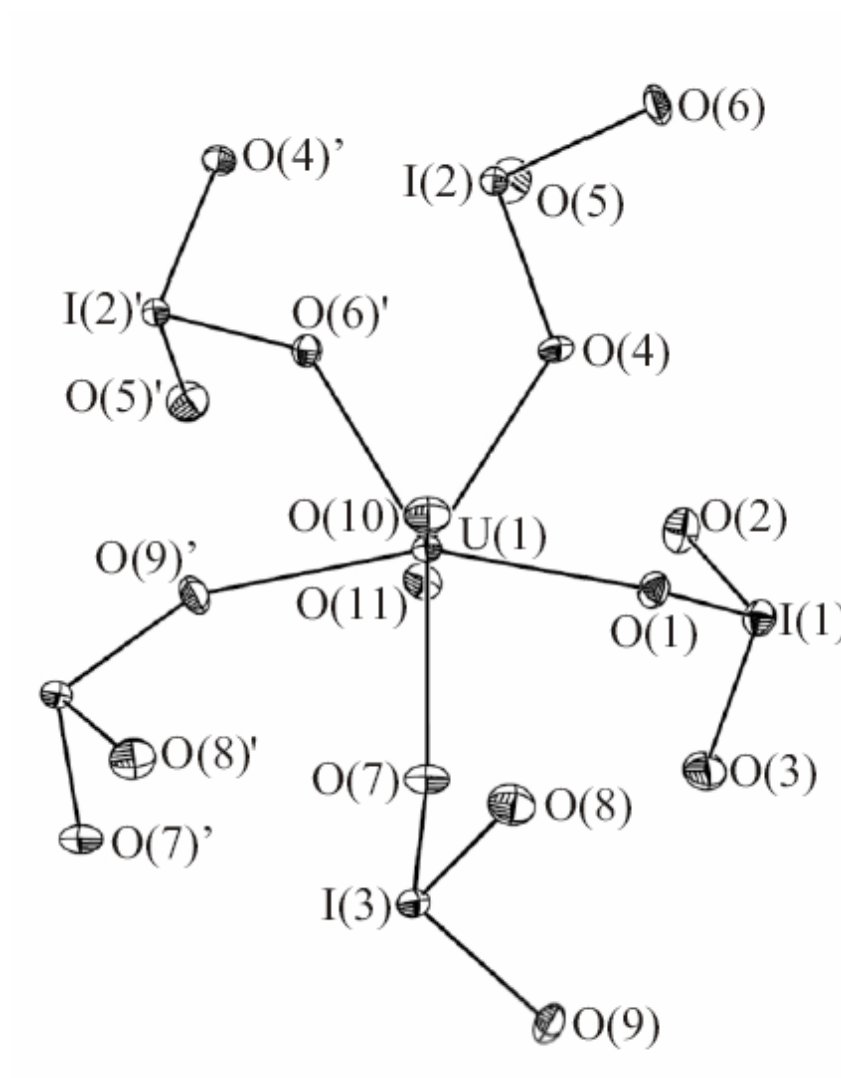


Figure 2.1. A view of the pentagonal bipyramidal coordination environment around uranium center in **KUI** that is formed from a UO_2^{2+} linear cation connected with five iodate groups through the equatorial plane.

The bridging of the uranyl cations by the iodate anions creates two-dimensional sheets in the $[ab]$ plane as shown in Figure 2.2. From this perspective it appears that the monodentate iodate anions reside in cavities within the layers. In fact, a view along the b axis (Figure 1.3) shows that these iodate anions protrude in between the layers and provides their terminal oxo atoms for forming interactions with the K^+ cations. The interactions between the K^+ cations and iodate anions stitch the structure together. The K^+ cations form long interactions with the terminal oxo atoms from both the monodentate iodate group as well as with the terminal oxo atoms from one of the bridging iodate anions. These cations also interact with the oxo atoms from the uranyl cations forming a surprisingly short contact of 2.715(3) Å.³⁴⁻³⁹ A total of eight $K^+ \cdots O$ contacts are formed, with distances ranging from 2.615(4) to 3.175(4) Å, creating a distorted dodecahedral environment around the potassium centers.

Ion-exchange Studies. The exchange of interlayer cations has been previously achieved in a number of layered uranyl compounds, most notably in the autunite and meta-autunite group.⁴⁰⁻⁴² In addition, certain uranyl compounds such as hydrogen uranyl phosphate (HUP)⁴³⁻⁴⁶ and $Cs_4[(UO_2)_2(V_2O_7)O_2]$ ⁴⁷ have been shown to exhibit high cationic conductivities. In order to evaluate the potential for ion-exchange reactions of alkali metal cations with **KUI**, samples were equilibrated with 0.01 M solutions of NaCl, KCl, or CsCl. The potential ion exchange of K^+ with Na^+ or Cs^+ was measured potentiometrically using ion-selective electrodes. In order to distinguish between absorption and actual ion exchange, the release of K^+ was also quantified. No measurable exchange was noted with Na^+ . Similarly, there was also no change noted in

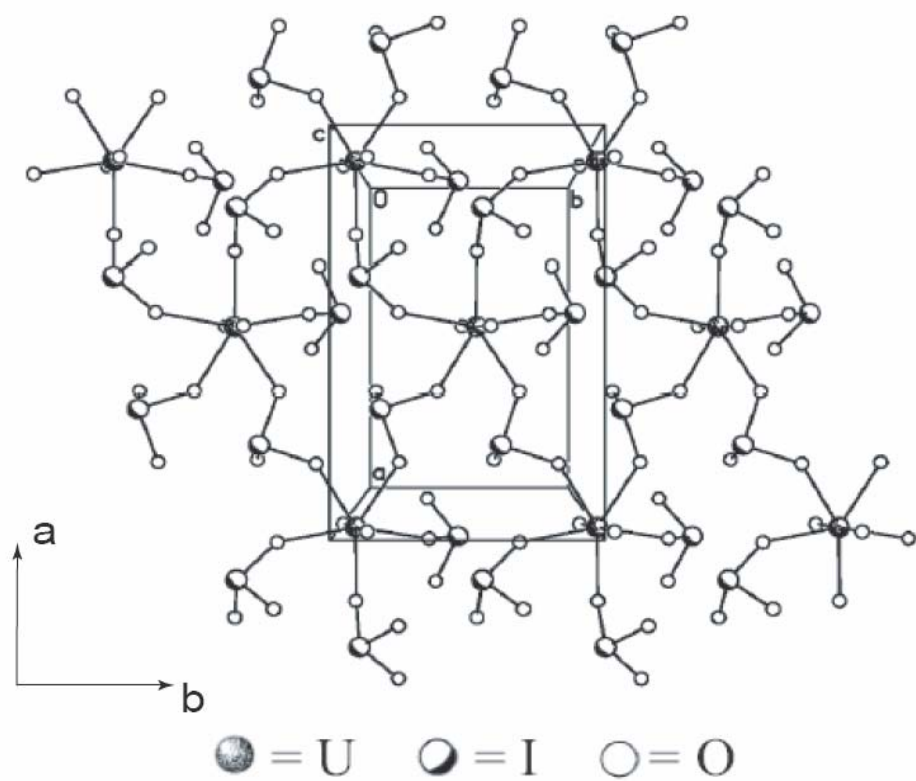


Figure 2.2. An illustration of the ${}^2_{\infty}[\text{UO}_2(\text{IO}_3)_3]^{1-}$ sheets in **KUI** that extend in the $[ab]$ plane.

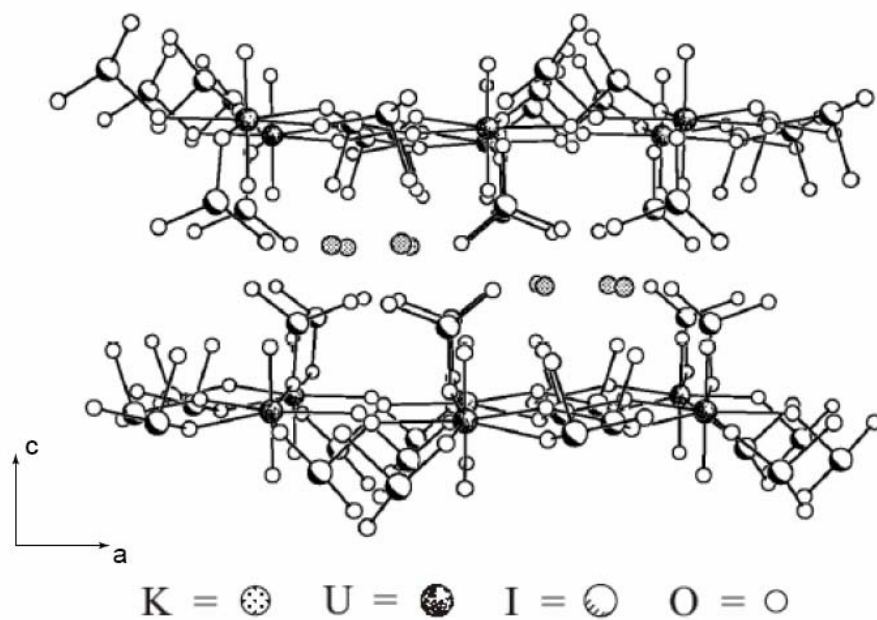


Figure 2.3. A view along the b axis of **KUI** showing that the monodentate iodate anion protrudes in between the layers, providing its terminal oxo atoms for forming interactions with the K^+ cations that reside between the layers.

the concentration of K^+ in solution in K^+ self-exchange reactions, which does not discount the possibility that equilibrium is established and exchange takes place. However, substantial Cs^+ ion exchange was noted with high uptake values of up to 3.7(1.2) meq/g. The Cs^+ ionophore is 2.53 orders of magnitude more selective for Cs^+ than K^+ . Therefore, the Cs^+ uptake value probably overestimates Cs^+ exchange because some K^+ is simultaneously being detected. In order to address this issue we also measured the release of K^+ back into solution and found a large value of 1.7 meq/g. This determination demonstrates that ion exchange is actually taking place. The resultant solids were examined using EDX, and these measurements demonstrate complete exchange of K^+ for Cs^+ with no measurable amount of K^+ being observed in the ion-exchanged solid. Given that the reaction takes place at room temperature in basic media, and that uranyl iodates are extremely insoluble in water even at low pH, we suggest that dissolution and recrystallization do not occur concomitantly with the exchange process. In order to confirm this, powder X-ray diffraction data were collected before and after ion exchange. The diffraction patterns were superimposable, indicating that there is virtually no structural change that occurs concomitantly with ion exchange.

CONCLUSIONS

The uranyl iodate system continues to provide remarkable new structure types unparalleled by other types of oxoanions. The formation of $K[UO_2(IO_3)_3]$ under less acidic conditions (final pH = 2.9 vs. ca. 1) than have been typically employed in the past to prepare uranyl iodates may point to a new family of compounds that form at higher pH. Studies to address this issue are underway. We note that attempts to prepare

$\text{Cs}[\text{UO}_2(\text{IO}_3)_3]$ directly under conditions equivalent to those used to prepare **KUI** failed. Instead a new polycrystalline phase forms with a Cs/U/I ratio of 1:3:1. We have been unable as yet to determine the structure of this new cesium uranyl iodate. This result suggests that the K^+ cations play a structure-directing role in the formation of **KUI**.

REFERENCES

1. Artmann, P. *Z. Anorg. Chem.* **1913**, 79, 327.
2. Venugopalan, M. *Z. Anal. Chem.* **1956**, 153, 187.
3. Ciavatta, L.; De Tommaso, G.; Iuliano, M. *Ann. Chim.* **2003**, 93, 269.
4. Karbowiak, M.; Fourest, B.; Hubert, S.; Moulin, C. *Radiochim. Acta* **2003**, 91, 505.
5. Hall, D. *J. Inorg. Nucl. Chem.* **1958**, 6, 3.
6. Weigel, F.; Engelhardt, L. W. H. *J. Less-Common Met.* **1983**, 91, 339.
7. Bean, A. C.; Peper, S. M.; Albrecht-Schmitt, T. E. *Chem. Mater.* **2001**, 13, 1266.
8. Bean, A. C.; Xu, Y.; Danis, J. A.; Albrecht-Schmitt, T. E.; Runde, W. *Inorg. Chem.* **2002**, 41, 6775.
9. Sykora, R. E.; McDaniel, S. M.; Wells, D. M.; Albrecht-Schmitt, T. E. *Inorg. Chem.* **2002**, 41, 5126.
10. Sykora, R. E.; Wells, D. M.; Albrecht-Schmitt, T. E. *Inorg. Chem.* **2002**, 41, 2304.
11. Bean, A. C.; Albrecht-Schmitt, T. E. *J. Solid State Chem.* **2001**, 161, 416.
12. Bean, A. C.; Ruf, M.; Albrecht-Schmitt, T. E. *Inorg. Chem.* **2001**, 40, 3959.
13. Sykora, R. E.; Bean, A. C.; Scott, B. L.; Runde, W. Albrecht-Schmitt, T. E. *J. Solid State Chem.* **2004**, 177, 725.
14. Bean, A. C.; Campana, C. F.; Kwon, O.; Albrecht-Schmitt, T. E. *J. Am. Chem. Soc.* **2001**, 123, 8806.
15. Burns, P. C.; Ewing, R. C.; Hawthorne, F. C. *Can. Mineral.* **1997**, 35, 1551.
16. Burns, P. C. In *Uranium: Mineralogy, Geochemistry and the Environment*; Burns, P. C.; Finch, R., Eds. Ch. 1, Mineralogical Society of America: Washington, DC, **1999**.
17. Burns, P. C.; Miller, M. L.; Ewing, R. C. *Can. Mineral.* **1996**, 34, 845.

18. Albrecht-Schmitt, T. E.; Almond, P. M.; Sykora, R. E. *Inorg. Chem.* **2003**, *42*, 3788.
19. Bean, A. C.; Scott, B. L.; Albrecht-Schmitt, T. E. ; Runde, W. *Inorg. Chem.* **2003**, *42*, 5632.
20. Runde, W.; Bean, A. C.; Albrecht-Schmitt, T. E.; Scott, B. L. *Chem. Commun. (Cambridge)* **2003**, *4*, 478.
21. Almond, P. M.; Albrecht-Schmitt, T. E. *Inorg. Chem.* **2002**, *41*, 1177.
22. Almond, P. M.; McKee, M. L.; Albrecht-Schmitt, T. E. *Angew. Chem.* **2002**, *114*, 3576.
23. Sykora, R. E.; King, J. E.; Illies, A. J.; Albrecht-Schmitt, T. E. *J. Solid State Chem.* **2004**, *177*, 1717
24. Hughes, K.-A.; Burns, P. C.; Kolitsch, U. *Can. Mineral.* **2003**, *41*, 677.
25. G. M. Sheldrick, SHELXTL PC, Version 6.12, An Integrated System for Solving, Refining, and Displaying Crystal Structures from Diffraction Data; Siemens Analytical X-Ray Instruments, Inc.: Madison, WI 2001.
26. *SADABS*. Program for absorption correction using SMART CCD based on the method of Blessing: Blessing, R. H. *Acta Crystallogr.* **1995**, *A51*, 33.
27. Buehlmann, P.; Pretsch, E.; Bakker, E. *Chem. Rev.* **1998**, *98*, 1593.
28. Sykora R. E.; Albrecht-Schmitt, T. E. *Inorg. Chem.* **2003**, *42*, 2179.
29. Abrahams, S. C.; Bernstein, J. L.; Elemans, J. B. A. A.; Verschoor, G. C. *J. Chem. Phys.* **1973**, *59*, 2007.
30. Burns, P. C.; Hawthorne, F. C. *Can. Mineral.* **1993**, *31*, 313.
31. Cooper, M. A.; Hawthorne, F. C.; Roberts, A. C.; Grice, J. D.; Stirling, J. A. R. E.; Moffatt, A. *Am. Mineral.* **1998**, *83*, 390.

32. Brown, I. D.; Altermatt, D. *Acta Crystallogr.* **1985**, *B41*, 244.
33. Brese, N. E.; O'Keeffe, M. *Acta Crystallogr.* **1991**, *B47*, 192.
34. Zachariasen, W. H. *Acta Crystallogr.* **1948**, *1*, 281.
35. Zachariasen, W. H. *Acta Crystallogr.* **1954**, *7*, 788.
36. Zachariasen, W. H. *Acta Crystallogr.* **1954**, *7*, 795.
37. Thuéry, P.; Masci, B. *Polyhedron* **2004**, *23*, 649.
38. Thuéry, P.; Masci, B. *J. Chem. Soc., Dalton Trans.* **2003**, *12*, 2411.
39. Sullens, T. A.; Jensen, R. A.; Shvareva, T. Y.; Albrecht-Schmitt, T. E. *J. Am. Chem. Soc.* **2004**, *126*, 2676.
40. Dieckmann, G. H.; Ellis, A. B. *Solid State Ionics* **1989**, *32/33*, 50.
41. Vochten, R. *Am. Mineral.* **1990**, *75*, 221.
42. Benavente, J.; Ramos Barrado, J. R.; Cabeza, A.; Bruque, S.; Martinez, M. *Colloids Surf.* **1995**, *A 97*, 13.
43. Grohol, D.; Blinn, E. L. *Inorg. Chem.* **1997**, *36*, 3422.
44. Johnson, C. H.; Shilton, M. G.; Howe, A. T. *J. Solid State Chem.* **1981**, *37*, 37.
45. Moreno-Real, L.; Pozas-Tormo, R.; Martinez-Lara, M.; Bruque-Gamez, S. *Mater. Res. Bull.* **1987**, *22*, 29.
46. Pozas-Tormo, R.; Moreno-Real, L.; Martinez-Lara, M.; Rodriguez-Castellon, E. *Can. J. Chem.* **1986**, *64*, 35.
47. Obbade, S.; Dion, C.; Saadi, M.; Abraham, F. *J. Solid State Chem.* **2004**, *177*, 1567.

CHAPTER 3

**SYNTHESES, STRUCTURES, AND ION-EXCHANGE PROPERTIES OF THE
THREE-DIMENSIONAL FRAMEWORK URANYL GALLIUM PHOSPHATES,
 $\text{Cs}_4[(\text{UO}_2)_2(\text{GaOH})_2(\text{PO}_4)_4] \cdot \text{H}_2\text{O}$ AND $\text{Cs}[\text{UO}_2\text{Ga}(\text{PO}_4)_2]$**

ABSTRACT

The reaction of $\text{UO}_2(\text{NO}_3)_2 \cdot 6\text{H}_2\text{O}$ with Cs_2CO_3 or CsCl , H_3PO_4 , and Ga_2O_3 under mild hydrothermal conditions results in the formation of $\text{Cs}_4[(\text{UO}_2)_2(\text{GaOH})_2(\text{PO}_4)_4] \cdot \text{H}_2\text{O}$ (**UGaP1**) or $\text{Cs}[\text{UO}_2\text{Ga}(\text{PO}_4)_2]$ (**UGaP2**). The structure of **UGaP1** was solved from a twinned crystal revealing a three-dimensional framework structure consisting of one-dimensional ${}^1_\infty[\text{Ga}(\text{OH})(\text{PO}_4)_2]^{4-}$ chains composed of corner-sharing GaO_6 octahedra and bridging PO_4 tetrahedra that extend along the c axis. The phosphate anions bind the UO_2^{2+} cations to form UO_7 pentagonal bipyramids. The UO_7 moieties edge-share to create dimers that link the gallium phosphate substructure into a three-dimensional ${}^3_\infty[(\text{UO}_2)_2(\text{GaOH})_2(\text{PO}_4)_4]^{4-}$ anionic lattice that has intersecting channels running down the b and c axes. Cs^+ cations and water molecules occupy these channels. The structure of **UGaP2** is also three-dimensional and contains one-dimensional ${}^1_\infty[\text{Ga}(\text{PO}_4)_2]^{3-}$ gallium phosphate chains that extend down the a axis. These chains are formed from fused eight-membered rings of corner-sharing GaO_4 and PO_4 tetrahedra. The chains are in turn linked together into a three-dimensional ${}^3_\infty[\text{UO}_2\text{Ga}(\text{PO}_4)_2]^{1-}$ framework by edge-sharing

UO₇ dimers as occurs in **UGaP1**. There are channels that run down the *a* and *b* axes through the framework. These channels contain the Cs⁺ cations. Ion-exchange studies indicate that the Cs⁺ cations in **UGaP1** and **UGaP2** can be exchanged for Ca²⁺ and Ba²⁺. Crystallographic data: **UGaP1**, monoclinic, space group *P2₁/c*, *a* = 18.872(1), *b* = 9.5105(7), *c* = 14.007(1) Å, β = 109.65(3), *Z* = 4 (T = 295 K); **UGaP2**, triclinic, space group *P1̄*, *a* = 7.7765(6), *b* = 8.5043(7), *c* = 8.9115(7) Å, α = 66.642(1), β = 70.563(1), γ = 84.003(2), *Z* = 2 (T = 193 K).

INTRODUCTION

The syntheses, structures, and physicochemical properties of gallium phosphates have been the subjects of intense interest for two decades owing to their enormously rich structural chemistry that is particularly well noted for forming microporous open-framework topologies that in some cases are similar to the AlPO₄ family of compounds.¹⁻
⁴ The diversity in this class of compounds finds its origins in the fundamental coordination chemistry of Ga(III), which occurs as GaO₄ tetrahedra (e.g. in [H₃N(CH₂)₃NH₃][GaH(PO₄)₂]⁵ and [Ga(HPO₄)(PO₄)(OH)]·[(C₂H₇N)₃N]·H₂O⁶), GaO₅ trigonal bipyramids (e.g. in [NH₄][Ga(OH)(PO₄)]⁷ and Ga₃(PO₄)₃·C₃H₉N·H₂O⁸), and GaO₆ octahedra (e.g. in [NH₄]₃[Ga₂(PO₄)₃]⁷ and Rb(GaPO₄)₂(OH)(H₂O)·H₂O⁹). In fact, there are examples of compounds where Ga exhibits multiple geometries in the same compound as has been found for Na[Ga₂(OH)(PO₄)₂]¹⁰ and Na₃Ga₅(PO₄)₄O₂(OH)₂·2H₂O,¹¹ which contain GaO₅ trigonal bipyramids and GaO₆ octahedra. These fundamental building units can combine with phosphate tetrahedra in a vast number of permutations to create zero-dimensional structures in

$[\text{Ga}(\text{HPO}_4)(\text{PO}_4)(\text{OH})] \cdot [(\text{C}_2\text{H}_7\text{N})_3\text{N}] \cdot \text{H}_2\text{O}^6$ and $[\text{C}_6\text{H}_5\text{NH}]_2[\text{H}_8\text{Ga}_4\text{P}_4\text{O}_{21}]$,¹² one-dimensional chains as found in the organically templated gallium phosphates $[\text{NH}_3(\text{CH}_2)_4\text{NH}_3][\text{Ga}(\text{PO}_4)(\text{PO}_3\text{OH})]$,¹³ $[(1\text{R},2\text{R})\text{-C}_6\text{H}_{10}(\text{NH}_3)_2][\text{Ga}(\text{OH})(\text{HPO}_4)_2] \cdot \text{H}_2\text{O}$,¹⁴ and $[\text{NH}_3(\text{CH}_2)_2(\text{NH}_3)][\text{Ga}(\text{H}_2\text{PO}_4)(\text{P}_2\text{O}_7)]$,¹⁵ two-dimensional sheets in $[\text{C}_5\text{H}_6\text{N}][\text{Ga}(\text{HPO}_4)_2(\text{H}_2\text{O})_2]$ ¹⁶ and $[\text{NH}_4]\text{Ga}(\text{OH})(\text{PO}_4)]$,⁷ and three-dimensional networks in $\text{NaGa}_2(\text{OH})(\text{PO}_4)_2$,¹⁰ $\text{Na}_3\text{Ga}_5(\text{PO}_4)_4\text{O}_2(\text{OH})_2 \cdot 2\text{H}_2\text{O}$,¹¹ and $[\text{NH}_3(\text{CH}_2)_3(\text{NH}_3)][\text{Ga}_3(\text{PO}_4)_3(\text{H}_2\text{O})]$.¹⁷

The structural complexity and properties of gallium phosphates can be expanded through the inclusion of transition metals into the anionic lattice. The incorporation of transition metals into gallium phosphates can take place in several ways. First, partial substitution at Ga sites can take place to yield disordered compounds, which is illustrated by $[\text{C}_5\text{H}_5\text{NH}][\text{CoGa}_2\text{P}_3\text{O}_{12}]$, where $\text{CoO}_4/\text{GaO}_4$ disorder exists.¹⁸ Anomalous X-ray scattering is a powerful tool in this regard, and has been used to establish the distribution of Zn^{2+} and Ga^{3+} in a series of zinc-substituted gallium phosphates.¹⁹ Second, the transition metal centers can force the adoptions of new structure types to accommodate additional building units as occurs in $\text{Rb}[(\text{VO})(\text{H}_2\text{O})\text{Ga}(\text{PO}_4)_2]$ ²⁰ and $\text{Mn}_3(\text{H}_2\text{O})_6\text{Ga}_4(\text{PO}_4)_6$,²¹ the latter of which forms gallium phosphate channels to house $\text{Mn}_3(\text{H}_2\text{O})_6\text{O}_8$ clusters. This compound also exhibits superexchange interactions between $\text{Mn}(\text{II})$ centers, illustrating one of the many properties that can be added to gallium phosphates by incorporating transition metals.²¹

In order to prepare uranyl compounds with three-dimensional open-framework structures, we have focused on the use of octahedral anions, such as periodate, IO_6^{5-} , as building units.^{22,23} The formation of three-dimensional network structures incorporating the approximately linear uranyl, UO_2^{2+} , cation are not common because uranyl-

containing polyhedra typically condense with uranyl units parallel to one another, and because the uranyl oxo atoms are typically terminal, layered structures most often result.²⁴ In spite of this structural propensity, a number of different uranyl systems have been shown to adopt three-dimensional framework structures including phosphates such as $[\text{C}_4\text{H}_{12}\text{N}_2](\text{UO}_2)[(\text{UO}_2)(\text{PO}_4)]_4 \cdot 2\text{H}_2\text{O}$ ²⁵ and $[(\text{UO}_2)_3(\text{PO}_4)\text{O}(\text{OH})(\text{H}_2\text{O})_2](\text{H}_2\text{O})$,²⁶ the fluorophosphate $[\text{C}_6\text{H}_{14}\text{N}_2]_2[(\text{UO}_2)_6(\text{H}_2\text{O})_2\text{F}_2(\text{PO}_4)_2(\text{HPO}_4)_4] \cdot 4\text{H}_2\text{O}$,²⁷ arsenates, e.g. $[\text{NH}(\text{C}_2\text{H}_5)_3][(\text{UO}_2)_2(\text{AsO}_4)(\text{AsO}_3\text{OH})]$,²⁵ vanadates, e.g. $\text{A}(\text{UO}_2)_4(\text{VO}_4)_3$ (A = Li, Na),²⁸ and oxides, e.g. $(\text{NH}_4)_3(\text{H}_2\text{O})_2\{[(\text{UO}_2)_{10}\text{O}_{10}(\text{OH})][(\text{UO}_4)(\text{H}_2\text{O})_2]\}$.²⁹ In this chapter we report the preparation and characterization of the first examples of actinide-containing gallium phosphates, $\text{Cs}_4[(\text{UO}_2)_2(\text{GaOH})_2(\text{PO}_4)_4] \cdot \text{H}_2\text{O}$ (**UGaP1**) and $\text{Cs}[\text{UO}_2\text{Ga}(\text{PO}_4)_2]$ (**UGaP2**), both of which possess three-dimensional framework structures.

EXPERIMENTAL

Syntheses. $\text{UO}_2(\text{NO}_3)_2 \cdot 6\text{H}_2\text{O}$ (98%, Alfa-Aesar), Ga_2O_3 (99.99%, Alfa-Aesar), Cs_2CO_3 (99.99%, Alfa-Aesar), H_3PO_4 (98%, Aldrich), KCl (99%, Aldrich), NaCl (99%, Aldrich), CsCl (99.9%, Cerac), CaCl_2 (99%, Aldrich), and BaCl_2 (99%, Aldrich) were used as received. Reactions were performed in the PTFE-lined Parr 4749 autoclaves. Distilled and Millipore filtered water with a resistance of 18.2 $\text{M}\Omega\cdot\text{cm}$ was used in all reactions. Standard precautions were performed for handling radioactive materials during work with $\text{UO}_2(\text{NO}_3)_2 \cdot 6\text{H}_2\text{O}$ and the products of the reactions. Semi-quantitative SEM/EDX analyses were performed using a JEOL 840/Link Isis instrument. Cs, U, Ga, and P percentages were calibrated against standards.

Cs₄[(UO₂)₂(GaOH)₂(PO₄)₄](H₂O) (UGaP1). UO₂(NO₃)₂·6H₂O (0.238 g, 0.474 mmol), Ga₂O₃ (0.112 g, 0.948 mmol), H₃PO₄ (0.186 g, 1.88 mmol), Cs₂CO₃ (0.464 g, 1.41 mmol), and 1 mL water were loaded into a 23 mL autoclave. The autoclave was then heated to 180 °C in a box furnace for 12 d and slow cooled at 3 °C/h to room temperature. The product mixture consisted of a colorless solution and a bright yellow precipitate. The solid was washed with water and methanol and allowed to dry. Rectangular shape tablets of **UGaP1** were then separated, with a yield of 130 mg (55% yield based on the U), from the mixture for further study. The Cs:U:Ga:P ratio determined from EDX analysis was approximately 2:1:1:2.

Cs[UO₂Ga(PO₄)₂] (UGaP2). UO₂(NO₃)₂·6H₂O (0.307 g, 0.611 mmol), Ga₂O₃ (0.144 g, 1.22 mmol), H₃PO₄ (0.239 g, 2.44 mmol), and CsCl (0.309 g, 1.83 mmol) were loaded into the 23 mL autoclave followed by the addition of 2 mL of water. The autoclave was heated for 4 d at 180 °C in a box furnace and then cooled to room temperature at 9 °C/h. The solid product consisted of a mixture of white and green-yellow crystals. After decanting the mother liquor, the product was washed with water and methanol and allowed to dry. Rectangular shape green-yellow tablets of **UGaP-2** were then separated from the mixture of yellow and white amorphous precipitates. The isolated yield was 46 mg (15% yield based on the U). EDX analysis provided Cs:U:Ga:P ratio of 1:1:1:2.

Crystallographic Studies. Crystals of Cs₄[(UO₂)₂(GaOH)₂(PO₄)₄]·H₂O (**UGaP1**) and Cs[UO₂Ga(PO₄)₂] (**UGaP2**) were mounted on glass fibers and aligned on a Bruker SMART APEX CCD X-ray diffractometer. Intensity measurements were performed using graphite monochromated Mo K α radiation from a sealed tube and

monocapillary collimator. SMART (v 5.624) was used for preliminary determination of the cell constants and data collection control. The intensities of reflections of a sphere were collected by a combination of 3 sets of exposures (frames). Each set had a different ϕ angle for the crystal and each exposure covered a range of 0.3° in ω . A total of 1800 frames were collected with an exposure time per frame of 30 s for **UGaP1** and 120 s for **UGaP2**.

Crystals of **UGaP1** suffered from two problems. First, the crystal cracked when cooled to 193 K, and the data was therefore collected at 295 K. Second, all of the crystals examined proved to be twinned. GEMINI was used to separated the individual components of the twin, and the structure was solved as follows.

For **UGaP1** and **UGaP2** determination of integrated intensities and global refinement were performed with the Bruker SAINT (v 6.02) software package using a narrow-frame integration algorithm. A face-indexed analytical absorption correction was initially applied using XPREP, where individual shells of unmerged data were corrected analytically.³⁰ These files were subsequently treated with a semiempirical absorption correction by SADABS.³¹ The program suite SHELXTL (v 6.12) was used for space group determination (XPREP), direct methods structure solution (XS), and least-squares refinement (XL).³⁰ The final refinements included anisotropic displacement parameters for all atoms. Secondary extinction was not noted for either crystal. Some crystallographic details are given in Table 3.1. Atomic coordinates, symmetry, displacement parameters and occupancy for **UGaP1** and **UGaP2** can be found in Tables 3.2 and 3.3 respectively.

Table 3.1. Crystallographic Data for $\text{Cs}_4[(\text{UO}_2)_2(\text{GaOH})_2(\text{PO}_4)_4] \cdot \text{H}_2\text{O}$ (**UGaP1**) and $\text{Cs}[\text{UO}_2\text{Ga}(\text{PO}_4)_2]$ (**UGaP2**).

Formula	$\text{Cs}_4[(\text{UO}_2)_2(\text{GaOH})_2(\text{PO}_4)_4] \cdot \text{H}_2\text{O}$	$\text{Cs}[\text{UO}_2\text{Ga}(\text{PO}_4)_2]$
Formula Mass	1641.04	662.60
Color and habit	yellow tablet	yellow-green tablet
Space group	$P2_1/c$ (No. 14)	$P\bar{1}$ (No. 2)
a (Å)	18.872(1)	7.7765(6)
b (Å)	9.5105(7)	8.5043(7)
c (Å)	14.007(1)	8.9115(7)
α (°)	90	66.642(1)
β (°)	109.65(3)	70.563(1)
γ (°)	90	84.003(2)
V (Å ³)	2367.5(3)	509.96(7)
Z	4	2
T (K)	295	193
λ (Å)	0.71073	0.71073
Maximum 2θ (deg.)	56.64	56.60
ρ_{calcd} (g cm ⁻³)	4.598	4.315
$\mu(\text{Mo } K\alpha)$ (cm ⁻¹)	223.20	223.65
$R(F)$ for $F_o^2 > 2\sigma(F_o^2)$	0.0424	0.0283
$R_w(F_o^2)^b$	0.0973	0.0626

$$^a R(F) = \sum \|F_o\| - |F_c| / \sum |F_o|. \quad ^b R_w(F_o^2) = \left[\sum \left[w(F_o^2 - F_c^2)^2 \right] / \sum wF_o^4 \right]^{1/2}.$$

Table 3.2. Atomic Coordinates and Equivalent Isotropic Displacement Parameters for
Cs₄[(UO₂)₂(GaOH)₂(PO₄)₄]·H₂O (**UGaP1**)

Atom	Symmetry ^a	<i>x</i>	<i>y</i>	<i>z</i>	<i>U</i> _{eq} (Å ²) ^b	Occup.
U(1)	4 <i>e</i> 1	0.53831(2)	-0.70597(4)	0.51964(3)	0.01196(9)	1
U(2)	4 <i>e</i> 1	0.96212(2)	-0.71325(4)	0.98701(3)	0.01205(9)	1
Ga(1)	4 <i>e</i> 1	1.25499(6)	-0.77386(9)	1.23126(8)	0.0119(2)	1
Ga(2)	4 <i>e</i> 1	1.25230(6)	-0.74603(9)	0.98122(8)	0.0116(2)	1
P(1)	4 <i>e</i> 1	0.65190(15)	-0.4630(3)	0.6033(2)	0.0125(5)	1
P(2)	4 <i>e</i> 1	1.37577(14)	-0.9350(3)	1.41044(19)	0.0114(5)	1
P(3)	4 <i>e</i> 1	1.13089(14)	-0.9361(3)	1.05030(19)	0.0119(5)	1
P(4)	4 <i>e</i> 1	0.84790(14)	-0.4578(3)	0.92909(19)	0.0121(5)	1
O(1)	4 <i>e</i> 1	0.6951(4)	-0.4196(8)	0.5334(6)	0.0191(16)	1
O(2)	4 <i>e</i> 1	0.6759(4)	-0.3792(8)	0.7011(5)	0.0214(17)	1
O(3)	4 <i>e</i> 1	0.5646(4)	-0.4485(8)	0.5480(6)	0.0201(16)	1
O(4)	4 <i>e</i> 1	0.6597(4)	-0.6228(8)	0.6239(6)	0.0194(16)	1
O(5)	4 <i>e</i> 1	1.4520(4)	-0.8644(8)	1.4320(6)	0.0221(17)	1
O(6)	4 <i>e</i> 1	1.3367(4)	-0.8782(8)	1.4808(5)	0.0189(16)	1
O(7)	4 <i>e</i> 1	1.3898(4)	-1.0935(7)	1.4311(6)	0.0191(16)	1
O(8)	4 <i>e</i> 1	1.3282(4)	-0.9177(7)	1.2987(5)	0.0171(16)	1
O(9)	4 <i>e</i> 1	1.1138(4)	-1.0931(8)	1.0239(5)	0.0167(15)	1
O(10)	4 <i>e</i> 1	1.1620(4)	-0.8683(7)	0.9734(5)	0.0157(15)	1
O(11)	4 <i>e</i> 1	1.0566(4)	-0.8644(8)	1.0469(6)	0.0207(16)	1
O(12)	4 <i>e</i> 1	1.1873(4)	-0.9266(7)	1.1595(5)	0.0132(14)	1
O(13)	4 <i>e</i> 1	0.8396(4)	-0.6171(7)	0.9056(5)	0.0160(15)	1
O(14)	4 <i>e</i> 1	0.9351(4)	-0.4443(8)	0.9846(6)	0.0193(16)	1
O(15)	4 <i>e</i> 1	0.8051(4)	-0.4207(7)	1.0013(6)	0.0186(16)	1

O(16)	4 <i>e</i> 1	0.8234(4)	-0.3690(7)	0.8332(5)	0.0158(15)	1
O(17)	4 <i>e</i> 1	0.5129(4)	-0.7187(7)	0.6326(5)	0.0203(16)	1
O(18)	4 <i>e</i> 1	0.5646(4)	-0.6883(8)	0.4085(5)	0.0204(16)	1
O(19)	4 <i>e</i> 1	0.9609(4)	-0.6969(7)	1.1141(6)	0.0205(16)	1
O(20)	4 <i>e</i> 1	0.9633(4)	-0.7357(8)	0.8610(5)	0.0183(16)	1
O(21)	4 <i>e</i> 1	1.2074(4)	-0.7272(7)	0.8361(5)	0.0143(15)	1
O(22)	4 <i>e</i> 1	1.2998(4)	-0.7656(7)	1.1254(5)	0.0139(14)	1
O(23)	4 <i>e</i> 1	0.7509(7)	-0.6656(13)	1.0535(10)	0.068(3)	1
Cs(1)	4 <i>e</i> 1	0.70707(4)	-0.81967(8)	0.83263(7)	0.0337(2)	1
Cs(2)	4 <i>e</i> 1	0.55975(5)	-0.47401(9)	0.80426(6)	0.03157(19)	1
Cs(3)	4 <i>e</i> 1	0.83707(4)	-0.60810(8)	0.67258(6)	0.02768(17)	1
Cs(4)	4 <i>e</i> 1	0.93184(4)	-0.45410(8)	1.23164(6)	0.02884(18)	1

^a Symmetry describes multiplicity, Wyckoff parameter and symmetry of the atomic site.

^b U_{eq} is defined as one-third of the trace of the orthogonalized U_{ij} tensor.

Table 3.3. Atomic Coordinates and Equivalent Isotropic Displacement Parameters for Cs[$\text{UO}_2\text{Ga}(\text{PO}_4)_2$] (**UGaP2**).

Atom	Symmetry ^a	<i>x</i>	<i>y</i>	<i>z</i>	$U_{\text{eq}} (\text{\AA}^2)$ ^b	Occup.
U(1)	2 <i>i</i> 1	0.21442(3)	0.92139(3)	0.33450(3)	0.00955(7)	1
Ga(1)	2 <i>i</i> 1	0.24602(10)	0.57980(9)	0.98833(9)	0.01023(14)	1
P(1)	2 <i>i</i> 1	-0.0413(2)	0.3270(2)	1.2841(2)	0.0103(3)	1
P(2)	2 <i>i</i> 1	0.5302(2)	0.7365(2)	1.0581(2)	0.0099(3)	1
O(1)	2 <i>i</i> 1	0.0560(6)	0.8460(6)	0.2720(6)	0.0159(10)	1
O(2)	2 <i>i</i> 1	0.3671(7)	0.9913(6)	0.4080(6)	0.0145(9)	1
O(3)	2 <i>i</i> 1	-0.2013(6)	0.3571(6)	0.0150(10)	0.0195(18)	1
O(4)	2 <i>i</i> 1	0.0248(7)	0.1492(6)	1.3771(6)	0.0140(9)	1
O(5)	2 <i>i</i> 1	-0.0888(6)	0.3241(6)	1.1313(6)	0.0137(9)	1
O(6)	2 <i>i</i> 1	0.1153(7)	0.4610(6)	1.2133(6)	0.0158(10)	1
O(7)	2 <i>i</i> 1	0.3828(7)	0.7476(6)	0.9725(6)	0.0153(10)	1
O(8)	2 <i>i</i> 1	0.5978(6)	0.5503(6)	1.1144(6)	0.0131(9)	1
O(9)	2 <i>i</i> 1	0.6848(7)	0.8614(6)	0.9304(6)	0.0156(10)	1
O(10)	2 <i>i</i> 1	0.4475(6)	0.7700(6)	1.2225(6)	0.0141(9)	1
Cs(1)	2 <i>i</i> 1	0.66307(6)	0.68745(6)	0.49084(6)	0.02003(11)	1

^a Symmetry describes multiplicity, Wyckoff parameter and symmetry of the atomic site.

^b U_{eq} is defined as one-third of the trace of the orthogonalized \mathbf{U}_{ij} tensor.

Ion-exchange Studies. An Accumet Basic AB 15 pH meter was used for potentiometric measurements. The ion-exchange properties of **UGaP1** and **UGaP2** were evaluated to determine the uptake values of Na^+ , K^+ , Ca^{2+} , and Ba^{2+} ions from NaCl, KCl, CaCl_2 , and BaCl_2 solutions respectively in the range of the concentrations from 0.0001 M to 0.1 M. The release values of Cs^+ ions were also measured. The concentrations of the solutions before and after uptake and release were determined using ion-selective electrodes.³² The volume to mass ratio was 200:1 (2 mL of the solution for 0.01 g of sample).

Uptake of Sr^{2+} and duplicated measurements of Ca^{2+} concentrations were performed on a Varian 240 AA spectrometer with Hollow cathode Ca and Sr lamps. The volume to mass ratio in these experiments was 200:1 (4 mL of the solution for 0.02 g of sample).

Thermal analysis. DSC data were collected using differential scanning calorimeter TA Instrument, model. The samples of known mass encapsulated in aluminum container, were heated under nitrogen atmosphere from 30 °C to 600 °C with heating rate 10°C /minute.

RESULTS AND DISCUSSION

Synthesis. While the syntheses of $\text{Cs}_4[(\text{UO}_2)_2(\text{GaOH})_2(\text{PO}_4)_4]\cdot\text{H}_2\text{O}$ (**UGaP1**) and $\text{Cs}[\text{UO}_2\text{Ga}(\text{PO}_4)_2]$ (**UGaP2**) appear superficially similar, the reaction stoichiometries, durations, and perhaps most importantly pH are dramatically different. For the preparation of both compounds, we noted a reduction in pH between the starting reaction mixtures and that of the final mother liquor. The pH decreased from 9.1 to 7.1 during the

crystallization of **UGaP1** and from 2.4 to 1.9 during the formation of **UGaP2**. The substitution of Cs₂CO₃ by CsCl in the preparation of **UGaP2** plays a significant role in controlling the pH of these reactions. The synthesis of **UGaP1** and **UGaP2** also proved to be highly sensitive to temperature, and changes by as little as 10 °C had dramatic effects on yield, product crystallinity, and crystal size.

Structure. Cs₄[(UO₂)₂(GaOH)₂(PO₄)₄]·H₂O (UGaP1). The structure of **UGaP1** was solved to reveal a three-dimensional framework of interconnected one-dimensional gallium phosphate and uranyl phosphate chains that run approximately perpendicular to one another. The gallium phosphate chain (Figure 3.1) is composed of corner-sharing GaO₆ octahedra and bridging PO₄ tetrahedra that extend along the *c* axis, and can be formulated as $\infty^1[\text{Ga}(\text{OH})(\text{PO}_4)_2]^{4-}$. We propose based on charge balance considerations and bond-valence sums that the Ga–O–Ga backbone that runs down the gallium phosphate chains is protonated. The bond-valence sums for the O(21) and O(22) atoms in this chain are 1.12 and 1.16, which are values expected for hydroxyl sites.^{33,34} Not surprisingly, given the presence of cesium and uranium in this structure, the hydrogen atoms could not be reliably located. This type of chain is similar to that found in the aluminophosphate mineral tancoite, LiNa₂H[Al(PO₄)₂(OH)],^{35,36} and has been recognized in a large number of aluminum, gallium, and transition metal phosphates.^{14,37-43} The Ga–O bond distances range from 1.940(7) to 2.036(7) Å. The P–O bond distances show little variation and occur from 1.515(7) to 1.574(7) Å. Selected bond distances and angles for **UGaP1** are given in Table 3.4.

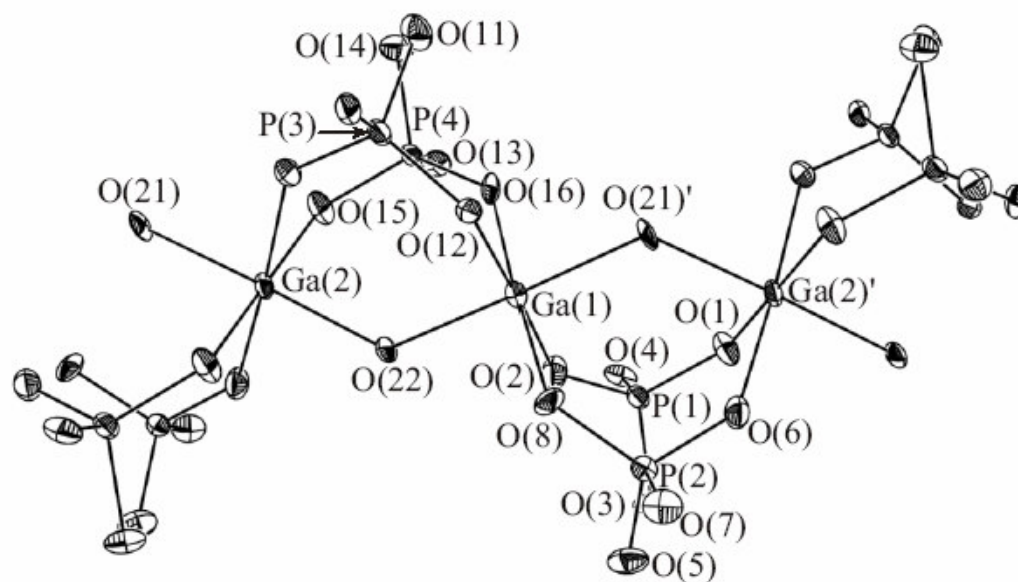


Figure 3.1. A view of the one-dimensional $^1_\infty[\text{Ga}(\text{OH})(\text{PO}_4)_2]^{4-}$ chains composed of corner-sharing GaO_6 octahedra and bridging PO_4 tetrahedra that extend along the c axis in $\text{Cs}_4[(\text{UO}_2)_2(\text{GaOH})_2(\text{PO}_4)_4] \cdot \text{H}_2\text{O}$ (**UGaP1**). 50% probability ellipsoids are depicted.

Table 3.4 Selected Bond Distances (Å) and Angles (°) for Cs₄[(UO₂)₂(GaOH)₂(PO₄)₄] (UGaP1).

Distances (Å)			
U(1)–O(3)	2.364(7)	Ga(2)–O(6)	1.984(7)
U(1)–O(3)'	2.503(7)	Ga(2)–O(10)	2.036(7)
U(1)–O(4)	2.400(7)	Ga(2)–O(15)	1.982(7)
U(1)–O(5)	2.255(8)	Ga(2)–O(21)	1.930(7)
U(1)–O(7)	2.307(7)	Ga(2)–O(22)	1.924(7)
U(1)–O(17)	1.805(7)	P(1)–O(1)	1.526(7)
U(1)–O(18)	1.794(7)	P(1)–O(2)	1.516(8)
U(2)–O(9)	2.306(7)	P(1)–O(3)	1.574(7)
U(2)–O(11)	2.223(7)	P(1)–O(4)	1.544(8)
U(2)–O(13)	2.390(7)	P(2)–O(5)	1.523(8)
U(2)–O(14)	2.376(7)	P(2)–O(6)	1.515(7)
U(2)–O(14)	2.606(7)	P(2)–O(7)	1.542(7)
U(2)–O(19)	1.795(7)	P(2)–O(8)	1.529(7)
U(2)–O(20)	1.786(7)	P(3)–O(9)	1.546(8)
Ga(1)–O(2)	1.971(7)	P(3)–O(10)	1.531(7)
Ga(1)–O(8)	1.948(7)	P(3)–O(11)	1.546(8)
Ga(1)–O(12)	1.971(7)	P(3)–O(12)	1.545(7)
Ga(1)–O(16)	1.988(7)	P(4)–O(13)	1.547(7)
Ga(1)–O(21)	1.962(7)	P(4)–O(14)	1.571(8)
Ga(1)–O(22)	1.940(7)	P(4)–O(15)	1.532(7)
Ga(2)–O(1)	1.973(7)	P(4)–O(16)	1.521(7)

Angles (°)			
O(18)–U(1)–O(17)	178.3(3)	O(20)–U(2)–O(19)	178.1(3)

There are two crystallographically unique uranium centers in **UGaP1**. Both of these U atoms are found as part of uranyl, UO_2^{2+} , cations with short $\text{U}=\text{O}$ bond distances of 1.794(7) and 1.805(7) Å to U(1), and 1.786(7) and 1.795(7) Å to U(2). In both cases the uranyl cations are nearly linear with $\text{O}(18)\text{--U}(1)\text{--O}(17)$ and $\text{O}(20)\text{--U}(2)\text{--O}(19)$ bond angles of $178.3(3)^\circ$ and $178.1(3)^\circ$, respectively. The phosphate anions bind the UO_2^{2+} cations to form UO_7 pentagonal bipyramids with $\text{U}(1)\text{--O}$ and $\text{U}(2)\text{--O}$ distances being found from 2.255(8) to 2.503(7) Å and 2.223(7) to 2.606(7) Å, respectively. These bond distances can be used to calculate bond-valence sums for the U(1) and U(2) centers of 5.94 and 5.96, which are consistent with hexavalent uranium.^{33,34,44} The bond angles in the pentagonal plane show substantial variation because the phosphate anions are found in both chelating and bridging modes. Therefore, there is an acute angle of $58.9(3)^\circ$ in the equatorial plane ascribed to the chelation of the uranyl cation containing U(1) by a phosphate anion. The remaining angles in this plane range from $63.1(3)^\circ$ to $81.7(3)^\circ$. The same situation occurs for U(2) with an acute angle of $57.6(2)^\circ$ and the other angles ranging from $61.9(3)^\circ$ to $84.8(3)^\circ$. The UO_7 moieties edge-share to create dimers that are bridged by phosphate anions to create one-dimensional chains, shown in the Figure 3.2, that can be formulated as ${}^\infty[\text{UO}_2(\text{PO}_4)_2]^{4-}$. There are two different uranyl phosphate chains, one chain exclusively contains U(1) and the other U(2). The one-dimensional topology of these chains is similar to that found in $\text{Sr}[\text{UO}_2(\text{SeO}_3)_2]\cdot 2\text{H}_2\text{O}$ where one of the P–O bonds on each phosphate anion has been replaced by a stereochemically active lone-pair on Se(IV).⁴⁵ These chains are distinct from those found in the one-dimensional uranyl phosphate, parsonite, $\text{Pb}_2[\text{UO}_2(\text{PO}_4)_2]$.⁴⁶

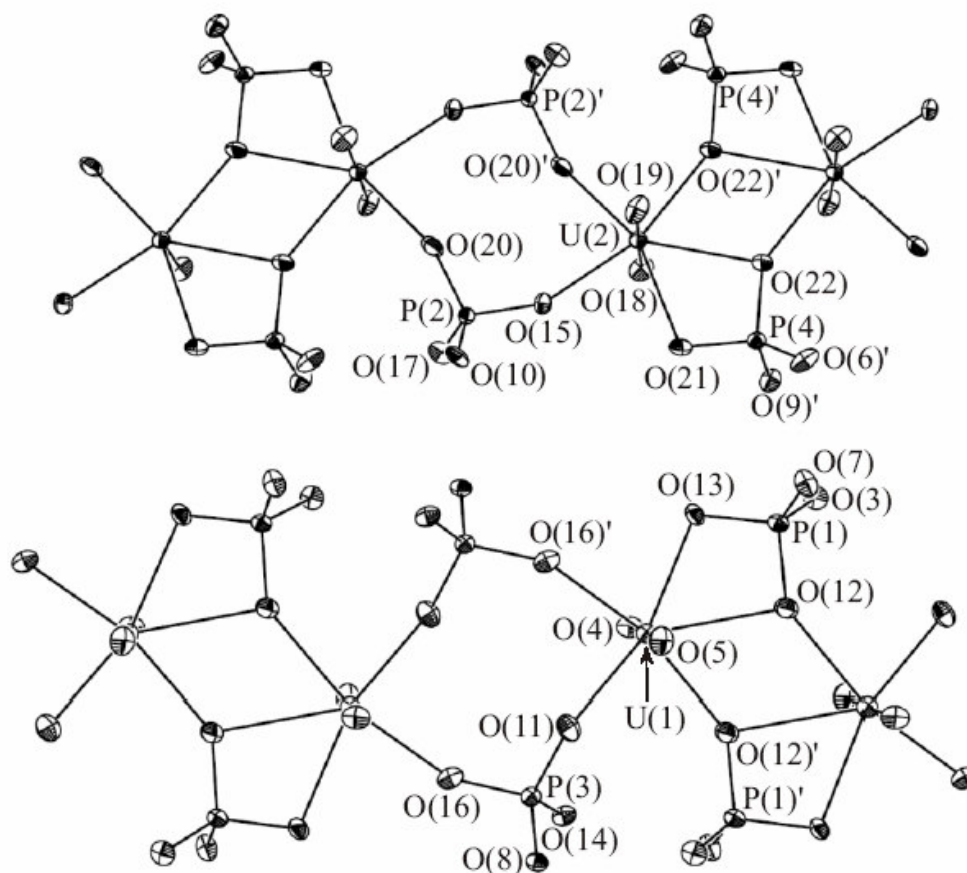


Figure 3.2. A depiction of the one-dimensional $[UO_2(PO_4)_2]^{4-}$ chains in $Cs_4[(UO_2)_2(GaOH)_2(PO_4)_4] \cdot H_2O$ (**UGaP1**). 50% probability ellipsoids are depicted.

The interconnection of the ${}^1_{\infty}[\text{Ga}(\text{OH})(\text{PO}_4)_2]^{4-}$ and ${}^1_{\infty}[\text{UO}_2(\text{PO}_4)_2]^{4-}$ substructures creates a three-dimensional ${}^3_{\infty}[(\text{UO}_2)_2(\text{GaOH})_2(\text{PO}_4)_4]^{4-}$ anionic lattice that has intersecting channels running down the b and c axes. Small tunnels also extend down $[111]$. A view showing the largest channels, which measure approximately $3.5 \times 7.3 \text{ \AA}$, extending along b is shown in Figure 3.3. There are four crystallographically unique Cs^+ cations and a water molecule in **UGaP1** that occupy these channels. The Cs^+ cations form between eight and ten long contacts with oxygen atoms in the structure with average distances of $3.254(8)$, $3.374(8)$, $3.171(8)$, and $3.243(8) \text{ \AA}$ to $\text{Cs}(1)$, $\text{Cs}(2)$, $\text{Cs}(3)$, and $\text{Cs}(4)$, respectively. There is a short interaction of $2.869(13) \text{ \AA}$ between the water molecule and $\text{Cs}(3)$. In addition, the water molecule forms hydrogen-bonding interactions of $2.740(8)$ and $2.821(8) \text{ \AA}$ with phosphate oxygen atoms in the gallium phosphate chain.

Cs[UO₂Ga(PO₄)₂] (UGaP2). The structure of **UGaP2** is three-dimensional, being constructed from one-dimensional ${}^1_{\infty}[\text{Ga}(\text{PO}_4)_2]^{3-}$ gallium phosphate chains and one-dimensional uranyl phosphate chains, the former of which extend down the a axis. These gallium phosphate chains are formed from fused eight-membered rings of alternating corner-shared GaO_4 and PO_4 tetrahedra. (Figure 3.4) These types of rings are important building units in gallium phosphate chemistry and have been observed before in compounds such as $[\text{Ga}(\text{HPO}_4)(\text{PO}_4)(\text{OH})] \cdot [(\text{C}_2\text{H}_7\text{N})_3\text{N}] \cdot \text{H}_2\text{O}^6$ and $[\text{NH}_3(\text{CH}_2)_4\text{NH}_3][\text{Ga}(\text{PO}_4)(\text{HPO}_4)]$.⁴⁷ The Ga atoms are the sites of ring fusion for these chains. The Ga and P sites are easily distinguished from one another in these rings with average Ga–O and P–O bond distances of $1.814(5)$ and $1.532(5) \text{ \AA}$, respectively. The

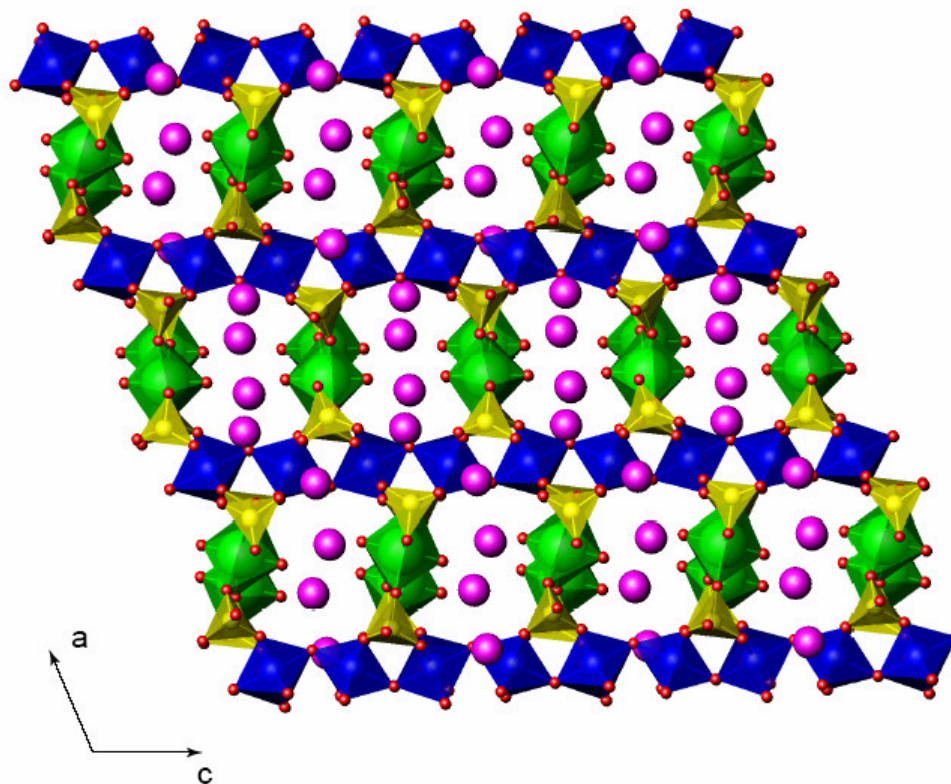


Figure 3.3. An illustration of the three-dimensional ${}^3_{\infty}[(\text{UO}_2)_2(\text{GaOH})_2(\text{PO}_4)_4]^{4-}$ anionic lattice of $\text{Cs}_4[(\text{UO}_2)_2(\text{GaOH})_2(\text{PO}_4)_4] \cdot \text{H}_2\text{O}$ (**UGaP1**) that has intersecting channels running down the b and c axes. These channels house Cs^+ cations and water molecules. Cs is shown in magenta, UO_7 pentagonal bipyramids are shown in green, GaO_6 octahedra in blue, and PO_4 tetrahedra in yellow.

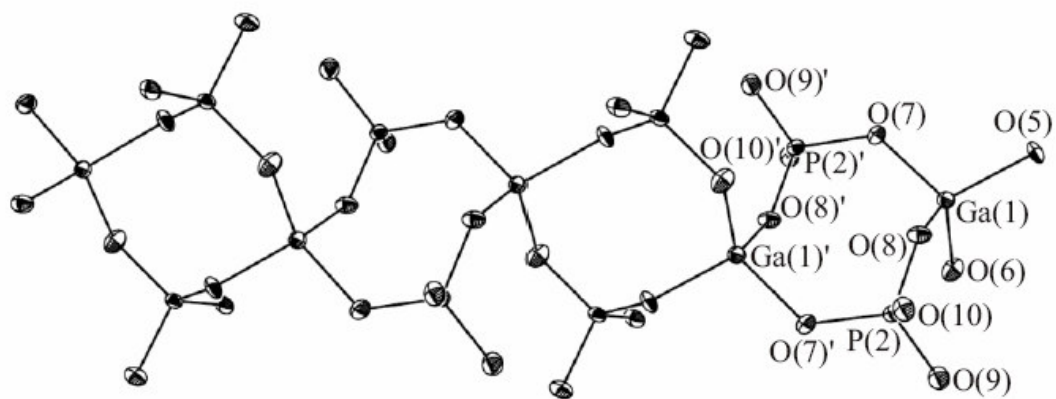


Figure 3.4. A view of the one-dimensional $[\text{Ga}(\text{PO}_4)_2]^{3-}$ gallium phosphate chains in $\text{Cs}[\text{UO}_2\text{Ga}(\text{PO}_4)_2]$ (**UGaP2**) formed from fused eight-membered rings of alternating corner-shared GaO_4 and PO_4 tetrahedra. 50% probability ellipsoids are depicted.

two crystallographically unique PO_4^{3-} anions each use two oxygen atoms to bridge between Ga centers. The oxygen atoms that are not used in this fashion instead bind the uranium centers in the structure. Selected bond distances and angles for **UGaP2** can be found in Table 3. 5.

Unlike **UGaP1** there is only one crystallographically unique U center in **UGaP2** that is found in the form of a UO_7 pentagonal bipyramid. There are two short $\text{U}=\text{O}$ bonds of 1.774(5) and 1.779(5) Å that make up the approximately linear uranyl cation with an $\text{O}-\text{U}-\text{O}$ angle of $177.2(2)^\circ$. The equatorial $\text{U}-\text{O}$ distances range from 2.283(5) to 2.501(5) Å and are within normal limits. Bond-valence sum calculations on U yield a value of 5.97, which is consistent with U(VI) .^{33,34,44} The UO_7 units edge-share to create dimers with a central inversion center. These dimers are bridged by phosphate anions to create one-dimensional chains whose formula can be described as ${}^\infty_1[\text{UO}_2(\text{PO}_4)_2]^{4-}$, and are illustrated in Figure 3.5 As can be seen from this figure, these chains are essentially the same as those found in **UGaP1**.

The gallium phosphate and uranyl phosphate chains run approximately perpendicular to one another to create a three-dimensional ${}^\infty_3[\text{UO}_2\text{Ga}(\text{PO}_4)_2]^{1-}$ framework with intersecting channels running down the *a* and *b* axes. (Figure 3.6) These channels at their largest are 3.1 x 6.7 Å, and are of the size expected to house Cs^+ cations in the absence of occluded water molecules. The Cs^+ cations form long ionic contacts with the surrounding anionic lattice with eight contacts ranging from 3.115(5) Å to 3.440(5) Å.

Thermal analysis. DSC data for **UGaP1** demonstrate that the structure of the compound remains relatively stable at temperatures below 400 °C. (Figure 3.7) The loss

Table 3.5. Selected Bond Distances (Å) and Angles (°) for Cs[$\text{UO}_2\text{Ga}(\text{PO}_4)_2$] (**UGaP2**).

Distances (Å)			
U(1)–O(1)	1.774(5)	P(1)–O(3)	1.512(5)
U(1)–O(2)	1.779(5)	P(1)–O(4)	1.538(5)
U(1)–O(3)	2.482(5)	P(1)–O(5)	1.534(5)
U(1)–O(4)	2.385(5)	P(1)–O(6)	1.546(5)
U(1)–O(4)'	2.501(5)	P(2)–O(7)	1.552(5)
U(1)–O(9)	2.283(5)	P(2)–O(8)	1.552(5)
U(1)–O(10)	2.295(5)	P(2)–O(9)	1.505(5)
Ga(1)–O(5)	1.807(5)	P(2)–O(10)	1.519(5)
Ga(1)–O(6)	1.824(5)		
Ga(1)–O(7)	1.801(5)		
Ga(1)–O(8)	1.822(5)		
Angles (°)			
O(1)–U(1)–O(2)	177.2(2)		

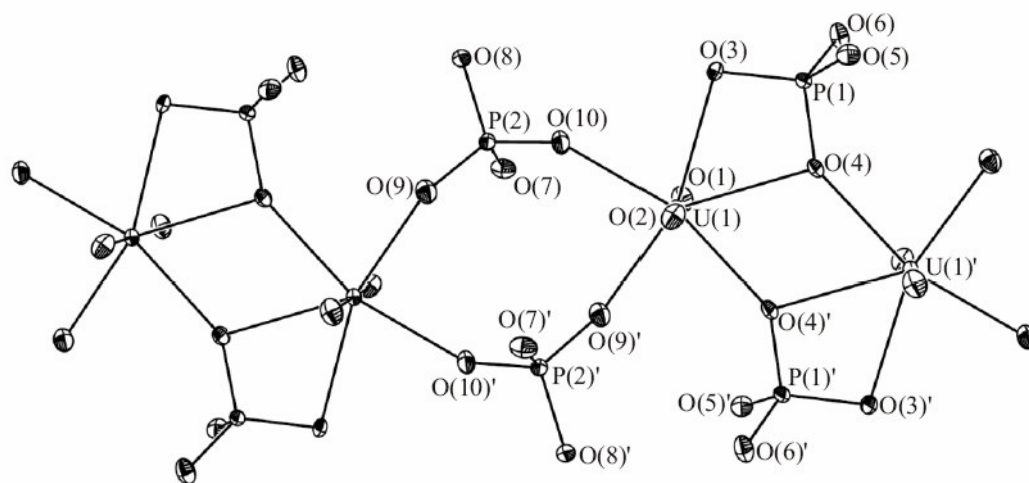


Figure 3.5 An illustration of the one-dimensional ${}^1_{\infty}[\text{UO}_2(\text{PO}_4)_2]^{4-}$ chains in $\text{Cs}[\text{UO}_2\text{Ga}(\text{PO}_4)_2]$ (**UGaP2**). 50% probability ellipsoids are depicted.

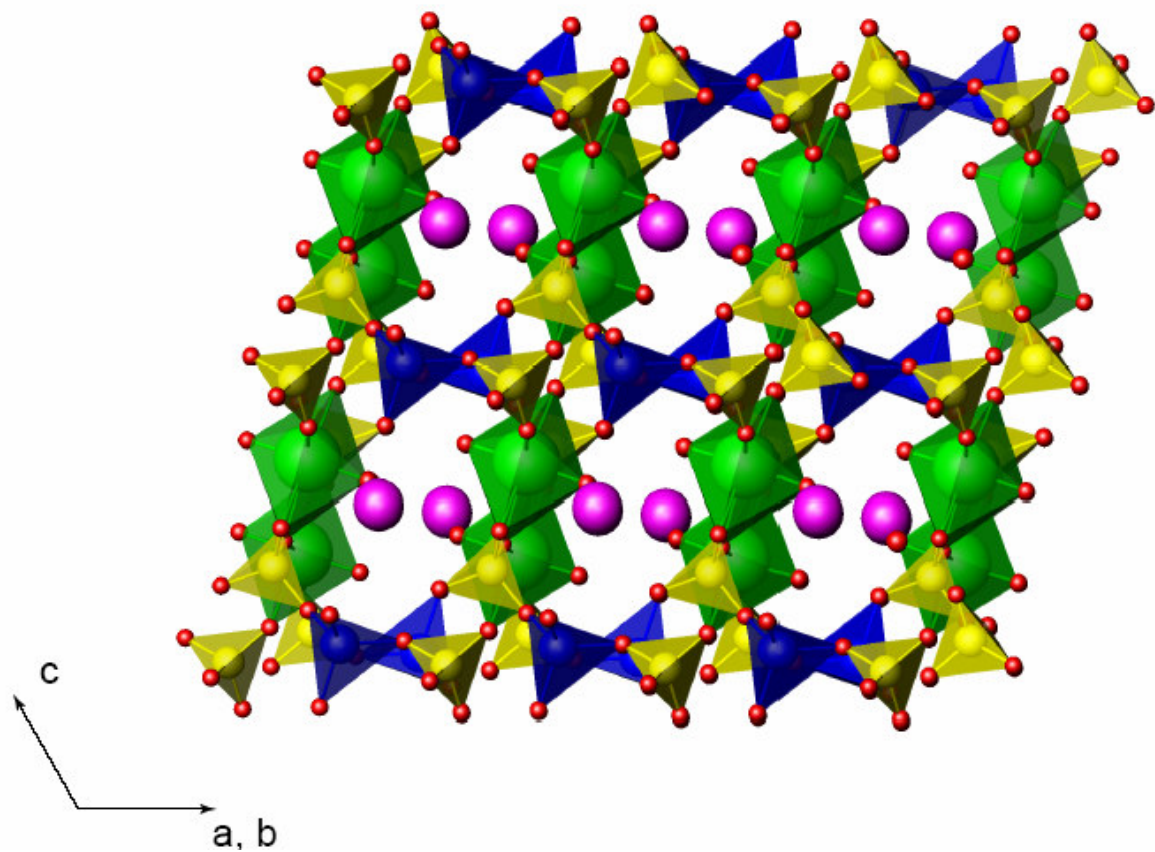


Figure 3.6. A depiction of the three-dimensional ${}^3[\text{UEO}_2\text{Ga}(\text{PO}_4)_2]^{1-}$ framework in $\text{Cs}[\text{UEO}_2\text{Ga}(\text{PO}_4)_2]$ (**UGaP2**) with intersecting channels running down the a and b axes. Cs is shown in magenta, UEO_7 pentagonal bipyramids are shown in green, GaO_4 tetrahedra in blue, and PO_4 tetrahedra in yellow.

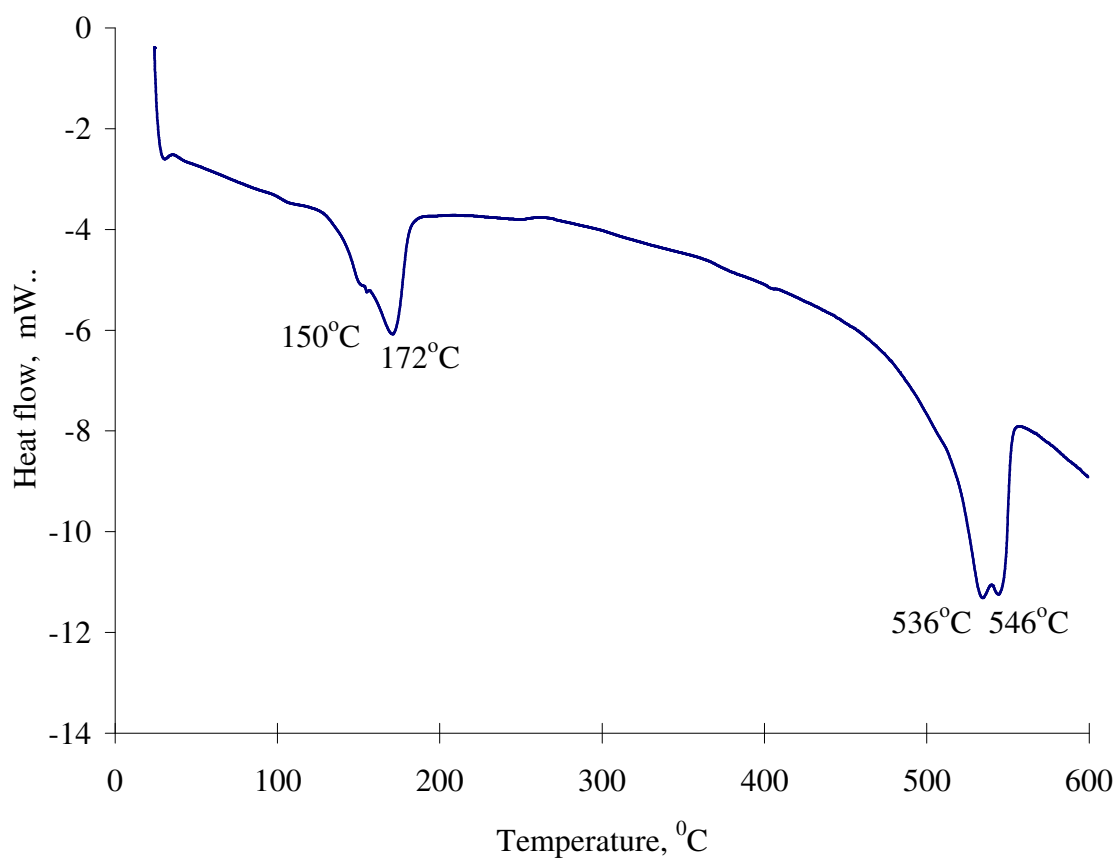


Figure 3.7. DSC data of **UGaP1** demonstrate relative stability of the structure at temperatures below 400 °C. Two peaks at 150 °C and 172 °C correspond to loss of surface and interstitial water respectively.

of surface and interstitial water occurs at 150 °C and 172 °C, respectively. Loss of hydroxyl groups and overall sluggish decomposition of the structure take place at temperatures above 400 °C. The peaks cannot be assigned to defined events due to approach of the instrumentation limits.

The data for **UGaP2** surprisingly exhibit a significant exothermic peak at 87 °C, followed by a series of three successive endothermic peaks in the temperature range of 127 °C – 155 °C and single endothermic events at 260 °C, 365 °C, 508 °C and 528 °C. (Figure 3.8) The data clearly show that **UGaP2** undergoes different structural rearrangements and phase transformations upon increases in temperature.

Ion-Exchange Studies. The exchange and mobility of interlayer cations in two-dimensional uranyl compounds have been studied in great detail, particularly for layered uranyl phosphates.⁴⁸ Both layered⁴⁹ and open-framework uranyl vanadates, such as $A(UO_2)_4(VO_4)_3$ ($A = Li, Na$),²⁸ have been shown to exhibit high cationic conductivities. We have also shown that the layered uranyl iodate, $K[UO_2(IO_3)_3]$, shows selective ion-exchange of K^+ for Cs^+ .⁵⁰ Given the three-dimensional framework structures of **UGaP1** and **UGaP2**, we were interested in evaluating the potential exchange of Cs^+ with H^+ , Na^+ , K^+ , Ca^{2+} , Sr^{2+} and Ba^{2+} ions. The concentrations of K^+ , Na^+ , Ca^{2+} and Ba^{2+} solutions were determined by potentiometric measurements using ion-selective electrodes.^{32,50} This technique allows for the determination of both uptake and release of different ions by using different ion-selective electrodes. Sr^{2+} and duplicated Ca^{2+} measurements were performed using atomic adsorption spectroscopy.

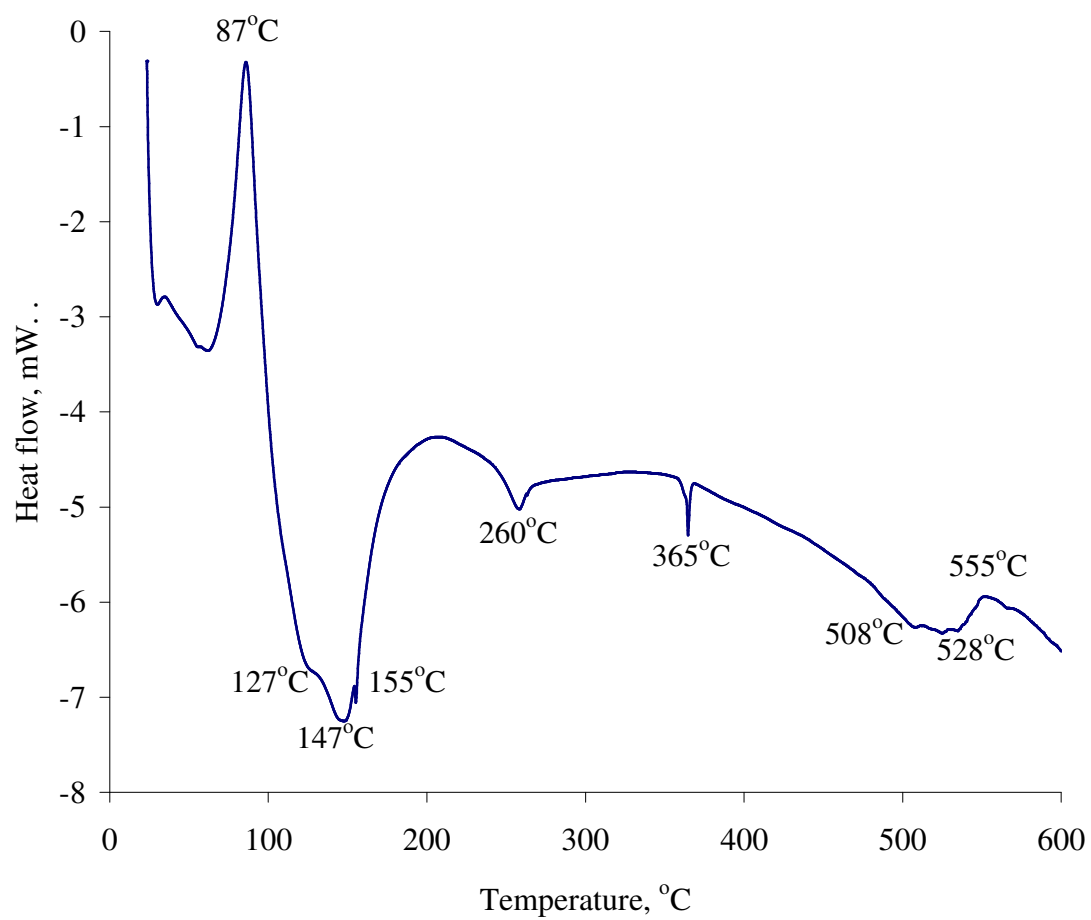


Figure 3.8. DSC data of **UGaP2**.

Direct measurement of cation uptake often over- or underestimates actual ion-exchange values owing to the typically large concentration of the exchanging ion in solution relative to the ion initially present in the material, as well as simple sorption by the material. Therefore more realistic values can be obtained by measuring the concomitant release of Cs^+ cations into solution. For **UGaP1** and **UGaP2** no exchange of Cs^+ was noted with H^+ , Na^+ , or K^+ . However, the Cs^+ cations in **UGaP1** can be exchanged for Ca^{2+} , Sr^{2+} and Ba^{2+} cations. Direct Ca^{2+} uptake measured by ion-selective electrodes of 0.63(10) meq/g was found. Cs^+ cation release for this process yielded a similar value of 0.57(10) meq/g. These values are in perfect match with uptake, 0.61(10) meq/g, measured by atomic adsorption spectroscopy. Sr^{2+} ion-exchange capacity was determined as 0.40(7) meq/g. In the mixed 1:1 $\text{SrCl}_2/\text{NaCl}$ solutions again no Na^+ uptake and reduced 0.35(5) meq/g Sr^{2+} uptake were detected. The smaller Sr^{2+} uptake value in the mixed solutions could be ascribed to the reduced concentration of Sr^{2+} and therefore increased volume to mass ratio during the exchange. When Cs^+ cations are exchanged for Ba^{2+} cations a release value of 0.36(10) meq/g was found. The smaller channel size of **UGaP2** apparently better accommodates Ca^{2+} than **UGaP1** does, and a large uptake value of 1.79(30) meq/g was found; the Cs^+ release was 1.06(20) meq/g. At the same time exchange of Cs^+ with Sr^{2+} was not detected for **UGaP2**. **UGaP1** and **UGaP2** show similar ability to exchange Cs^+ for Ba^{2+} , and a release of 0.31(20) meq/g was measured for **UGaP2**. Crystallinity and absence of structural change in the both **UGaP1** and **UGaP2** sample were monitored by powder diffraction analysis of all samples before and after ion-exchange.

CONCLUSIONS

In this work we have demonstrated that uranyl gallium phosphates can be prepared under mild hydrothermal conditions. Our original goal was to prepare three-dimensional framework compounds by incorporating octahedral GaO_6 building units. The crystal structure of $\text{Cs}_4[(\text{UO}_2)_2(\text{GaOH})_2(\text{PO}_4)_4] \cdot \text{H}_2\text{O}$ (**UGaP1**) indicates that this strategy was successful. However, the structure of $\text{Cs}[\text{UO}_2\text{Ga}(\text{PO}_4)_2]$ (**UGaP2**), which contains tetrahedral GaO_4 units, demonstrates that octahedral gallium is not necessary for the construction of open-framework uranyl gallium phosphates.

Thermal analysis revealed the absence of any structural of **UGaP1** up to 400 °C. Ion-exchange experiments show that the Cs^+ cations in **UGaP1** can be highly selectively exchanged with Sr^{2+} with the uptake of 0.4 meq/g in the presence of Na^+ cations. Summarizing these data we can recommend **UGaP1**, as a potential ^{90}Sr selective material, which should be studied further under conditions more closely approximating those present in nuclear waste.

REFERENCES

1. Cheetham, A. K.; Férey, G.; Loiseau, T. *Angew. Chem., Int. Ed. Engl.* **1999**, 38, 3268.
2. Wilson, T.; Lok, B. M.; Flanigen, E. M. **1982**, U.S. patent no. 4 310 440.
3. Wilson, T.; Lok, B. M.; Messina, C. A.; Cannan, T. R.; Flanigen, E. M. *J. Am. Chem. Soc.* **1982**, 104, 1146.
4. Parise, J. B. *J. Chem. Soc., Chem. Commun.* **1985**, 9, 606.
5. Loiseau, T.; Serpaggi, F.; Férey, G. *J. Chem. Soc., Chem. Commun. (Cambridge)* **1997**, 12, 1093.
6. Serpaggi, F.; Loiseau, T.; Férey, G. *Acta Crystallogr.* **1997**, C53, 1568.
7. Bonhomme, F.; Thoma, S. G.; Nenoff, T. M. *Micropor. Mesopor. Mater.* **2002**, 53, 87.
8. Parise, J. B. *Acta Crystallogr.* **1986**, C42, 144.
9. Beitone, L.; Loiseau, T.; Férey, G. *Acta Crystallogr.* **2002**, C58, i103.
10. Guesdon, A.; Monnin, Y.; Raveau, B. *J. Solid State Chem.* **2003**, 172, 237.
11. Attfield, M. P.; Morris, R. E.; Gutierrez-Puebla, E.; Monge-Bravo, A.; Cheetham, A. K. *J. Chem. Soc., Chem. Commun.* **1995**, 8, 843.
12. Wragg, D. S.; Morris, R. E. *J. Am. Chem. Soc.* **2000**, 122, 11246.
13. Chippindale, A. M.; Bond, A. D.; Law, A. D. Cowley, A. R. *J. Solid State Chem.* **1998**, 136, 227.
14. Lin, H.-M.; Lii, K.-H. *Inorg. Chem.* **1998**, 37, 4220.
15. Chippindale, A. M. *Chem. Mater.* **2000**, 12, 227.
16. Leech, M. A.; Cowley, A. R.; Prout, K.; Chippindale, A. M. *Chem. Mater.* **1998**, 10, 451.

17. Brouca-Cabarrecq, C.; Mosset, A. *J. Mater. Chem.* **2000**, *10*, 445.
18. Chippindale, A. M.; Walton, R. I. *J. Chem. Soc., Chem. Commun.* **1994**, *21*, 2453.
19. Cowley, A. R.; Jones, R. H.; Teat, S. J. Chippindale, A. M. *Micropor. Mesopor. Mater.* **2002**, *51*, 51.
20. Hammond, R. P.; Zubieta, J. A. *J. Solid State Chem.* **1999**, *144*, 442.
21. Hsu, K.-F.; Wang, S.-L. *Inorg. Chem.* **2000**, *39*, 1773.
22. Sykora, R. E.; Albrecht-Schmitt, T. E. *Inorg. Chem.* **2003**, *42*, 2179.
23. Sullens, T. A.; Jensen, R. A.; Shvareva, T. Y.; Albrecht-Schmitt, T. E. *J. Am. Chem. Soc.* **2004**, *126*, 2676.
24. a) Burns, P. C.; Miller, M. L.; Ewing, R. C. *Can. Mineral.* **1996**, *34*, 845. b) Burns, P. C. In Burns, P. C.; Finch, R., Eds. *Uranium: Mineralogy, Geochemistry and the Environment*; Mineralogical Society of America: Washington, DC, 1999; Chapter 1. c) Burns, P. C. *Mater. Res. Soc. Symp. Proc.* **2004**, *802*, 89.
25. Locock, A. J.; Burns, P. C. *J. Solid State Chem.* **2004**, *177*, 2675.
26. Burns, P. C.; Alexopoulos, C. M.; Hotchkiss, P. J.; Locock, A. J. *Inorg. Chem.* **2004**, *43*, 1816.
27. Doran, M. B.; Stuart, C. L.; Norquist, A. J.; O'Hare, D. *Chem. Mater.* **2004**, *16*, 565.
28. Obbade, S.; Dion, C.; Rivenet, M.; Saadi, M.; Abraham, F. *J. Solid State Chem.* **2004**, *177*, 2058.
29. Li, Y.; Cahill, C. L.; Burns, P. C. *Chem. Mater.* **2001**, *13*, 4026.
30. Sheldrick, G. M. SHELXTL PC, Version 6.12, An Integrated System for Solving, Refining, and Displaying Crystal Structures from Diffraction Data; Siemens Analytical X-Ray Instruments, Inc.: Madison, WI 2001.

31. Sheldrick, G. M. *SADABS* 2001, Program for absorption correction using SMART
CCD based on the method of Blessing: Blessing, R. H. *Acta Crystallogr.* **1995**, *A51*,
33.
32. Buehlmann, P.; Pretsch, E.; Bakker, E. *Chem. Rev.* **1998**, *98*, 1593.
33. Brown, I. D.; Altermatt, D. *Acta Crystallogr.* **1985**, *B41*, 244.
34. Brese, N. E.; O'Keeffe, M. *Acta Crystallogr.* **1991**, *B47*, 192.
35. Ramik, R. A.; Sturman, B. D.; Dunn, P. J.; Povarennykh, A. S. *Can. Mineral.* **1980**,
18, 185.
36. Hawthorne, F. C. *Tsch. Mineral. Petro. Mitt.* **1983**, *31*, 121.
37. Attfield, M. P.; Morris, R. E.; Burshtein, I.; Campana, C. F.; Cheetham, A. K. *J. Solid
State Chem.* **1995**, *118*, 412.
38. Cavellec, M.; Riou, D.; Greneche, J.-M.; Férey, G. *Inorg. Chem.* **1997**, *36*, 2187.
39. Lethbridge, Z. A. D.; Lightfoot, P.; Morris, R. E.; Wragg, D. S.; Wright, P. A.; Kvik,
A.; Vaughan, G. J. *Solid State Chem.* **1999**, *142*, 455.
40. Walton, R. I.; Millange, F.; O'Hare D.; Paulet, C.; Loiseau, T.; Férey, G. *Chem.
Mater.* **2000**, *12*, 1977.
41. Mahesh, S.; Green, M. A.; Natarajan, S. *J. Solid State Chem.* **2002**, *165*, 334.
42. Mandal, S.; Green, M. A.; Natarajan, S. *J. Solid State Chem.* **2004**, *177*, 1117.
43. Harvey, H. G.; Teat, S. J.; Tang, C. C.; Cranswick, L. M.; Attfield, M. P. *Inorg.
Chem.* **2003**, *42*, 2428.
44. Burns, P. C.; Ewing, R. C.; Hawthorne, F. C. *Can. Mineral.* **1997**, *35*, 1551.
45. Almond, P. M.; Peper, S. M.; Bakker, E.; Albrecht-Schmitt, T. E. *J. Solid State
Chem.* **2002**, *168*, 358.

46. Burns, P. C. *Am. Mineral.* **2000**, 85, 801.
47. Kissick, J. L.; Cowley, A. R.; Chippindale, A. M. *J. Solid State Chem.* **2002**, 167, 17.
48. a) Dieckmann, G. H.; Ellis, A. B. *Solid State Ionics* **1989**, 32/33, 50. b) Vochten, R. *Am. Mineral.* **1990**, 75, 221. c) Benavente, J.; Ramos Barrado, J. R.; Cabeza, A.; Bruque, S.; Martinez, M. *Colloids Surf.* **1995**, A97, 13.
49. Obbade, S.; Dion, C.; Saadi, M.; Abraham, F. *J. Solid State Chem.* **2004**, 177, 1567.
50. Shraveva, T. Y.; Almond, P. M.; Albrecht-Schmitt, T. E. *J. Solid State Chem.* **2004**, 178, 499.

CHAPTER 4

SYNTHESIS, STRUCTURES, AND PROPERTIES OF THE MULTIFUNCTIONAL URANYL VANADIUM PHOSPHATE FRAMEWORKS

ABSTRACT

Two novel framework uranyl vanadium phosphate materials were synthesized under hydrothermal conditions. Similar reactions of $\text{UO}_2(\text{NO}_3)_2 \cdot 6\text{H}_2\text{O}$, V metal, H_3PO_4 and various alkaline metal chlorides CsCl, KCl, or RbCl yielded different types of structures. Three-dimensional $\text{Cs}_2[\text{UO}_2(\text{VO}_2)_2(\text{PO}_4)_2] \cdot n\text{H}_2\text{O}$ (**UV^VP**) is constructed from uranyl phosphate chains, that are joined together by chains of corner-sharing VO_5 distorted square pyramids. Channels along the *b* and *c* axes are filled with Cs^+ cations. Alignment of terminal V=O bonds in all VO_5 units along the *c* axis creates the overall polarity of the structure. Due to the polar structure, **UV^VP** exhibits non-linear optical properties. Isostructural $\text{K}_4(\text{UO}_2)(\text{VO})_4(\text{OH})_2(\text{PO}_4)_4$ (**KUV^{IV}P**) and $\text{Rb}_4(\text{UO}_2)(\text{VO})_4(\text{OH})_2(\text{PO}_4)_4$ (**RbUV^{IV}P**) contain V^{IV} in an octahedral coordination environment. Their frameworks are constructed from vanadyl phosphate layers, interconnected by uranyl tetragonal bipyramids. There are channels, filled with K^+ or Rb^+ , in all three perpendicular directions. Antiferromagnetic ordering at 52 K and Cs^+ -selective ion-exchange properties were found and characterized.

INTRODUCTION

Rich and diverse crystal chemistry of the vanadium compounds arises from the ability of trivalent, tetravalent and pentavalent vanadium to adopt a wide range of coordination environments, from tetrahedral through trigonal bipyramidal and square pyramidal to octahedral.¹ For instance, the family of vanadium phosphates, most recognized for their magnetic and catalytic properties,^{2,3} is composed of more than 130 members with one, two or three-dimensional crystal structures.²⁻⁵ To a certain degree, this structural flexibility is replicated in the class of uranyl-containing vanadium compounds. In the layered compounds with the structure of mineral carnotite of the general formula $M_2(UO_2)_2V_2O_8 \cdot nH_2O$,⁶⁻⁸ ($M = K, Na, Ag$, etc.) the centrosymmetric $V_2O_8^{6-}$ groups are formed from two edge-shared VO_5 square pyramids with terminal oxygen atoms pointed in opposite directions. Three-dimensional $A(UO_2)_2(VO_4)_3$ compounds, ($A = Li$ and Na),⁹ that have the cation conductivity properties, comparable with $NaSiCON$ and $LiSiCON$ materials, as well as $Pb(UO_2)(V_2O_7)$,¹⁰ also crystallized in the centrosymmetric space groups $I4_1/mad$ and $P2_1/n$ respectively, and contain vanadium tetrahedra in the structure. On the other hand, the structure of $K_2[(UO_2)_2(VO)_2(IO_6)_2O] \cdot H_2O$,¹¹ composed completely of only distorted octahedra, including distorted VO_6 , is polar and crystallized in the $Pba2$ space group. Due to the polarity of the structure this material demonstrates non-linear optical properties.

In all described uranyl-containing vanadium materials, either with layered or three-dimensional structures, vanadium is present in the +5 oxidation state. Numerous vanadium phosphates, that incorporate only tetravalent vanadium, or mixed valent V^{IV}/V^V units, such as $\beta\text{-LiV}^{IV}\text{OPO}_4$,¹² $Zn_2(V^{IV}O)(PO_4)_2$,¹³ $Ba_3V^{IV}/V^VO_3(PO_4)_3$,¹⁴

$\text{Na}_5(\text{V}^{\text{IV}}\text{O})_2(\text{PO}_4)_3 \cdot \text{H}_2\text{O}$,¹⁵ and many others² demonstrate paramagnetic behavior in the range of temperatures between 50 and 300 K, due to the presence of d^1 unpaired electron on the vanadium center, and antiferromagnetic or ferromagnetic ordering at temperatures 5-40 K as a consequence of different super-exchange mechanisms of the various types of V-P-O chains present in the structures.

In this chapter we describe the structure of two novel framework uranyl vanadium phosphates: $\text{Cs}_2[\text{UO}_2(\text{VO}_2)_2(\text{PO}_4)_2] \cdot n\text{H}_2\text{O}$ (**UV^VP**) and isostructural $\text{K}_4(\text{UO}_2)(\text{VO})_4(\text{OH})_2(\text{PO}_4)_4$ (**KUV^{IV}P**) and $\text{Rb}_4(\text{UO}_2)(\text{VO})_4(\text{OH})_2(\text{PO}_4)_4$ (**RbUV^{IV}P**), along with their physical properties: the thermal behavior, second harmonic generation (SHG) of laser light of **UV^VP**, selective ion-exchange properties and magnetic properties for **KUV^{IV}P** and **RbUV^{IV}P**.

EXPERIMENTAL

Syntheses. $\text{UO}_2(\text{NO}_3)_2 \cdot 6\text{H}_2\text{O}$ (98%, Alfa-Aesar), V powder (99.99%, Sigma Aldrich), H_3PO_4 (98%, Aldrich), KCl (99.997%, Alfa-Aesar), RbCl (99.975%, Alfa-Aesar), and CsCl (99.9%, Cerac) were used as received. V powder stored in the glove box was loaded in argon atmosphere. The reactions were run in PTFE-lined Parr 4749 reaction vessels. Distilled and Millipore filtered water with a resistance of $18.2 \text{ M}\Omega \cdot \text{cm}$ was used in all experiments.

$\text{Cs}_2[\text{UO}_2(\text{VO}_2)_2(\text{PO}_4)_2] \cdot n\text{H}_2\text{O}$ (UV^VP). $\text{UO}_2(\text{NO}_3)_2 \cdot 6\text{H}_2\text{O}$ (0.289 g, 0.576 mmol), H_3PO_4 (0.169 g, 1.72 mmol), CsCl (0.484 g, 2.88 mmol), and 1 mL of Millipore-filtered water were mixed in the 23 mL autoclave, followed by addition of V metal powder (0.080 g, 1.16 mmol), separately weighed in the glove box. The reaction was run

in sealed autoclave at 190 °C in a box furnace for 5 days and then cooled at a rate of 9 °C/hour to room temperature. Clusters of large bright yellow crystals of **UV^VP**, reaching several mm in length, were isolated, washed with methanol, and allowed to dry. Yield, 515 mg (98% yield based on U).

K₄(UO₂)(VO)₄(OH)₂(PO₄)₄ (KUV^{IV}P). UO₂(NO₃)₂·6H₂O (0.395 g, 0.787 mmol), H₃PO₄ (0.231 g, 2.36 mmol), KCl (0.293 g, 3.94 mmol) and V (0.080 g, 1.6 mmol) were mixed in 23 mL PTFE-lined autoclave with 1 mL of water. Then reaction was heated at 190 °C for five days and cooled to room temperature at a rate of 9 °C/hour. After decantation of the mother liquid the only solid product of the reaction - bright blue prismatic crystals of **KUV^{IV}P** were revealed. The yield of **KUV^{IV}P** was 0.340 g (40.5 % yield based on the U).

Rb₄(UO₂)(VO)₄(OH)₂(PO₄)₄ (RbUV^{IV}P). UO₂(NO₃)₂·6H₂O (0.334 g, 0.665 mmol), H₃PO₄ (0.196 g, 1.99 mmol), RbCl (0.402 g, 3.33 mmol) and V (0.068 g, 1.3 mmol) were mixed in 23 mL PTFE-lined autoclave followed by addition of 1 mL of water. After heating at 190 °C for five days and cooling at a 9 °C/hour to room temperature, the reaction vessel was opened and the product mixture, containing blue prism crystals of **RbUV^{IV}P** and yellow powder product, was washed with methanol and dried at the air. The yield of **RbUV^{IV}P** was 0.426 mg (50.9 % yield based on the U).

Crystallographic Studies. Crystals of **UV^VP**, **KUV^{IV}P**, and **RbUV^{IV}P** were mounted on glass fibers and aligned on a Bruker SMART APEX CCD X-ray diffractometer. Intensity measurements were performed using graphite monochromated Mo K α radiation from a sealed tube and monocapillary collimator. SMART (v 5.624) was used for preliminary determination of the cell constants and data collection control.

The intensities of reflections of a sphere were collected by a combination of 3 sets of exposures (frames). Each set had a different ϕ angle for the crystal and each exposure covered a range of 0.3° in ω . A total of 1800 frames were collected with an exposure time per frame of 30 s for the crystals of **UV^VP**, **KUV^{IV}P**, and **RbUV^{IV}P**.

Determination of integrated intensities and global refinement were performed with the Bruker SAINT (v 6.02) software package using a narrow-frame integration algorithm. A face-indexed analytical absorption correction was initially applied using XPREP, where individual shells of unmerged data were corrected analytically.¹⁶ These files were subsequently treated with a semiempirical absorption correction by SADABS.¹⁷ The program suite SHELXTL (v 6.12) was used for space group determination (XPREP), direct methods structure solution (XS), and least-squares refinement (XL).¹⁶ The final refinements included anisotropic displacement parameters for all atoms. Secondary extinction was not noted for the crystals of **UV^VP**, **KUV^{IV}P**, and **RbUV^{IV}P**. Some crystallographic details are given in Table 4.1. Atomic coordinates, symmetry information, displacement parameters, and occupancy for all atoms can be found in the Tables 4.2, 4.3, and 4.4 for **UV^VP**, **KUV^{IV}P**, and **RbUV^{IV}P** respectively.

Thermal analysis. The data were collected using differential scanning calorimeter TA Instrument, model 2920. The samples of known mass encapsulated in an aluminum container, were heated under nitrogen atmosphere from 30 °C to 600 °C with a heating rate of 10 °C /minute.

Non-linear optical properties. SHG was investigated using 1064 nm excitation laser pulses from a Q-switched Nd:YAG laser (Continuum Surelite I-10). A

Table 4.1. Crystallographic Data for $\text{Cs}_2[\text{UO}_2(\text{VO}_2)_2(\text{PO}_4)_2] \cdot n\text{H}_2\text{O}$ (**UV^VP**), $\text{K}_4(\text{UO}_2)(\text{VO})_4(\text{OH})_2(\text{PO}_4)_4$ (**KUV^{IV}P**) and $\text{Rb}_4(\text{UO}_2)(\text{VO})_4(\text{OH})_2(\text{PO}_4)_4$ (**RbUV^{IV}P**)

Compound	UV^VP	KUV^{IV}P	RbUV^{IV}P
Formula Mass	901.99	1106.07	1243.26
Color and habit	yellow prism	blue plate	blue plate
Crystal System	orthorhombic	orthorhombic	Orthorhombic
Space group	<i>Cmc</i> 2 ₁ (No. 36)	<i>Immm</i> (No.71)	<i>Immm</i> (No.71)
<i>a</i> (Å)	20.7116(14)	7.3803(7)	7.4370(7)
<i>b</i> (Å)	6.8564(5)	9.1577(8)	9.1662(8)
<i>c</i> (Å)	10.5497(7)	17.0898(16)	17.2415(15)
<i>V</i> (Å ³)	1498.13(18)	1155.04(18)	1175.34(18)
<i>Z</i>	4	2	2
<i>T</i> (K)	193	193	193
λ (Å)	0.71073	0.71073	0.71073
Maximum 2 θ (deg.)	56.62	56.58	56.74
ρ_{calcd} (g cm ⁻³)	3.999	3.180	3.513
$\mu(\text{Mo } K\alpha)$ (cm ⁻¹)	170.76	96.48	158.39
$R(F)$ for $F_o^2 > \sigma(F_o^2)$ ^a	0.0265	0.0533	0.0551
$R_w(F_o^2)$ ^b	0.0602	0.1407	0.1461

$$^a R(F) = \sum \|F_o| - |F_c|\| / \sum |F_o|. \quad ^b R_w(F_o^2) = \left[\sum \left[w(F_o^2 - F_c^2)^2 \right] / \sum wF_o^4 \right]^{1/2}.$$

Table 4.2. Atomic Coordinates and Equivalent Isotropic Displacement Parameters for $\text{Cs}_2[\text{UO}_2(\text{VO}_2)_2(\text{PO}_4)_2] \cdot n\text{H}_2\text{O}$ (**UV^VP**)

Atom	Symmetry ^a	<i>x</i>	<i>y</i>	<i>z</i>	$U_{\text{eq}} (\text{\AA}^2)^b$	Occup.
U(1)	4 <i>a m</i>	0	0.0326(5)	-0.02493(4)	0.01259(10)	1
V(1)	8 <i>b 1</i>	-0.25770(5)	-0.2961(16)	0.18303(13)	0.0134(3)	1
P(1)	8 <i>b 1</i>	-0.12106(9)	-0.0815(3)	0.2254(2)	0.0132(4)	1
O(1)	8 <i>b 1</i>	-0.0809(3)	-0.1215(9)	0.3441(5)	0.0215(12)	1
O(2)	8 <i>b 1</i>	-0.1609(2)	0.1081(8)	0.2442(6)	0.0207(11)	1
O(3)	8 <i>b 1</i>	-0.0767(3)	-0.0678(9)	0.1113(6)	0.0241(13)	1
O(4)	8 <i>b 1</i>	-0.1657(2)	-0.2593(8)	0.2052(5)	0.0160(10)	1
O(5)	8 <i>b 1</i>	-0.2709(3)	-0.0641(7)	0.2323(6)	0.0195(13)	1
O(6)	8 <i>b 1</i>	-0.2648(3)	-0.2942(9)	0.0320(6)	0.0232(13)	1
O(7)	4 <i>a m</i>	0	-0.2040(12)	-0.0944(7)	0.0196(16)	1
O(8)	4 <i>a m</i>	0	0.2726(11)	-0.9540(9)	0.0184(16)	1
O(9)	4 <i>a m</i>	0	0.544(3)	0.241(3)	0.068(11)	0.59(5)
Cs(1)	8 <i>b 1</i>	-0.12432(2)	-0.46363(7)	-0.05798(4)	0.02101(15)	1

^a Symmetry describes multiplicity, Wyckoff parameter and symmetry of the atomic site.

^b U_{eq} is defined as one-third of the trace of the orthogonalized \mathbf{U}_{ij} tensor.

Table 4.3. Atomic Coordinates and Equivalent Isotropic Displacement Parameters for $\text{K}_4(\text{UO}_2)(\text{VO})_4(\text{OH})_2(\text{PO}_4)_4$ (**KUV^{IV}P**)

Atom	Symmetry ^a	<i>x</i>	<i>y</i>	<i>z</i>	$U_{\text{eq}}(\text{\AA}^2)$ ^b	Occup.
U(1)	2 <i>a mmm</i>	½	½	½	0.0078(3)	1
V(1)	8 <i>m m</i>	0.7058(3)	½	0.76487(11)	0.0092(4)	1
P(1)	8 <i>l m</i>	½	0.7579(3)	0.66892(17)	0.0081(6)	1
O(1)	4 <i>e 2mm</i>	0.7435(18)	½	½	0.016(2)	1
O(2)	8 <i>l m</i>	½	0.6805(10)	0.5902(5)	0.0166(18)	1
O(3)	8 <i>l m</i>	½	0.6429(10)	0.7368(5)	0.0123(17)	1
O(4)	16 <i>o 1</i>	0.6721(9)	0.8479(7)	0.6743(4)	0.0155(13)	1
O(5)	8 <i>m m</i>	0.8080(13)	½	0.6825(5)	0.0175(19)	1
O(6)	4 <i>i mm2</i>	½	½	0.8660(9)	0.023(3)	1
K(1)	8 <i>l m</i>	0	0.3052(8)	0.4122(3)	0.048(2)	0.751(18)
K(2)	2 <i>d mmm</i>	½	0	½	0.114(9)	1

^a Symmetry describes multiplicity, Wyckoff parameter and symmetry of the atomic site.

^b U_{eq} is defined as one-third of the trace of the orthogonalized \mathbf{U}_{ij} tensor.

Table 4.4. Atomic Coordinates and Equivalent Isotropic Displacement Parameters for $\text{Rb}_4(\text{UO}_2)(\text{VO})_4(\text{OH})_2(\text{PO}_4)_4$ (**RbUV^{IV}P**)

Atom	Symmetry ^a	<i>x</i>	<i>y</i>	<i>z</i>	$U_{\text{eq}}(\text{\AA}^2)^b$	Occup.
U(1)	2 <i>a mmm</i>	½	½	½	0.0072(3)	1
V(1)	8 <i>m m</i>	0.7052(3)	½	0.76599(12)	0.0083(5)	1
P(1)	8 <i>l m</i>	½	0.7571(3)	0.66934(17)	0.0082(6)	1
O(1)	4 <i>e 2mm</i>	0.7397(19)	½	½	0.015(3)	1
O(2)	8 <i>l m</i>	½	0.6779(11)	0.5910(5)	0.0145(19)	1
O(3)	8 <i>l m</i>	½	0.6432(10)	0.7367(5)	0.0108(18)	1
O(4)	16 <i>o 1</i>	0.6711(9)	0.8473(7)	0.6742(4)	0.0128(13)	1
O(5)	8 <i>m m</i>	0.8047(13)	½	0.6842(6)	0.017(2)	1
O(6)	4 <i>I mm2</i>	½	½	0.8644(9)	0.023(3)	1
Rb(1)	8 <i>l m</i>	0	0.3083(4)	0.41202(15)	0.0313(10)	0.608(8)
Rb(2)	2 <i>d mmm</i>	½	0	½	0.0724(16)	1

^a Symmetry describes multiplicity, Wyckoff parameter and symmetry of the atomic site.

^b U_{eq} is defined as one-third of the trace of the orthogonalized \mathbf{U}_{ij} tensor.

Sciencetech volume absorbing calorimeter was used to measure average laser power. SHG at 532 nm was visually observed in a darkened room from a polycrystalline sample of $\text{UV}^{\text{V}}\text{P}$ contained in a glass tube and was quantified using a band-pass optical filter, IR insensitive photomultiplier (1P28), and a signal averaging digital storage oscilloscope (Tektronix TDS 640A), as the intensity of the unfocused laser beam was increased above the SHG threshold. At a beam cross section averaged intensity of 3.6 MW/cm^2 , the SHG intensity from $\text{UV}^{\text{V}}\text{P}$ was 1500 times weaker than the signal observed from a commercial rare-earth-based ceramic frequency upconverting laser beam finder (Kentek View-It).

Magnetic properties. Magnetic susceptibility measurements were conducted using a Quantum Design superconducting interference device (SQUID), under applied fields ranging from 100 to 10000 gauss as a function of temperature over the range of 5 – 320 K and magnetization data were collected at 5K in fields ranging from 0 – 10,000 gauss. Samples were doubly encapsulated in aluminum containers, which contributed significantly to the measured signal, especially at higher temperatures and for samples with a low inherent susceptibility. Empty containers were run independently under the same conditions and the data used directly for background subtraction. Diamagnetic contributions to the data were also calculated and used to correct the measured susceptibility.

The temperature dependent magnetic susceptibility data were analyzed assuming Curie-Weiss behavior with an added temperature independent term, $\chi = C / (T-\theta) + \chi_{\text{TIP}}$, where C and θ are Curie and Weiss constants and χ_{TIP} is the temperature-independent contribution to the susceptibility. C is related to the effective magnetic moment

$\mu_{eff} = \left(\frac{3kC}{N_0\mu_B^2} \right)^{1/2}$ in which N_0 is Avogadro's number and μ_B is the Bohr magneton (0.927×10^{-20} erg/Gauss). For cases in which χ_{TIP} is small, the effective magnetic moment can be obtained directly from the slope of the temperature dependence versus inverse magnetic susceptibility.

Ion-Exchange Studies. NaCl, KCl, CsCl, CaCl₂ and SrCl₂ solutions with concentrations of 1×10^{-3} M and 1×10^{-2} M were used in order to estimate ion-exchange capacities of all materials. Ion-exchange properties, in actual fact, concentrations of the solutions of different cations were measured with two different methods: classic potentiometric method with ion-selective electrodes for K⁺, Na⁺ and Cs⁺ uptake,¹⁸ using Accumet A15 pH meter, and atomic adsorption spectroscopy, using Varian 240 AA spectrometer with hollow cathode Ca and Sr lamps for Ca²⁺ and Sr²⁺ uptake.

Ion-selective electrodes were made in accordance with Fluka-recommended compositions and silver/silver chloride electrode as a reference.¹⁸ In order to prevent contamination of tested solutions with KCl the reference electrode with double junction and lithium acetate as a bridging electrolyte were utilized.

In all cases samples were equilibrated in capped 5 mL vials with different cation solutions of known concentration for 48 hours at constant shaking, and then the change in the concentrations was determined.

The approximate volume to mass ratio 200:1 (4 mL of the solution for 0.02 g of sample) was used in all experiments.

RESULTS AND DISCUSSION

Syntheses. The utilization of the same reaction with only varied alkali metal chloride, CsCl - in the case of $\text{UV}^{\text{V}}\text{P}$, KCl - $\text{KUV}^{\text{IV}}\text{P}$, and RbCl - $\text{RbUV}^{\text{IV}}\text{P}$, reveals the products, distinct not only in oxidation state and coordination number of vanadium, but also in the construction pattern of the structures. All our attempts to synthesize the identical to $\text{UV}^{\text{V}}\text{P}$ structure with K^+ and Rb^+ charge-balancing cations, as well as $\text{KUV}^{\text{IV}}\text{P}$ and $\text{RbUV}^{\text{IV}}\text{P}$ in the Cs-form, or even in the mixed-cations form failed. But at the same time $\text{KUV}^{\text{IV}}\text{P}$ and $\text{RbUV}^{\text{IV}}\text{P}$ did not undergo any structural changes after substitution of K^+ or Rb^+ with Cs^+ by ion-exchange. We expect that the reason for this phenomena can be found in the thermodynamics of the synthetic reactions. In situ scanning microcalorimetry with slowly increasing temperature may be useful in order to solve this discrepancy, because it will give a possibility to observe all heat effects that correspond to all stages of synthesis of both $\text{UV}^{\text{V}}\text{P}$ and $\text{K(Rb)UV}^{\text{IV}}\text{P}$. Running of multiple identical reactions also helps to identify every intermediate product of the reactions at different temperatures and make conclusions about driving forces and limitations and thus about major thermodynamic factors for both reactions.¹⁹⁻²¹

Vanadium metal powder was used as a source of vanadium. This synthetic method was previously studied with Ti and V, and in both cases yielded mixed-valent $\text{Ti}^{\text{III}}/\text{Ti}^{\text{IV}}$ and $\text{V}^{\text{III}}/\text{V}^{\text{IV}}$ compounds.^{22,23} We suggest that for oxidation of $\text{V}^0/\text{V}^{\text{III}}$, protons from the phosphoric acid serve as oxidizer with subsequent release of hydrogen gas. In further oxidation of V^{III} to V^{IV} and V^{V} oxygen from air, present in the reaction vessel, or dissolved in water, can possible be involved.

Structures. $\text{Cs}_2[\text{UO}_2(\text{VO}_2)_2(\text{PO}_4)_2] \cdot n\text{H}_2\text{O}$ ($\text{UV}^{\text{V}}\text{P}$). The structure of $\text{UV}^{\text{V}}\text{P}$ consists of uranyl cations bound by phosphate to yield UO_6 tetragonal bipyramids. These units are bridged by phosphate to yield one-dimensional chains that run down the c axis. This basic one-dimensional topology is recognized to occur in several uranyl phases including $\text{Cu}_2[\text{UO}_2(\text{PO}_4)_2]$.²⁴ The uranyl phosphate chains are in turn linked by chains of corner-sharing VO_5 distorted square pyramids that run down the b axis into a novel open-framework structure that has intersecting channels that occur along the b and c axes as is shown in Figure 4.1. The channels running down the b axis are approximately $5.5 \text{ \AA} \times 10.9 \text{ \AA}$, whereas those running down the c axis are $5.0 \times 9.5 \text{ \AA}$. These channels are occupied by Cs^+ cations and water molecules. One the most apparent features of this structure is that the VO_5 units are aligned so that the single terminal oxo atoms of these polyhedra are all aligned along the c axis as is shown in Figure 4.1. $\text{Cs}_2[\text{UO}_2(\text{VO}_2)_2(\text{PO}_4)_2] \cdot n\text{H}_2\text{O}$ crystallizes in polar orthorhombic space group $Cmc2_1$. As such, c is the polar axis, and the origin of this polarity lies in the alignment of the vanadyl units. The alignment of the vanadyl units is reminiscent of the alignment of titanyl units in the key NLO material KTiOPO_4 (KTP).^{25, 26}

The selected U-O, V-O and P-O bond distances, and angles are shown in Table 4.5. The UO_6 units in $\text{Cs}_2[\text{UO}_2(\text{VO}_2)_2(\text{PO}_4)_2] \cdot n\text{H}_2\text{O}$ display two short $\text{U}=\text{O}$ bond distances of $1.772(7)$ and $1.781(8) \text{ \AA}$, that define the uranyl cation. These bond distances are within the typical range for $\text{U}=\text{O}$ distances. Longer U–O bonds to the equatorial oxygen atoms from the phosphate anions range from $2.250(6)$ to $2.256(5) \text{ \AA}$. These distances were used to calculate a bond-valence sum for the U center of 6.32, which is consistent with U(VI).²⁸

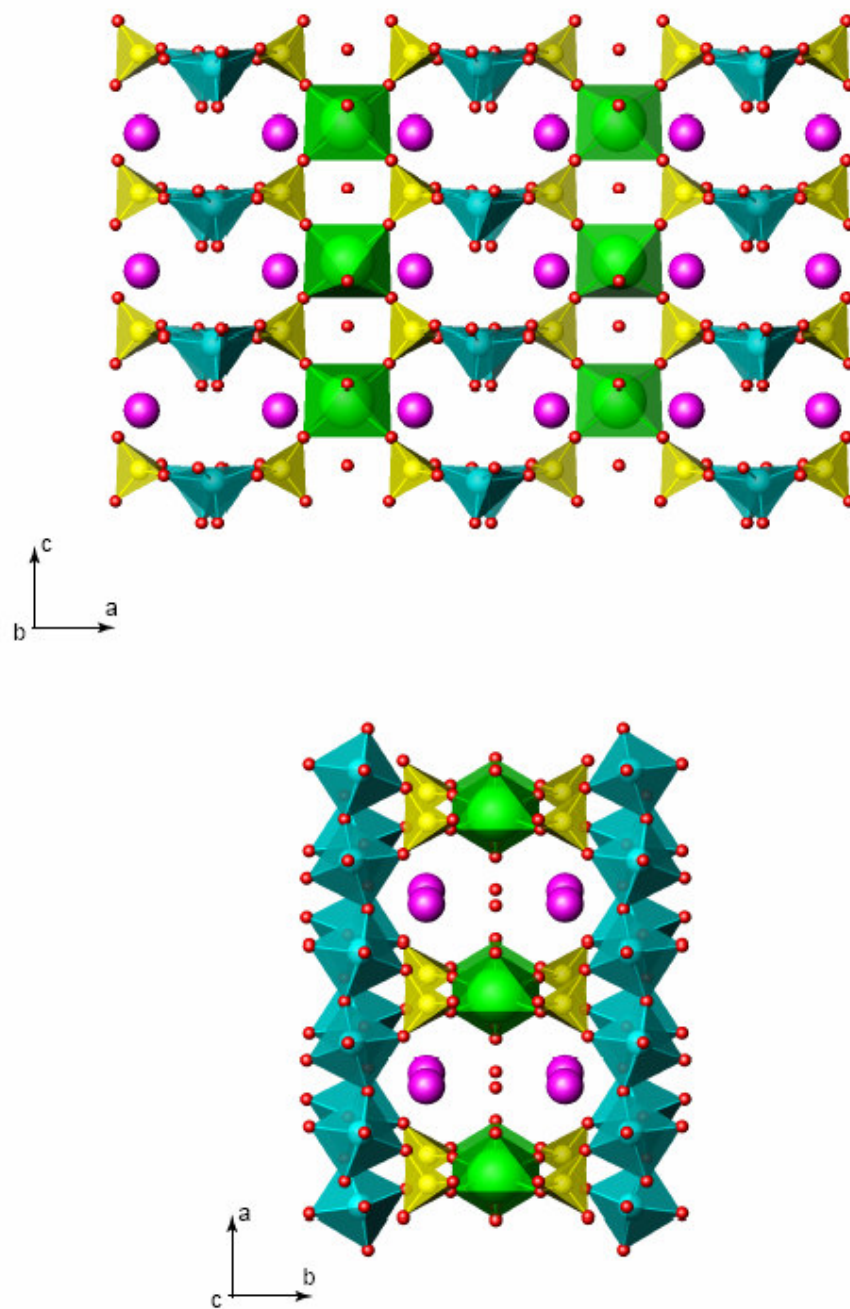


Figure 4.1. Depiction of the channels of $UV^V P$, extended along b and c axes, occupied by Cs^+ cations. Green – uranium, blue – vanadium, yellow – phosphorus, purple – cesium centers.

Table 4.5. Selected Bond Distances (Å) and Angles (°) for Cs₂[UO₂(VO₂)₂(PO₄)₂].nH₂O (UV^VP)

Distances (Å)			
U(1)-O(8)	1.772(7)	V(1)-O(4)	1.936(5)
U(1)-O(7)	1.781(8)	V(1)-O(5')	1.999(5)
U(1)-O(3)	2.250(6)	P(1)-O(3)	1.518(6)
U(1)-O(1)	2.256(5)	P(1)-O(1)	1.527(5)
V(1)-O(6)	1.600(6)	P(1)-O(4)	1.545(5)
V(1)-O(5)	1.696(5)	P(2)-O(2)	1.552(6)
V(1)-O(2)	1.921(5)		
Angles (°)			
O(8)–U(1)–O(7)	177.5(4)	O(5)–V(1)–O(2)	94.4(3)
O(5)–V(1)–O(6)	106.4(3)	O(5)–V(1)–O(4)	89.9(2)

The VO_5 units contain VO_2^+ vanadyl cations with two short $\text{V}=\text{O}$ bonds of 1.600(6) and 1.696(5) Å. The shorter of these bonds is to the terminal oxo atom. The remaining three $\text{V}-\text{O}$ bonds range from 1.921(5) to 1.999(5) Å, yielding a bond-valence sum for the V atom of 5.08.^{28, 29} The tetrahedral phosphate anion shows typical $\text{P}-\text{O}$ distances ranging from 1.518(6) to 1.552(6) Å. Finally, charge balance for the anionic lattice formed by the UO_6 , VO_5 , and PO_4 units is maintained by the Cs^+ cations that form contacts with surrounding oxygen atoms that occur from 3.105(6) to 3.395(6) Å. There are also partially occupied water molecules within smaller channels in the structure. There are 0.59 water molecules per formula unit. The fundamental building unit in $\text{UV}^{\text{V}}\text{P}$ is shown in Figure 4.2.

$\text{K}_4(\text{UO}_2)(\text{VO})_4(\text{OH})_2(\text{PO}_4)_4$ ($\text{KUV}^{\text{IV}}\text{P}$) and $\text{Rb}_4(\text{UO}_2)(\text{VO})_4(\text{OH})_2(\text{PO}_4)_4$ ($\text{RbUV}^{\text{IV}}\text{P}$). $\text{KUV}^{\text{IV}}\text{P}$ and $\text{RbUV}^{\text{IV}}\text{P}$ have similar framework structures based on the interconnection of vanadyl phosphate layers by uranyl tetragonal bipyramids. The fundamental building unit of $\text{KUV}^{\text{IV}}\text{P}$ and $\text{RbUV}^{\text{IV}}\text{P}$ is shown in Figure 4.3. Selected bond distances and angles are given in the Table 4.6. The vanadyl phosphate layer includes one crystallographically unique vanadium atom connected to six oxygen atoms. This connection leads to the formation of distorted coordination octahedra with one short vanadyl $\text{V}-\text{O}(5)$ distance 1.598(9) Å (1.592(10) Å), one long $\text{V}-\text{O}6$ bond - 2.301(11) Å (2.282(12) Å) in trans position to vanadyl, and four equatorial bonds with lengths ranging from 1.958(6) Å to 2.061(6) Å (from 1.966(7) Å to 2.075(6) Å). Distances and angles given in parenthesis represent the data for $\text{RbUV}^{\text{IV}}\text{P}$. The bond valency sum calculated from these distances confirms vanadium +4 oxidation state.²⁸ Close packing of two

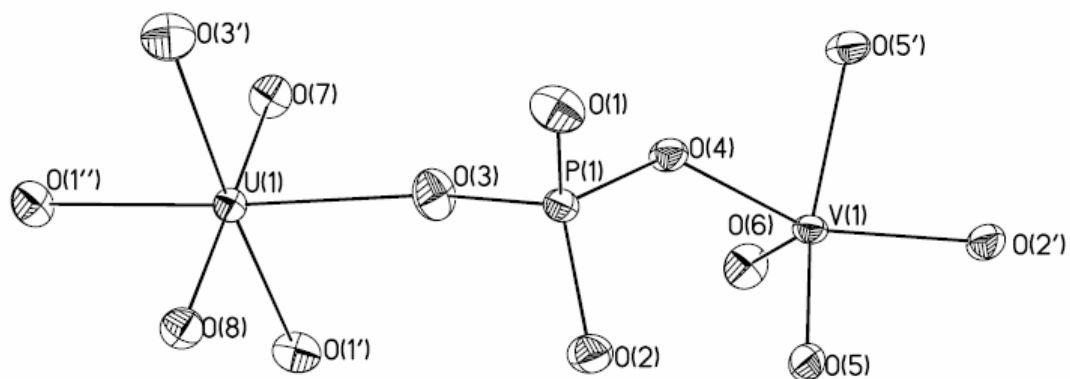


Figure 4.2. The fundamental building unit of UV^P shown in 50% probability thermal ellipsoids.

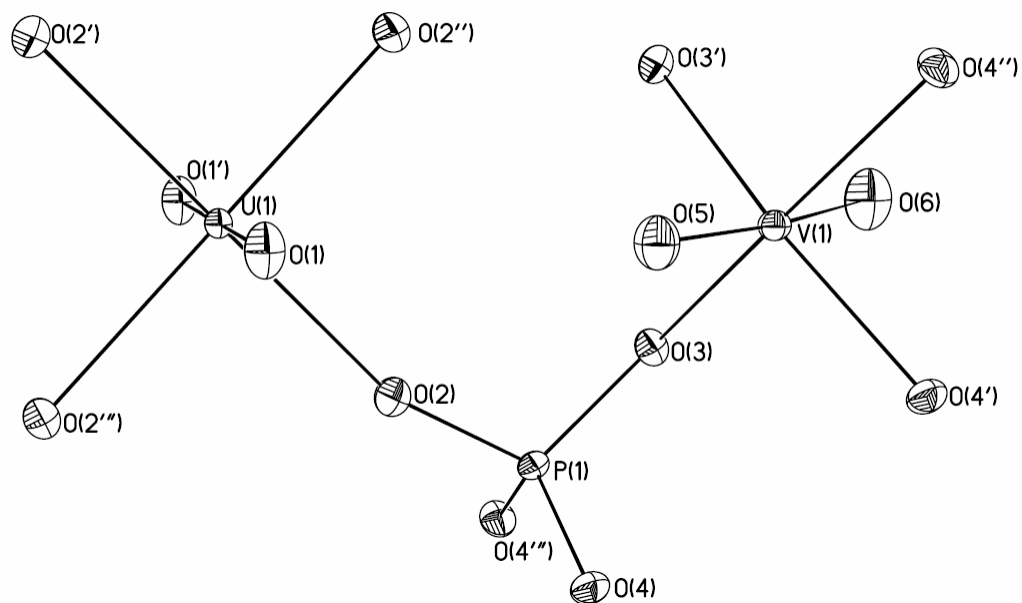


Figure 4.3. Thermal ellipsoid plot of the fundamental unit of $\text{K}_4(\text{UO}_2)(\text{VO})_4(\text{OH})_2(\text{PO}_4)_4$ (**KUV^{IV}P**) and $\text{Rb}_4(\text{UO}_2)(\text{VO})_4(\text{OH})_2(\text{PO}_4)_4$ (**RbUV^{IV}P**) at 50% probability.

Table 4.6. Selected Bond Distances (Å) and Angles (°) for $\text{K}_4(\text{UO}_2)(\text{VO})_4(\text{OH})_2(\text{PO}_4)_4$ (**KUV^{IV}P**). Data for $\text{Rb}_4(\text{UO}_2)(\text{VO})_4(\text{OH})_2(\text{PO}_4)_4$ (**RbUV^{IV}P**) are given in parathensis.

Distances (Å)					
U(1)-O(1)	1.797(13)	(1.783(14))	V(1)-O(6)	2.301(11)	(2.282(12))
U(1)-O(2)	2.261(9)	(2.262(9))	V(1)-V(1)	3.038(4)	(3.053(4))
V(1)-O(5)	1.598(9)	(1.592(10))	P(1)-O(4)	1.517(6)	(1.520(7))
V(1)-O(4)	1.958(6)	(1.966(7))	P(1)-O(2)	1.520(9)	(1.534(10))
V(1)-O(3)	2.061(6)	(2.075(6))	P(2)-O(3)	1.567(9)	(1.562(9))
Angles (°)					
O(8)–U(1)–O(7)	180.00(1)	(180.00(2))	O(4)–V(1)–O(3)	90.6(3)	(91.2(3))
O(5)–V(1)–O(6)	166.9(4)	(165.7(5))	V(1)–O(6)–V(1)	82.6(5)	(83.9(5))

vanadium centers with V-V distance 3.038(4) Å (3.053(4) Å) results in the formation of face-shared V₂O₉ dimers where two equatorial O(4) and axial O(6) atoms belong to both coordination polyhedra. (Figure 4.4) These dimers were previously described in the literature, and for the first time were reported as a part of the (VO)₂H₄P₂O₉ structure.^{30,31} (VO)₂H₄P₂O₉ is a key precursor for the synthesis of vanadyl pyrophosphate (VO)₂P₂O₇, which is a well known technologically important catalyst in the oxidation of butane to the maleic anhydride^{3,32} that has been studied in detail.

Six equatorial oxygen atoms of the V₂O₉ building units are bridged to the six other vanadium dimers through phosphate groups, while two vanadyl O(5) and one opposite axial O(6) atoms remain terminal. There is an undefined electron density area located at the distance 1.55(2) Å from O(6). We speculate that the density could be assigned to one more, highly disordered H₂PO₄ phosphate group, but there is not enough structural information to prove this suggestion.

Each PO₄ group is tetrahedral with three typical P-O bonds 1.517(6) Å - 1.520(9) Å (1.520(7) Å - 1.534(10) Å) and one longer 1.567(9) Å (1.562(9) Å) bond, which corresponds to the μ₃-oxo bridge. The interaction of V₂O₉ and PO₄ units create the layer in the *[ab]* plane, as is shown in the Figure 4.4. The vanadium phosphate layers with similar topology are found in the structures of (NH₄)Zn(H₂O)(VO)₂(PO₄)₂(H₂PO₄)³³ and MZn(H₂O)(VO)₂(PO₄)₂(H₂PO₄) (M = K⁺, Rb⁺, and Cs⁺).³⁴ It is important to note that highly disordered phosphate groups in these structures are also found at the same location relative to the vanadium phosphate layer, as undefined electron density in **KUV^{IV}P** and **RbUV^{IV}P**. The layers are joined together by uranyl tetragonal bipyramids. There is one

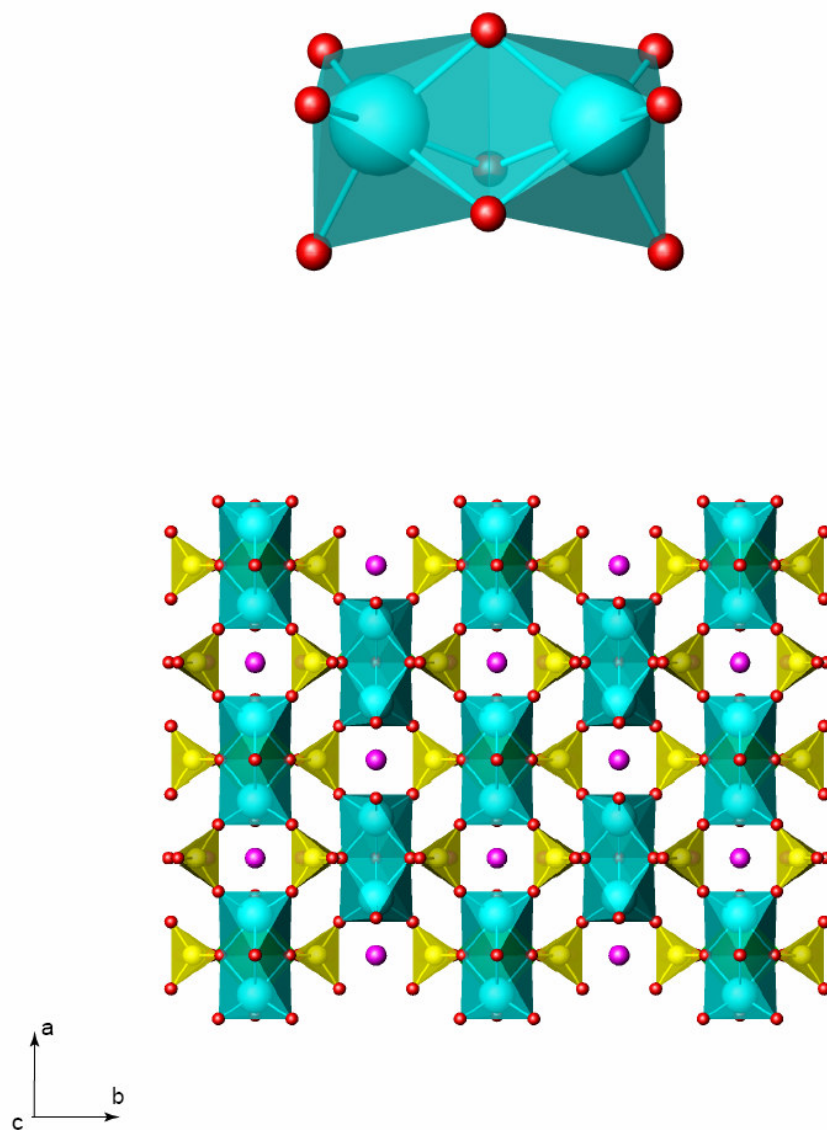


Figure 4.4. Depiction of essential building blocks of the structures of **KUV^{IV}P** and **RbUV^{IV}P**. V₂O₉ dimer, constructed from two vanadium octahedra, sharing two equatorial and one axial oxygen atoms (top) and vanadyl phosphate layer (bottom). Cations (purple) occupy the channels 2.8 Å × 4.4 Å along *c* axis. Blue - vanadium polyhedra, yellow – phosphate groups.

crystallographically unique uranium center in the structure that belongs to linear UO_2^{2+} cation and indeed has two axial uranyl oxygen atoms with a distance of 1.797(13) Å (1.783(14) Å) and an angle of 180.000(1)° (180.000(2)°). Four equatorial oxygen bonds with lengths 2.261(9) Å (2.262(9) Å) are bridged to phosphate groups of vanadium phosphate layer creating a negatively charged framework of $[(\text{UO}_2)(\text{VO})_4(\text{OH})_2(\text{PO}_4)_4]^{4-}$ with a system of channels, parallel to the *a*, *b*, and *c* axes, filled with K^+ (Rb^+) cations. The channels along the *a* and *b* axes are shown in the Figures 4.5 and 4.6 respectively. There are two crystallographically distinct cationic sites in this structure. One is fully occupied with an alkali metal cation, either K^+ , or Rb^+ , coordinated to 12 oxygen atoms with coordination distances ranging from 3.163(8) Å to 3.308(9) Å (3.343(10) Å - 3.550(7) Å). The other cation is in an 8-coordinate environment. It is disordered and only partially occupied with 0.751(18) of K^+ and 0.608(8) of Rb^+ , in the unit cell. This partial occupancy creates the small positive charge deficiency, that can be neutralized by protonation of terminal oxygen atoms of the framework and again, could be ascribed to the presence of an additional disordered phosphate group in the structure. Finally, the formula of the compound is proposed as ideal $\text{M}_4[(\text{UO}_2)(\text{VO})_4(\text{OH})_2(\text{PO}_4)_4]$, that does not reflect the partial occupancy of the cationic sites.

Thermal analysis. We have studied the thermal behavior of $\text{UV}^{\text{V}}\text{P}$ and $\text{KUV}^{\text{IV}}\text{P}$ as potential Cs^+ and Sr^{2+} selective ion-exchange materials, in order to test their ability to preserve the structure at high-temperature conditions of actual nuclear waste.

DSC data for the $\text{UV}^{\text{V}}\text{P}$ reveal two significant endothermic events upon an increase in temperature to 600 °C. (Figure 4.7) The first peak occurs at 150 °C, which can

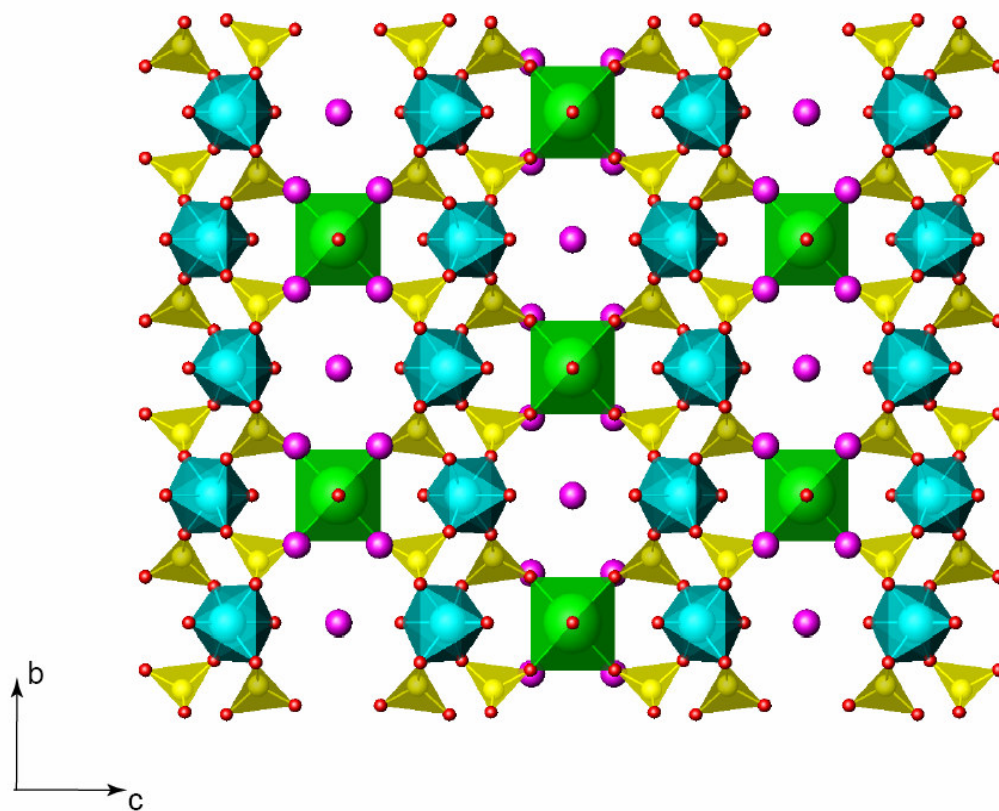


Figure 4.5. Depiction of the channels in the framework of $\text{KUV}^{\text{IV}}\text{P}$ and $\text{RbUV}^{\text{IV}}\text{P}$, filled with K^+ or Rb^+ cations, extended along the a axis. Blue- vanadium, yellow – phosphorus, green – uranium centers, purple – K^+ or Rb^+ cations.

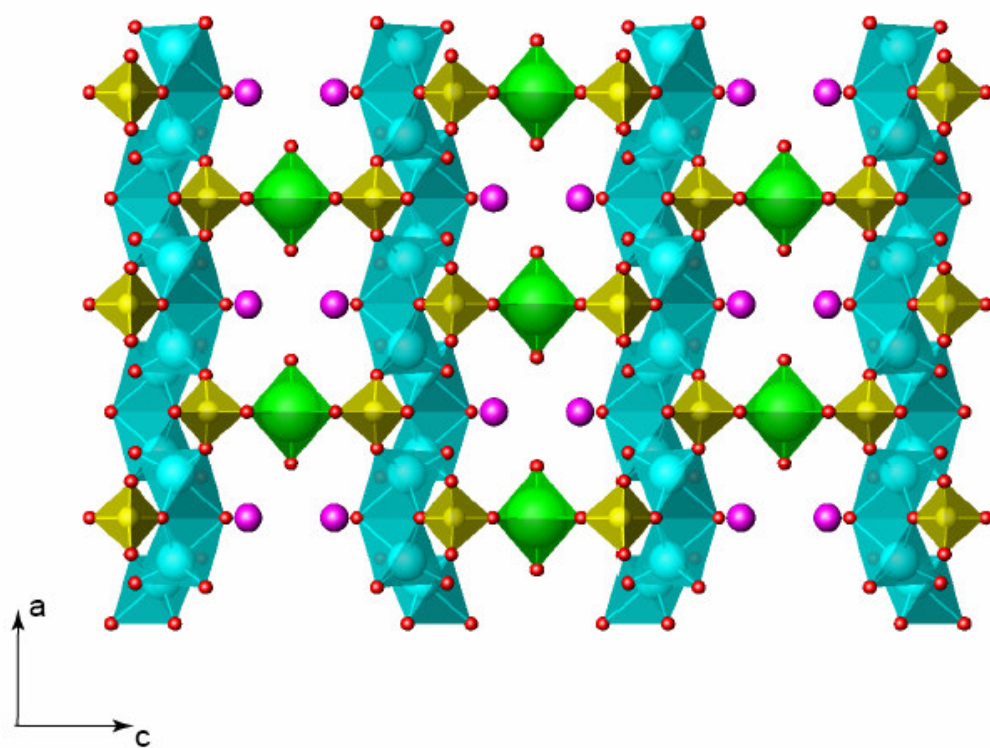


Figure 4.6. A view of the framework of $\text{KUV}^{\text{IV}}\text{P}$ and $\text{RbUV}^{\text{IV}}\text{P}$ along the b axis.

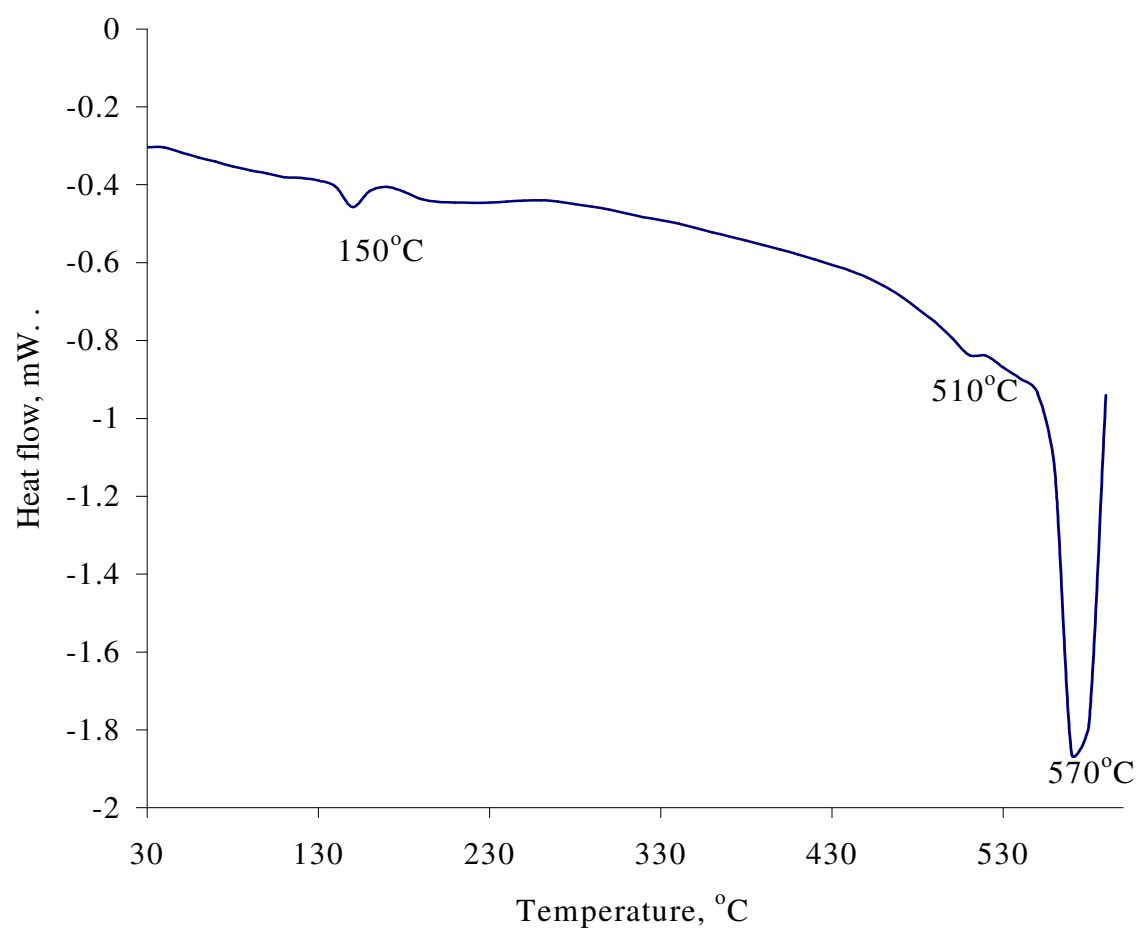


Figure 4.7. DSC data for UV^VP demonstrate thermal stability up to 510 °C.

be assigned to the removal of the surface and interstitial 0.59 water molecules. The second event, composed of two peaks, the smaller at 510 °C and the larger – at 550 °C, corresponds to the decomposition of material. We can suggest that the structure of $\text{UV}^{\text{V}}\text{P}$ remains stable and maintains crystallinity at the temperatures under 500 °C.

The data for $\text{KUV}^{\text{IV}}\text{P}$ demonstrate the loss of water content at 160 °C, and a series of sequential reconstructions of the framework at 310 °C, 330 °C, 510 °C and 550 °C. (Figure 4.8) Amorphization of the structure after heating to 600 °C is confirmed by powder diffraction.

Non-linear optical properties. One of the consequences of the polarity in the structure of $\text{UV}^{\text{V}}\text{P}$ is that the compound should exhibit the SHG of laser light; that is, it should act as a NLO material. SHG was investigated using 1064 nm excitation laser pulses from a Q-switched Nd:YAG laser. SHG at 532 nm was observed from a polycrystalline sample of $\text{UV}^{\text{V}}\text{P}$. The response is substantially weaker than that of a commercial ceramic frequency doubling laser beam finder (Kentek View-It). At the same time the sample of $\text{UV}^{\text{V}}\text{P}$ shows a 70 times larger response than α -quartz. Thus, observed non-linear optical properties can confirm the polar nature of the structure, but $\text{UV}^{\text{V}}\text{P}$ cannot be considered as an effective NLO material.

Magnetic properties. Magnetization of $\text{UV}^{\text{V}}\text{P}$ varies linearly with magnetic field, as is shown in Figure 4.9. The temperature dependence of the magnetic susceptibility of $\text{UV}^{\text{V}}\text{P}$, measured in a constant field of 10000 G, is shown in Figure 4.10. The magnetic signal at high temperatures is almost equal to the background, consistent with the expectation that V in this compound is present as non-magnetic V^{5+} . Our measurements

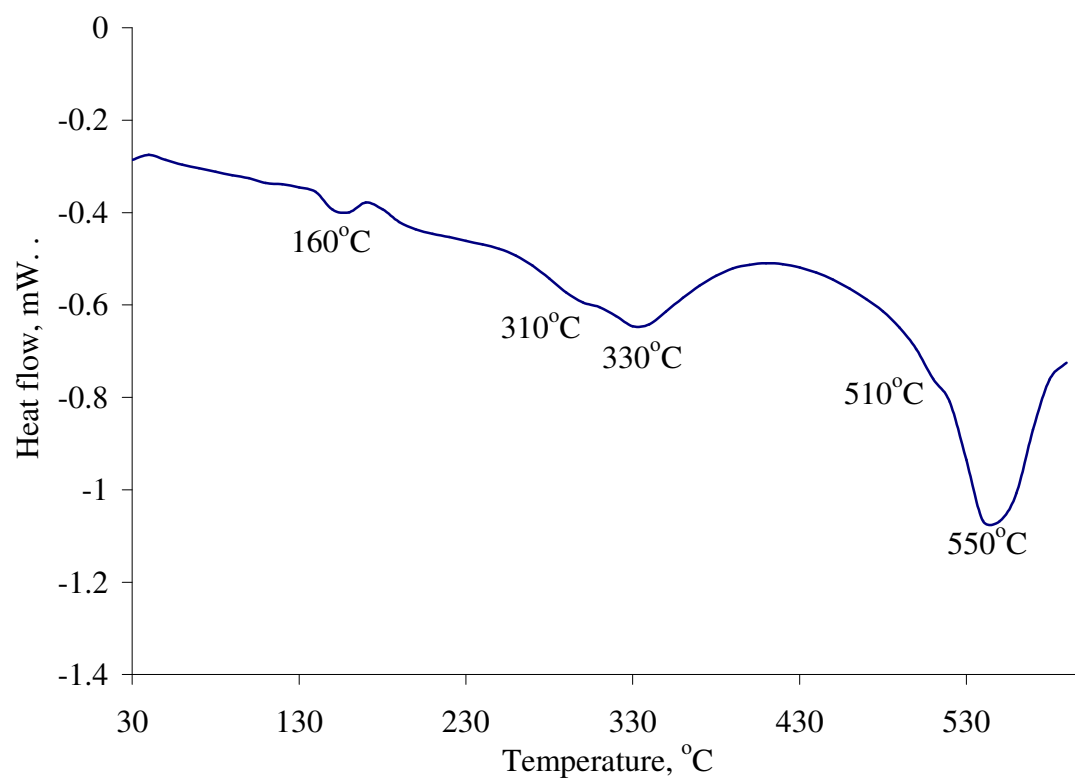


Figure 4.8. DSC data for **KUV^{IV}P**. Several endothermic events between 160 °C and 550 °C reveal gradual structural transformations with increase of temperature.

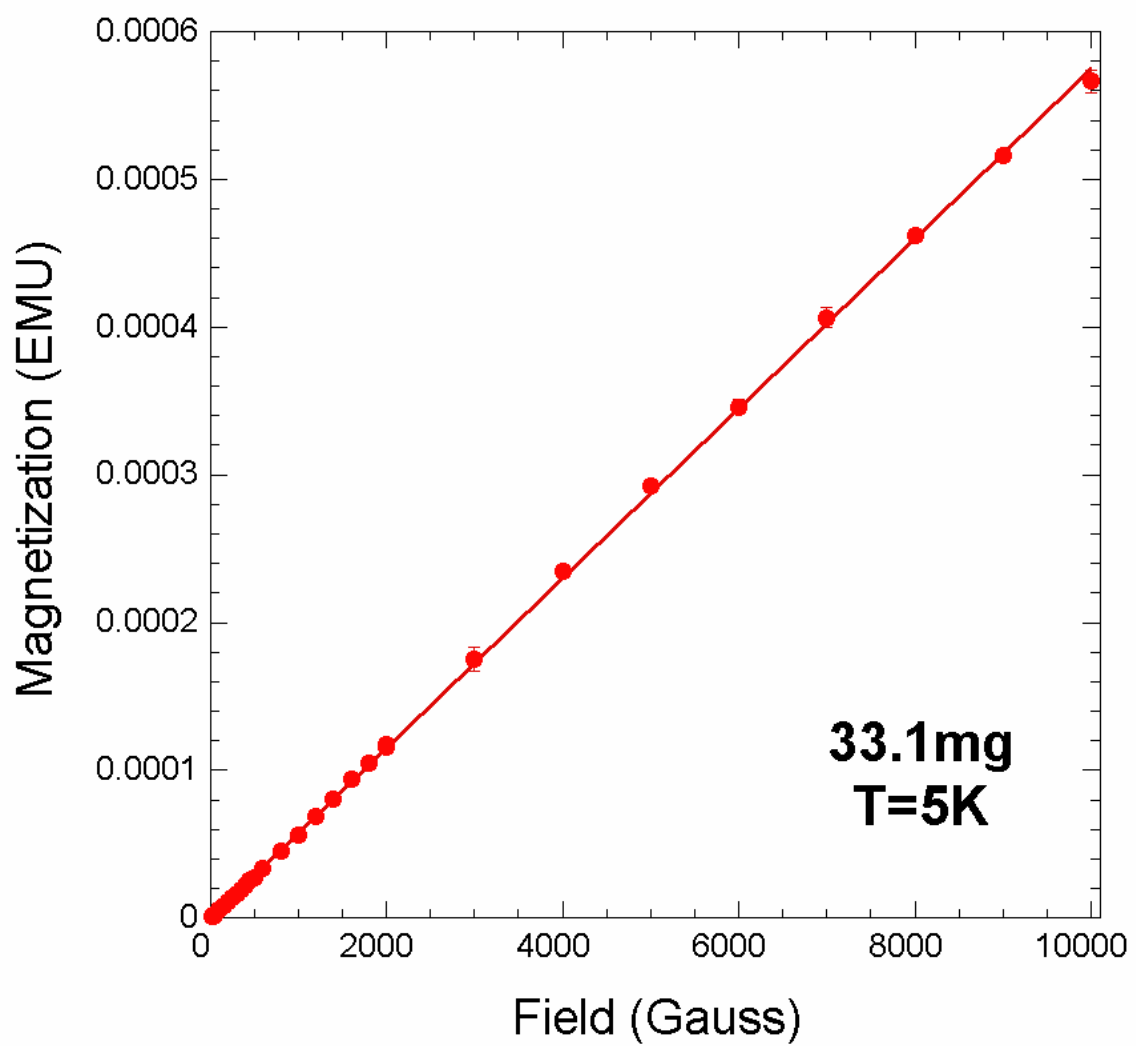


Figure 4.9. Magnetization of $\text{UV}^{\text{V}}\text{P}$ as a function of applied magnetic field at 5 K. Line is the linear fit to the data.

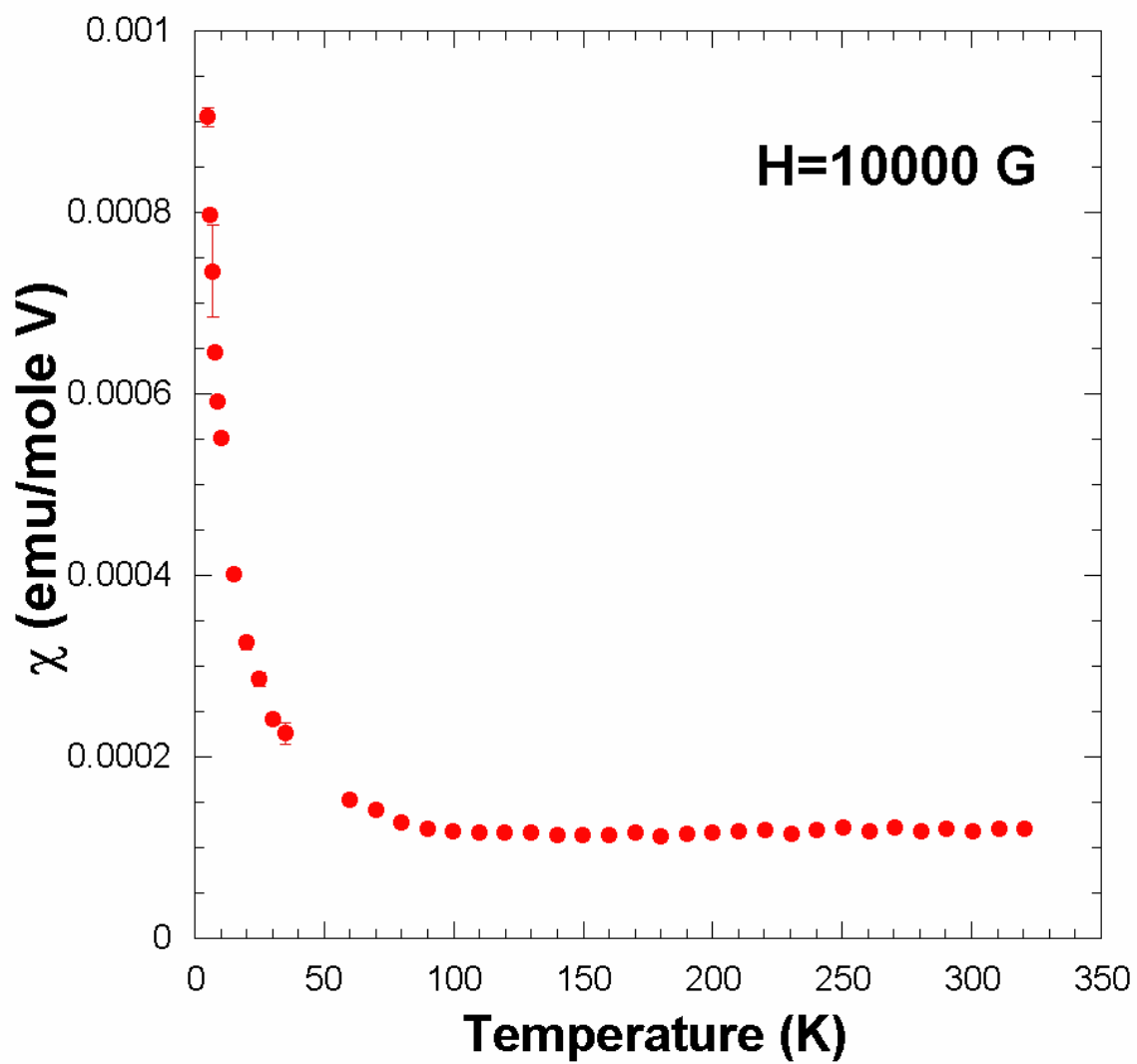


Figure 4.10. Magnetic susceptibility of $\text{UV}^{\text{V}}\text{P}$ as a function of temperature with a 10000 G magnetic field.

indicate that effective moment is smaller than $0.24 \mu_B$. If this magnetic contribution is arising from a V^{4+} , and the spin only moment of $1.73 \mu_B$ is assumed, then the results are consistent with less than 2% of the total V as V^{4+} .

Magnetization measurements of **RbUV^{IV}P**, obtained at 5 K, increase linearly with magnetic field up to the highest measured field, 10,000 G, as shown in Figure 4.11. About 75% of the magnetic signal arises from the background at high temperatures, necessitating susceptibility data acquisition in a 10,000 G field. The temperature dependence of the magnetic susceptibility of **RbUV^{IV}P**, together with its inverse, is depicted in Figure 4.12. The data show complex behavior with temperature. Susceptibility data obtained at lower fields, 500 and 2000 Gauss show a similar temperature dependence. The data indicate a long-range ordering of the moments at 52(2) K. Above that temperature the sample of **RbUV^{IV}P** appears paramagnetic and the data between 100 and 320 K are fit to the modified Curie law and the effective magnetic moment is determined to be $1.73(10) \mu_B$. The effective magnetic moment obtained from a Curie-Weiss fit to the temperature dependence of inverse magnetic susceptibility is $1.82(10) \mu_B$. The difference between these two values reflects the difference in emphasis of the lower or higher temperature data respectively and reflects the inherent error in working with such small magnetic signals. χ_{TIP} and θ are also determined from the modified Curie law fit as $-0.00008(4)$ emu/mole and $-41(8)$ K, respectively. The large, negative Weiss constant is consistent with an antiferromagnetic component to the ordering, as is the shape of the χ versus T plot. There is an additional feature in the data that occurs at about 15(1) K that could be a re-ordering of the moments as the temperature is lowered through the ordered state from 52 K, or it could be a paramagnetic

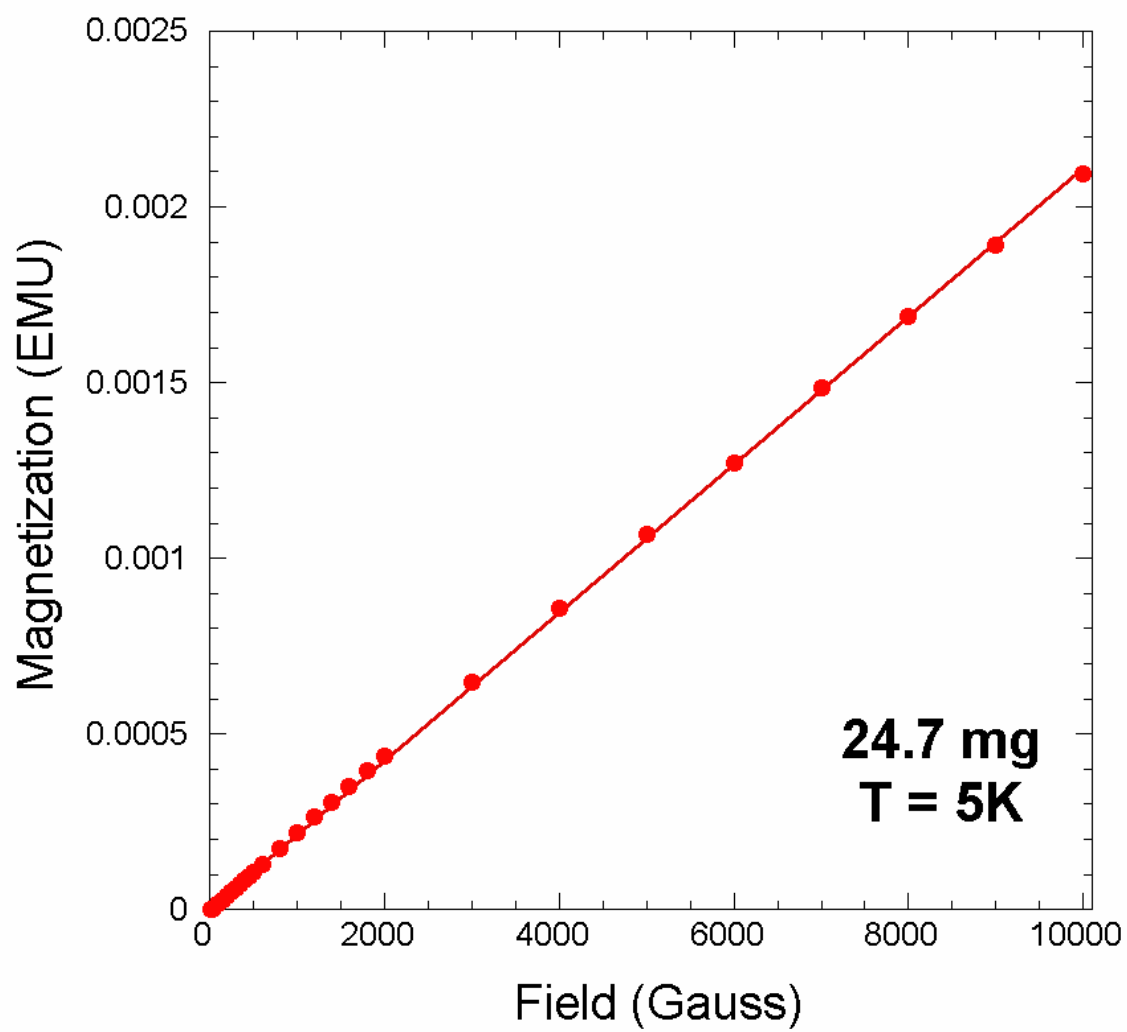


Figure 4.11. Magnetization of **RbUV^{IV}P** as a function of applied magnetic field at 5 K.

Line is the linear fit to the data.

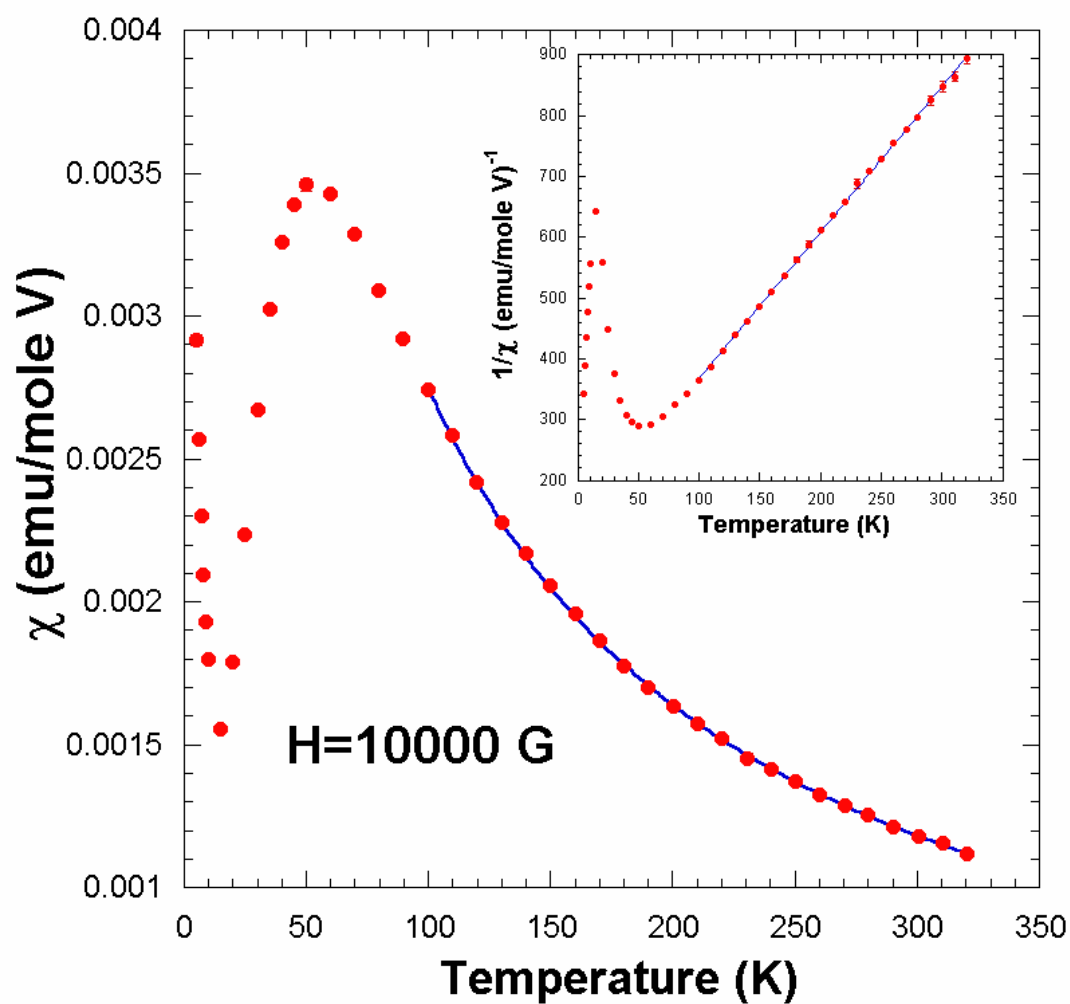


Figure 4.12. Magnetic susceptibility of **RbUV^{IV}P** as a function of temperature. Line is the fit to Curie-Weiss behavior. Inset shows the temperature dependence of the inverse magnetic susceptibility.

impurity phase. The effective moment at 5 K, determined from the M vs. H curve, is 0.34 μ_B . It is not possible to distinguish between these two options without further studies.

Ion-exchange study. Due to the framework type of the structure, the ion-exchange experiments were run for both $UV^V P$ and $KUV^{IV} P$. After equilibration of all samples of $UV^V P$ with NaCl, KCl, $CaCl_2$, $SrCl_2$ solutions the change of the color of solutions, decrease of the sample amount, and consequently, the partial dissolution of $UV^V P$ was detected. In contrast, the structure of $KUV^{IV} P$ in all exchanged probes, was conserved, as was proved by the identity of powder diffraction patterns of the samples, tested before and after ion-exchange experiments.

There is no uptake of the cations found from the pure 1×10^{-2} M and 1×10^{-3} M solutions of $CaCl_2$ and $SrCl_2$. Small exchange was observed in 1×10^{-2} M NaCl solutions with an uptake value 0.25(6) meq/g. In the mixed 1:1 solutions of NaCl/ $CaCl_2$ and NaCl/ $SrCl_2$ slightly smaller Na^+ - exchange capacities of 0.18(5) meq/g and 0.17(5) meq/g were detected, probably owing not to the competition of Na^+/Ca^{2+} and Na^+/Sr^{2+} cationic pairs in the probe, but to the overall dilution of the Na^+ solutions. Ca^{2+} and Sr^{2+} uptake were not found in the mixed solutions either.

Exchange with Cs^+ from 1×10^{-2} M CsCl solution reveals notable uptake 0.87(10) meq/g. The amount of the exchanged Cs^+ cations per taken mass of the sample is close to 50% ($46.8\% \pm 0.9\%$) of total cation content, in other words, half of the theoretical capacity, calculated from the formula. These results are in good agreement with the structural data. We suggest that the larger channels along the *a* and *b* axes with size $5.8 \text{ \AA} \times 4.6 \text{ \AA}$ and $3.8 \text{ \AA} \times 4.6 \text{ \AA}$, respectively, are not available for exchange due to the presence of undefined electron density, pointed inside of these channels. Therefore, we

propose that ion-exchange occurs only through smaller channels $2.8 \text{ \AA} \times 4.4 \text{ \AA}$ along the c axis, occupied by one out of two K^+ cations, present in the structure. The high selectivity of the framework toward Cs^+ versus K^+ can be explained in the radii and hydration energy terms. At the hydrated state the radii of K^+ and Cs^+ are the same and correspond to 3.3 \AA .³⁵ Due to the lower dehydration energy Cs^+ is able to lose its hydration sphere and enter the channels easier than K^+ .

In the mixed Cs^+/Na^+ solutions with equal concentrations of both cations, again only half of the total cation content is exchanged. Three quarters of exchanged cations are Cs^+ and only one quarter is Na^+ . If the concentration of Na^+ is doubled in the initial mixed solutions, the ratio of exchanged Cs^+/Na^+ remains the same. From this data we can conclude that **KUV^{IV}P** is Cs^+ -selective ion-exchange material with high capacity 0.87(10) meq/g.

CONCLUSIONS

Two novel uranyl vanadium phosphate framework materials have been synthesized and studied. One material is thermally stable up to $500 \text{ }^\circ\text{C}$ and demonstrates non-linear optical properties. The other exhibits remarkable magnetic properties and selective Cs^+ uptake from mixed Cs^+/Na^+ solutions, as would be required by actual nuclear waste conditions. Several issues need to be explained, such as structural uncertainty of **K(Rb)UV^{IV}P** or the reason for the formation of different compounds under similar conditions. We are currently working on the detailed elemental analysis of **RbUV^{IV}P** that will help to solve the structural uncertainties of **KUV^{IV}P** and **RbUV^{IV}P** members of uranyl vanadium phosphate family.

REFERENCES

1. Cotton, F. A.; Wilkinson, G.; Murillo, C. A.; Bochmann, M. *Advanced Inorganic Chemistry*, 6th ed.; Wiley-Interscience: New-York, 1999, pp 714-736.
2. Boudin, S.; Guesdon, A.; Leclaire, A.; Borel, M.-M. *Int. J. Inorg. Mater.* **2000**, 2, 561.
3. Hutchings, G. J. *J. Mater. Chem.* **2004**, 14, 3385.
4. Beltran-Porter, D.; Beltran-Porter, A.; Amoros, P.; Ibanez, R.; Martinez, E.; Le Bail, A.; Ferey, G.; Villeneuve, G. *Eur. J. Solid State Inorg. Chem.* **1999**, 28, 131.
5. Amoros, P.; Marcos, D. M.; Beltran-Porter, A.; Beltran-Porter, D. *Curr. Opin. Solid State Mat. Science* **1999**, 4, 123.
6. Abraham, F.; Dion, C.; Saadi, M. *J. Mater. Chem.* **1993**, 3, 459.
7. Abraham, F.; Dion, C. ; Tancrét, N. ; Saadi, M. *Adv. Mater. Res.* **1994**, 1–2, 511.
8. Dickens, P. G.; Stuttard, G. P.; Ball, R. G. J.; Powell, A. V. ; Hull, S. ; Patat, S. *J. Mater. Chem.* **1992**, 2, 161.
9. Obbade, S.; Dion, C.; Rivenet, M. ; Saadi, M.; Abraham F. *J. Solid State Chem.* **2004**, 177, 2058.
10. Obbade, S.; Dion, C.; Saadi, M.; Yagoubi, S.; Abraham, F. *J. Solid State Chem.* **2004**, 177, 3909.
11. Sykora, R. E.; Albrecht-Schmitt, T. E. *Inorg. Chem.* **2003**, 42, 2179.
12. Lii, K. H.; Li, C. H.; Cheng, C. Y.; Wang, S. L. *J. Solid State Chem.* **1991**, 95, 352.
13. Bayi, F.; Pourroy, G.; Belaiche, M.; Legall, P.; Drillon, M.; Kuentzler, R. *Eur. J. Solid State Inorg. Chem.* **1993**, 30, 55.

14. Borel, M. M.; Leclaire, A.; Chardon, J.; Michel, C.; Provost, J.; Raveau, B. *J. Solid State Chem.* **1998**, *135*, 302.
15. Roca, M.; Amoros, P.; Cano, J.; Marcos, M. D.; Alamo, J.; Beltran-Porter, A.; Beltran-Porter, D. *Inorg. Chem.* **1998**, *37*, 3167.
16. Sheldrick, G. M. SHELXTL PC, Version 6.12, An Integrated System for Solving, Refining, and Displaying Crystal Structures from Diffraction Data; Siemens Analytical X-Ray Instruments, Inc.: Madison, WI 2001.
17. Sheldrick, G. M. SADABS 2001, Program for absorption correction using SMART CCD based on the method of Blessing; Blessing, R. H. *Acta Crystallogr.* **1995**, *A51*, 33.
18. Buehlmann, P.; Pretsch, E.; Bakker, E. *Chem. Rev.* **1998**, *98*, 1593.
19. Navrotsky, A. *Curr. Opin. in Colloid & Interface Science* **2005**, *10*, 195.
20. Yang, S.; Li, Q.; Wang, M.; Navrotsky, A. *Micropor. Mesopor. Mater.* **2006**, *87*, 261.
21. Yang, S.; Navrotsky, A.; Phillips, B. L. *J. Phys. Chem.* **2000**, *104*, 6071.
22. Ekambaram, S.; Serre, C.; Ferey, G.; Sevov, S. C. *Chem. Mater.* **2000**, *12*, 444.
23. Calin, N.; Serre, C.; Sevov, S. C. *J. Mater. Chem.* **2003**, *13*, 531.
24. Guesdon, A.; Charon, J.; Provost, J.; Raveau, B. *J. Solid State Chem.* **2002**, *165*, 89.
25. Masse, R.; Grenier, J. C. *Bull. Soc. Fran. Mineral. Cristallogr.* **1971**, *94*, 437.
26. Tordjman, I.; Masse, R.; Guitel, J. C. *Z. Kristallogr., Kristallgeom., Kristallphys., Kristallchem.* **1974**, *139*, 103.
27. Burns, P. C.; Ewing, R. C.; Hawthorne, F. C. *Can. Mineral.* **1997**, *35*, 1551.
28. Brese, N. E.; O'Keefe, M. *Acta Crystallogr.* **1991**, *B47*, 192.
29. Brown, I. D.; Altermatt, D. *Acta Crystallogr.* **1985**, *B41*, 244.

30. Torardi C. C.; Calabrese, J. C. *Inorg. Chem.* **1984**, 23, 1308.
31. Leonowicz, M. E.; Johnson, J. W.; Brody, J. F.; Shannon H.; Newsam J. M. *J. Solid State Chem.* **1985**, 56, 370.
32. Bordes, E.; Courtine, P. *J. Catal.* **1979**, 57, 236.
33. Le Fur, E.; Peña, O.; Pivan, J. Y. *J. Mater. Chem.* **2002**, 12, 132.
34. Messaoudi, S.; Furet, E.; Gautier, R.; Le Fur, E.; Peña, O.; Pivan, J. Y. *Chem. Mater.* **2004**, 16, 435.
35. Nightingale, E.R. *J. Phys. Chem.* **1959**, 63, 1381.

CHAPTER 5

HYDROTHERMAL SYNTHESIS AND STRUCTURAL CHARACTERIZATION OF $\text{Cs}_{1.52}[(\text{UO}_2)(\text{TiOH}_{0.48})(\text{PO}_4)_2] \cdot n\text{H}_2\text{O}$ and $\text{Cs}_{1.35}[(\text{UO}_2)(\text{GeOH}_{0.65})(\text{PO}_4)_2] \cdot n\text{H}_2\text{O}$

ABSTRACT

Two novel uranyl-containing three-dimensional materials $\text{Cs}_{1.52}[(\text{UO}_2)(\text{TiOH}_{0.48})(\text{PO}_4)_2] \cdot n\text{H}_2\text{O}$ (**UTiP**) and $\text{Cs}_{1.35}[(\text{UO}_2)(\text{GeOH}_{0.65})(\text{PO}_4)_2] \cdot n\text{H}_2\text{O}$ (**UGeP**) were synthesized under hydrothermal conditions. The materials are isostructural and have identical frameworks, constructed from the perpendicular intersection of one-dimensional uranyl phosphate and titanium or germanium phosphate chains. The channels are occupied by disordered Cs^+ cations and disordered water molecules. The compounds crystallize in monoclinic space group $C2/m$. Crystallographic data: **UTiP**: $a = 19.715(4) \text{ \AA}$, $b = 7.1207(14) \text{ \AA}$, $c = 9.4756(19) \text{ \AA}$, $\beta = 115.93(3)^\circ$, $V = 1196.3(4) \text{ \AA}^3$, $Z = 4$, $T = 193\text{K}$. **UGeP**: $a = 19.5123(17) \text{ \AA}$, $b = 6.8639(6) \text{ \AA}$, $c = 9.3731(8) \text{ \AA}$, $\beta = 116.125(2)^\circ$, $V = 1127.09(17) \text{ \AA}^3$, $Z = 4$, $T = 193\text{K}$.

INTRODUCTION

Potential technical applications of inorganic crystalline three-dimensional structures, due to their non-linear optical properties, magnetism, conductivity, or ion-exchange, leads to a continued search for novel compounds and methods for their preparation.¹ Three-dimensional uranyl-containing materials have come to the forefront because there are thousands of tons of depleted uranium, with very low level radioactivity stored at the Savannah River Site and several other locations. The incorporation of U^{VI} in the form of uranyl, UO_2^{2+} cations, into crystalline frameworks has the potential of yielding functional materials while at the same time expanding our knowledge on the crystal chemistry of U^{VI} .

The formation of uranyl-containing three-dimensional structures is a very challenging task due to the reduced dimensionality along axial uranyl-oxygen double bonds.²⁹⁻³⁰ There are several synthetic strategies known today to facilitate the formation of frameworks. We focused our study on the incorporation of octahedral building units, such as IO_6^{5-} ,²⁸ in order to allow the bond formation in the direction parallel to uranyl axis. In previous chapters we have already shown that, indeed, the structure of **UGaP1**²⁵ and **KUV^{IV}P (RbUV^{IV}P)** are formed according to this new synthetic method. In this chapter we continue to investigate the conditions of the formation of frameworks by the introduction of Ti and Ge coordination polyhedra.

The formation of six-coordinate complexes is common in the structural chemistry of Ti(IV). In the structures of ETS-4 and ETS-10 molecular sieves,³¹ Cs^+ and Sr^{2+} -selective titanium silicates $\text{Na}_2\text{Ti}_2\text{O}_3(\text{SiO}_4)\cdot\text{H}_2\text{O}$ and $\text{HM}_3\text{Ti}_4\text{O}_4(\text{SiO}_4)\cdot\text{H}_2\text{O}$ ³² and many other compounds, as well as in recently synthesized organically templated framework

mixed-valent Ti(III)/Ti(IV) phosphates^{33,34} and mixed-valent Ti(III)/Ti(IV) gallium phosphate,³⁵ Ti metal centers form octahedra with different degrees of distortion. In the latter structures of $\text{Ti}^{\text{III}}\text{Ti}^{\text{IV}}(\text{PO}_4)(\text{HPO}_4)_2(\text{H}_2\text{O})_2 \cdot 0.5\text{NH}_2\text{CH}_2\text{CH}_2\text{CH}_2\text{NH}_2$, $\text{Ti}^{\text{III}}\text{Ti}^{\text{IV}}(\text{HPO}_4)_4 \cdot \text{C}_2\text{N}_2\text{H}_9 \cdot \text{H}_2\text{O}$ ^{33,34} and $[\text{C}_5\text{NH}_6][\text{Ti}_3\text{Ga}(\text{PO}_4)_5(\text{H}_2\text{O})_2]$ ³⁵ both Ti(III) and Ti(IV) have a six-folded coordination environment, with small differences in the bond length range.

The knowledge about crystal chemistry of uranium-titanium oxocompounds is restricted to only a series of structures of $\text{UTi}_x\text{Nb}_{3-x}\text{O}_{10}$ ($x = 0.33, 1$) and its intercalated compound $\text{Li}_{0.9}\text{UTiNb}_2\text{O}_{10}$, where Ti plays only a substitution role,³⁶ and in several mineral structures.³⁷ The most abundant uranium-titanium mineral brannerite, UTi_2O_6 , is an important component of the Synroc pyrochlore-type ceramics,³⁸ studied as a storage material for Pu isotopes in a geological environment.^{39, 40} At room temperature naturally occurring brannerite is amorphous. It crystallizes only at temperatures above 1000 °C in monoclinic $C2/m$ structure, consisting of layers of titanium edge-sharing octahedra, linked together with uranium tetragonal bipyramids.⁴¹ One of the proposed mechanisms for the stabilization of brannerite-phase formation could be incorporation of doping cations such as Ca^{2+} , La^{3+} , and Ga^{3+} in the structure.⁴²⁻⁴⁴ We suggest that the formation of crystal structures based on uranium and titanium at hydrothermal temperatures can be reached through addition of phosphate groups, which improve the solubility of components and stabilize the resultant structure.

The coordination polyhedra of germanium can also be used as potential octahedral building unit, due to the ability to have coordination numbers 4, 5, or 6, unlike its closest neighbor Si.⁴⁵ This originates from larger Ge, then Si, atomic radius and

therefore longer Ge–O bonds and more flexible Ge-O-Ge angle. The variations in the coordination modes of germanium allows it to form structures incorporating tetrahedral,^{46,47} trigonal bipyramidal or square pyramidal^{48,49} and octahedral⁵⁰⁻⁵² coordination environments, as well as structures where all three types of polyhedra are combined together⁵³⁻⁵⁵ and frameworks entirely constructed from germanate units.⁵⁶⁻⁵⁸ There are a number of features of the germanate frameworks that make this class of structures extremely diverse and attractive for detailed studies. First is the ability of germanate units to form clusters. [Ge₉O₁₈(OH)₄] clusters synthesized with different organic templates^{57,59} and Ge₉O₁₉(OH)₂(N₂C₂H₁₀)₂(N₂C₂H₈)_{0.5}H₂O⁶⁰ are just a few examples of three-dimensional structures with remarkable porosity due to the cluster construction. Second, the germanate framework compounds with odd-membered rings can be formed.^{50,52,61,62} Finally, the capacity to build the porous structures with chiral channels makes germanates attractive for enantioselective catalysis and separation.^{60,63,64}

All known uranyl germanates have layered structures.^{65,66} The germanate anions there exhibit only tetrahedral arrangements. In this chapter, as a continuation of previous work, we intend to investigate the potential of Ti and Ge centers to form octahedral polyhedra in order to synthesize the first uranyl-containing titanium and germanium phosphate framework materials.

EXPERIMENTAL

Syntheses. UO₂(NO₃)₂·6H₂O (98%, Alfa-Aesar), Ti powder (99.99%, Sigma Aldrich), Ge powder (99.99%, Sigma Aldrich), H₃PO₄ (98%, Aldrich), and CsCl (99.9%, Cerac) were used as received. Ti and Ge powder were handled in the glovebox under an

Ar atmosphere due to the potential rapid oxidation in air. For all reactions PTFE-lined Parr 4749 vessels were loaded with reaction mixture and 1 mL of distilled and Millipore filtered water with a resistance of 18.2 M Ω ·cm. Despite the presence of only depleted uranium in UO₂(NO₃)₂·6H₂O and products of the reactions, and therefore very low level of radioactivity, all studies were carried out with precautions. Semi-quantitative SEM/EDX analyses were performed using a JEOL JSM-7000F instrument. Cs, U, Ti, Ge, and P percentages were calibrated against standards.

Cs_{1.52}[(UO₂)(TiOH_{0.48})(PO₄)₂]·nH₂O (UTiP). UO₂(NO₃)₂·6H₂O (0.276 g, 0.549 mmol), H₃PO₄ (0.161 g, 1.64 mmol) and CsCl (0.554 g, 2.75 mmol) were combined together in 23 mL PTFE liner with 1 mL of water with stirring until homogenous. The Ti (0.026g, 0.55 mmol) was quickly added to the reaction mixture, the autoclave was rapidly sealed, placed in a box furnace, and heated at 195 °C for seven days. Then reaction was slowly cooled with an average rate 1 °C/hour. The solid part of the product mixture was washed with water and methanol and dried in air. The final composition of the mixture was identified as small fractions of pale yellow crystals of **UTiP**, mixed together with yellow crystals of uranyl phosphate and excess Ti metal, and larger portions of amorphous **UTiP**. The isolated yield of crystalline **UTiP** was 0.028 g (7.1 % yield based on the U). EDX analysis provided Cs:U:Ti:P ratio of 1.5:1:1:2.

Cs_{1.35}[(UO₂)(GeOH_{0.65})(PO₄)₂]·nH₂O (UGeP). UO₂(NO₃)₂·6H₂O (0.282 g, 0.561 mmol), H₃PO₄ (0.165 g, 1.64 mmol) and CsCl (0.472 g, 2.81 mmol) were mixed in a 23 mL PTFE-lined autoclave with 1 mL of water and Ge (0.081 g, 1.1 mmol) powder, weighed separately in the glovebox.. The sealed vessel was heated at 195 °C for five days and cooled to room temperature at the rate of 9°C/hour. After decantation of the mother

liquid small yellow crystals of **UGeP**, grown on the surface of non-crystalline product were found. The yield of **UGeP** was near quantitative. EDX analysis provided Cs:U:Ge:P ratio of 1.5:1:1:2.

Crystallographic Studies. Crystals of **UTiP** and **UGeP** were mounted on glass fibers and aligned on a Bruker SMART APEX CCD X-ray diffractometer. Intensity measurements were performed using graphite monochromated Mo K α radiation from a sealed tube and monocapillary collimator. SMART (v 5.624) was used for preliminary determination of the cell constants and data collection controls. The intensities of reflections of a sphere were collected by a combination of 3 sets of exposures (frames). Each set had a different ϕ angle for the crystal and each exposure covered a range of 0.3° in ω . A total of 1800 frames were collected with an exposure time per frame of 120 s for both **UTiP** and **UGeP** due to the extremely small dimensions of the crystals.

Determination of integrated intensities and global refinement were performed with the Bruker SAINT (v 6.02) software package using a narrow-frame integration algorithm. A face-indexed analytical absorption correction was initially applied using XPREP, where individual shells of unmerged data were corrected analytically.⁶⁷ These files were subsequently treated with a semiempirical absorption correction by SADABS.⁶⁸ The program suite SHELXTL (v 6.12) was used for space group determination (XPREP), direct methods structure solution (XS), and least-squares refinement (XL).⁶⁷ The final refinements included anisotropic displacement parameters for all atoms. Secondary extinction was not noted for either crystal. Some crystallographic details are given in Table 5.1. Atomic coordinates and displacement parameters for all atoms of **UTiP** can be found in Table 5.2, **UGeP** – in Table 5.3.

Table 5.1. Crystallographic Data for Cs_{1.52}[(UO₂)(TiOH_{0.48})(PO₄)₂]·nH₂O (**UTiP**) and Cs_{1.35}[(UO₂)(GeOH_{0.65})(PO₄)₂]·nH₂O (**UGeP**).

Compound	UTiP	UGeP
Formula Mass	740.16	742.28
Color and habit	yellow plate	yellow plate
Crystal System	Monoclinic	Monoclinic
Space group	<i>C2/m</i> (No. 12)	<i>C2/m</i> (No. 12)
<i>a</i> (Å)	19.715(4)	19.5123(17)
<i>b</i> (Å)	7.1207(14)	6.8639(6)
<i>c</i> (Å)	9.4756(19)	9.3731(8)
β (°)	115.93(3)	116.125(2)
<i>V</i> (Å ³)	1196.3(4)	1127.09(17)
<i>Z</i>	4	4
<i>T</i> (K)	193	193
λ (Å)	0.71073	0.71073
Maximum 2 θ (deg.)	56.64	56.52
ρ_{calcd} (g cm ⁻³)	4.110	4.374
$\mu(\text{Mo } K\alpha)$ (cm ⁻¹)	190.8	213.6
$R(F)$ for $F_o^2 > 2\sigma(F_o^2)$	0.0371	0.0412
$R_w(F_o^2)^b$	0.0747	0.0977

$$^a R(F) = \sum \|F_o| - |F_c|\| / \sum |F_o|. \quad ^b R_w(F_o^2) = \left[\sum \left[w(F_o^2 - F_c^2)^2 \right] / \sum wF_o^4 \right]^{1/2}.$$

Table 5.2. Atomic Coordinates and Equivalent Isotropic Displacement Parameters for $\text{Cs}_{1.52}[(\text{UO}_2)(\text{TiOH}_{0.48})(\text{PO}_4)_2] \cdot n\text{H}_2\text{O}$ (**UTiP**).

Atom	Symmetry ^a	<i>x</i>	<i>y</i>	<i>z</i>	$U_{\text{eq}}(\text{\AA}^2)^b$	s.o.f.
U(1)	4 <i>i m</i>	0.04052(2)	0	-0.66748(5)	0.0109(1)	1
Ti(1)	4 <i>e</i> $\bar{1}$	$\frac{1}{4}$	$\frac{1}{4}$	0	0.0156(4)	1
P(1)	4 <i>i m</i>	0.12604(16)	0	-0.9415(3))	0.0115(6)	1
P(2)	4 <i>i m</i>	0.15447(16)	0	-0.3148(3)	0.0115(6)	1
O(1)	4 <i>i m</i>	0.1665(5)	0	-0.4635(9)	0.027(2)	1
O(2)	8 <i>j</i> 1	0.1866(4)	0.1742(8)	-0.2172(7)	0.0287(15)	1
O(3)	4 <i>i m</i>	0.0670(4)	0	-0.3835(9))	0.024(2)	1
O(4)	4 <i>i m</i>	-0.0517(5)	0	-0.9137(10)	0.037(2)	1
O(5)	4 <i>i m</i>	0.1134(5)	0	-0.7976(10)	0.037(3)	1
O(6)	8 <i>j</i> 1	0.0413(4)	0.2490(8)	-0.6652(7)	0.0269(14)	1
O(7)	8 <i>j</i> 1	0.1715(3)	0.1769(8)	-0.9408(8)	0.0295(16)	1
O(8)	4 <i>i m</i>	0.2912(4)	0	-0.9540(9)	0.0139(16)	1
O(9)	4 <i>i m</i>	0.3640(7)	0	-0.2041(17)	0.047(5)	0.85(3)
Cs(1)	4 <i>i m</i>	0.30542(5)	0	-0.5527(1)	0.0289(3)	0.874(3)
Cs(2)	4 <i>i m</i>	0.4233(3)	0	-0.6394(7)	0.046(2)	0.194(4)
Cs(3)	4 <i>i m</i>	0.45520(11)	0	0.0264(3)	0.0405(8)	0.457(3)

^a Symmetry describes multiplicity, Wyckoff parameter and symmetry of the atomic site.

^b U_{eq} is defined as one-third of the trace of the orthogonalized \mathbf{U}_{ij} tensor.

Table 5.3. Atomic Coordinates and Equivalent Isotropic Displacement Parameters for $\text{Cs}_{1.35}[(\text{UO}_2)(\text{GeOH}_{0.65})(\text{PO}_4)_2] \cdot n\text{H}_2\text{O}$ (**UGeP**).

Atom	Symmetry ^a	<i>x</i>	<i>y</i>	<i>z</i>	$U_{\text{eq}} (\text{\AA}^2)^b$	s.o.f.
U(1)	4 <i>i m</i>	0.04126(2)	0.0000	-0.66805(5)	0.00962(15)	1
Ge(1)	4 <i>e</i> $\bar{1}$	$\frac{1}{4}$	$\frac{1}{4}$	0	0.0174(3)	1
P(1)	4 <i>i m</i>	0.12860(19)	0	-0.9417(4)	0.0128(6)	1
P(2)	4 <i>i m</i>	0.15654(18)	0	-0.3081(4)	0.0110(6)	1
O(1)	4 <i>i m</i>	0.1692(6)	0	-0.4552(11)	0.027(2)	1
O(2)	8 <i>j</i> 1	0.1886(6)	0.1811(11)	-0.2092(9)	0.050(3)	1
O(3)	4 <i>i m</i>	0.0689(6)	0	-0.3787(12)	0.055(5)	1
O(4)	4 <i>i m</i>	-0.0523(7)	0	-0.9147(13)	0.052(4)	1
O(5)	4 <i>i m</i>	0.1180(6)	0	-0.7930(12)	0.057(5)	1
O(6)	8 <i>j</i> 1	0.0404(4)	0.2571(12)	-0.6643(11)	0.042(2)	1
O(7)	8 <i>j</i> 1	0.1756(6)	0.1797(12)	-0.9392(17)	0.060(3)	1
O(8)	4 <i>i m</i>	0.2929(6)	0	-0.9512(11)	0.020(2)	1
O(9)	4 <i>i m</i>	0.3707(17)	0	-0.186(3)	0.062(10)	0.63(7)
Cs(1)	4 <i>i m</i>	0.30512(7)	0	-0.54392(16)	0.0383(5)	0.812(6)
Cs(2)	4 <i>i m</i>	0.4159(11)	0	-0.682(2)	0.069(7)	0.100(7)
Cs(3)	4 <i>i m</i>	0.45559(14)	0	0.0046(4)	0.0396(10)	0.435(5)

^a Symmetry describes multiplicity, Wyckoff parameter and symmetry of the atomic site.

^b U_{eq} is defined as one-third of the trace of the orthogonalized \mathbf{U}_{ij} tensor.

RESULTS AND DISCUSSION

Syntheses. The syntheses of **UTiP** and **UGeP** appear to be similar and yield isostructural compounds. Both Ti and Ge starting materials are pure elements. Ti powder was previously used in the production of several titanium phosphates,³³⁻³⁵ which often led to the partial oxidation of titanium and synthesis of mixed-valent materials. **UTiP** also could be synthesized from titanium isopropoxide $\text{Ti}(\text{OC}_3\text{H}_7)_4$ as a source of Ti, but crystals were very small and could be seen only using SEM. We speculated that the choice of the source material can play a crucial role in crystal growth. In the study of synthetic conditions for the formation of jarosites, Grohol and Nocera⁶⁸ suggested that slow oxidation of vanadium metal can be the rate-determining step in the crystallization of the final vanadium sulfate mineral. This could also be true for the development of **UTiP** and **UGeP** as well. Slow delivery of oxidized reactants to the reaction mixture of uranyl nitrate and phosphoric acid aids in the formation of a multicomponent system instead of separate titanium or germanium phosphates and uranyl phosphate, and gives the possibility of growing crystals with dimensions acceptable for single-crystal X-ray diffraction.

Structure. The crystallographic data (Table 5.1) and atomic coordinates (Tables 5.2 and 5.3) of $\text{Cs}_{1.52}[(\text{UO}_2)(\text{TiOH}_{0.48})(\text{PO}_4)_2] \cdot n\text{H}_2\text{O}$ (**UTiP**) and $\text{Cs}_{1.35}[(\text{UO}_2)(\text{GeOH}_{0.65})(\text{PO}_4)_2] \cdot n\text{H}_2\text{O}$ (**UGeP**) are closely related. This indicates that **UTiP** and **UGeP** are isostructural compounds. The variation in the *b* axis of the unit cell (7.1207 Å for **UTiP** and 6.8639 Å for **UGeP**) can be explained in the terms of ionic radii of Ti^{+4} (0.61 Å) and Ge^{+4} (0.39 Å) and, indeed, corresponds to the difference in the radii and average difference between Ti-O and Ge-O bond length (1.939 Å and 1.856 Å

respectively).

The structures of **UTiP** and **UGeP** are closely related to the structure of $\text{Cs}_4[(\text{UO}_2)_2(\text{GaOH})_2(\text{PO}_4)_4]\cdot\text{H}_2\text{O}$,²⁵ described in Chapter 3. In general, it is a framework structure, built out of perpendicularly intersecting one-dimensional uranyl phosphate and titanium or germanium phosphate chains. The channels, formed along the *c* axis, are filled with Cs^+ cations. The fundamental building unit of **UTiP** (or **UGeP**) is shown in Figure 5.1.

Uranyl phosphate chains of **UTiP** and **UGeP** extended in the *c* direction, and have the same topology as uranyl phosphate chains in the structures of $\text{Cs}_4[(\text{UO}_2)_2(\text{GaOH})_2(\text{PO}_4)_4]\cdot\text{H}_2\text{O}$ and $\text{Cs}[\text{UO}_2\text{Ga}(\text{PO}_4)_2]^{25}$. (Figure 5.2) These chains have been previously described as ${}^\infty_1[\text{UO}_2(\text{PO}_4)_2]^{4-25,70}$. They differ from $\text{Cs}_4[(\text{UO}_2)_2(\text{GaOH})_2(\text{PO}_4)_4]\cdot\text{H}_2\text{O}$, in that there are two crystallographically unique uranium centers. In **UTiP** and **UGeP** structures only one unique uranium is present, and therefore only one uranyl phosphate chain is formed. This phenomenon can also be secondarily confirmed by the unit cell comparison. In $\text{Cs}_4[(\text{UO}_2)_2(\text{GaOH})_2(\text{PO}_4)_4]\cdot\text{H}_2\text{O}$, the dimension of the unit cell axis, containing two crystallographically unique uranyl phosphate chains, is doubled compare to **UTiP** and **UGeP**.

The uranium center is connected to five phosphate oxygen atoms in the equatorial plane and two uranyl oxygen atoms, almost linearly with angles $178.7(4)^\circ$ and $177.1(7)^\circ$ for **UTiP** and **UGeP**, respectively, in the axial direction, to form a pentagonal bipyramid environment. The U-O distances in the equatorial plane are long and range between

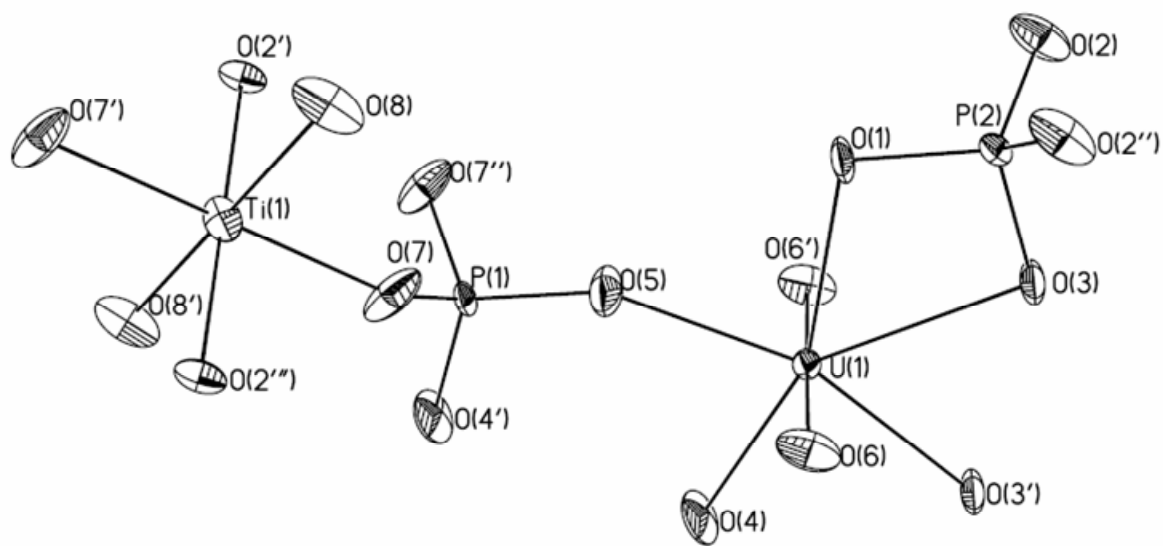


Figure 5.1. Thermal ellipsoid plot of $\text{Cs}_{1.52}[(\text{UO}_2)(\text{TiOH}_{0.48})(\text{PO}_4)_2] \cdot n\text{H}_2\text{O}$ (UTiP) shown at 50% probability.

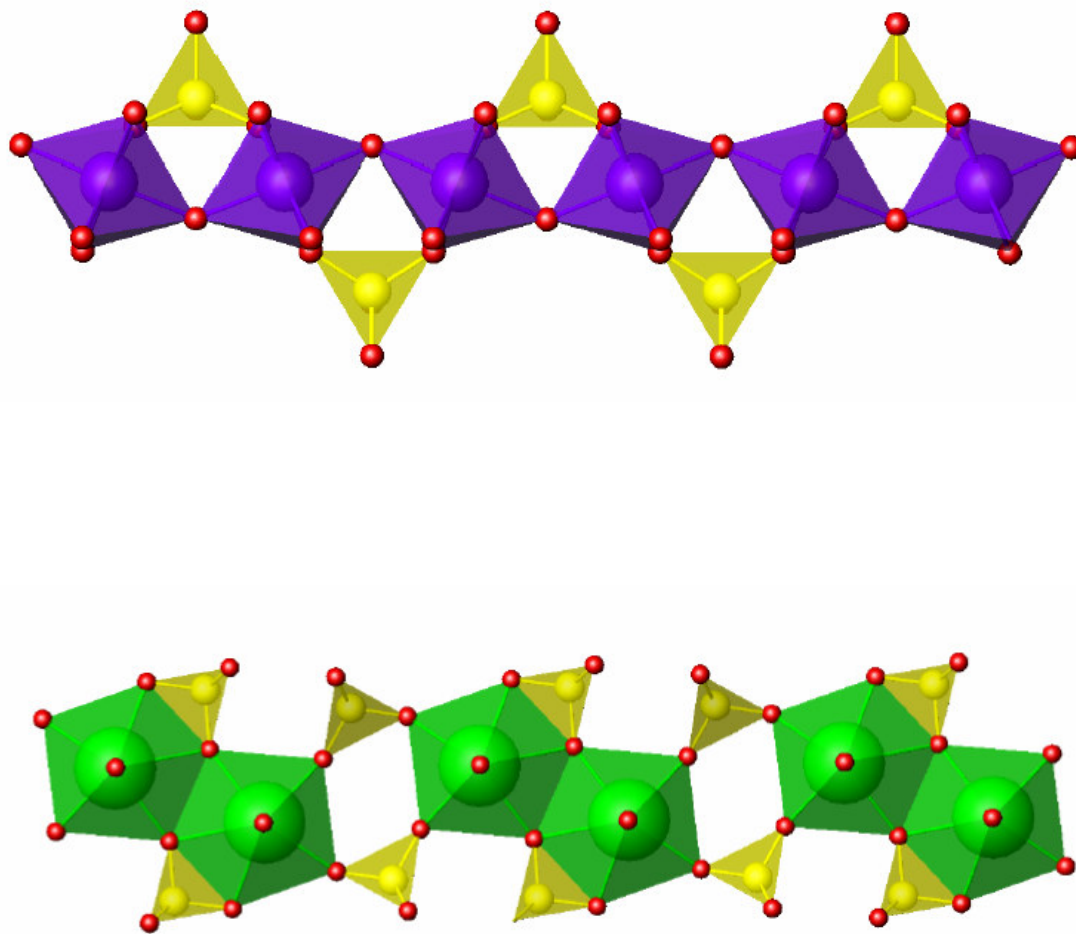


Figure 5.2 Depiction of one-dimensional titanium phosphate or germanium phosphate (top) and uranyl phosphate (bottom) chains in **UTiP** or **UGeP**. Violet - titanium or germanium polyhedra, yellow-phosphate tetrahedra, green-uranyl building units.

2.245(9) Å and 2.507(8) Å for **UTiP** and between 2.227(11) Å and 2.521(10) Å for **UGeP**, compared to the short uranyl distances of 1.773(6) Å for **UTiP** and 1.765(8) Å for **UGeP**. Two uranyl pentagonal bipyramids share edges to form dimers, connected to the chain by phosphate anions. The bond-valence sums, calculated according to these data, correspond to uranium in the +6 oxidation state.

Titanium and germanium phosphate chains $\infty[\text{Ti}(\text{OH}_{0.48})(\text{PO}_4)_2]^{2-}$ and $\infty[\text{Ge}(\text{OH}_{0.65})(\text{PO}_4)_2]^{2-}$, are also very similar to gallium phosphate chain in $\text{Cs}_4[(\text{UO}_2)_2(\text{GaOH})_2(\text{PO}_4)_4]\cdot\text{H}_2\text{O}$.²⁵ Titanium and germanium each form bonds with six oxygen atoms, four from phosphate anions and two from the neighbouring titanium or germanium unit, in octahedral environments. Due to the difference in the ionic size of Ti(IV) and Ge(IV), as well as the nature of the orbitals, participating in the bond formation, Ti-O and Ge-O distances are different. For Ti-O, the distances range from 1.926 Å to 1.960 Å, which is within the normal distance range for Ti in an octahedral environment. In the different Ge octahedra, Ge-O bonds vary from 1.77 Å to 2.06 Å, and again bond lengths in **UGeP** fit in this range. These distances are also much longer than Ge-O distances in the tetrahedra, where they can range between 1.70 Å and 1.79 Å. The bond-valence sums are consistent with Ti and Ge present in a +4 oxidation state. Selected bond distances and angles for **UTiP** and **UGeP** are summarized in Tables 5.4 and 5.5.

The intersection of the uranyl phosphate chains, extended in the *c* direction, and titanium or germanium phosphate chains, run along the *b* axis, giving rise to the tunnels filled with Cs^+ cations. (Figure 5.3) There are four strongly disordered atomic sites in the channels. According to the refinement of occupancy of these atomic sites, we suggest that

Table 5.4. Selected Bond Distances (Å) and Angles (°) for $\text{Cs}_{1.52}[(\text{UO}_2)(\text{TiOH}_{0.48})(\text{PO}_4)_2] \cdot n\text{H}_2\text{O}$ (**UTiP**)

Distances (Å)			
U(1)-O(6)	1.773(6)	Ti(1)-O(2)	1.960(6)
U(1)-O(4)	2.245(9)	P(1)-O(5)	1.490(9)
U(1)-O(5)	2.265(8)	P(1)-O(4)	1.508(9)
U(1)-O(3)	2.371(8)	P(1)-O(7)	1.545(6)
U(1)-O(1)	2.389(8)	P(2)-O(1)	1.511(6)
U(1)-O(3')	2.507(8)	P(2)-O(2)	1.528(8)
Ti(1)-O(8)	1.926(3)	P(2)-O(3)	1.555(8)
Ti(1)-O(7)	1.933(6)		
Angles (°)			
O(6)-U(1)-O(6')	178.7(4)	O(7)-Ti(1)-O(7')	180.00(15)
O(8)-Ti(1)-O(8')	180.0(5)	O(2)-Ti(1)-O(2')	180.000(2)

Table 5.5. Selected Bond Distances (Å) and Angles (°) for $\text{Cs}_{1.35}[(\text{UO}_2)(\text{GeOH}_{0.65})(\text{PO}_4)_2] \cdot n\text{H}_2\text{O}$ (**UGeP**)

Distances (Å)			
U(1)-O(6)	1.765(8)	Ge(1)-O(2)	1.853(7)
U(1)-O(4)	2.227(11)	P(1)-O(5)	1.497(10)
U(1)-O(5)	2.271(10)	P(1)-O(4)	1.505(12)
U(1)-O(3)	2.376(10)	P(1)-O(7)	1.531(8)
U(1)-O(1)	2.414(10)	P(2)-O(2)	1.512(8)
U(1)-O(3')	2.521(10)	P(2)-O(1)	1.504(10)
Ge(1)-O(8)	1.875(4)	P(2)-O(3)	1.538(11)
Ge(1)-O(7)	1.842(8)		
Angles (°)			
O(6)-U(1)-O(6')	177.1(7)	O(7)-Ge(1)-O(7')	180.0(3)
O(8)-Ge(1)-O(8')	180.000(1)	O(2)-Ge(1)-O(2')	180.000(2)

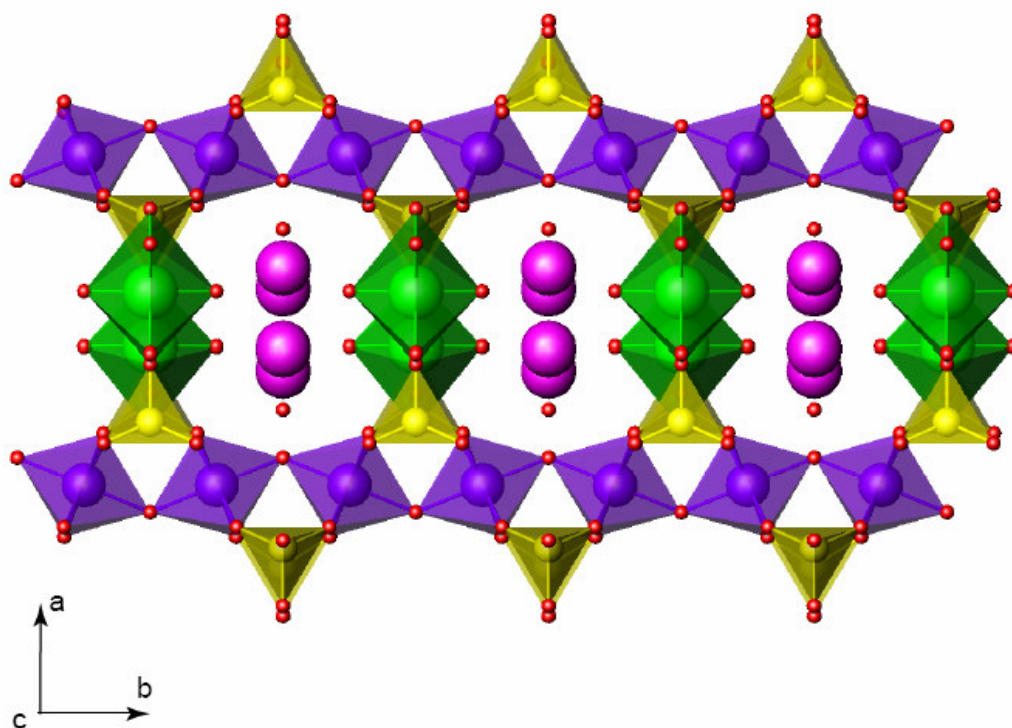


Figure 5.3. The framework of **UTiP** and **UGeP**. The channels along the *c* axis are filled with Cs^+ cations (purple) and water molecules (red). Violet octahedra represent Ti or Ge, yellow – phosphate, and green – uranium centers.

three partially occupied Cs^+ cations reside in the channels with Cs-O distances ranging from 3.029(8) Å to 3.6172(17) Å for **UTiP** and from 2.856(15) Å to 3.631(10) Å for **UGeP**. The fourth electron density peak is assigned to the partially occupied water molecule. It is 0.85 water molecules per unit cell for **UTiP** and 0.63 for **UGeP**. Due to the incompletely filled Cs positions, the overall structure has a positive charge deficiency. This can be balanced by protonation of the titanium phosphate or germanium phosphate backbone. The bond-valence sum for O(8) corresponds to 1.38 and 1.42 for **UTiP** and **UGeP**, respectively, which is consistent with the degree of protonation in these structures. This type of protonation is also found in aluminophosphate mineral tancoite, $\text{LiNa}_2\text{H}[\text{Al}(\text{PO}_4)_2(\text{OH})]$,^{71,72} $\text{Cs}_4[(\text{UO}_2)_2(\text{GaOH})_2(\text{PO}_4)_4]\cdot\text{H}_2\text{O}$ ²⁵ and large number of aluminum, gallium, and transition metal phosphates.⁷³⁻⁸⁰ It is important to note that in $\text{Cs}_4[(\text{UO}_2)_2(\text{GaOH})_2(\text{PO}_4)_4]\cdot\text{H}_2\text{O}$ ²⁵ and $\text{LiNa}_2\text{H}[\text{Al}(\text{PO}_4)_2(\text{OH})]$,^{71,72} protons are assigned to stabilize the structure with Ga and Al in oxidation state +3, but in the case of **UTiP** and **UGeP**, the proton's role is restricted only to equilibrate the Cs^+ cations deficiency.

CONCLUSIONS

In this chapter we have described two novel isostructural uranium-containing framework compounds incorporating Ti or Ge polyhedra. According to the structural characterization, we can imply that these compounds can have promising ion-exchange and conductivity properties due to the presence of highly disordered cationic sites. For further investigations, more detailed analysis of the Cs and water content, as well as knowledge about physical properties of structure are necessary. We are currently

investigating the methods for the synthesis of **UTiP** and **UGeP** with higher yields that will allow us to conduct detailed studies of the compounds.

REFERENCES

1. Chetham, A. K.; Ferey, G.; Loiseau, T. *Angew. Chem., Int. Ed. Engl.* **1999**, 38, 3268.
2. Li, Y.; Cahill, C. L.; Burns, P. *Chem. Mater.* **2001**, 13, 4026.
3. Halasyamani, P. S.; Walker, S. M.; O'Hare, D. *J. Amer. Chem. Soc.* **1999**, 121, 7415.
4. Doran, M.; Walker, S. M.; O'Hare, D. *Chem. Commun. (Cambridge)* **2001**, 19, 1988.
5. Locock, A. J.; Burns, P. C. *J. Solid State Chem.* **2002**, 163, 275.
6. Locock, A. J.; Burns, P. C. *J. Solid State Chem.* **2002**, 167, 226.
7. Locock, A. J.; Burns, P. C. *J. Solid State Chem.* **2003**, 175, 372.
8. Locock, A. J.; Burns, P. C. *J. Solid State Chem.* **2003**, 176, 18.
9. Burns, P. C.; Alexopoulos, C. M.; Hotchkiss, P. J.; Locock, A. J. *Inorg. Chem.* **2004**, 43, 1816.
10. Locock, A. J.; Burns, P. C. *J. Solid State Chem.* **2004**, 177, 2675.
11. Doran, M.; Norquist, A. J.; O'Hare, D. *Chem. Commun. (Cambridge)* **2002**, 24, 2946.
12. Li, Y.; Burns, P. C. *J. Nucl. Materials* **2001**, 299, 219.
13. Wang, X.; Huang, J.; Liu, L.; Jacobson, A. J. *J. Mater. Chem.* **2002**, 12, 406.
14. Wang, X.; Huang, J.; Jacobson, A. J. *J. Amer. Chem. Soc.* **2002**, 124, 15190.
15. Huang, J.; Wang, X.; Jacobson, A. J. *J. Mater. Chem.* **2003**, 13, 19115.
16. Chen, C.-S.; Kao, H.-M.; Lii, K.-H. *Inorg. Chem.* **2005**, 44, 935.
17. Chen, C.-S.; Chiang, R.-K.; Kao, H.-M.; Lii, K.-H. *Inorg. Chem.* **2005**, 44, 3914.
18. Obbade, S.; Dion, C.; Rivenet, M.; Saadi, M.; Abraham, F. *J. Solid State Chem.* **2004**, 177, 2058.

19. Obbade, S.; Dion, C.; Saadi, M.; Yagoubi, S.; Abraham, F. *J. Solid State Chem.* **2004**, *177*, 3909.
20. Obbade, S.; Yagoubi, S.; Dion, C.; Saadi, M.; Abraham, F. *J. Solid State Chem.* **2004**, *177*, 1681.
21. Krivovichev, S. V.; Burns, P. C.; Armbruster, Th.; Nazarchuk, E. V.; Depmeier, W. *Micropor. Mesopor. Mater.* **2005**, *78*, 217.
22. Krivovichev, S. V.; Cahill, C. L.; Nazarchuk, E. V.; Burns, P. C.; Armbruster, Th.; Depmeier, W. *Micropor. Mesopor. Mater.* **2005**, *78*, 209.
23. Krivovichev, S. V.; Cahill, C. L.; Burns, P. C. *Inorg. Chem.* **2003**, *42*, 2459.
24. Krivovichev, S. V.; Armbruster, Th.; Chernorukov, D. Yu.; Burns, P. C.; Nazarchuk, E. V.; Depmeier, W. *Micropor. Mesopor. Mater.* **2005**, *78*, 225.
25. Shvareva, T. Y.; Sullens, T. A.; Shehee, T. C.; Albrecht-Schmitt, T. E. *Inorg. Chem.* **2005**, *44*, 300.
26. Shvareva, T. Y.; Beitz, J. V.; Duin, E.C.; Albrecht-Schmitt, T. E. *Chem. Mater.* **2005**, *17*, 6219.
27. Shvareva, T. Y.; Albrecht-Schmitt, T. E. *Inorg. Chem.* **2005**, *45*, 1900.
28. Sykora, R. E.; Albrecht-Schmitt, T. E. *Inorg. Chem.* **2003**, *42*, 2179.
29. Burns, P. C.; Miller, M. L.; Ewing, R. C. *Can. Mineral.* **1996**, *34*, 845.
30. Burns, P. C. *Can. Mineral.* **2005**, *43*, 1839.
31. Kuznicki, S. M.; Thrush, K. A.; Allen, F. M.; Levine, S. M.; Hamil, M. M.; Hayhurst, D. T.; Mansour, M. *Synth. Microporous Mater.* **1992**, *1*, 427.
32. Clearfield, A. *Solid State Sci.* **2001**, *3*, 103.
33. Ekambaram, S.; Sevov, S. C. *Angew. Chem., Int. Ed. Engl.* **1999**, *38*, 372.

34. Ekambaram, S.; Serre, C.; Ferey, G.; Sevov, S. C. *Chem. Mater.* **2000**, *12*, 444.
35. Chippindale, A. M.; Grimshaw, M. R.; Powell, A. V.; Cowley, A. R. *Inorg. Chem.* **2005**, *44*, 4121.
36. Dickens, P. G.; Flynn, G. J.; Patat, S.; Stüttgen, G. P. *J. Mater. Chem.* **1997**, *7*, 537
37. Burns, P. C. *Rev. Mineral.* **1999**, *38*, 23.
38. Ringwood, A. E.; Kesson, S. E.; Ware, N. G.; Hibberson, W. ; Major, A. *Nature (London)*, **1979**, 278, 219.
39. Szymanski, J. T.; Scott, J. D. *Can. Mineral.* **1982**, *20*, 271.
40. Vance, E. R.; Watson, J.N.; Carter, M.L.; Day, R.A., Begg, B.D.; *J. Am. Ceram. Soc.* **2001**, *84*, 141.
41. James, M.; Watson, J. N. *J. Solid State Chem.* **2002**, *165*, 261.
42. James, M.; Carter, M. L.; Watson, J. N. *J. Solid State Chem.* **2003**, *174*, 329.
43. Wells, A. F. *Structural Inorganic Chemistry*, 5th ed., Oxford, 1984, p 1173.
44. Li, H.; Yaghi, O. M. *J. Am. Chem. Soc.* **1998**, *120*, 10569.
45. Conradsson, T. M.; Dadachov, S.; Zou, X. *Micropor. Mesopor. Mater.* **2000**, *41*, 183.
46. Cascales, C.; Gutierrez-Puebla, E.; Iglesia, M.; Monge, M.A.; Ruiz-Valero, C.; Snejko, N. *Chem. Commun. (Cambridge)* **2000**, 56, 1092.
47. Cascales, C.; Gomez-Lor, B.; Gutierrez-Puebla, E.; Iglesia, M.; Monge, M. A.; Ruiz-Valero, C.; Snejko, N. *Chem. Mater.* **2002**, *14*, 677.
48. Cascales, C.; Gutierrez-Puebla, E.; Monge, M.A.; Ruiz-Valero, C. *Angew. Chem. , Int. Ed. Engl.* **1998**, *37*, 129.
49. Cascales, C.; Gutierrez-Puebla, E.; Iglesia, M.; Monge, M. A.; Ruiz-Valero, C. *Angew. Chem., Int. Ed. Engl.* **1999**, *38*, 2436.

50. Feng, P. Y.; Bu, X. H.; Stucky, G. D. *Chem. Mater.* **1999**, *11*, 3025.
51. Li, H. L.; Eddaoudi, M.; Yaghi, O. M. *Angew. Chem., Int. Ed. Engl.* **1999**, *38*, 653.
52. Plévert, J.; Gentz, T. M.; Laine, A.; Li, H. L.; Young, V. G.; Yaghi, O. M.; O'Keefe, M. *J. Am. Chem. Soc.* **2001**, *123*, 12706.
53. Plévert, J.; Gentz, T. M.; Groy, T. L.; O'Keefe, M.; Yaghi, O. M. *Chem. Mater.* **2003**, *15*, 714.
54. Zhou, Y.; Zhu, H.; Chen, Z.; Chen, M.; Xu, Y.; Zhang, H.; Zhao, D. *Angew. Chem., Int. Ed. Engl.* **2001**, *40*, 2166.
55. Xu, Y.; Ogura, M.; Okubo, T. *Micropor. Mesopor. Mater.* **2004**, *70*, 1.
56. Snejko, N.; Medina, M. E.; Gutierrez-Puebla, E.; Monge, M. A. *Inorg. Chem.* **2006**, *45*, 1591.
57. Lin, Z.-E.; Zhang, J.; Zheng, S.-T.; Yang, G.-Y. *Micropor. Mesopor. Mater.* **2004**, *74*, 205.
58. Medina, M.E.; Iglesias, M.; Snejko, N.; Gutierrez-Puebla, E.; Monge, M. A. *Chem. Mater.* **2004**, *16*, 594.
59. Bu, X.; Feng, P.; Gier, T. E.; Zhao, D.; Stucky, G. D. *J. Am. Chem. Soc.* **1998**, *120*, 13389.
60. Lin, Z.-E.; Zhang, J.; Yang, G.-Y. *Inorg. Chem.* **2003**, *42*, 1797.
61. Zhang, H.-X.; Zhang, J.; Zheng, S.-T.; Yang, G.-Y. *Inorg. Chem.* **2003**, *42*, 6595.
62. Lin, Z.-E.; Zhang, J.; Zhao, J.-T.; Zheng, S.-T.; Pan, C.-Y.; Wang, G.-M.; Yang, G.-Y. *Angew. Chem., Int. Ed. Engl.* **2005**, *44*, 6884.
63. Legros, J. P.; Jeannin, Y. *Acta Crystallogr.* **1975**, *B31*, 1133.
64. Legros, J. P.; Jeannin, Y. *Acta Crystallogr.* **1975**, *B31*, 1140.

65. Sheldrick, G. M. SHELXTL PC, Version 6.12, An Integrated System for Solving, Refining, and Displaying Crystal Structures from Diffraction Data; Siemens Analytical X-Ray Instruments, Inc.: Madison, WI 2001.
66. Sheldrick, G. M. *SADABS* 2001, Program for absorption correction using SMART CCD based on the method of Blessing; Blessing, R. H. *Acta Cryst.* **1995**, *A51*, 33.
67. Grohol, D.; Nocera, D. G. *J. Am. Chem. Soc.* **2002**, *124*, 2641
68. Almond, P. M.; Peper, S. M.; Bakker, E.; Albrecht-Schmitt, T. E. *J. Solid State Chem.* **2002**, *168*, 358.
69. Ramik, R. A.; Sturman, B. D.; Dunn, P. J.; Povarennykh, A. S. *Can. Mineral.* **1980**, *18*, 185.
70. Hawthorne, F. C. *Tsch. Mineral. Petro. Mitt.* **1983**, *31*, 121.
71. Lin, H.-M.; Lii, K.-H. *Inorg. Chem.* **1998**, *37*, 4220.
72. Attfield, M. P.; Morris, R. E.; Burshtein, I.; Campana, C. F.; Cheetham, A. K. *J. Solid State Chem.* **1995**, *118*, 412.
73. Cavellec, M.; Riou, D.; Greneche, J.-M.; Férey, G. *Inorg. Chem.* **1997**, *36*, 2187.
74. Lethbridge, Z. A. D.; Lightfoot, P.; Morris, R. E.; Wragg, D. S.; Wright, P. A.; Kvick, A.; Vaughan, G. J. *Solid State Chem.* **1999**, *142*, 455.
75. Walton, R. I.; Millange, F.; O'Hare D.; Paulet, C.; Loiseau, T.; Férey, G. *Chem. Mater.* **2000**, *12*, 1977.
76. Mahesh, S.; Green, M. A.; Natarajan, S. *J. Solid State Chem.* **2002**, *165*, 334.
77. Mandal, S.; Green, M. A.; Natarajan, S. *J. Solid State Chem.* **2004**, *177*, 1117.
78. Harvey, H. G.; Teat, S. J.; Tang, C. C.; Cranswick, L. M.; Attfield, M. P. *Inorg. Chem.* **2003**, *42*, 2428.

CHAPTER 6

GENERAL ROUTE TO THREE-DIMENSIONAL FRAMEWORK URANYL TRANSITION METAL PHOSPHATES WITH ATYPICAL STRUCTURAL MOTIFS: THE CASE EXAMPLES OF $\text{Cs}_2\{(\text{UO}_2)_4[\text{Co}(\text{H}_2\text{O})_2]_2(\text{HPO}_4)(\text{PO}_4)_4\}$, $\text{Cs}_2\{(\text{UO}_2)_4[\text{Ni}(\text{H}_2\text{O})_2]_2(\text{HPO}_4)(\text{PO}_4)_4\}$ AND $\text{Cs}_{3+x}[(\text{UO}_2)_3\text{CuH}_{4-x}(\text{PO}_4)_5]\cdot\text{H}_2\text{O}$

ABSTRACT

The reaction of $\text{UO}_2(\text{NO}_3)_2\cdot 6\text{H}_2\text{O}$ with Co, Ni, or Cu metal, phosphoric acid, and CsCl under mild hydrothermal conditions results in the formation of $\text{Cs}_2\{(\text{UO}_2)_4[\text{Co}(\text{H}_2\text{O})_2]_2(\text{HPO}_4)(\text{PO}_4)_4\}$ (**UCoP**), $\text{Cs}_2\{(\text{UO}_2)_4[\text{Ni}(\text{H}_2\text{O})_2]_2(\text{HPO}_4)(\text{PO}_4)_4\}$ (**UNiP**) or $\text{Cs}_{3+x}[(\text{UO}_2)_3\text{CuH}_{4-x}(\text{PO}_4)_5]\cdot\text{H}_2\text{O}$ (**UCuP**). **UCoP** and **UNiP** are isostructural compounds. Their structures contain uranium atoms in pentagonal bipyramidal and hexagonal bipyramidal environments. The interaction of the uranyl cations and phosphate anions creates layers in the $[ab]$ plane. The uranyl phosphate layers are joined together by octahedral Co or Ni centers wherein the Co and Ni are bound by phosphate and two cis water molecules. In addition, the Co and Ni ions are also ligated by a uranyl oxo atom. The presence of these octahedral building units stitches the structure together into a three-dimensional framework where void spaces are filled by Cs^+ cations.

The structure of **UCuP** contains uranium centers in UO_6 tetragonal bipyramidal and UO_7 pentagonal bipyramidal geometries. The uranyl moieties are bridged by

phosphate anions into sinusoidal sheets that extend into the $[bc]$ plane and are linked into a three-dimensional structure by Cu^{II} . The Cu centers reside in square planar environments. Charge balance is maintained by Cs^+ cations. Both the structure types and the uranyl phosphate layers in **UCoP**, **UNiP**, and **UCuP** are novel.

INTRODUCTION

The structural chemistry of U^{VI} is dominated by the formation of layered compounds containing uranyl, UO_2^{2+} , cations wherein the uranyl units are aligned in a roughly parallel fashion.^{1,2} These layered compounds have been shown to display several important and potentially useful properties including fast proton conductivity and ion exchange that is particularly well-known for uranyl phosphates.³⁻⁸ More recently, attention has been focused on preparing uranyl phases that adopt three-dimensional networks that may find applications in the storage of key radionuclides from spent nuclear fuel and as new selective ion-exchange materials.⁹ One of the most appealing features of constructing new solids from uranyl-containing polyhedra is that the uranium centers in these compounds can adopt coordination environments seldom seen in transition metal chemistry such as UO_7 pentagonal bipyramids and UO_8 hexagonal bipyramids.^{1,2}

In previous chapters we have reported the syntheses and structures of the first uranyl gallium,⁹ vanadium,¹⁰ titanium and germanium phosphates with open-framework structures. As we demonstrated, **UGaP1**, **UGaP2**, and **KUV^{IV}P** (**RbUV^{IV}P**) have ion-exchange properties. Herein we have devoted our research to preparing additional first row transition metal uranyl phosphates where the gallium, germanium, vanadium, or

titanium centers have been replaced by other transition metals, which may, in turn, lead to new architectures, and, therefore, to properties, not previously found. We also report a relatively general and quite facile route to preparing first row transition metal uranyl phosphates with three-dimensional structures with varying degrees of openness. We illustrate this with the examples of the Co^{II} , Ni^{II} , and Cu^{II} compounds, $\text{Cs}_2\{(\text{UO}_2)_4[\text{Co}(\text{H}_2\text{O})_2]_2(\text{HPO}_4)(\text{PO}_4)_4\}$ (**UCoP**), $\text{Cs}_2\{(\text{UO}_2)_4[\text{Ni}(\text{H}_2\text{O})_2]_2(\text{HPO}_4)(\text{PO}_4)_4\}$ (**UNiP**) or $\text{Cs}_{3+x}\{[(\text{UO}_2)_3\text{-CuH}_{4-x}(\text{PO}_4)_5]\cdot\text{H}_2\text{O}\}$ (**UCuP**), all three of which display new methods of constructing three-dimensional uranyl-containing frameworks.¹¹⁻²²

EXPERIMENTAL

Syntheses. $\text{UO}_2(\text{NO}_3)_2\cdot 6\text{H}_2\text{O}$ (98%, Alfa-Aesar), Co powder (99.99%, Sigma Aldrich), Ni powder (99.99%, Sigma Aldrich), Cu powder (99.99%, Sigma Aldrich), H_3PO_4 (98%, Aldrich), and CsCl (99.9%, Cerac) were used as received. Co, Ni, and Cu powders were weighed separately under the inert atmosphere due to their potential rapid oxidation in the air. The PTFE liners were used for all reactions. *While the UO_3 contains depleted U, standard precautions for handling radioactive materials should be followed. Old sources of depleted U should not be used, as the daughter elements of natural decay are highly radioactive and present serious health risks.*

$\text{Cs}_2\{(\text{UO}_2)_4[\text{Co}(\text{H}_2\text{O})_2]_2(\text{HPO}_4)(\text{PO}_4)_4\}$ (UCoP). $\text{UO}_2(\text{NO}_3)_2\cdot 6\text{H}_2\text{O}$ (0.285 g, 0.568 mmol), Co powder (0.067 g, 1.1 mmol), H_3PO_4 (0.167 g, 1.72 mmol), CsCl (0.479 g, 2.85 mmol), and 1.5 mL of Millipore-filtered water were loaded into a 23-mL autoclave. The reaction was run at 195 °C in a box furnace for 7 days and then cooled at a rate of 9 °C/h to room temperature. The product mixture contained bright-orange crystals

of **UCoP** and water-soluble blue crystals of cesium tetrachlorocobalt(II). The desired product was isolated by washing the mixture with water and methanol. Yield: 0.286 mg (100% based on U).

Cs₂{(UO₂)₄[Ni(H₂O)₂]₂(HPO₄)(PO₄)₄} (**UNiP**). UO₂(NO₃)₂·6H₂O (0.286 g, 0.57 mmol), Ni powder (0.067 g, 1.1 mmol), H₃PO₄ (0.167 g, 1.72 mmol) and CsCl (0.479 g, 2.85 mmol), were mixed together in a 23-mL autoclave and followed by addition of 1.5 mL of Millipore-filtered water. The reaction was run at 195 °C in a box furnace for 5 days and then slowly cooled to room temperature with average rate 3°C/hour. The product mixture contained precipitate of greenish-yellow plates of **UNiP** and bright green mother liquid. **UNiP** precipitate was washed with water, methanol and dried by air. Yield: 285 mg (82.4 % based on U).

Cs_{3+x}[(UO₂)₃CuH_{4-x}(PO₄)₅]·H₂O (**UCuP**). UO₂(NO₃)₂·6H₂O (0.285 g, 0.567 mmol), Cu powder (0.072 g, 1.1 mmol), H₃PO₄ (0.167 g, 1.72 mmol) and CsCl (0.477 g, 2.85 mmol), were mixed together in a 23-mL autoclave followed by addition of 1.5 mL of Millipore-filtered water. The reaction was run at 220 °C in a box furnace for 7 days and then cooled at a rate of 9 °C/h to room temperature. Due to the large size of the crystals, green **UCuP** product was easily separated from the product mixture, that also included also crystals of cesium tetrachlorocopper and cesium uranyl pyrophosphate. Yield: 330 mg (97.6 % based on U).

X-ray structural analysis. Crystals of **UCoP**, **UNiP**, and **UCuP** were mounted on glass fibers and aligned on a Bruker SMART APEX CCD X-ray diffractometer. Intensity measurements were performed using graphite monochromated Mo K α radiation from a sealed tube and monocapillary collimator. SMART (v 5.624) was used for

preliminary determination of the cell constants and data collection control. The intensities of reflections of a sphere were collected by a combination of 3 sets of exposures (frames). Each set had a different ϕ angle for the crystal and each exposure covered a range of 0.3° in ω . A total of 1800 frames were collected with an exposure time per frame of 30 s for the crystals of **UCoP**, **UNiP**, and **UCuP**.

Determination of integrated intensities and global refinement were performed with the Bruker SAINT (v 6.02) software package using a narrow-frame integration algorithm. A face-indexed analytical absorption correction was initially applied using XPREP, where individual shells of unmerged data were corrected analytically.²³ These files were subsequently treated with a semiempirical absorption correction by SADABS.²⁴ The program suite SHELXTL (v 6.12) was used for space group determination (XPREP), direct methods structure solution (XS), and least-squares refinement (XL).²³ The final refinements included anisotropic displacement parameters for all atoms. Secondary extinction was not noted for either crystal. Crystallographic details are given in Table 6.1. Atomic coordinates, equivalent isotropic displacement parameters, symmetry and occupancy for **UCoP**, **UNiP**, and **UCuP** are given in Tables 6.2, 6.3, and 6.4 respectively.

Thermal analysis. The data were collected using differential scanning calorimeter TA Instrument, model 2920. The samples of known mass encapsulated in the aluminum container, was heated under nitrogen atmosphere from 30 °C to 600 °C with heating rate of 10°C /minute.

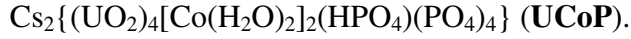
Table 6.1. Crystallographic Data for $\text{Cs}_2\{(\text{UO}_2)_4[\text{Co}(\text{H}_2\text{O})_2]_2(\text{HPO}_4)(\text{PO}_4)_4\}$ (**UCoP**), $\text{Cs}_2\{(\text{UO}_2)_4[\text{Ni}(\text{H}_2\text{O})_2]_2(\text{HPO}_4)(\text{PO}_4)_4\}$ (**UNiP**) and $\text{Cs}_{3+x}[(\text{UO}_2)_3\text{CuH}_{4-x}(\text{PO}_4)_5]\cdot\text{H}_2\text{O}$

(UCuP).

Compound	UCoP	UNiP	UCuP
Formula Mass	2003.65	2003.21	1788.35
Color and habit	orange plate	yellow-green	green plate
Crystal System	monoclinic	monoclinic	orthorhombic
Space group	<i>C2/c</i> (No.15)	<i>C2/c</i> (No.15)	<i>Pbcm</i> (No. 57)
<i>a</i> (Å)	18.0551(8)	18.0443(13)	7.5867(4)
<i>b</i> (Å)	10.7478(5)	10.7375(8)	19.9574(10)
<i>c</i> (Å)	15.3504(7)	15.2268(11)	17.9726(9)
β °, C	99.2420(10)	99.1520(10)	90
<i>V</i> (Å ³)	2940.1(2)	2912.6(4)	2721.2(2)
<i>Z</i>	4	4	4
<i>T</i> (K)	193	193	193
λ (Å)	0.71073	0.71073	0.71073
Maximum 2 θ (deg.)	56.56	56.58	56.58
ρ_{calcd} (g cm ⁻³)	4.524	4.595	4.348
$\mu(\text{Mo } K\alpha)$ (cm ⁻¹)	258.86	262.82	231.04
$R(F)$ for $F_o^2 > \sigma(F_o^2)$	0.0281	0.0319	0.0354
$R_w(F_o^2)^b$	0.0692	0.0709	0.0835

$$^a R(F) = \sum \|F_o\| - \|F_c\| / \sum \|F_o\|. \quad ^b R_w(F_o^2) = \left[\sum \left[w(F_o^2 - F_c^2)^2 \right] / \sum wF_o^4 \right]^{1/2}.$$

Table 6.2. Atomic Coordinates and Equivalent Isotropic Displacement Parameters for



Atom	Symmetry ^a	x	y	z	U_{eq} (\AA^2) ^b	Occup.
U(1)	4 <i>e</i> 2	0	-0.28631(3)	$\frac{1}{4}$	0.00974(9)	1
U(2)	4 <i>e</i> 2	0	0.09385(3)	$\frac{1}{4}$	0.00892(9)	1
U(3)	8 <i>f</i> 1	0.20409(1)	0.28203(2)	0.29034(2)	0.00778(7)	1
Co(1)	8 <i>f</i> 1	0.21057(5)	0.33986(9)	0.05694(6)	0.01051(19)	1
P(1)	8 <i>f</i> 1	0.0001(2)	0.3800(3)	0.2841(3)	0.0104(7)	0.50
P(2)	8 <i>f</i> 1	0.34785(10)	0.44837(16)	0.20623(12)	0.0085(3)	1
P(3)	8 <i>f</i> 1	0.31032(10)	0.10909(16)	0.15358(12)	0.0079(3)	1
O(1)	4 <i>e</i> 2	0	0.4966(8)	$\frac{1}{4}$	0.069(4)	1
O(2)	8 <i>f</i> 1	-0.0192(6)	0.4143(9)	0.3795(7)	0.012(2)	0.50
O(3)	8 <i>f</i> 1	0.0647(3)	0.2934(5)	0.2844(6)	0.045(2)	1
O(4)	8 <i>f</i> 1	0.4309(3)	0.4041(4)	0.2155(3)	0.0102(10)	1
O(5)	8 <i>f</i> 1	0.3640(3)	0.5903(4)	0.2212(3)	0.0096(10)	1
O(6)	8 <i>f</i> 1	0.3115(3)	0.3939(4)	0.2801(3)	0.0091(10)	1
O(7)	8 <i>f</i> 1	0.3057(3)	0.4264(5)	0.1153(3)	0.0125(10)	1
O(8)	8 <i>f</i> 1	0.2775(3)	0.1403(5)	0.2362(3)	0.0113(10)	1
O(9)	8 <i>f</i> 1	0.3140(3)	-0.0325(4)	0.1410(3)	0.0111(10)	1
O(10)	8 <i>f</i> 1	0.2604(3)	0.1628(5)	0.0701(3)	0.0102(10)	1
O(11)	8 <i>f</i> 1	0.3897(3)	0.1638(5)	0.1593(3)	0.0118(10)	1
O(12)	8 <i>f</i> 1	0.0407(3)	-0.2874(6)	0.1515(4)	0.0260(14)	1
O(13)	8 <i>f</i> 1	0.1595(3)	0.5213(5)	0.0361(4)	0.0232(13)	1
O(14)	8 <i>f</i> 1	0.1051(3)	0.2584(5)	0.0071(3)	0.0164(11)	1
O(15)	8 <i>f</i> 1	0.2387(3)	0.2303(5)	0.3998(3)	0.0129(10)	1
O(16)	8 <i>f</i> 1	0.1722(3)	0.3329(5)	0.1793(3)	0.0141(10)	1
O(17)	8 <i>f</i> 1	0.0092(3)	0.0926(5)	0.1371(4)	0.0160(11)	1

Cs(1)	8 <i>f</i> 1	0.37456(3)	0.44843(6)	0.47121(3)	0.02451(13)	1
-------	--------------	------------	------------	------------	-------------	---

^a Symmetry describes multiplicity, Wyckoff parameter and symmetry of the atomic site.

^b U_{eq} is defined as one-third of the trace of the orthogonalized \mathbf{U}_{ij} tensor.

Table 6.3. Atomic Coordinates and Equivalent Isotropic Displacement Parameters for $\text{Cs}_2\{(\text{UO}_2)_4[\text{Ni}(\text{H}_2\text{O})_2]_2(\text{HPO}_4)(\text{PO}_4)_4\}$ (**UNiP**).

Atom	Symmetry ^a	<i>x</i>	<i>y</i>	<i>z</i>	$U_{\text{eq}} (\text{\AA}^2)^b$	occup.
U(1)	4 <i>e</i> 2	0	-0.28780(4)	¼	0.01120(11)	1
U(2)	4 <i>e</i> 2	0	0.09224(4)	¼	0.00986(11)	1
U(3)	8 <i>f</i> 1	0.20419(2)	0.28060(3)	0.29040(2)	0.00887(9)	1
Ni(1)	8 <i>f</i> 1	0.21041(6)	0.33766(10)	0.05657(7)	0.0109(2)	1
P(1)	8 <i>f</i> 1	0.0001(2)	0.3792(4)	0.2849(3)	0.0130(9)	0.50
P(2)	8 <i>f</i> 1	0.34763(12)	0.4467(2)	0.20535(15)	0.0094(4)	1
P(3)	8 <i>f</i> 1	0.31001(12)	0.1083(2)	0.15224(15)	0.0093(4)	1
O(1)	4 <i>e</i> 2	0	0.4951(11)	¼	0.062(4)	1
O(2)	8 <i>f</i> 1	-0.0180(7)	0.4136(10)	0.3857(11)	0.026(3)	0.50
O(3)	8 <i>f</i> 1	0.0647(4)	0.2910(6)	0.2841(7)	0.044(3)	1
O(4)	8 <i>f</i> 1	0.4311(3)	0.4027(5)	0.2147(4)	0.0115(12)	1
O(5)	8 <i>f</i> 1	0.3642(3)	0.5885(5)	0.2204(4)	0.0123(13)	1
O(6)	8 <i>f</i> 1	0.3121(3)	0.3919(5)	0.2799(4)	0.0113(12)	1
O(7)	8 <i>f</i> 1	0.3053(3)	0.4240(5)	0.1136(4)	0.0139(13)	1
O(8)	8 <i>f</i> 1	0.2771(3)	0.1380(5)	0.2358(4)	0.0133(13)	1
O(9)	8 <i>f</i> 1	0.3143(3)	-0.0340(5)	0.1390(4)	0.0112(12)	1
O(10)	8 <i>f</i> 1	0.2600(3)	0.1629(5)	0.0691(4)	0.0104(12)	1
O(11)	8 <i>f</i> 1	0.3894(3)	0.1632(5)	0.1582(4)	0.0119(12)	1
O(12)	8 <i>f</i> 1	0.0405(4)	-0.2884(7)	0.1508(4)	0.0247(16)	1
O(13)	8 <i>f</i> 1	0.1591(3)	0.5150(6)	0.0383(4)	0.0185(14)	1
O(14)	8 <i>f</i> 1	0.1075(3)	0.2553(6)	0.0084(4)	0.0159(14)	1
O(15)	8 <i>f</i> 1	0.2389(3)	0.2285(5)	0.4004(4)	0.0155(13)	1
O(16)	8 <i>f</i> 1	0.1732(3)	0.3316(6)	0.1779(4)	0.0151(13)	1

O(17)	8 <i>f</i> 1	0.0102(3)	0.0921(6)	0.1360(4)	0.0165(14)	1
Cs(1)	8 <i>f</i> 1	0.37476(3)	0.44631(6)	0.47172(4)	0.02446(15)	1

^a Symmetry describes multiplicity, Wyckoff parameter and symmetry of the atomic site.

^b U_{eq} is defined as one-third of the trace of the orthogonalized U_{ij} tensor.

Table 6.4. Atomic Coordinates and Equivalent Isotropic Displacement Parameters for $\text{Cs}_{3+x}[(\text{UO}_2)_3\text{CuH}_{4x}(\text{PO}_4)_5]\cdot\text{H}_2\text{O}$ (**UCuP**).

Atom	Symmetry ^a	<i>x</i>	<i>y</i>	<i>z</i>	$U_{\text{eq}}(\text{\AA}^2)^b$	Occup.
U(1)	4 <i>d</i> $\bar{2}m$	-0.50309(5)	0.39763(2)	$\frac{3}{4}$	0.01050(10)	1
U(2)	8 <i>e</i> 1	0.21145(4)	0.65898(1)	0.55377(2)	0.00997(9)	1
Cu(1)	4 <i>d</i> $\bar{2}m$	0.00099(18)	0.40714(6)	$\frac{3}{4}$	0.0115(3)	1
P(1)	4 <i>d</i> $\bar{2}m$	0.1054(4)	0.66578(14)	$\frac{3}{4}$	0.0140(6)	1
P(2)	8 <i>e</i> 1	0.2132(3)	0.48119(10)	0.62264(11)	0.0132(4)	1
P(3)	8 <i>e</i> 1	0.2080(3)	0.66171(10)	0.38077(11)	0.0121(4)	1
O(1)	4 <i>d</i> $\bar{2}m$	-0.0435(13)	0.7196(4)	$\frac{3}{4}$	0.038(3)	1
O(2)	8 <i>e</i> 1	0.2183(8)	0.6708(3)	0.6816(3)	0.0227(14)	1
O(3)	4 <i>d</i> $\bar{2}m$	-0.0119(10)	0.6016(4)	$\frac{3}{4}$	0.0195(18)	1
O(4)	8 <i>e</i> 1	0.3853(8)	0.4639(3)	0.6600(4)	0.0293(16)	1
O(5)	8 <i>e</i> 1	0.1881(15)	0.4311(4)	0.5578(4)	0.069(3)	1
O(6)	8 <i>e</i> 1	0.0592(9)	0.4756(3)	0.6755(4)	0.0366(18)	1
O(7)	8 <i>e</i> 1	0.2257(9)	0.5501(3)	0.5885(4)	0.0258(14)	1
O(8)	8 <i>e</i> 1	0.1900(7)	0.7231(3)	0.4337(3)	0.0142(12)	1
O(9)	8 <i>e</i> 1	0.3862(7)	0.6660(3)	0.3397(3)	0.0159(12)	1
O(10)	8 <i>e</i> 1	0.0542(8)	0.6601(3)	0.3261(3)	0.0182(12)	1
O(11)	8 <i>e</i> 1	0.2038(8)	0.6030(3)	0.4357(3)	0.0173(12)	1
O(12)	8 <i>e</i> 1	-0.0215(8)	0.6564(3)	0.5581(3)	0.0163(12)	1
O(13)	8 <i>e</i> 1	0.4452(8)	0.6641(3)	0.5502(3)	0.0183(12)	1
O(14)	4 <i>d</i> $\bar{2}m$	0.3061(10)	0.4482(4)	$\frac{3}{4}$	0.0178(17)	1
O(15)	4 <i>d</i> $\bar{2}m$	-0.6992(11)	0.3485(4)	$\frac{3}{4}$	0.0170(17)	1
O(16)	4 <i>d</i> $\bar{2}m$	-0.394(2)	0.6575(10)	$\frac{3}{4}$	0.132(9)	1
Cs(1)	8 <i>e</i> 1	-0.28867(8)	0.54778(3)	0.60995(3)	0.02581(15)	1

Cs(2)	8 e 1	-0.2761(1)	0.77973(5)	0.57516(6)	0.0260(4)	0.569(3)
-------	-------	------------	------------	------------	-----------	----------

^a Symmetry describes multiplicity, Wyckoff parameter and symmetry of the atomic site.

^b U_{eq} is defined as one-third of the trace of the orthogonalized U_{ij} tensor.

UV-vis-NIR Diffuse Reflectance Spectra. The diffuse reflectance spectra of **UCoP**, **UNiP**, and **UCuP** were measured from 1800 to 200 nm on a Shimadzu UV3100 spectrophotometer equipped with an integrating sphere attachment with BaSO₄ as the standard. Kubelka-Monk function was used in order to transfer reflectance data to arbitrary absorbance units.

Magnetic properties. Magnetic susceptibility measurements were conducted using a Quantum Design superconducting interference device (SQUID), under applied fields ranging from 100 to 10000 gauss as a function of temperature over the range of 5 – 320 K and magnetization data were collected at 5 K in fields ranging from 0 – 10,000 gauss. Samples were doubly encapsulated in aluminum containers, which contributed significantly to the measured signal, especially at higher temperatures and for samples with a low inherent susceptibility. Empty containers were run independently under the same conditions and the data used directly for background subtraction. Diamagnetic contributions to the data were also calculated and used to correct the measured susceptibility.

The temperature dependent magnetic susceptibility data were analyzed assuming Curie-Weiss behavior with an added temperature independent term, $\chi = C / (T-\theta) + \chi_{TIP}$, where C and θ are Curie and Weiss constants and χ_{TIP} is the temperature-independent contribution to the susceptibility. C is related to the effective magnetic moment

$\mu_{eff} = \left(\frac{3kC}{N_0 \mu_B^2} \right)^{1/2}$ in which N_0 is Avogadro's number and μ_B is the Bohr magneton (0.927 x 10⁻²⁰ erg/Gauss). For cases in which χ_{TIP} is small, the effective magnetic moment can

be obtained directly from the slope of the temperature dependence versus inverse magnetic susceptibility.

Ion-exchange Studies. NaCl, KCl, CsCl, CaCl₂, and SrCl₂ solutions were used in order to estimate ion-exchange capacities of **UCoP** and **UCuP**. Concentrations of the solutions of different cations were measured with classic potentiometric methods with ion-selective electrodes for K⁺, Na⁺, and Cs⁺ uptake,²⁵ using an Accumet A15 pH meter, and atomic adsorption spectroscopy, using a Varian 240 AA spectrometer with hollow cathode Ca and Sr lamps for Ca²⁺ and Sr²⁺ uptake.

K⁺-, Na⁺- and Cs⁺-selective membranes were made in according with Fluka recommended compositions. Silver/silver chloride electrode was used as a reference.²⁵ In order to prevent contamination of tested solutions with KCl the reference electrode with double junction and lithium acetate as a bridging electrolyte were utilized.

In all cases samples were equilibrated in the 5 ml capped vials with different cation solutions of known concentration for 48 hours at constant shaking, and then the change in the concentrations were determined. The approximate volume to mass ratio 200:1 (4 ml of the solution for 0.02 g of sample) was used in all experiments.

Additionally the kinetic of Sr²⁺ uptake was studied using a ⁹⁰Sr source. 10 µL of ⁹⁰Sr²⁺ with initial activity 20 µCi/milliliter was added to the Sr²⁺ solution. One milliliter aliquots were taken at different time intervals, mixed with 19 mL of scintillation cocktail, placed in a scintillation counter and counted for 200 sec.

RESULTS AND DISCUSSION

Syntheses. In order to investigate new pathways to the formation of uranyl-containing framework materials we have studied the interaction of pure transition metals with an acidic reaction mixture that contains uranyl nitrate, phosphoric acid, and alkali metal chloride under hydrothermal conditions. As Grohol and Nocera discussed for vanadium jarosites formation,²⁶ slow oxidation of metallic vanadium, due to the passivation of the vanadium surface, can be the rate-limiting step in the formation of the product. We suggest that rate-limiting oxidation and therefore the dissolving step provides slow introduction of the transition metal to the reaction and enforces the formation of the multicomponent system instead of a mixture of separate metal and uranyl phosphates. But due to passivation of the metal surface the reaction is not completed and traces of metal particles can be found in the product mixture. In the same study the authors have searched for potential oxidants for the vanadium metal. They proposed that oxygen, dissolved in water, or protons could be simultaneously reduced, and therefore could serve as oxidants. But reaction under a nitrogen atmosphere yielded the same product as under oxygen atmosphere. That result revealed the oxidation nature of the protons.²⁶ The oxidation potential of the $\text{Co}^0/\text{Co}^{2+}$, $\text{Ni}^0/\text{Ni}^{2+}$, and $\text{Cu}^0/\text{Cu}^{2+}$ are +0.28 V, +0.25 V and +0.15 V respectively and therefore metals can extrude the hydrogen from the phosphoric acid. Hence we can summarize that protons act as oxidizing agents in our uranyl-transition metal-phosphate formation reaction.

This statement has three important practical consequences. At first, we can conclude that the formation of all uranyl-transition metal-phosphates **UCoP**, **UNiP**, **UCuP**, **UTiP**, **UV^VP** and **KUV^{IV}P** (**RbUV^{IV}P**) could proceed only in acidic conditions

and an increase in pH usually led to the lower product content. In addition, according to suggested rate-limiting oxidation of transition metals, we could obtain near quantitative yield of the desired products by increasing the temperature and time of the reaction. Finally these general rules can be applied to most members of first-row transition metals, enabling uranyl-first row transition metal phosphate framework products with different structures and therefore with different properties to be produced in high yield.

Structure. $\text{Cs}_2\{(\text{UO}_2)_4[\text{Co}(\text{H}_2\text{O})_2]_2(\text{HPO}_4)(\text{PO}_4)_4\}$ (**UCoP**) and $\text{Cs}_2\{(\text{UO}_2)_4[\text{Ni}(\text{H}_2\text{O})_2]_2(\text{HPO}_4)(\text{PO}_4)_4\}$ (**UNiP**). The structure of **UCoP** and **UNiP** contain three crystallographically unique uranium atoms, two of which are in pentagonal bipyramidal environments and one of which is in a hexagonal bipyramidal geometry. The fundamental building unit of **UCoP** and **UNiP** is shown in Figure 6.1. In each case, there is a central uranyl core designated by two short U=O distances. The uranyl bond distances are within expected limits and range from 1.767(5) to 1.800(6) Å. The uranyl units form longer interactions with the oxygen atoms from the phosphate anions. These distances range from 2.263(5) Å to 2.507(6) Å for **UCoP** and from 2.308(6) Å to 2.505(6) Å for **UNiP**. The interaction of the uranyl cations and phosphate anions creates layers in the $[ab]$ plane. These layers are a new topology for a uranium oxide.^{1,2} (Figure 6.2) There is one crystallographically unique disordered phosphate anion present in the layer. Other than the disordered unit, the phosphate units are approximately tetrahedral with normal P-O bond distances. The uranyl phosphate layers are joined together by octahedral Co or Ni centers wherein the Co (Ni) is bound by phosphate and two cis water molecules. In addition, the Co or Ni ions are also ligated by a uranyl oxo atom from the

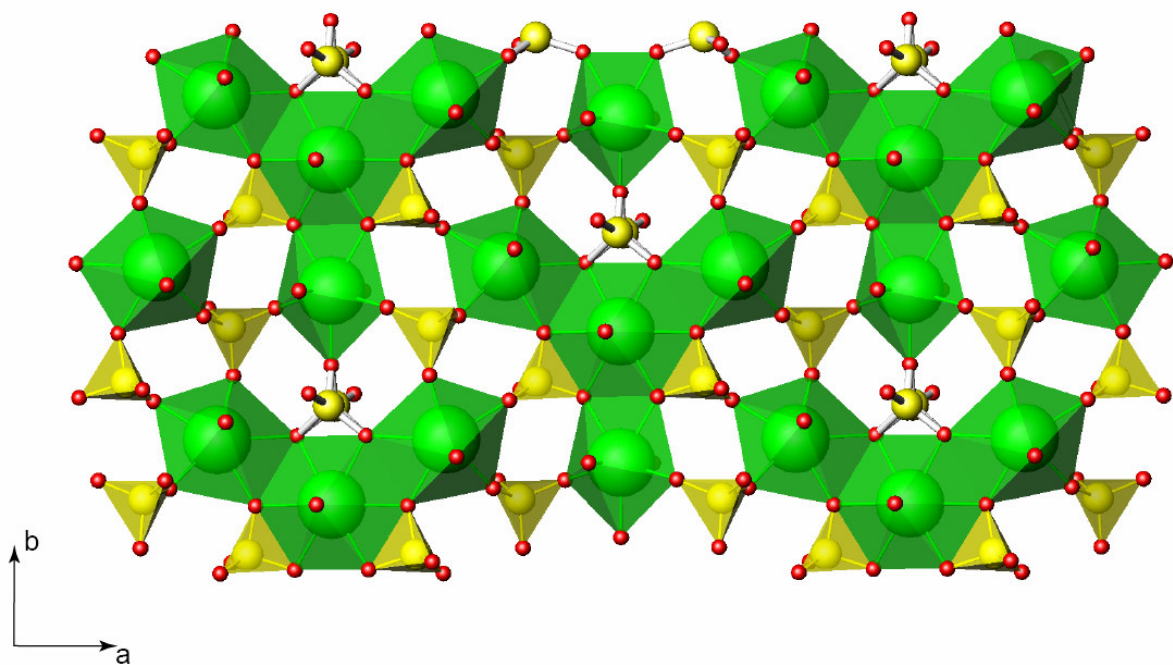


Figure 6.2. View down the c axis of the uranyl phosphate layers in **UCoP** and **UNiP**. One of the phosphate anions is disordered and is shown in ball-and-stick format. Uranium polyhedra are in green and phosphate are in yellow.

U(3) uranyl unit. This Co-O bond distance is 2.105(5) Å and Ni-O distance is 2.065(6) Å, and it fits well within the other Co-O or Ni-O bond distances, which range from 2.031(5) Å to 2.159 (6) Å in UCoP and from 2.018(6) Å to 2.116(6) Å in **UNiP**. Bond distances and angles are summarized in Tables 6.5 and 6.6. This kind of interaction is rare,²⁷⁻³² but is known from compounds such as [Cu(H₂O)₄](UO₂HGeO₄)₂·2H₂O.³² The Co and Ni centers form dimers via two μ₃-oxo atoms from two phosphate anions. The presence of these octahedral building units stitches the structure together into a three-dimensional framework where void spaces are filled by Cs⁺ cations. (Figure 6.3) There are channels 5.0 Å × 5.0 Å in this structure that extend down the *b* axis. The method of construction of this mixed metal phosphate differs from that of **UGaP1**, **UGaP2**, **UTiP**, **UGeP**, **UV^VP**, **KUV^{IV}P**, and **RbUV^{IV}P**. Bond-valence sum calculations provide values of 6.08 (6.10), 6.24 (6.22), and 6.07 (6.04) for U(1), U(2), and U(3), respectively, confirming the expected oxidation state of +6.³³ More importantly, the sum for the Co and Ni center is 1.98 and 1.95 respectively, consistent with that of Co^{II} and Ni^{II}.^{34,35}

Totalling the charges of the metal centers and phosphate anions reveals that there must be one proton within the structure. This proton most likely resides on the terminal oxygen atom of the phosphate anion containing P(1). Unfortunately, the disorder of this anion does not allow for conclusive bond distance comparisons.

Cs_{3+x}[(UO₂)₃CuH_{4x}(PO₄)₅]·H₂O (UCuP). Similar to the structure of **UCoP** and **UNiP**, **UCuP** contains two-dimensional uranyl phosphate layers that are linked into a three-dimensional structure by a transition metal center. Beyond this general similarity, the structures of **UCoP** (**UNiP**) and **UCuP** are dramatically different for a number of reasons. One of these is that there are two crystallographically unique uranium centers in

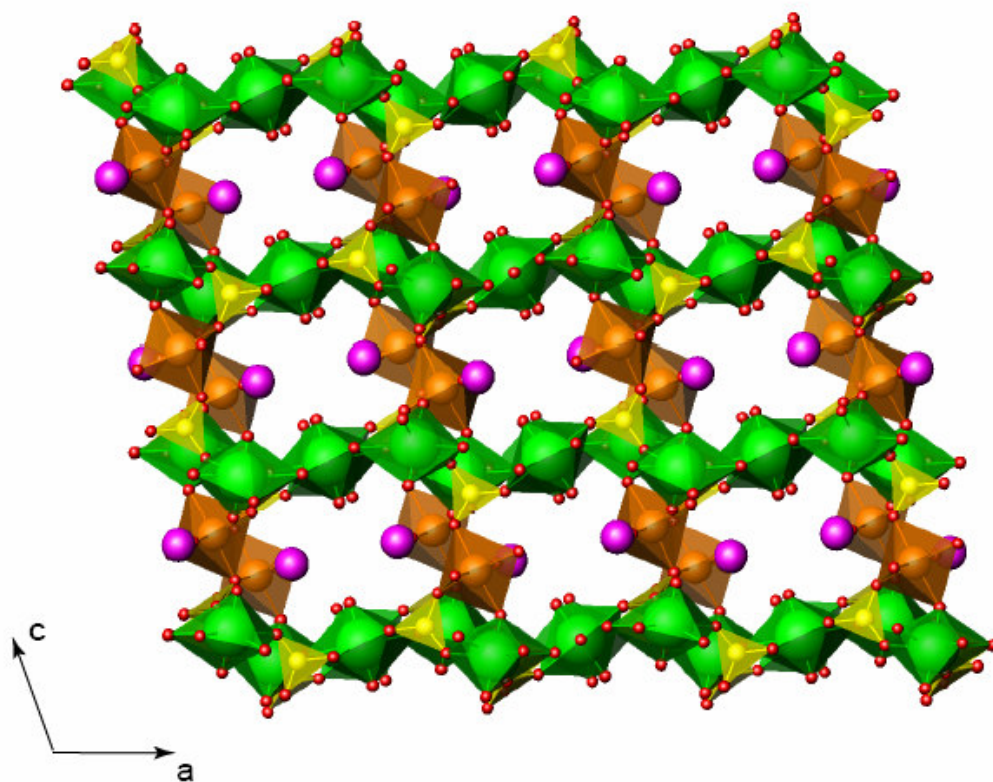


Figure 6.3. An illustration of the three-dimensional structure of **UCoP** and **UNiP** as viewed down the *b* axis. Uranium polyhedra are in green, phosphate in yellow, cobalt or nickel in orange. Purple centers represent the Cs⁺ cations.

Table 6.5. Selected Bond Distances (Å) and Angles (°) for $\text{Cs}_2\{(\text{UO}_2)_4[\text{Co}(\text{H}_2\text{O})_2]_2(\text{HPO}_4)(\text{PO}_4)_4\}$ (**UCoP**).

Distances (Å)			
U(1)-O(12)	1.785(6)	Co(1)-O(10)	2.101(5)
U(1)-O(11)	2.302(5)	Co(1)-O(16)	2.105(5)
U(1)-O(1)	2.333(9)	Co(1)-O(14)	2.123(5)
U(1)-O(4)	2.411(5)	Co(1)-O(13)	2.159(6)
U(2)-O(17)	1.767(5)	P(1)-O(1)	1.358(9)
U(2)-O(4)	2.405(5)	P(1)-O(2)	1.602(11)
U(2)-O(5)	2.425(5)	P(1)-O(3)	1.491(7)
U(2)-O(3)	2.459(6)	P(2)-O(7)	1.497(5)
U(3)-O(15)	1.786(5)	P(2)-O(6)	1.516(5)
U(3)-O(16)	1.794(5)	P(2)-O(4)	1.557(5)
U(3)-O(8)	2.263(5)	P(2)-O(5)	1.563(5)
U(3)-O(9)	2.302(5)	P(3)-O(8)	1.521(5)
U(3)-O(6)	2.308(5)	P(3)-O(9)	1.536(5)
U(3)-O(5)	2.391(5)	P(3)-O(10)	1.555(5)
U(3)-O(3)	2.507(6)	P(3)-O(11)	1.539(5)
Co(1)-O(7)	2.031(5)	P(1)-P(1)	1.045(8)
Co(1)-O(10)	2.099(5)		
Angles (°)			
O(12)-U(1)-O(12)	179.2(4)	O(7)-Co(1)-O(14)	173.6(2)
O(17)-U(2)-O(17)	179.2(3)	O(10)-Co(1)-O(13)	177.0(2)
O(15)-U(3)-O(16)	178.1(2)	O(10)-Co(1)-O(16)	174.5(2)

Table 6.6. Selected Bond Distances (Å) and Angles (°) for $\text{Cs}_2\{(\text{UO}_2)_4[\text{Ni}(\text{H}_2\text{O})_2]_2(\text{HPO}_4)(\text{PO}_4)_4\}$ (**UNiP**).

Distances (Å)			
U(1)-O(12)	1.780(7)	Ni(1)-O(10)	2.067(6)
U(1)-O(11)	2.308(6)	Ni(1)-O(16)	2.065(6)
U(1)-O(1)	2.331(11)	Ni(1)-O(14)	2.083(6)
U(1)-O(4)	2.410(5)	Ni(1)-O(13)	2.116(6)
U(2)-O(17)	1.774(6)	P(1)-O(1)	1.352(11)
U(2)-O(4)	2.401(6)	P(1)-O(2)	1.661(15)
U(2)-O(5)	2.420(6)	P(1)-O(3)	1.504(8)
U(2)-O(3)	2.449(6)	P(2)-O(7)	1.501(6)
U(3)-O(15)	1.783(6)	P(2)-O(6)	1.509(6)
U(3)-O(16)	1.800(6)	P(2)-O(4)	1.562(6)
U(3)-O(8)	2.261(6)	P(2)-O(5)	1.562(6)
U(3)-O(9)	2.312(6)	P(3)-O(8)	1.521(6)
U(3)-O(6)	2.311(6)	P(3)-O(9)	1.544(6)
U(3)-O(5)	2.396(5)	P(3)-O(10)	1.548(6)
U(3)-O(3)	2.505(6)	P(3)-O(11)	1.538(6)
Ni(1)-O(10)	2.074(6)	P(1)-P(1)	1.061(9)
Ni(1)-O(7)	2.018(6)		
Angles (°)			
O(12)-U(1)-O(12)	179.6(5)	O(7)-Co(1)-O(14)	174.2(2)
O(17)-U(2)-O(17)	179.9(4)	O(10)-Co(1)-O(13)	177.8(2)
O(15)-U(3)-O(16)	177.4(3)	O(10)-Co(1)-O(16)	175.6(2)

UCuP that are found as UO_6 tetragonal bipyramids and UO_7 pentagonal bipyramids. (Figure 6.4) The uranyl $\text{U}=\text{O}$ bond distances for these two polyhedra range from 1.770(6) Å to 1.803(8) Å.

The equatorial U-O distances range from 2.236(5) Å to 2.514(5) Å. Selected bond distances and angles for **UCuP** are given in Table 6.7. Taking into account the differences in coordination number, these distances were used to calculate bond-valence sums of 5.96 and 6.08 for U(1) and U(2), respectively.³³ The uranyl moieties are bridged by phosphate anions into sinusoidal sheets that extend into the $[bc]$ plane. (Figure 6.5) Again, this is apparently a new layered topology for a uranium oxide compound.^{1,2} The uranyl phosphate layers in **UCuP** are interconnected by Cu centers that reside in square planar environments, being bound by four phosphate anions with two Cu-O distances of 1.962(6) Å and 1.964(6) Å. The bond-valence sum for the Cu site is 1.85 and is consistent with that of Cu^{II} .^{34,35}

The overall structure is three-dimensional. However, the structure is much less open than that of **UCoP** and **UNiP** or other mixed-metal uranyl transition metal phosphates prepared thus far. Channels for the Cs^+ cations and water molecules that are observed in other mixed-metal uranyl phosphate structures are not as distinct in **UCuP**, although there are found channels $3.2 \text{ Å} \times 4.1 \text{ Å}$ extending down the c axis. (Figure 6.6) Of interest, however, is that there are two Cs^+ sites within the channels. One of these sites is fully occupied. The second site is occupied by 0.57. This has important consequences for the degree of protonation for **UCuP**. There are two phosphate anions with terminal oxo atoms in the structure. For the phosphate anion containing P(1), there

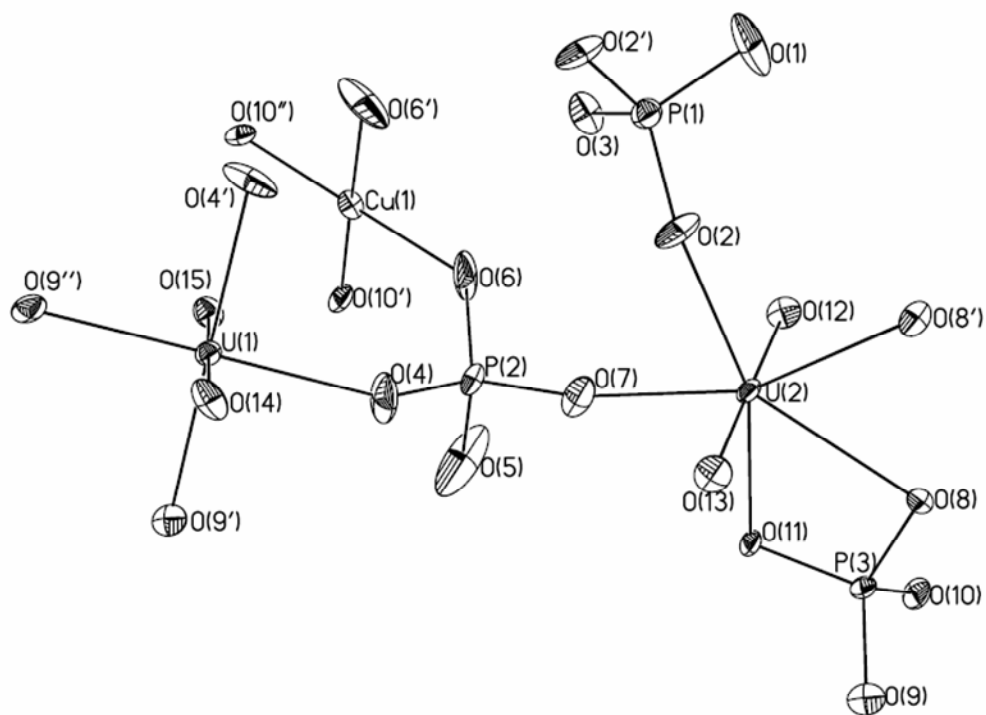


Figure 6.4. A view of the uranyl tetragonal and pentagonal bipyramids, square planar Cu and phosphate tetrahedra in **UCuP** with 50% probability ellipsoids.

Table 6.7. Selected Bond Distances (Å) and Angles (°) for $\text{Cs}_{3+x}[(\text{UO}_2)_3\text{CuH}_{4x}(\text{PO}_4)_5]\cdot\text{H}_2\text{O}$ (**UCuP**).

Distances (Å)			
U(1)-O(15)	1.782(8)	Cu(1)-O(6)	1.964(6)
U(1)-O(14)	1.803(8)	P(1)-O(2)	1.501(6)
U(1)-O(9)	2.236(5)	P(1)-O(1)	1.560(9)
U(1)-O(4)	2.254(6)	P(1)-O(3)	1.560(8)
U(2)-O(12)	1.770(6)	P(2)-O(4)	1.509(6)
U(2)-O(13)	1.777(6)	P(2)-O(6)	1.509(7)
U(2)-O(7)	2.263(6)	P(2)-O(7)	1.509(7)
U(2)-O(2)	2.310(6)	P(2)-O(5)	1.548(7)
U(2)-O(8)	2.369(5)	P(3)-O(10)	1.525(6)
U(2)-O(11)	2.399(5)	P(3)-O(11)	1.531(6)
U(2)-O(8)	2.514(5)	P(3)-O(9)	1.543(6)
Cu(1)-O(10)	1.962(6)	P(3)-O(8)	1.557(6)
Angles (°)			
O(15)–U(1)–O(14)	179.4(3)	O(10)–Cu(1)–O(6)	178.7(3)
O(9)–U(2)–O(4)	178.4(2)	O(6)–Cu(1)–O(6)	86.0(5)
O(10)–Cu(1)–O(10)	88.4(3)		

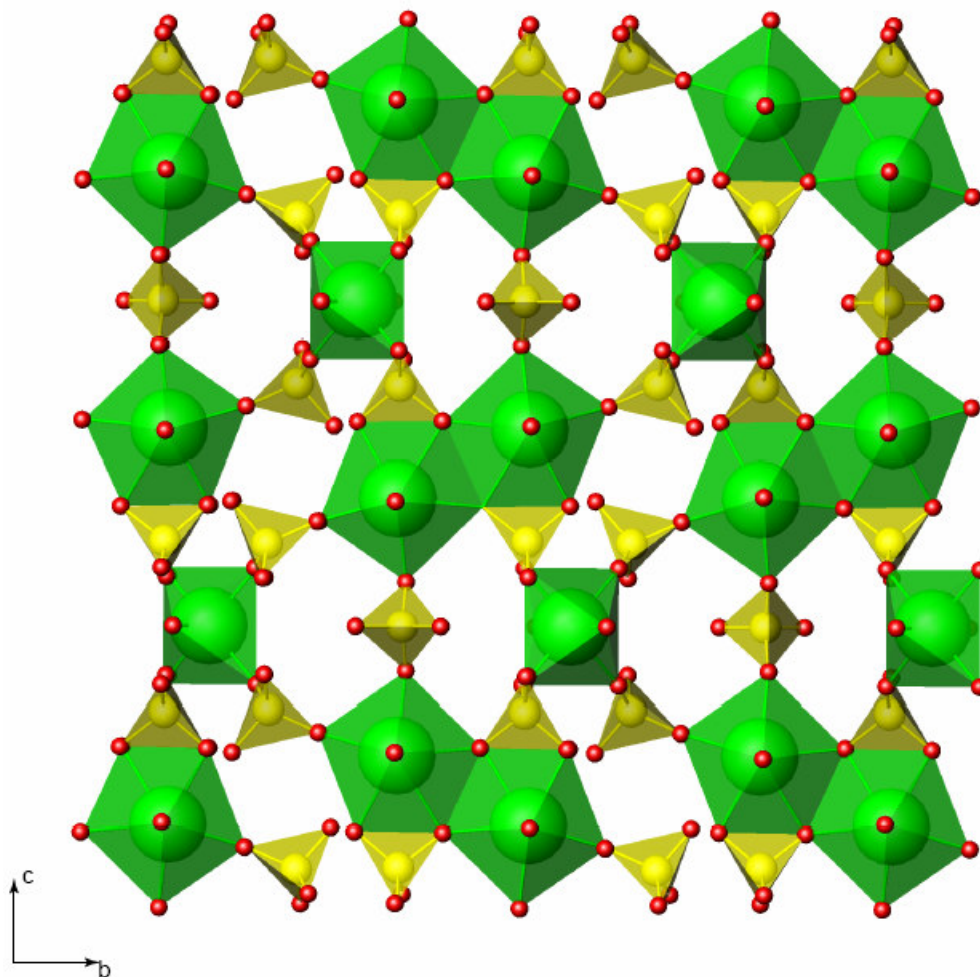


Figure 6.5. Depiction of uranyl phosphate layers in UCuP . Uranyl polyhedra are in green and phosphates are in yellow.

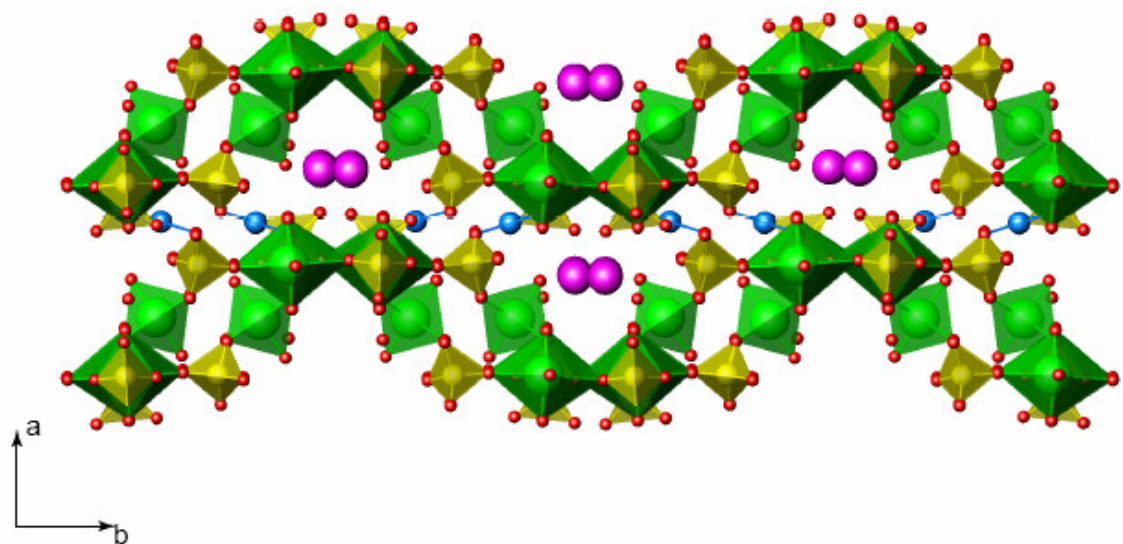


Figure 6.6. View of the three-dimensional structure of **UCuP** wherein the Cu^{II} centers link uranyl phosphate layers together. Uranium polyhedra are in green, phosphate in yellow, and copper in blue. Some of the Cs^+ sites have been omitted for clarity.

are two terminal oxo atoms with P-O bond distances of 1.560(9) Å, as compared to the bridging P-O bond distances of 1.501(6) Å. We propose that both of these aforementioned sites are protonated. A second phosphate anion containing P(2) has three bridging P-O bond distances of 1.509(7) Å and one terminal distance of 1.548(7) Å. This latter site is likely to be protonated also. However, if all three of these terminal sites are fully protonated, then there is an excess positive charge of 0.14. A closer look at the terminal oxygen atom around P(2) reveals an elongated thermal ellipsoid for this atom. We speculate that this elongation represents an average of protonated and deprotonated oxygen positions. Therefore, a potentially correct formula for **UCuP** can be written as $\text{Cs}_{3.14}[(\text{UO}_2)_3\text{Cu}(\text{H}_2\text{PO}_4)(\text{H}_{1.93}\text{PO}_4)_2(\text{PO}_4)_2]\cdot\text{H}_2\text{O}$.

UV-vis-NIR diffuse reflectance study. Spectroscopic verification of the oxidation state for Co, Ni and Cu was provided by UV-vis-NIR diffuse reflectance spectroscopy. In the case of **UCoP** (Figure 6.8) the spectrum yields three main bands that are expected for octahedral Co^{II} .³⁶ ${}^4\text{T}_{2g} \rightarrow {}^4\text{T}_{1g}$ transition is located at 9700 cm^{-1} (1030 nm). The band at 19100 cm^{-1} (525 nm) matches with ${}^4\text{T}_{1g}(\text{P}) \rightarrow {}^4\text{T}_{1g}$, that is usually seen in the visible region. Additionally, a very weak band located around 13000 cm^{-1} (770 nm), corresponds to an ${}^4\text{A}_{2g}$ transition, which usually appears as a shoulder.

The spectrum of **UNiP** (Figure 6.9) reveals three main bands at 10100 cm^{-1} (990 nm), 16700 cm^{-1} (600 nm) and 21200 cm^{-1} (470 nm), that correspond to spin allowed transitions from ${}^3\text{A}_{2g}$ to ${}^3\text{T}_{2g}$, ${}^3\text{T}_{1g}$ ${}^3\text{T}_{1g}(\text{P})$ respectively. Also two weak features of spin forbidden transitions to ${}^1\text{E}_g$ and ${}^1\text{T}_{2g}$ at 14100 cm^{-1} (710 nm) and 18000 cm^{-1} (560 nm) might be seen at the spectra. These data are consistent with octahedral Ni^{II} .³⁶

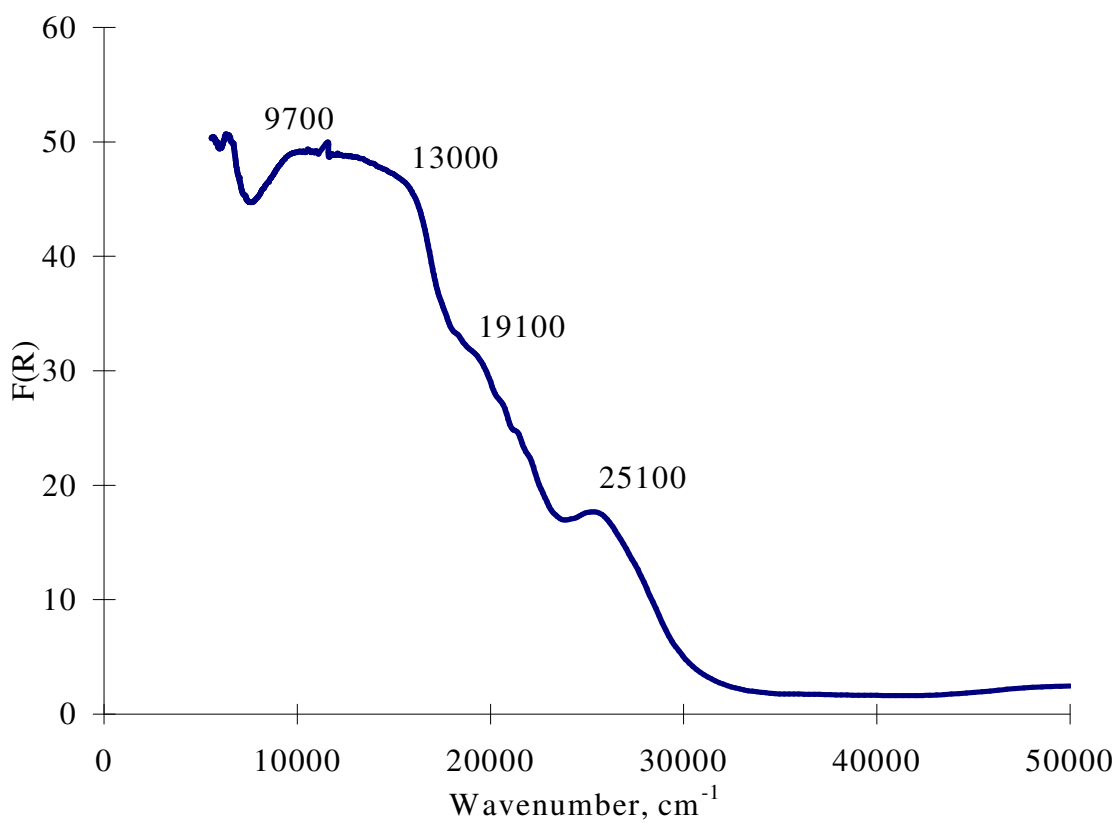


Figure 6.7. UV-vis-NIR diffuse reflectance spectrum of **UCoP**. F(R) corresponds to Kubelka-Monk function and relates reflectance data to the absorption spectra.³⁷

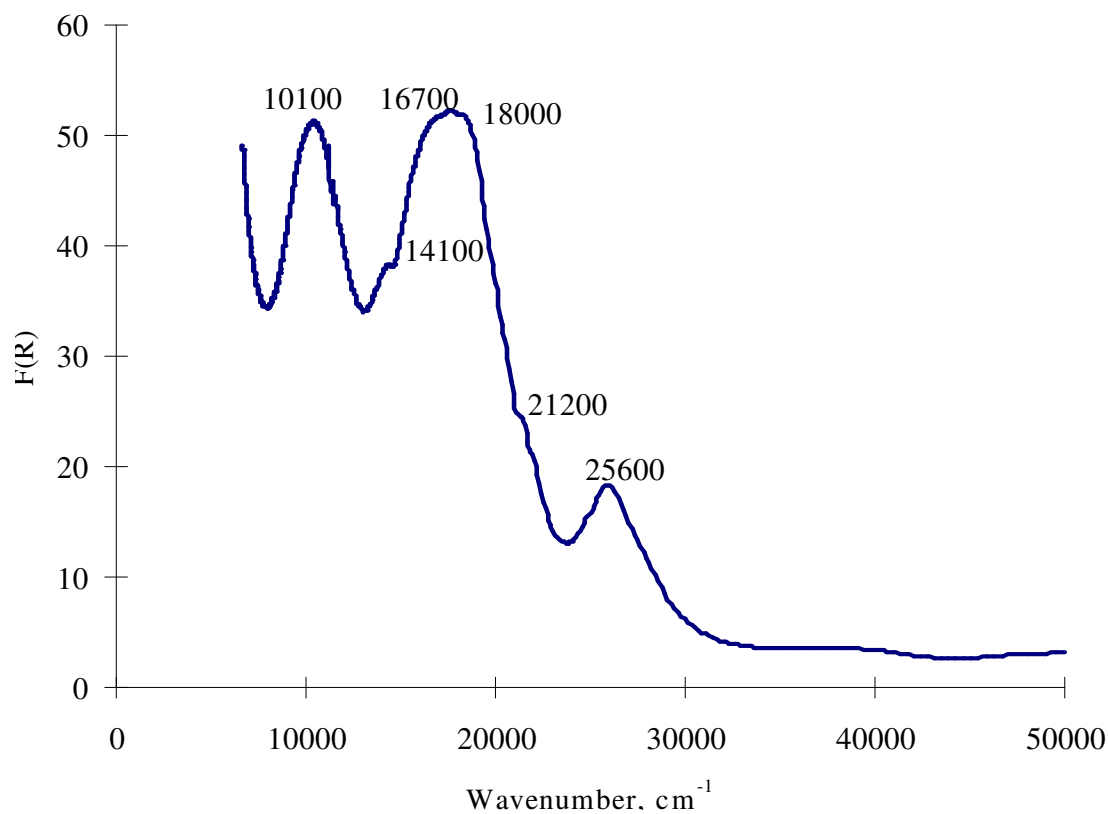


Figure 6. 8. UV-vis-NIR diffuse reflectance spectrum of **UNiP**. $F(R)$ corresponds to Kubelka-Monk function and relates reflectance data to the absorption spectra.³⁷

There is a broad band with a maximum at 17800 cm^{-1} (560 nm) in the spectra of **UCuP** corresponding to the d-d z^2 to $x^2 - y^2$ transition expected for square planar Cu^{II} .³⁶ (Figure 6.9)

In addition in all spectra, absorption features centered between 25100 cm^{-1} – 26000 cm^{-1} (380 – 400 nm) are present with considerable fine structure. These features are assigned to absorption by the uranyl cation.^{38,39}

Magnetization Measurements. The magnetic susceptibility of **UCoP** was measured as a function of temperature under a constant field of 2000 G. Such a large field was necessary to assure adequate counting statistics at higher temperature. Even at such a high field, only about 40% of the measured signal arises from the sample at higher temperatures. The linearity of the susceptibility of **UCoP** was verified by independent measurements of the magnetization at 5 K as a function of field at fields up to 2000 G. (Figure 6.10) The temperature dependence of the magnetic susceptibility of **UCoP**, along with its inverse, is shown in Figure 6.11. From the temperature dependence, there is no indication of any magnetic ordering down to 5 K, the lowest temperature measured. The absence of significant ferromagnetic or spin-glass behavior is supported by a comparison of field-cooled and zero-field-cooled data, which showed no significant differences. The effective magnetic moment, per mole of **UCoP** sample, was determined to be $4.95(10)\mu_{\text{B}}$ from the fit to the Curie-Weiss law, and measured χ_{TIP} and θ are $-0.00012(2)\text{ emu/mole Co}$ and $0.3(5)\text{ K}$, respectively. The effective magnetic moment obtained from the temperature dependence of inverse magnetic susceptibility between 100 and 300K is $4.99(5)$, which is consistent with moments observed in other

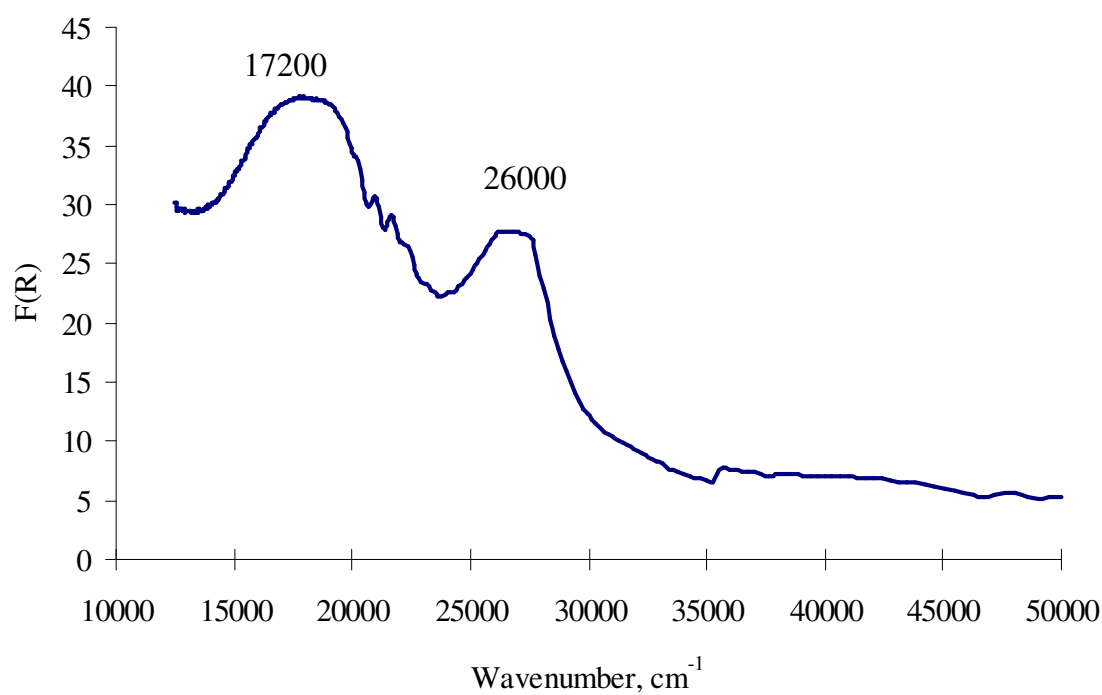


Figure 6.9. UV-vis-NIR diffuse reflectance spectrum for **UCuP**. F(R) corresponds to Kubelka-Monk function and relates reflectance data to the absorption spectra.³⁷

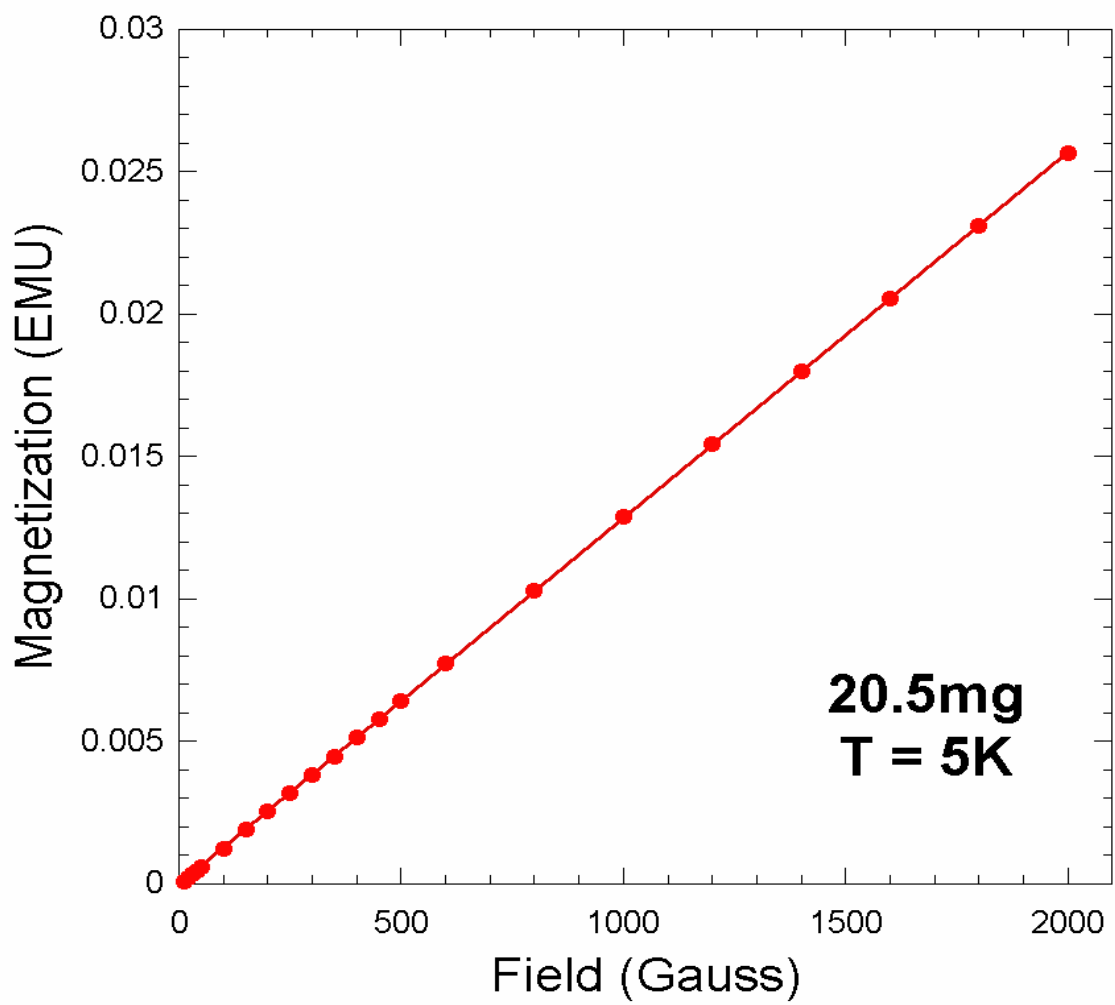


Figure 6.10. Magnetization of **UCoP** as a function of applied magnetic field at 5 K. Line is the linear fit to the data.

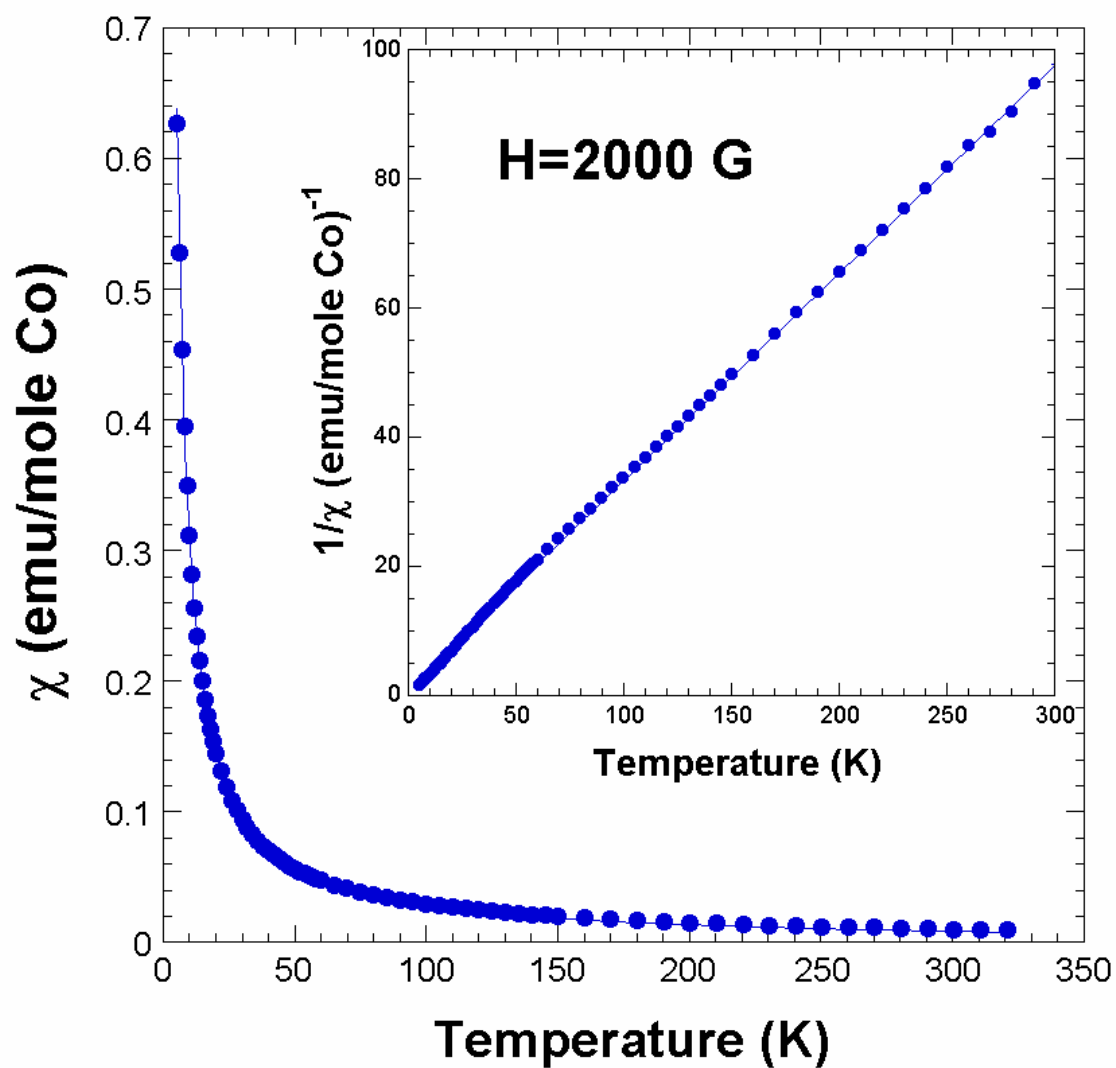


Figure 6.11. Magnetic susceptibility of **UCoP** as a function of temperature. Line is the fit to Curie-Weiss behavior. Inset shows the temperature dependence of the inverse magnetic susceptibility with a linear fit.

systems with octahedrally coordinated Co^{2+} ion. The χ_{TIP} is small and is consistent with isolated Co^{2+} spins, as is the Weiss constant.

The magnetization and the temperature dependence of the magnetic susceptibility of **UCuP** (Figure 6.12 and 6.13) show no evidence of magnetic ordering. Both field cooled and zero field cooled magnetic susceptibilities of **UCuP** were measured and are statistically indistinguishable, adding support to the absence of magnetic ordering seen from the temperature dependence. The effective magnetic moment for Cu^{2+} ion in this compound was determined to be $1.9(1) \mu_{\text{B}}$ from the fit to the Curie-Weiss law, and measured χ_{TIP} and θ are $0.0004(1) \text{ emu/mole Co}$ and $-0.3(5) \text{ K}$, respectively. The effective magnetic moment obtained is consistent with moments observed in other systems with Cu^{2+} ions.

Thermal analysis. In order to estimate the thermal stability of samples we have collected DSC data for **UCoP** and **UCuP** compounds. Both structural types demonstrate complicated thermal behavior. Loss of surface water of **UCoP** at 155°C is followed by a series of the endothermic events corresponding to the structural rearrangements, beginning at 273°C . (Figure 6.14) Two major events at 400°C and 414°C could be assigned to the loss of two crystallographically distinct water molecules bonded to the Co center. **UCuP** consequently loses surface and interstitial water at 130°C and 160°C . (Figure 6.15) The series of peaks, exothermic - at 290°C and endothermic - at the temperature above 400°C , clearly indicate decomposition of the structure and loss of crystallinity at high temperatures.

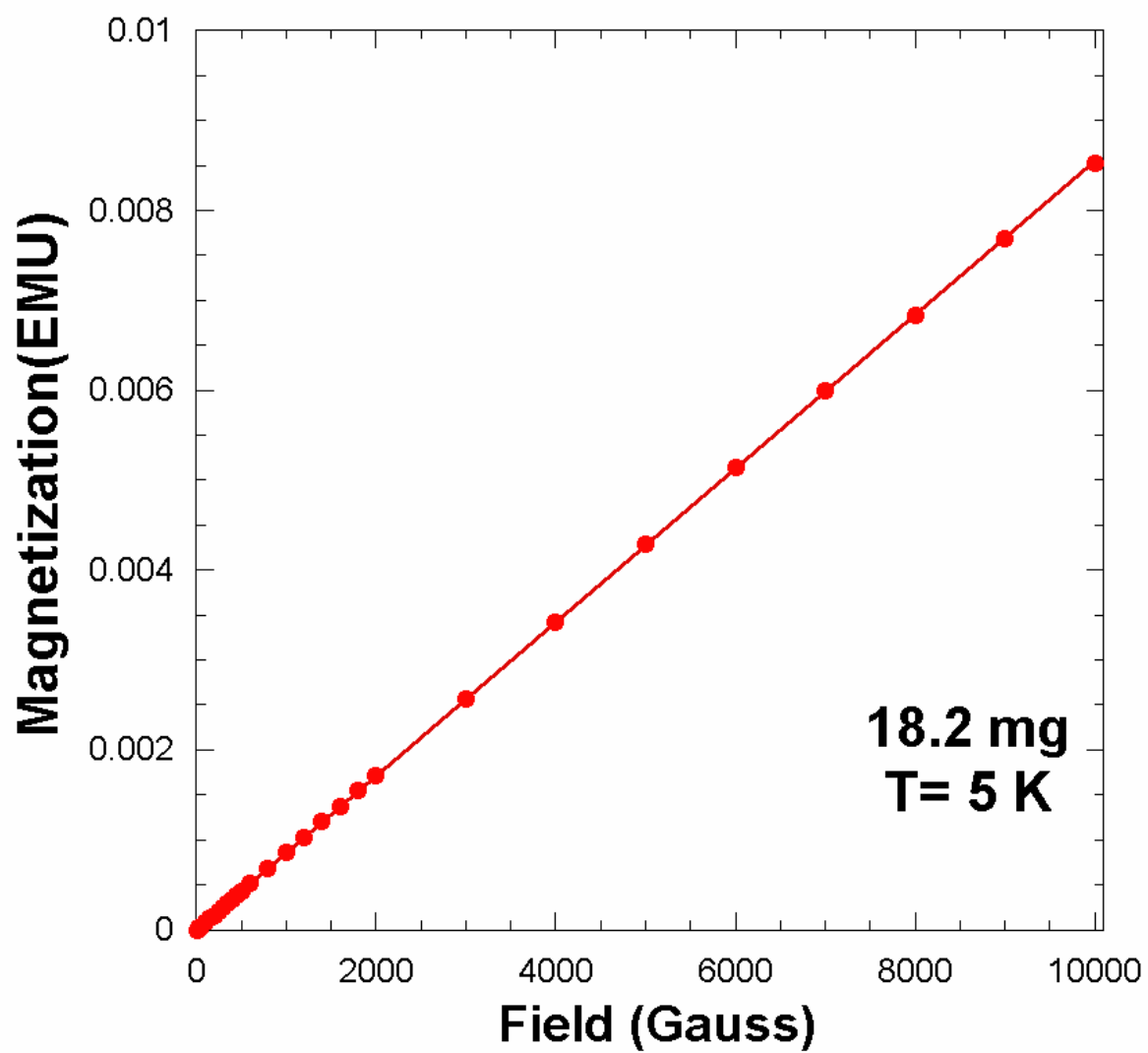


Figure 6.12. Magnetization of **UCuP** as a function of applied magnetic field at 5 K. Line is the linear fit to the data.

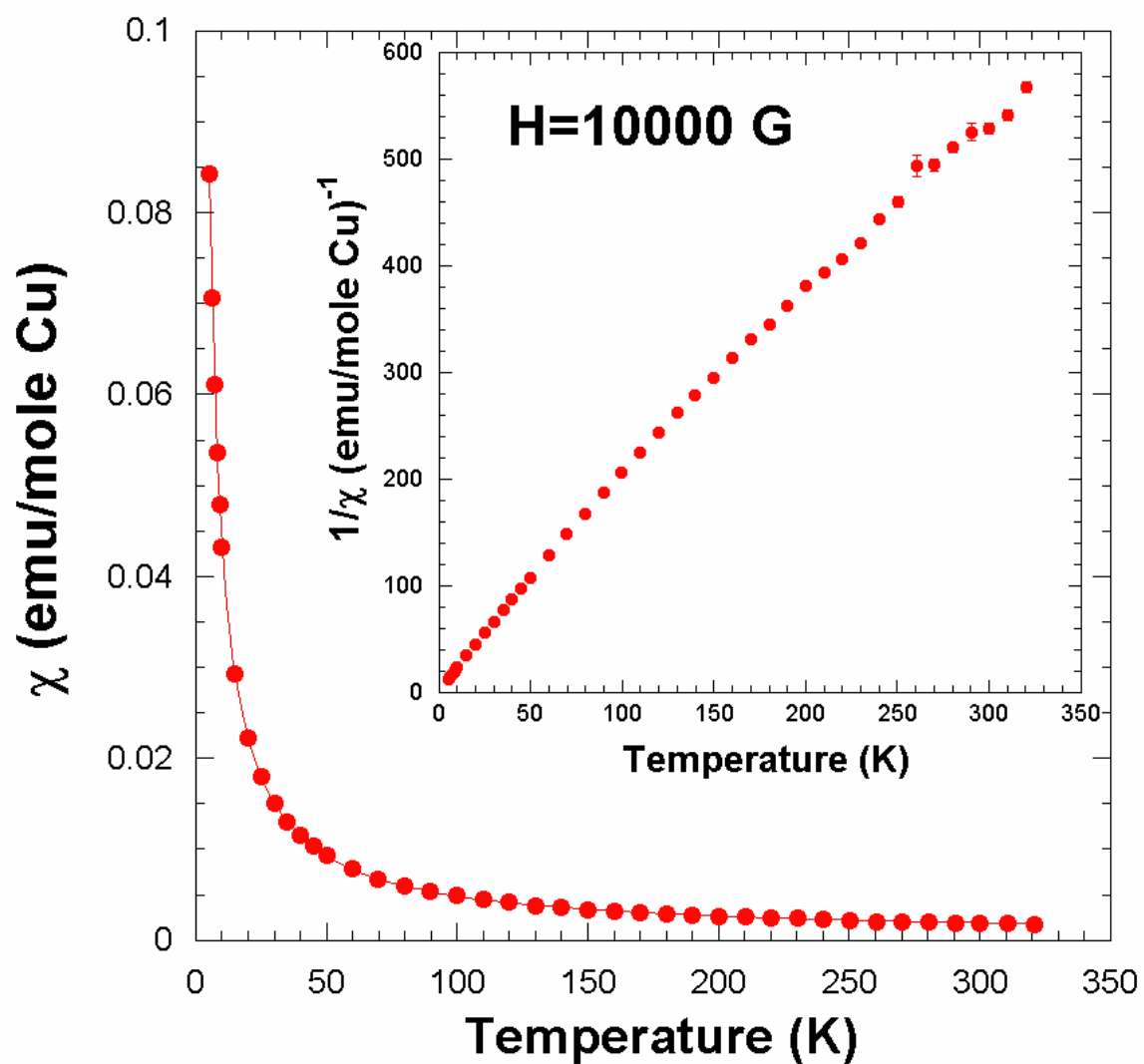


Figure 6.13. Magnetic susceptibility of **UCuP** as a function of temperature. Line is the fit to Curie-Weiss behavior. Inset shows the temperature dependence of the inverse magnetic susceptibility.

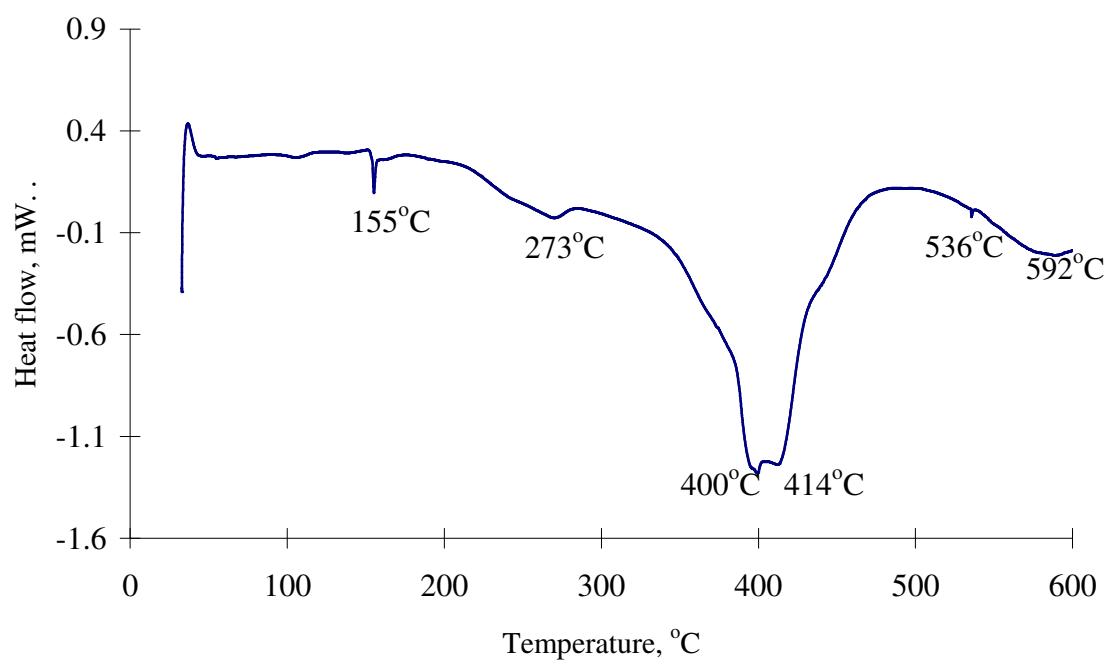


Figure 6.14. DSC data for UCoP.

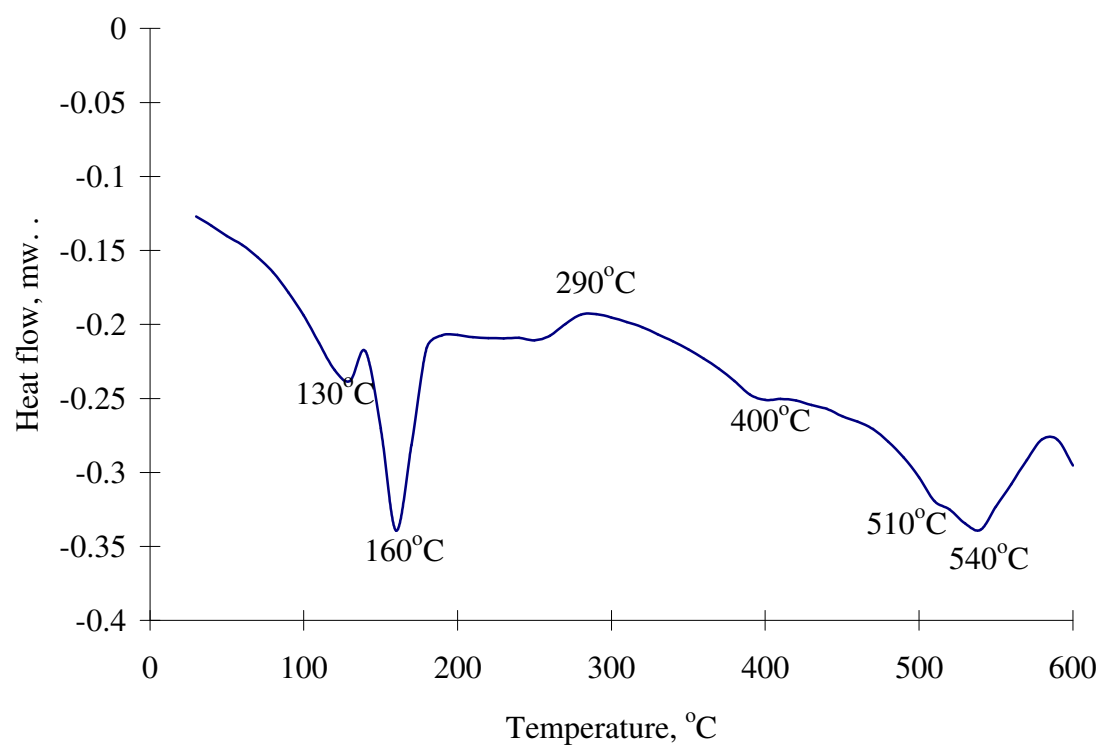


Figure 6.15. DSC data for UCuP.

Ion exchange properties. The difference in the structures of **UCoP** and **UCuP** leads to their different ion-exchange capabilities. The highest uptake from 1×10^{-2} M solutions of **UCoP** demonstrates toward Na^+ cations. The value is 0.6(1) meq/g that roughly corresponds to one half of the theoretical capacity and is consistent with the exchange of one out of two Cs^+ cations that occupy the channels. The pH of the solutions is not changed significantly during the exchange experiments that suggests protons do not participate in the exchange. The equilibration of the **UCoP** with CsCl solutions has also revealed no change of pH and Cs^+ concentration, which implies that there are no exchangeable protons in the structure. The capability toward Sr^{2+} and Ca^{2+} is smaller (0.28(6) meq/g and 0.20(8) meq/g, respectively). Assuming that 2 moles of Cs^+ are necessary for exchange with 1 mol of Sr^{2+} or Ca^{2+} , Sr^{2+} exchange corresponds only to one quarter of the calculated capacity. These results are significantly higher than Sr^{2+} uptake 0.1(2) meq/g, measured by radiotracer method. The measurements of radioactivity of Sr solution, containing ^{90}Sr isotope, after different time intervals of exchange, allow one to assume that 80% of exchange occurs within first 10 minutes after mixing. The lower uptake values can be explained by the much higher volume to mass ratio, exceeding 3000:1.

In the mixed solutions $\text{Ca}^{2+}/\text{Na}^+$, $\text{Sr}^{2+}/\text{Na}^+$ and $\text{Ca}^{2+}/\text{Sr}^{2+}$, the uptake of alkaline earth cations by **UCoP** is highly preferable with no exchange of Na^+ occurring. This selectivity can result from the relatively large size of the channels ($5.0 \text{ \AA} \times 5.0 \text{ \AA}$). Those channels are large enough to accommodate even hydrated cations, and radii of Ca^{2+} (4.1 Å) and Sr^{2+} (3.9 Å)⁴⁰ in their hydrated shells fit better than smaller Na^+ (3.6 Å).⁴⁰ Finally,

there is no selectivity found between Sr^{2+} and Ca^{2+} . They are taken from the mixed solutions in a 1:1 ratio.

UCuP ion-exchange experiments showed strong ion-exchange capacities toward double-charged cations with uptake values of 0.49 meq/g and 0.51 meq/g for Ca^{2+} and Sr^{2+} respectively and no exchange for Na^+ and K^+ . Again no selectivity between Ca^{2+} and Sr^{2+} is found in the mixed solutions. During the experiments it was noted that the pH of the solutions at ion-exchange equilibrium drops by approximately 3 units in all solutions. This might be explained either as participation of the structural protons that belong to the phosphoric acid in the exchange or presence of the excess of phosphoric acid on the surface of material. But due to the very similar change of pH, ranging within 0.4 units for all solutions and no notable dependence of this change from the concentration of present cation, we can rather accept that pH of the solutions is defined by the amount of phosphoric acid remaining on the surface after the synthesis.

CONCLUSION

The combination of the work reported herein along with our previous disclosures on $\text{Cs}_4[(\text{UO}_2)_2(\text{GaOH})_2(\text{PO}_4)_4] \cdot \text{H}_2\text{O}$,⁹ $\text{Cs}[\text{UO}_2\text{Ga}(\text{PO}_4)_2]$,⁹ $\text{Cs}_{1.52}[(\text{UO}_2)(\text{TiOH}_{0.48})(\text{PO}_4)_2] \cdot n\text{H}_2\text{O}$, $\text{Cs}_{1.35}[(\text{UO}_2)(\text{GeOH}_{0.65})(\text{PO}_4)_2] \cdot n\text{H}_2\text{O}$, $\text{Cs}_2[(\text{UO}_2(\text{VO}_2)_2(\text{PO}_4)_2] \cdot n\text{H}_2\text{O}$ ¹⁰ and $\text{K}_4(\text{UO}_2)(\text{VO})_4(\text{OH})_2(\text{PO}_4)_4$ ($\text{Rb}_4(\text{UO}_2)(\text{VO})_4(\text{OH})_2(\text{PO}_4)_4$) demonstrates that the construction of mixed-metal uranyl phosphates with three-dimensional framework structures can be accomplished by the interconnection of one-dimensional uranyl phosphate and main group or transition metal phosphate substructures, the linking of uranyl phosphate layers by transition metal centers, or linking of metal-phosphate layers

by uranyl centers. The main group or metal centers contained in these structures span from tetrahedral environments in **UGaP2** to square planar geometries in **UCuP**, to square pyramidal coordination in **UV^VP** to octahedral **UGaP1**, **KUV^{IV}P**, **RbUV^{IV}P**, **UCoP**, and **UNiP**. Likewise, the UO_6 tetragonal bipyramid, the UO_7 pentagonal bipyramid, and the UO_8 hexagonal bipyramid all occur in this small group of compounds, illustrating the remarkable structural diversity of U^{VI} . It is now clear that the incorporation of additional metal centers into uranyl phosphates provides for substantial enhancement in their ion-exchange, nonlinear optical, and magnetic properties.

REFERENCES

1. Burns, P. C.; Miller, M. L.; Ewing, R.C. *Can. Mineral.* **1996**, 34, 845.
2. Burns, P. C. *Can. Mineral.* **2005**, 43, 1839.
3. Johnson, C. H.; Shilton, M. G.; Howe, A. T. *J. Solid State Chem.* **1981**, 37, 37.
4. Pozas-Tormo, R.; Moreno-Real, L.; Martinez-Lara, M.; Rodriguez-Castellon, E. *Can. J. Chem.* **1986**, 64, 35.
5. Moreno-Real, L.; Pozas-Tormo, R.; Martinez-Lara, M.; Bruque-Gamez, S. *Mater. Res. Bull.* **1987**, 22, 19.
6. Dieckmann, G. H.; Ellis, A. B. *Solid State Ionics* **1989**, 32/33, 50.
7. Grohol, D.; Blinn, E. L. *Inorg. Chem.* **1997**, 36, 3422.
8. Shvareva, T. Y.; Almond, P. M.; Albrecht-Schmitt, T. E. *J. Solid State Chem.* **2005**, 178, 499.
9. Shvareva, T. Y.; Sullens, T. A.; Shehee, T. C.; Albrecht-Schmitt, T. E. *Inorg. Chem.* **2005**, 44, 300.
10. Shvareva, T. Y.; Beitz, J. V.; Duin, E. C.; Albrecht-Schmitt, T. E. *Chem. Mater.* **2005**, 17, 6219.
11. Locock, A. J.; Burns, P. C. *J. Solid State Chem.* **2004**, 177, 2675.
12. Burns, P. C.; Alexopoulos, C. M.; Hotchkiss, P. J.; Locock, A. *Inorg. Chem.* **2004**, 43, 1816.
13. Locock, A. J.; Burns, P. C. *J. Solid State Chem.* **2003**, 176, 18.
14. Locock, A. J.; Burns, P. C. *J. Solid State Chem.* **2003**, 175, 372.
15. Locock, A. J.; Burns, P. C. *J. Solid State Chem.* **2002**, 167, 226.
16. Locock, A. J.; Burns, P. C. *J. Solid State Chem.* **2002**, 163, 275.

17. Doran, M. B.; Stuart, C. L.; Norquist, A. J.; O'Hare, D. *Chem. Mater.* **2004**, *16*, 565.
18. Huang, J.; Wang, X.; Jacobson, A. J. *J. Mater. Chem.* **2003**, *13*, 191.
19. Krivovichev, S. V.; Burns, P. C.; Armbruster, Th.; Nazarchuk, E. V.; Depmeier, W. *Micropor. Mesopor. Mater.* **2005**, *78*, 217.
20. Doran, M.; Norquist, A. J.; O'Hare, D. *Chem. Commun.* **2002**, *24*, 2946.
21. Doran, M.; Walker, S. M.; O'Hare, D. *Chem. Commun.* **2001**, *19*, 1988.
22. Walker, S. M.; Halasyamani, P. S.; Allen, S.; O'Hare, D. *J. Am. Chem. Soc.* **1999**, *121*, 10513.
23. Sheldrick, G. M. SHELXTL PC, Version 6.12, An Integrated System for Solving, Refining, and Displaying Crystal Structures from Diffraction Data; Siemens Analytical X-Ray Instruments, Inc.: Madison, WI 2001.
24. Sheldrick, G. M. SADABS 2001, Program for absorption correction using SMART CCD based on the method of Blessing: Blessing, R. H. *Acta Crystallogr.* **1995**, *A51*, 33.
25. Buehlmann, P.; Pretsch, E.; Bakker, E. *Chem. Rev.* **1998**, *98*, 1593.
26. Grohol, D.; Nocera, D. G. *J. Amer. Chem. Soc.* **2002**, *124*, 2641
27. Rose, D.; Chang, Y.-D.; Chen, Q.; Zubieta, J. *Inorg. Chem.* **1994**, *33*, 5167.
28. Thue'ry, P.; Nierlich, M.; Souley, B.; Asfari, Z.; Vicens, J. *J. Chem. Soc., Dalton Trans.* **1999**, *15*, 2589.
29. Taylor, J. C.; Ekstrom, A.; Randall, C. H. *Inorg. Chem.* **1978**, *17*, 3285.
30. Brandenburg, N. P.; Loopstra, B. *Acta Crystallogr.* **1978**, *B34*, 3734.
31. Sullens, T. A.; Jensen, R. A.; Shvareva, T. Y.; Albrecht-Schmitt, T. E. *J. Am. Chem. Soc.* **2004**, *126*, 2676.

32. Legros, J. P.; Jeannin, Y. *Acta Crystallogr.* **1975**, *B31*, 1133.
33. Burns, P. C.; Ewing, R. C.; Hawthorne, F. C. *Can. Mineral.* **1997**, *35*, 1551.
34. Brown, I. D.; Altermatt, D. *Acta Crystallogr.* **1985**, *B41*, 244.
35. Brese, N. E.; O'Keeffe, M. *Acta Crystallogr.* **1991**, *B47*, 192.
36. Lever, A. B. P. *Inorganic Electronic Spectroscopy*, 2nd ed.; Elsevier: New York, 1984.
37. Kortum, G. *Reflectance Spectroscopy*, Springer-Verlag: New York, 1969.
38. Carnall, W. T.; Crosswhite, H. M. In *The Chemistry of the Actinide Elements*; Katz, J. J., Seaborg, G. T., Morss, J. R., Eds.; Chapman and Hall: London, 1986; Chapter 16.
39. Denning, R. G.; Norris, J. O. W.; Short, I. G.; Snellgrove, T. R.; Woodward, D. R. In *Lanthanide and Actinide Chemistry and Spectroscopy*; Edelstein, N. M., Ed.; ACS Symposium Series 131; American Chemical Society: Washington, DC, 1980; Chapter 15.
40. Nightingale, E.R. *J. Phys. Chem.* **1959**, *63*, 1381.

CHAPTER 7

SUMMARY

This chapter is a summary of data and discussions reported in the dissertation, as well as general conclusions.

All reported compounds are crystalline solids synthesized under hydrothermal conditions at the temperatures between 180 °C and 220 °C. The structures were determined using single crystal X-ray diffraction. Spectroscopic data, second-harmonic generation of light, thermal analysis, magnetic susceptibility, and ion-exchange were employed in order to characterize these materials.

Chapter 2 describes the structure and ion-exchange properties of the potassium uranyl iodate, $\text{K}[\text{UO}_2(\text{IO}_3)_3]$ (**KUI**). This compound was prepared as a continuation of the search for novel uranyl iodates, conducted in our group. **KUI** has a structure consisting of layers of uranyl iodate with potassium cations located between the layers. The K^+ can be exchanged with Cs^+ with uptake value of 1.7 meq/g.

Two novel uranyl gallium phosphates, $\text{Cs}_4[(\text{UO}_2)_2(\text{GaOH})_2(\text{PO}_4)_4] \cdot \text{H}_2\text{O}$ (**UGaP1**) and $\text{Cs}[\text{UO}_2\text{Ga}(\text{PO}_4)_2]$ (**UGaP2**) with open-framework structures are discussed in Chapter 3. These two compounds are the first result of our program for preparing uranyl compounds with three-dimensional open-framework structures with a particular focus on the use of octahedral centers, as building units. We suggested that incorporation of the octahedral building blocks in the structure, where bond formation is allowed in axial and

equatorial planes, will aid in the formation of frameworks. The three-dimensional structure of **UGaP1** is constructed in accordance with this hypothesis from uranyl pentagonal bipyramids, phosphate tetrahedra, and gallium octahedra. The **UGaP2** open-framework structure contains uranyl pentagonal bipyramids, phosphate and gallium tetrahedra, and no octahedral building blocks.

Both **UGaP1** and **UGaP2** structures have channels filled with Cs^+ cations. Ion-exchange experiments show the ability of the Cs^+ cations in **UGaP1** to be exchanged with divalent Ca^{2+} , Sr^{2+} , and Ba^{2+} , in **UGaP2** - with Ca^{2+} and Ba^{2+} . We were focused on the measurements of Sr^{2+} uptake in the presence of Na^+ due to the potential application of the ion-exchange materials for the removal of $^{90}\text{Sr}^{2+}$ from HLNW. The Sr^{2+} uptake in the presence of Na^+ cations is 0.4 meq/g. The thermal analysis revealed the absence of any structural changes of **UGaP1** up to 400 °C. These data indicate that **UGaP1** could be a potential ^{90}Sr selective material and should be studied further.

In Chapter 4,5, and 6 we have proposed a new synthetic approach of utilizing pure element powders as starting materials for hydrothermal synthesis. **UV^VP**, **KUV^{IV}P** (**RbUV^{IV}P**), **UTiP**, **UGeP**, **UCoP**, **UNiP**, and **UCuP** are obtained using this method. The presence of protons from phosphoric acid and oxygen in reaction vessel allow for slow oxidation of transition metals or germanium and rate-limiting delivery of oxidized reactant to the reaction mixture.

In Chapter 4 we reported three novel open-framework uranyl vanadium phosphates $\text{Cs}_2[\text{UO}_2(\text{VO}_2)_2(\text{PO}_4)_2] \cdot n\text{H}_2\text{O}$ (**UV^VP**), and isostructural $\text{K}_4(\text{UO}_2)(\text{VO})_4(\text{OH})_2(\text{PO}_4)_4$ (**KUV^{IV}P**) and $\text{Rb}_4(\text{UO}_2)(\text{VO})_4(\text{OH})_2(\text{PO}_4)_4$ (**RbUV^{IV}P**). The structure of **UV^VP** is built of tetragonal bipyramidal uranium, tetrahedral phosphate,

and square pyramidal vanadium building units. The terminal oxo atoms of vanadyl are aligned in one direction, causing the polarity of $\text{UV}^{\text{V}}\text{P}$ (space group $Cmc2_1$) and, as result, non-linear optical properties.

$\text{KUV}^{\text{IV}}\text{P}$ and $\text{RbUV}^{\text{IV}}\text{P}$ are constructed from uranyl tetragonal bipyramids, tetrahedral phosphate and vanadyl octahedral building blocks. K^+ or Rb^+ cations are located in the channels and can be exchanged by Cs^+ in the presence of Na^+ . Again, this material can be proposed for removal of $^{137}\text{Cs}^+$ from nuclear waste. $\text{KUV}^{\text{IV}}\text{P}$ and $\text{RbUV}^{\text{IV}}\text{P}$ also demonstrate paramagnetic behavior at the temperatures between 100 K and 320 K and antiferromagnetic ordering at 52 K.

The isostructural compounds $\text{Cs}_{1.52}[(\text{UO}_2)(\text{TiOH}_{0.48})(\text{PO}_4)_2] \cdot n\text{H}_2\text{O}$ (UTiP) and $\text{Cs}_{1.35}[(\text{UO}_2)(\text{GeOH}_{0.65})(\text{PO}_4)_2] \cdot n\text{H}_2\text{O}$ (UGeP) are described in Chapter 5. The open-framework structures of these compounds include Ti or Ge in octahedral coordination environments. Ti and Ge octahedra form corner-sharing chains along the same direction as the terminal uranyl oxygen atoms are aligned, providing for the formation of three-dimensional structures.

In Chapter 6 we present the structures and properties of $\text{Cs}_2\{(\text{UO}_2)_4[\text{Co}(\text{H}_2\text{O})_2]_2(\text{HPO}_4)(\text{PO}_4)_4\}$ (UCoP), $\text{Cs}_2\{(\text{UO}_2)_4[\text{Ni}(\text{H}_2\text{O})_2]_2(\text{HPO}_4)(\text{PO}_4)_4\}$ (UNiP), isostructural with UCoP , and $\text{Cs}_{3+x}[(\text{UO}_2)_{3-x}\text{CuH}_{4-x}(\text{PO}_4)_5] \cdot \text{H}_2\text{O}$ (UCuP). Co and Ni in octahedral coordination environment are utilized in order to build UCoP and UNiP open-framework structures. Cu is incorporated in the three-dimensional structure of UCuP in square planar environments. All three open-framework structures have channels, occupied by Cs^+ cations. Cs^+ can be replaced by Sr^{2+} in the presence of Na^+ with uptake values 0.28 meq/g for UCoP and 0.51 meq/g for UCuP .

Thus, we can summarize that ten uranyl-containing open-framework and one layered material have been produced. The novel strategy of incorporation of octahedral building units in order to synthesize open-framework structures was successful. **UGaP1**, **KUV^{IV}P**, **RbUV^{IV}P**, **UCoP**, and **UNiP** are constructed in accordance with this strategy. Two of the materials (**KUI** and **KUV^{IV}P (RbUV^{IV}P)**) possess ion-exchange properties, selective for Cs⁺. Cations in four materials (**UGaP1**, **UCoP**, **UNiP**, and **UCuP**) can be selectively exchanged with Sr²⁺. These properties make **KUI**, **KUV^{IV}P (RbUV^{IV}P)**, **UGaP1**, **UCoP**, **UNiP**, and **UCuP** promising materials for the selective removal of ¹³⁷Cs⁺ and ⁹⁰Sr²⁺ from the highly radioactive nuclear waste. Thermally stable **UGaP1** could be recommended for the further investigations under the conditions simulating HLNW.